Development of QCM Gas Sensors for the Detection of Important Volatile Organic Compounds from Indian Cardamoms

Thesis Submitted By

Nilava Debabhuti

Doctor of Philosophy (Engineering)

Dept. of Instrumentation and Electronics Engineering

Faculty Council of Engineering and Technology

Jadavpur University

Kolkata- 700032, India

2022

JADAVPUR UNIVERSITY

KOLKATA – 700 032, INDIA

Index no: 192/17/E

Title of the thesis: **Development of QCM Gas Sensors for the Detection of Important Volatile Organic Compounds from Indian Cardamoms**

Name & Dept. of the Supervisor/s:

i) Dr. Prolay Sharma

Associate Professor
Department of Instrumentation and Electronics Engineering
Jadavpur University, Salt Lake Campus
Kolkata-700106, India.

ii) Prof. (Dr.) Mousumi Poddar Sarkar

Professor
Department of Life Sciences
3rd floor, Baker Laboratory,
Presidency University, Kolkata-700073, India.

iii) Prof. (Dr.) Nabarun Bhattacharyya

Director
School of Information Science and Technology
Maulana Abul Kalam Azad University of Technology (MAKAUT)
(Formerly West Bengal University of Technology)
Haringhata, Nadia- 741249, India.

List of Publications

Paper Published in International journals:

[1] N. Debabhuti, S. Neogi, S. Mukherjee, A. Dhar, P. Sharma, R.L. Vekariya, M.P. Sarkar, B. Tudu, N. Bhattacharyya, R. Bandyopadhyay, Mohd. Muddassir, Development of QCM sensor to detect α-terpinyl acetate in cardamom, Sensors and Actuators A: Physical. 319 (2021) 112521.

[2] N. Debabhuti, S. Mukherjee, S. Neogi, P. Sharma, U.H. Sk, S. Maiti, M.P. Sarkar, B. Tudu, N. Bhattacharyya, R. Bandyopadhyay, A study of vegetable oil modified QCM sensor to detect β-pinene in Indian cardamom, Talanta. 236 (2022) 122837.

[3] N. Debabhuti, S. Mukherjee, S. Manna, A. Sengupta, P. Sharma, M.P. Sarkar, B. Tudu, N. Bhattacharyya, R. Bandyopadhyay, Development of a portable and low-cost device for QCM sensor-based detection of α-pinene in Cardamom, Sensors and Actuators B: Chemical (under review).

[4] N. Debabhuti, S. Mukherjee, S. Manna, P. Sharma, M.P. Sarkar, B. Tudu, N. Bhattacharyya, R. Bandyopadhyay, Development of modified castor oil coated QCM sensor for the detection and estimation of 1,8-cineole in Indian large cardamom, Sensors and Actuators B: Chemical (under review).

Publication as Book Proceeding: NIL

Publication as Book chapter: NIL

Papers published in International Conference Proceedings:

[1] N. Debabhuti, A. Sengupta, P. Sharma, R. Sen, B. Tudu, R. Bandyopadhyay, Development of the Data Acquisition System and GUI for QCM Sensor Based System, Social Science Research Network, Rochester, NY, 2020.

[2] N. Debabhuti, S. Neogi, A. Dhar, P. Sharma, B. Tudu, R. Bandyopadhyay, N. Bhattacharyya, Identification of The Important Volatile Organic Component in

Cardamom based on Silica-Modified Piezoelectric Resonator, 2020 IEEE 1st International Conference for Convergence in Engineering (ICCE), 2020: pp. 95–99.

[3] N. Debabhuti, S. Mukherjee, S. Malik, S. Manna, P. Sharma, B. Tudu, N. Bhattacharyya, R. Bandyopadhyay, Discrimination of Indian cardamom using an array of QCM sensors, International Symposium on Olfaction and Electronic Nose (ISOEN), 2022 (Accepted).

List of Patents: NIL

Statement of Originality

*I, **Nilava Debabhuti**, registered on the 8th of August, 2017, declare that this thesis entitled **"Development of QCM gas sensors for the detection of important volatile organic compounds from Indian cardamoms"** contains a literature survey and original research work done by the undersigned candidate as part of doctoral studies. All information in this thesis has been obtained and presented following existing academic rules and ethical conduct. I declare that, as required by these rules and conduct, I have fully cited and referred all materials and results that are not original to this work. I also declare that I have checked this thesis per the **"Policy on Anti Plagiarism, Jadavpur University, 2019"**, and the level of similarity as checked by iThenticate software is **4%.***

Nilava Debabhuti

Nilava Debabhuti

Index No. 192/17/E
Date: 25.07.2022

Prolay Sharma 25/07/2022

Dr. Prolay Sharma

Associate Professor
Department of Instrumentation and Electronics Engg.
Jadavpur University, Salt Lake Campus
Kolkata-700106, India.

Associate Professor
Dept. of Instrumentation & Electronics Engg.
Jadavpur University
Saltlake, 2nd Campus
Kolkata-700 098

Mousumi Poddar Sarkar 25/07/2022

Prof. (Dr.) Mousumi Poddar Sarkar

Professor
Department of Life Sciences
3rd floor, Baker Laboratory, Presidency University,
Kolkata-700073, India.

DR. MOUSUMI PODDAR SARKAR
PROFESSOR
Department of Life Sciences
Presidency University

25/07/2022

Prof. (Dr.) Nabarun Bhattacharyya

Director
School of Information Science and Technology
Maulana Abul Kalam Azad University of Technology
(MAKAUT)
(Formerly West Bengal University of Technology)
Haringhata, Nadia- 741249, India.

Prof. (Dr.) Nabarun Bhattacharyya
Director
School of Info. Sc. & Tech.
Maulana Abul Kalam Azad University
of Technology, West Bengal
(Formerly Known as West Bengal University of Technology)
Haringhata, Nadia - 741249, India

Certificate from the supervisors

Date: 25-07-2022

This is to certify that the thesis titled **"*Development of QCM gas sensors for the detection of important volatile organic compounds from Indian cardamoms*"** submitted by **Mr Nilava Debabhuti**, who got his name registered on 8th August 2017 for the award of Ph.D. (Engineering) degree of Jadavpur University, is based upon his work under the joint supervision of the undersigned; and neither that his thesis nor any part of it has been submitted for any degree/diploma or any other academic award anywhere before.

Prolay Sharma 25/07/2022

Dr. Prolay Sharma

Associate Professor
Department of Instrumentation and Electronics Engg.
Jadavpur University, Salt Lake Campus
Kolkata-700106, India.

Associate Professor
Dept. of Instrumentation & Electronics Engg.
Jadavpur University
Saltlake, 2nd Campus
Kolkata-700 098

Mousumi Poddar Sarkar 25/07/2022

Prof. (Dr.) Mousumi Poddar Sarkar

Professor
Department of Life Sciences
3rd floor, Baker Laboratory, Presidency University,
Kolkata-700073, India.

DR. MOUSUMI PODDAR SARKAR
PROFESSOR
Department of Life Sciences
Presidency University

25/07/2022

Prof. (Dr.) Nabarun Bhattacharyya

Director
School of Information Science and Technology
Maulana Abul Kalam Azad University of Technology
(MAKAUT)
(Formerly West Bengal University of Technology)
Haringhata, Nadia- 741249, India.

Prof. (Dr.) Nabarun Bhattacharyya
Director
School of Info. Sc. & Tech.
Maulana Abul Kalam Azad University
of Technology, West Bengal
(Formerly Known as West Bengal University of Technology)

Dedicated to my parents

Acknowledgements

First and foremost, I am incredibly grateful to my supervisors, **Dr. Prolay Sharma**, Associate Professor, Department of Instrumentation and Electronics Engineering, Jadavpur University, Kolkata, **Prof. Mousumi Poddar Sarkar**, Professor, Department of Life Sciences, Presidency University, Kolkata, and **Prof. (Dr.) Nabarun Bhattacharyya**, Director, School of Information Science and Technology Maulana Abul Kalam Azad University of Technology (MAKAUT), for their invaluable advice, continuous support, and patience during my PhD study. Their immense knowledge and ample experience have encouraged me throughout my academic research and daily life.

I express my gratitude to **Prof. Rajib Bandyopadhyay** and **Prof. Bipan Tudu**, Professor, Department of Instrumentation and Electronics Engineering, Jadavpur University, Kolkata, for their treasured support, which was influential in shaping my experiment methods and critiquing my results. I am also grateful to **Dr. Runu Banerjee Roy**, Professor, Department of Instrumentation and Electronics Engineering, Jadavpur University, Kolkata, for the suggestions and encouragement throughout the research work.

I am thankful to the Department of Instrumentation and Electronics Engineering, Jadavpur University, Kolkata, for allowing me to carry out my research works with all the necessary support and assistance. I want to express my sincere thanks to all of the faculties in our department for their consistent aid and insightful advice on many occasions. Additionally, I want to thank the entire Instrumentation & Electronics Engineering Department staff at Jadavpur University for their cooperation and support in completing this task.

I am highly obliged to **Dr. Ugir Hossain Sk**., Scientist, Clinical and Translational Research, Chittaranjan National Cancer Institute, Kolkata, for his valuable suggestions and chemical explanations for different experimental procedures.

I sincerely acknowledge the technical cooperation of CRNN, University of Calcutta, for SEM and FTIR analysis, Department of Physics, Jadavpur University, Kolkata, for the FESEM analysis. I

also would like to thank **Mr. Bhaskar Basu**, Central Instrument facility, CSIR-IICB, for sharing his valuable expertise regarding AFM analysis.

I sincerely acknowledge the financial support from the funding agencies, Fund for Improvement of S&T infrastructure in universities & higher educational institutions (FIST), Department of Science and Technology, Government of India, Rashtriya Uchchatar Shiksha Abhiyan (RUSA) 2.0, Jadavpur University, India. Additionally, I would like to express my profound gratitude to Spices Board India, Gangtok, India (Ministry of Commerce and Industry, Government of India) Indian Cardamom Research Institute (ICRI), Karnataka, and Institute Of Bioresources & Sustainable development (IBSD), Manipur for providing the necessary samples to carry on with the study.

I want to thank **Mr. Sourav Manna,** Ph.D. research scholar, Department of Life sciences, Presidency University, **Mrs. Sumani Mukherjee**, Assistant professor, Department of Electronics and Communication Engineering, St. Thomas' College of Engineering and Technology, and **Ms. Swarnali Neogi,** Postgraduate researcher, the University of Surrey, for their continuous support during the experimentation, data collection and analysis.

I want to express my sincere gratitude to all my fellow labmates, colleagues, and seniors in the **Department of Instrumentation and Electronics Engineering, Jadavpur University, Kolkata** and **Semiochemical and Lipid Chemistry Lab, Department of Life Sciences, Presidency University, Kolkata,** for providing me with a research environment to carry out my work and providing continuous cooperation in every possible way making this journey less stressful.

Finally, my appreciation goes out to my parents and my sister. Without their tremendous understanding and encouragement over the past few years, it would be impossible for me to complete my study.

Date: 25.07.2022

Place: Kolkata

Nilava Debabhuti

(Nilava Debabhuti)

Abstract

Cardamom is a well-known spice worldwide due to its flavour, aroma, various health benefits and culinary uses. Both large and small cardamom is considered costly spices and thus provide significant economic benefits in global trading. India is the leading producer of large cardamom and small cardamom globally and is the largest producer and exporter of small cardamom, significantly impacting the Indian spice industry. Because of the high demand for cardamom in the international market, the quality of the spice must be as high as possible, and proper analytical gradation of spices can result in improved export chances, consumer appeal, and financial benefit to the producers. However, there is a severe deficiency of appropriate post-harvest practices and quality evaluation of cardamom in India, where post-harvest production primarily relies on ancient procedures with little contemporary technological input. Since cardamom is highly aromatic, the volatile organic compound (VOCs) and semi-VOCs profile of spices are essential aspects of consumer's perception and can be considered an appropriate benchmark to assess quality. Quartz crystal microbalance (QCM) is a valuable gas sensor detecting VOCs in multiple aromatic products. QCM sensors offer reliable, accurate time detection of VOCs because of their specificity, sensitivity, high accuracy, stability, and repeatability. This thesis reported VOCs of 24 (21 large; 3 small) cardamoms samples using Solid Phase Micro Extraction guided Gas Chromatography-Mass Spectrometry (GC-MS) based analysis. Following this, four QCM sensors were prepared to detect the significant volatiles influencing the aroma of large and small cardamom, **i.e., α-pinene, β-pinene, 1,8-cineole and α-terpinyl acetate**. A portable instrument has been developed to identify the VOCs using QCM sensors. The system is comprised of an 8284A oscillation circuit, a Teensy 3.2-based counter module, and a Raspberry Pi 4 with a 7-inch touch display for data monitoring and control. A customized Python-based graphical user interface was designed to facilitate the recording and storing of sensor data. For the detection of **β-pinene a QCM sensor was with the olive (OLV-QCM) oil to detect this marker VOC β-pinene**, in Indian cardamom. The developed sensor shows high sensitivity towards β-pinene with a sensitivity of 0.3105 Hz/ ppm with R^2 = 0.9979 for volatile concentration ranging between 10-1000 ppm. Furthermore, the sensor is adequately selective towards β-pinene in the presence of other dominant VOCs present in the cardamoms. The average reproducibility and repeatability of the OLV-QCM sensor have

been calculated to be 93% and 95.14% within a 95% confidence interval. Similarly, **QCM sensor coated with rice bran oil was developed for the detection of α-pinene.** The sensor showed sensitivity measuring 0.367 Hz/ppm and having an R^2 of 0.9976. Furthermore, even in the presence of other main VOCs present in cardamom, the sensor is adequately selective for α-pinene. Again, at 67.7 %RH, the developed sensor exhibits quick recovery, long-term stability, short-term stability, little humidity impact, and 95.91% average repeatability. Following that, **a modified castor oil-coated QCM (phenolated phenyl ricinoleate by derivatization) sensor was developed to identify 1,8-cineole in cardamom.** The designed sensor showed high sensitivity to 1,8-cineole, as indicated by its sensitivity of 0.262 Hz/ppm and its R^2 value of 0.9964. In addition, the sensor has acceptable selectivity for 1,8-cineole. The GC-MS was used for validation for twenty-one large cardamom samples, and the findings indicated a correlation of 0.98 with the 1,8-cineole peak areas of the chromatogram. Moreover, a mathematical model has been formulated to predict the 1,8-cineole content from the samples using the developed sensor responses. The results showed an accuracy of 89.09% in predicting the 1,8-cineole content from the samples. Finally, **molecularly imprinted polymer (MIP) based QCM gas sensor was fabricated to detect α-terpinyl acetate in cardamom.** The sensor shows high responsive towards aTA with sensitivity of 0.3876 Hz/ppm. The average repeatability and reproducibility of the sensor are obtained as 94.72% and 93.76%, respectively. In all cases, structure and surface morphology of the sensor responses were analyzed by Fourier Transform Infra-Red (FTIR) spectroscope, Scanning Electron Microscope (SEM) and Atomic Force Microscope (AFM) and in each cases the sensor responses were tested with GCMS estimate of natural cardamom samples. Therefore, it is concluded that these developed QCM sensors which are user-friendly, portable and cost-effective can be used by gradual modification for quality assurance of large and small cardamom of our country in near future.

Table of Contents

Chapter 1: Introduction and scope of the thesis

Chapter 2: Determination of volatile organic compounds (VOCs) from Indian cardamom using GCMS analysis

Chapter 3: Development of a portable volatile organic compound detection system using QCM sensor

Chapter 5: Development of rice bran oil modified QCM sensor to detect α-pinene in Indian cardamom

Chapter 6: Sensitive detection and estimation of 1,8-cineole content in large cardamom using modified castor oil coated QCM sensor

Chapter 7: Development of QCM sensor to detect α-terpinyl acetate in cardamom

Chapter 8: Conclusion and future scope

List of Figures

List of Tables

List of abbreviations

A		
	ABCN	1,1′-Azobis(cyclohexanecarbonitrile)
	AC	Alternating current
	AFM	Atomic force microscopy
	ANOVA	Analysis of variance
B		
	BET	Brunauer–Emmett–Teller
	BVD	Butterworth-Van Dyke
C		
	CAR	Carboxen
	CEO	Cardamom essential oil
	CLD	Chemiluminescence detector
	CMOS	Complementary metal-oxide semiconductor
	CNT	Carbon nanotube
	CO	Carbon monoxide
	CV	Coefficient of variation
D		
	DVB	Divinyl benzene
E		
	EGDMA	Ethylene glycol dimethacrylate
F		
	FA	Fatty acid
	FESEM	Field Emission Scanning Electron Microscope
	FET	Field-effect transistor
	FID	Flame ionization detector
	FTIR	Fourier transform infrared spectroscopy
G		
	GC	Gas chromatography
	GCMS	Gas chromatography mass spectrometry
	GUI	Graphical user interface
H		
	HBW	Half bandwidth
	HDMI	High definition multimedia interface
	HS	Headspace
	HSV	Headspace volatile
I		
	IOT	Internet of Things
	IR	Infrared
	ISFET	Ion-sensitive field-effect transistor

L

LC	Large cardamom
LDA	Linear discriminant analysis
LOD	Limit of detection
LOQ	Limit of quantitation
LPTMR	Low power timer

M

MAA	Methacrylic Acid
MANOVA	Multivariate analysis of variance
MEMS	Micro-electro mechanical system
MHz	Megahertz
MIP	Molecularly imprinted polymer
MISG	Molecularly imprinted sol-gel
MOEF	Ministry of Environment, Forest & Climate Change
MOS	Metal-oxide semiconductor
MOSFET	Metal-oxide field-effect transistor
MS	Mass spectrometry

N

NEMS	Nano-electromechanical system
NIP	Non-imprinted polymer
NIST	National Institute of Standards and Technology
NO	Nitric oxide
NT	Nanotube

P

PA	Photoacoustic
PC	Principal component
PCA	Principal component analysis
PDMS	polydimethylsiloxane
PID	Photo-ionization detector
PMT	Photomultiplier tube

R

RB	Rice bran
RFID	Radio frequency identification
RH	Relative humidity
RI	Retention index
RMS	Root mean square
RMSD	Root mean square deviation
RP	Repeatability
RSD	Relative standard deviation
RTIL	Room-temperature ionic liquid

S

SAW	Surface acoustic wave
SC	Small cardamom
SEM	Scanning electron microscope

	SFT	supercritical fluid extraction technique
	SIMPER	Similarity percentage
	SPME	Solid phase microextraction
	SWCNT	Single walled carbon nanotubes
T		
	TD-GC-MS	Thermal desorption–gas chromatography-mass spectrometry
	TG	Triglyceride
	TGA	Thermogravimetric analysis
	TIC	Total ion chromatogram
U		
	USB	Universal serial bus
	UV-Vis	Ultraviolet–visible
V		
	VOC	Volatile organic compound
W		
	WCOT	Wall-coated open tubular

Chapter 1

Introduction and scope of the thesis

1.1. Introduction

Indian cardamom is one of the major spice crops, owing to its high economic value. Cardamom is recognised as the "queen of spices" due to its strong aroma, usefulness as a flavour enhancer for various meals and beverages, and extensive usage in local traditional medicines. It ranks alongside saffron and vanilla as one of the three most costly spices [1,2].

Two types of cardamom are commercially available- large/black variety and small/green variety (Fig. 1.1). Large cardamom (*Amomum subulatum*; Family: Zingiberaceae) is cultivated in subtropical and cold climates of northern and northeastern India. Regarding production, India is considered the largest cultivator of black cardamom, with 54% of the world's production share. It is estimated that nearly 14 lakh families depend on this sector for income [3]. Sikkim, Darjeeling district of West Bengal, Arunachal Pradesh, Nagaland, and Uttarakhand are the central region of cultivation for large cardamom [4,5]. The Spices Board asserts that most of India's spices come from Sikkim [6]. Alongside India, in recent times, other Himalayan countries like Nepal and Bhutan are also considered significant producers of this spice. The Economic Times report (2016) states that the auction value of large cardamom boosted to 1600 Rs/Kg in 2016 from 250 Rs/Kg in 2010, which directly mirrors the importance of large cardamom in global and indigenous markets.

Small/ green cardamom (*Elettaria cardamomum* (L.) Maton, Family: Zingiberaceae) is another valuable spice due to its aroma and flavour. Like black cardamom, India is the biggest producer and exporter of small cardamom, and this spice significantly impacts the Indian spice industry. Small cardamom is grown extensively in parts of southern India's monsoon forests of the Western Ghats [3,7,8]. Every year, India exports around 130000 metric tonnes of small cardamom, with a global value of 609.08 crores [Ministry of Environment, Forest & Climate Change, MOEF&CC]. Cultivated cardamom is classified into three types based on the nature of the panicle. These are 'Malabar', 'Mysore' and 'Vazhukka'. Moreover, the cultivation of small cardamom is also done in Sri Lanka, Tanzania, Africa, and Guatemala. The fruit is ovoid or oblong, yellow-green pod (1–2 cm long) containing about 15–20 black and brown seeds. The seeds are submerged inside the cardamom pod, and essential oil is extracted from the dried seeds. The essential oil combines volatile and non-volatile compounds [9–11]. The quality and the grade of spice can be analysed by the size, texture, shape, and presence of volatile organic compounds (VOCs).

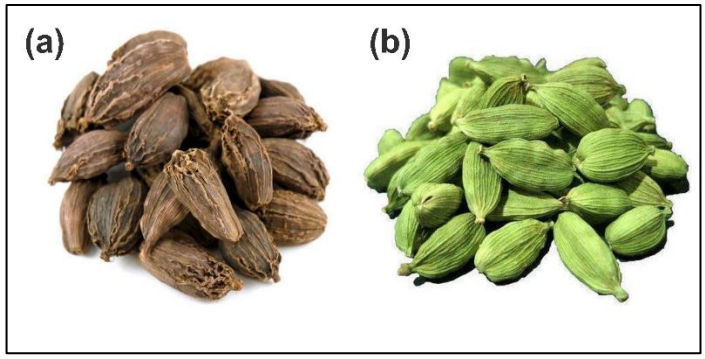

Fig. 1.1. Indian cardamom types: (a) large (b) small cardamom.

Cardamom is utilised commercially in fragrances and as a flavouring agent in the culinary business, where it is added to meats, baked goods, soups, fruit items, jams, and pickles. Its rich aroma has been characterised as sweet, lemony, toasty, minty, spicy, and flowery, among other descriptors [12–14]. It may be used to flavour both sweet and savoury recipes and, depending on the recipe, can be used as pods or seeds, intact or as seed powder, often in teaspoon amounts. In India, whole pods are commonly used in meat and rice meals, whereas crushed pods are used in Scandinavian bread. Cardamom has many applications in the food, cosmetics, and medicinal industries. Cardamom powder and its extracted essential oil are commonly used in food processing industries like beverages, flavoured tea, flavoured coffee, and flavoured milk [8].

Cardamom essential oil has many potential medicinal uses and was used in traditional medical practices. According to Hamzaa et al. and Khan et al., cardamom capsules have been used to treat asthma, nausea, diarrhoea, cataracts, tooth and gum infections, and digestive, renal, and heart diseases [15,16]. Potential applications in contemporary medicine have been researched in addition to traditional medicinal usage [17,18]. Das et al. reported that cardamom powder acts as a chemopreventive agent to cure skin cancer [19]. Furthermore, cardamom extract contains a high amount of antioxidant and diuretic properties, which helps reduce blood pressure. [20]. The study by Rahman et al. showed that cardamom powder has anti-inflammatory agents that can protect from chronic diseases [21]. Research also showed that cardamom extract prevents cavities, eliminates common oral bacteria, and is frequently used to cure bad breath [22]. Further, usage of cardamom shows a cardiopreventive effect, as reported by Goyal et al. [23]. According to Bhaswant et al., it exhibits anti-hepatotoxic properties [24]. The impact of cardamom on obesity, hypothyroidism, diabetes, hepatomegaly, dyslipidaemia, and fast hyperglycaemia were all

documented by Nitasha Bhat et al. [25]. One of the most common respiratory ailments is a cold and cough, which can be relieved with this herbal remedy. Small cardamom was also shown to be anti-asthmatic by Nitasha Bhat et al. [25]. Cardamom extracts have been shown to have antihistaminic properties on isolated rabbit trachea tissues by Khan et al. [16]. According to Kumar et al. (2016), the antidepressant effects of small cardamom have been proven [26].

Cardamom is high in bioactive metabolites such as flavonoids, carotenoids, and terpenes [27–30]. The bioactive compounds in essential oil generate their distinct and fragrant aroma. The characteristics of volatile cardamom oil have a high value of monoterpene hydrocarbons (16.3%), oxygenated monoterpenes (75.2%), and sesquiterpenes (6.3%) comprise the major components in the VOCs of cardamom [31,32]. The monoterpenes play a vital role in detecting the VOCs in different odour-based fruits and spices. VOCs like linalool, geraniol, and methyl salicylate in black tea, β-caryophyllene and 3-carene in mango has been detected [33–38]. The major constituents of cardamom VOCs according to different geographically cultivated cardamom are listed in Table 1.1.

Table 1.1. Different cardamom cultivars and their major VOCs.

Variety of cardamom	**Method of detection**	**Major VOC Components (%)**	**Refs.**
Large Indian Cardamoms (*Amomum subulatum*) from Sikkim	GC and GC-MS analysed by capillary Hydro-distillation process	1,8-cineole (65.39%), α-terpineol (10.15%), β-pinene (7.23%), α-pinene (4.06%), linalool oxide (3.23%), limonene (2.53%)	[39]
Large Indian Cardamoms (*Amomum subulatum*) from Sikkim	GC-MS analysis by Clevenger hydrodisttilation process	1,8-cineole (40.3%), α-pinene (7.0%), β-pinene, (26.4%), α-terpineol (9.9%), 4-terpineol (0.9%).	[40]
Large Indian Cardamom (*Amomum subulatum Roxb.)* from Uttarakhand	GC & GC-MS analysis by Hydro-distillation process	1,8-cineole (73.27%), α-terpineol (4.23%), limonene (4.2%), α-terpinyl acetate (3.33%), α-pinene (2.9%), terpinen-4-ol (2.82%), β-pinene (2.12%), γ-terpinene (1.8%), α-bisabolene (1.4%)	[41]

Small Indian cardamom (*E. cardamomum*)	DB-Wax column analysis by GC and GC-MS process.	1,8-cineole (27.9%), limonene (2.9%), Myrcene (1.7%), sabinene (3.1%), α-pinene (1.3%), β-pinene (0.3%)	[42]
Small cardamom from South India	GC-MS analysis of cardamom essential oil	α-terpinyl acetate (29.9-61.3%), 1,8-cineole (15.2 – 49.4%), α-terpineol (0.83-13.2%), β-linalool (0.44-11.0%), sabinene (1.9-4.9%)	[27]
Indian Large Cardamoms (*A. subulatum*)	GC & GC-MS analysis of Clevenger Hydro distillation process	1,8-cineole (38.7%), β-pinene (13.6%), α-terpineol (12.6%), spathulenol (8.3%), 4-terpineol (4.5%), germacrene-D (3.0%), α-pinene (2.8%), β-selinene (2.7%)	[43]
African Large Cardamoms (*Aframomum species*)	GC & GC-MS analysis Clevenger Hydro distillation process	1,8-cineole (59.8%), β-pinene (13.2%), α-terpineol (9.3%), α-pinene (4.3%), α-terpinyl acetate (3.2%)	[44]
Ethiopian cardamom (*Aframomum corrorima*)	GC/GC-MS process by hydro-distilation analysis	γ-terpinene (27.1%), β-pinene (15.4%), α-phellandrene (8.5%), 1,8-cineole (6.7%), p-cymene (6.4%)	[45]
Chinese black cardamom (*Amomum tsao-ko*)	DB-Wax column analysis by GC and GC/MS process	1,8-cineole (28.1%), geraniol (7.1%), limonene (2.7%), α-terpineol (3.5%), α-pinene (2.3%), β-pinene (2.1%)	[46]
Guatemala cardamom	Gas chromatography mass spectrometry of essential oil extracted by hydro distillation process	α-terpinyl acetate (27.14%), 1,8-cineole (15.40%), α-terpineol (7.44%), terpinen-4-ol (5.05%), linalyl acetate (4.49%), β-pinene (3.55%) β-selinene (3.23%)	[47]
Green cardamom (*E. cardamomum*) from Pakistan	GC-MS analysis of cardamom essential oil	α-terpinyl acetate (38.4%), 1,8-cineole (28.71%), linalool acetate (8.42%), sabinene (5.21%), linalool (3.97%)	[48]
Black cardamom (*A. subulatum*) from Pakistan	GC-MS analysis of essential oil supercritical fluid extraction technique (SFT-150)	1,8-cineole (44.24%), α-terpinyl acetate (12.25%), neridol (6.03%), and sabinene (5.96%)	[49]

The research outputs mentioned in the above table indicate that 1,8-cineole and α-terpinyl acetate are the two abundant and vital volatiles in the aroma of large and small cardamom essential oils, respectively. Ghosh et al. reported the most abundance of 1,8-cineole in cardamom using

supercritical carbon dioxide extraction [50]. Santos et al. [51] reported 1,8-cineole as the primary nutraceutical compound present in cardamom. According to Parthasarathy et al's [13] study, cardamom essential oil extracted by steam distillation and GC-MS has 26 components in total, including 1,8-cineole (61.50%), which was classified as a principal component. Previous research has shown α-terpinyl acetate as the most active and abundant VOC in small cardamom [52,53]. Ashokkumar et al. [27] reported 1,8-cineole and α-terpinyl acetate are the major constituents of CEO in small cardamom. Many research articles, however, claimed the absence of α-terpinyl acetate in the volatile profile of large cardamom essential oil [10,40,54]. However, Bhandari et al. [55] reported 3.3% α-terpinyl acetate, in the large cardamom oil from Uttarakhand. Similarly, Joshi et al. [56] also reported the presence of α-terpinyl acetate in the large cardamom collected from Himachal Pradesh. Likewise, Gilani et al. [57] identified 1,8-cineole (55.37%), α-terpinyl acetate (11.66%), and limonene (6.05%) as the primary components of essential oil of large cardamom. Significant components of large cardamom (*Amomum subulatum*) oil are 1,8-cineole, α-terpineol, D-limonene, nerolidol, 4-terpineol, δ-terpineol, δ-3-carene, β-myrcene, germacrene D, α-terpinene, and longifolenaldehyde [40]. Gurudutt et .al. confirmed that 1,8-cineole (61.31%), β-pinene (8.85%), α-terpineol (7.92%), α-pinene (3.79%), and allo-aromadendrene (3.17%) as significant components present in the essential oil of large cardamom seeds [10]. Moreover, two monoterpene hydrocarbons, α-pinene and β-pinene, are commonly present in the headspace of every cardamom cultivar. Moreover, α-pinene and β-pinene are found in several spices and fruits like rosemary, nutmeg, cumin, and mangoes [44,45,58–60], which is considered an important biomarker for aroma profile analysis of cardamom and different spices as well.

Four selective QCM sensors were developed in this thesis work to determine four major volatiles in cardamom: α-pinene, β-pinene, 1,8-cineole, and α-terpinyl acetate. The detailed physical and chemical properties of the selected VOCs are given in Table 1.2. Natural vegetable oils such as olive oil and rice bran oil were chosen as coating materials for detecting chemicals such as α-pinene and β-pinene. Vegetable oils are naturally hydrophobic, which showed affinity towards the hydrophobic monoterpenes. Moreover, the high vapour pressure of α-pinene and β-pinene facilitates effective adsorption towards the oil surface. To detect 1,8-cineole, which has a certain degree of hydrophilicity, modified castor oil was tested. However, due to the increased molecular complexity and low vapour pressure of α-terpinyl acetate, a more selective adsorption technique like molecularly imprinted polymer was prepared for sensing purposes. For every sensor, the

sensor fabrication steps, as well as sensor characteristics, were systematically studied. Throughout the research, several sensor material characterization techniques such as fourier transform infrared (FTIR) spectroscopy, field emission scanning electron microscope (FESEM) and ultra-violet visible (UV-Vis.) spectroscopy, and atomic force microscopy (AFM) were used. Each sensor was validated for its accuracy with the GC-MS results of actual cardamom samples.

Table 1.2. Physical and chemical properties of major VOCs in cardamom essential oil

Physical and chemical parameters	**α-Pinene**	**β-Pinene**	**1,8-cineole**	**α-terpinyl acetate**
Molecular weight	136.23	136.23	154.25	196.28
Hydrophobicity (log P)	4.83	4.16	2.74	3.96
Vapor pressure (mmHg at 25°C)	4.75	2.93	1.9	0.039
Flash point °C	32.22	35	50	99.44
Odour strength	High	High	High	Medium
Chemical nature	**Bicyclic monoterpene**	**Bicyclic moneterpene**	**Bicyclic monoterpene ether**	**Monocyclic monoterpene acetate**
Unsaturation number/type	1, Endocyclic	1, Exocyclic	0	1, Endocyclic
Functional group	None	None	Ether (-O-)	Carbonyl (-C=O)
Polar surface area	0	0	9	26.3
Molecular complexity	186	177	164	251

1.2. Gas Sensors: Overview

Gas sensors are devices that can detect the presence and concentration of gases in the environment. It comprises a transducer and an active layer for converting the components and concentration information of various gases into another form of electronic signals like frequency change, current change, or voltage change. Gas sensing technology has become more significant because of its widespread applications in the following areas, as shown in Table 1.3.

Table 1.3. Applications of gas sensors

Gas detection sector	Application	Refs
Agricultural	Determination of fruit ripeness	[61,62]
	Fruit aroma detection	[63]
	Shelf life of fruits	[64]
	Storage quality	[65]
	Soil pollution	[66]
	Soil microbial activities	[67]
Food quality	Freshness of meat	[68]
	Identification of fermented fish	[69]
	Spoilage of milk	[70]
	Detection of ageing of wine	[71]
	Quality estimation of black tea	[72]
	Classification of coffee	[73]
Diagnosis of disease	Breath analysis	[74,75]
	Cancer detection	[76–79]
	Gastrointestinal diseases	[80]
Environmental pollution	Air pollutants	[81–83]
	Air quality monitoring	[83]
Military application	Detection of explosives	[84–86]

1.2.1 Performance indicators of gas sensor

The performance of gas sensing methods or gas sensors can be evaluated based on primary indicators:

(1) **sensitivity:** the minimum value of target gases' volume concentration when they could be detected;

(2) **selectivity:** the ability of gas sensors to identify a specific gas among a gas mixture;

(3) **response time:** the period from the time when gas concentration reaches a specific value to that when the sensor generates a warning signal;

(4) **energy consumption:** the measure of how much energy a gas sensor uses during operation. It can be an important performance indicator because it can affect the overall efficiency of the sensor and its cost of use. A gas sensor that has a low energy consumption will be more cost-effective to operate and may be more suitable for use in applications where energy is limited, such as portable or battery-powered devices;

(5) **reversibility:** whether the sensing materials could return to their original state after detection;

(6) **fabrication cost:** it refers to the cost of producing a gas sensor, including the cost of materials, labour, and any other expenses associated with the manufacturing process. It can be an important performance indicator because it can affect the overall cost of the sensor and its availability;

1.3. Classification of gas sensing methods

Over decades, gas sensor technologies have been utilized to detect various gases, such as semiconductor gas, catalytic gas, electrochemical gas, optical gas, and acoustic gas. Every performance of the sensor can be determined by sensitivity, selectivity, detection limit, reaction time, and recovery time. This study categorizes gas sensor technologies into the following categories to give a comprehensive introduction to sensing fundamentals, as shown in Table 1.4.

Table 1.4. Classification of gas sensors based on their detection methods

Gas sensor		
Sensors based on the reactivity of gas	**Sensors based on the physical properties of gas**	**Sensors based on gas sorption**
Electrochemical sensors	Photoacoustic sensors	Fibre optics sensors
Semiconductor sensors	Thermal conductivity sensors	Conductive polymer sensors
Colorimetric paper tape type	Non-dispersive infrared	Reactive-gate semiconductor device/ Gas-FET/ISFET
Chemiluminescence type	-	Microbalance sensors
Combustible gas sensor/micro calorimetric gas sensor/pellistor	-	-

1.3.1. Sensors based on the reactivity of gas

1.3.1.1. Electrochemical sensors

Electrochemical sensors enable gases to permeate across a porous membrane and arrive at an electrode, where they are either reduced or oxidised depending on the function of the sensor. Electrochemical gas sensors are used in domestic and industrial settings to detect and monitor trace amounts of potentially harmful gases and oxygen [87–89]. Amperometric fuel cells with two electrodes are used in electrochemical gas sensors. The working (sensing) electrodes, the counter electrode, and the ion conductor are the three components that make up a two-electrode gas sensor. The toxic gas that comes into contact with the working electrode undergoes oxidation due to a chemical reaction between the water molecules in the surrounding air and the protons (H+) produced by the working electrode. The ion conductor makes it possible for the protons (H+) that

are produced at the working electrode to go in the direction of the counter electrode. Electrons are produced by traversing the counter electrode. The typical configuration of an electrochemical sensor is shown in Fig. 1.2.

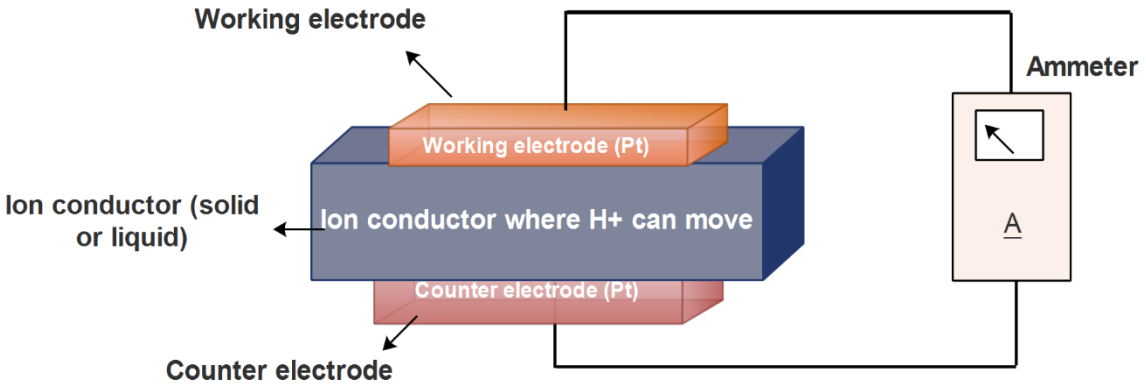

Fig. 1.2. Typical electrochemical sensor layout.

This electrochemical cell may be used as a gas sensor by monitoring the current between the working and counter electrodes. Electrochemical sensors are potentiometric, conductometric, resistive or voltammetric.

a) A potentiometric sensor measures the potential difference between a sensing electrode and a reference electrode.
b) Conductometric sensors determine the electrical characteristics that vary between two electrodes.
c) Resistive sensors detect changes in resistivity caused by deflection caused by atomic collision and hindrance, while capacitive sensors detect changes in capacitance caused by a change in the dielectric constant.
d) Voltammetric sensors detect the current generated by the charge transport of an electrochemical reaction on a detecting (working) electrode when a variable or constant voltage is placed between the working electrode and the solution (amperometric detection).

1.3.1.2. Semiconductor sensor

Among the many gas sensors, semiconductors are the most prevalently employed for chemical, biological, mechanical, and optical applications. Most semiconductor sensors are based on n-type semiconducting oxides, and their resistance in the air is impacted by oxygen adsorbed to the sensor surface. Oxygen atoms trap electrons on the semiconductor's surface, increasing the material's resistance. Most metal oxide semiconductors (i.e., SnO_2, ZnO etc.) sensors are n-type semiconductors. In the most extreme scenario, free electrons flow through the connected regions (grain boundary) of tin dioxide crystals when the metal oxide sensor material, typically tin dioxide (SnO_2-x), is heated to high temperatures such as 400 ^oC. Tin dioxide is generally used for these sensors. In an atmosphere devoid of contaminants, oxygen may be found adsorbed on the surfaces of metal oxides (approx. 21% O_2). With its strong electron affinity, adsorbed oxygen draws free electrons inside the metal oxide, resulting in a more considerable barrier (eVs in the air) at the grain boundaries. Because of this, the potential barrier prevents electron mobility, which results in a high sensor resistance in clean air. The oxidation process of a combustible or reducing gas (such as carbon monoxide) occurs at the surface of tin dioxide in a sensor when the sensor is subjected to a reducing or combustible gas (like carbon monoxide). The working principle of the semiconductor gas sensor is illustrated in Fig. 1.3.

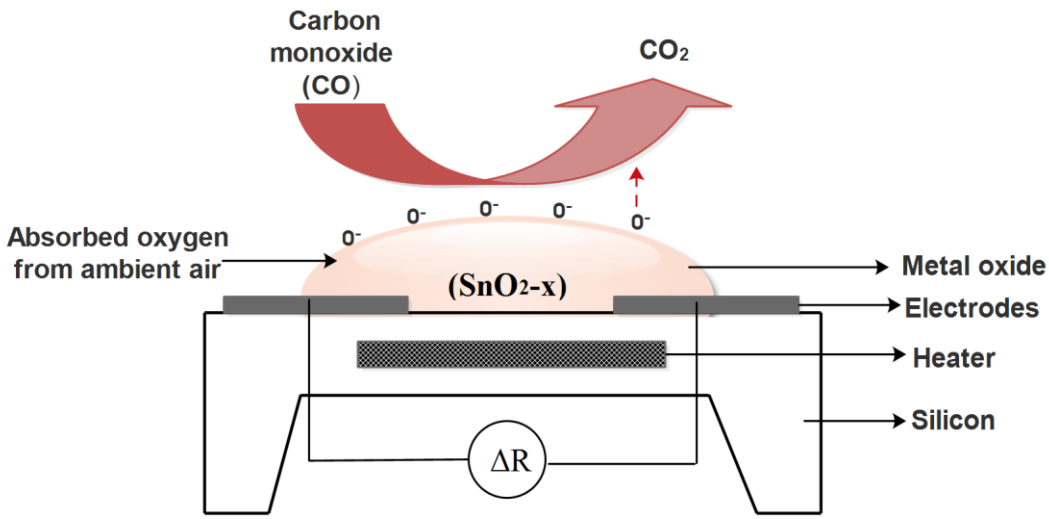

Fig. 1.3. Working principle of semiconductor gas sensor.

Consequently, the density of adsorbed oxygen on the surface of the tin dioxide decreases, and the potential barrier height also decreases. A decrease in the potential barrier height increases the movement of electrons, which reduces the sensor resistance. It is possible to measure the concentration of a gas in the air by analysing the change in resistance produced by gas sensors that use MOS technology. The reactivity of the detecting materials and the temperature at which the sensor is working affect the chemical reaction on the tin dioxide surface when gases and adsorbed oxygen are present.

1.3.1.3. Colorimetric paper type

A colorimetric paper tape type sensor is a paper tape-based instrument that allows much smaller concentrations to be detected with greater accuracy (Fig. 1.4). This type of sensor detects gases like isocyanates, arsine, phosphine, and chlorine by noting the colour changes of paper tapes in the presence of this gas. Light reflectance technology can also measure colour change [90,91].

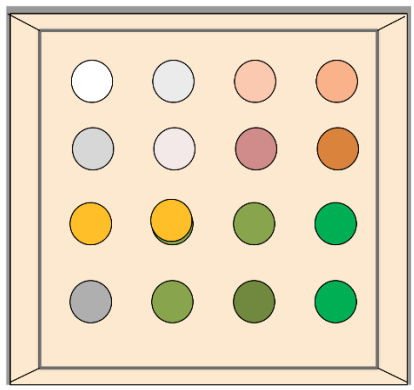

Fig. 1.4. Colorimetric paper tape type gas sensor.

1.3.1.4. Chemiluminescence

After receiving external energy from electromagnetic waves, heat, friction, electric fields, or chemicals, matter emits light of a specified wavelength without producing heat and returns to a ground state. This phenomenon is known as chemiluminescence, when the energy absorbed results from a chemical reaction. When luminescence resulting from this chemical reaction reaches its maximum intensity, it is measured using a photomultiplier tube. The chemiluminescence detector (CLD) is the industry-standard technology for detecting the content of nitric oxide (NO).

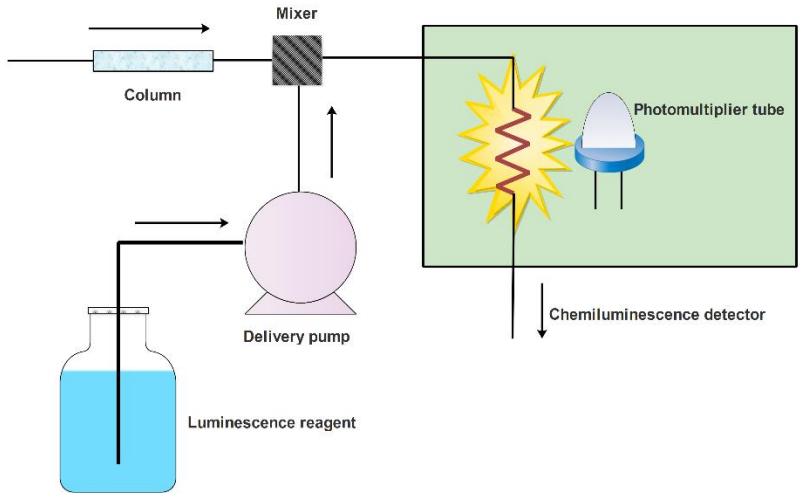

Fig. 1.5. Chemiluminescence type gas sensor.

Light is emitted via the interaction between NO and O_3 (ozone) [92]. This reaction serves as the foundation for the CLD, in which photons are detected by a photomultiplier tube (PMT). NO concentration is proportional to the CLD output voltage. Fig. 1.5 depicts the experimental setup using a chemiluminescence-type gas sensor.

1.3.1.5. Combustible gas sensor/micro calorimetric gas sensor/pellistor

There are several conditions under which the ignition temperature of a combustible gas combination can be reduced, allowing the gas to begin to ignite at lower temperatures. The output of the catalytic gas sensor is measured using a Wheatstone bridge. There are two types of catalytic gas sensors: pellistor and thermoelectric. An early platinum wire catalytic gas sensor was depicted in Figure 1.6(a). Detecting hydrocarbons requires a temperature between 500 °C and 600 °C, but platinum begins to vaporise at this temperature, and the platinum wire's resistance rises. Another issue with platinum wire is that it softens when heated over 1000 °C. Coating the platinum with other metal oxides and treating the sensor with a catalyst like palladium, or thoria compounds are the best solutions to this problem. Catalytic bead sensors with metal oxide coatings are more robust, stable, and resistant to stress and vibrations, as shown in Fig. 1.6(b).

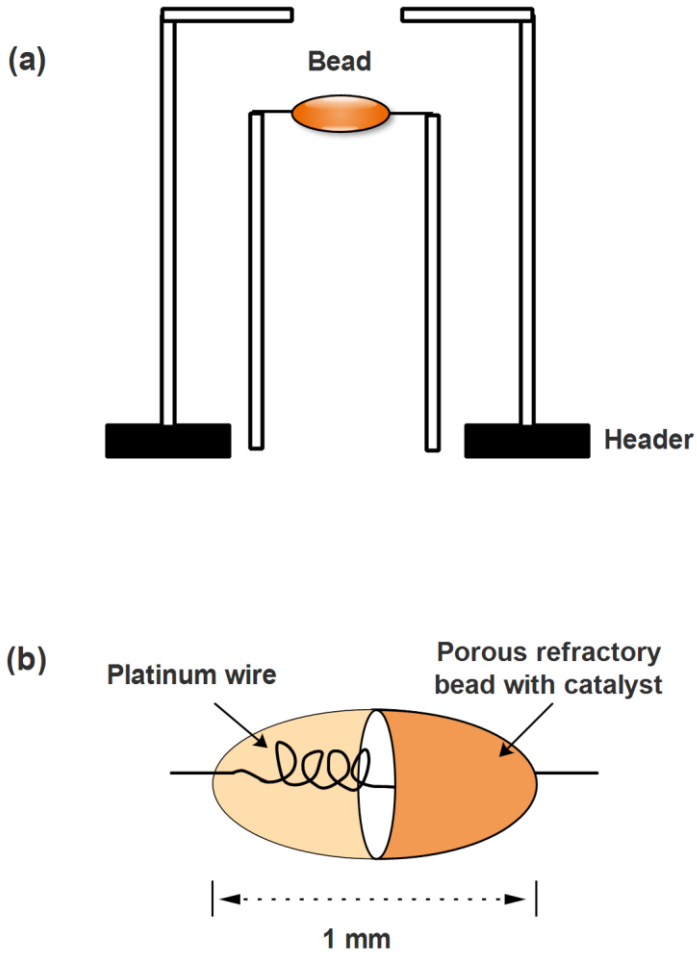

Fig. 1.6 Combustible gas sensor (pellistor).

1.3.2. Sensors based on physical properties of the gas

1.3.2.1. Photoacoustic sensors

Depending on the absorptive infrared technology, photoacoustic gas spectroscopy measures gas composition. The sample is contained inside a photoacoustic (PA) cell during a photoacoustic measurement. The molecules in the sample absorb part of the energy when the modulated infrared light strikes it, causing the temperature to increase. A pressure wave and an expansion will be generated as a result of the temperature increase. A periodic pressure can be recorded wave by putting a microphone in a photoacoustic cell to capture the sound. Due to the absence of photometric error, these sensors can detect sensitively. Figure 1.7 depicts the experimental setup.

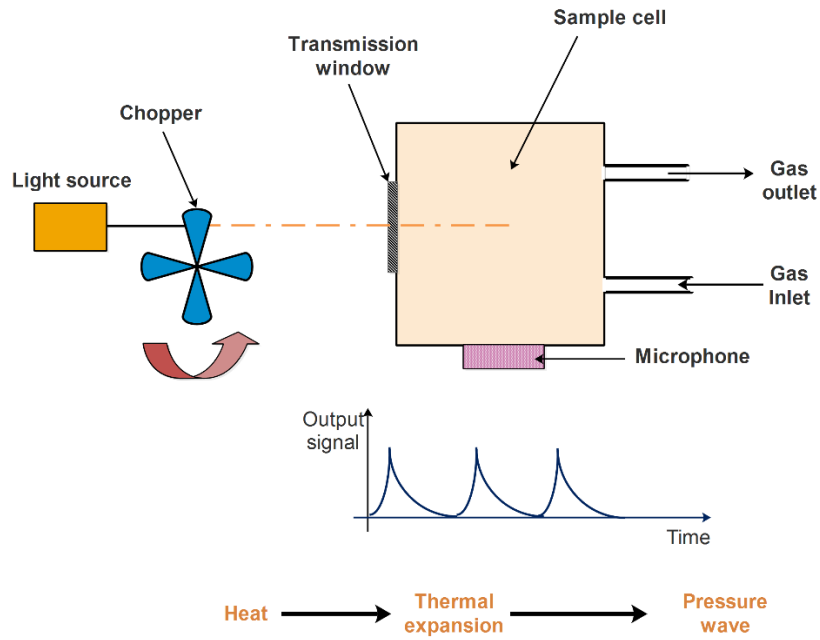

Fig. 1.7. Schematic representation of photoacoustic sensing unit.

1.3.2.2. Thermal conductivity sensors

A heated platinum filament is exposed to the sample gas in the case of a thermal conductivity sensor, while another gas, which serves as the reference gas, is confined in a sealed-off chamber. If the thermal conductivity of the sample gas is lower than that of the reference gas, the temperature of the exposed filament will rise. Alternatively, if the thermal conductivity of the sample gas is greater than that of the reference gas, heat will be lost from the exposed element, decreasing its temperature. Temperature variations cause changes in electrical resistance, which may be detected using a bridge circuit. Although this method is not nearly as sensitive or selective as others when identifying flammable gases, it is helpful when large gas concentrations are present and in operations that include gas purging [93]. Figure 1.8 depicts the schematic of the gas sensing setup.

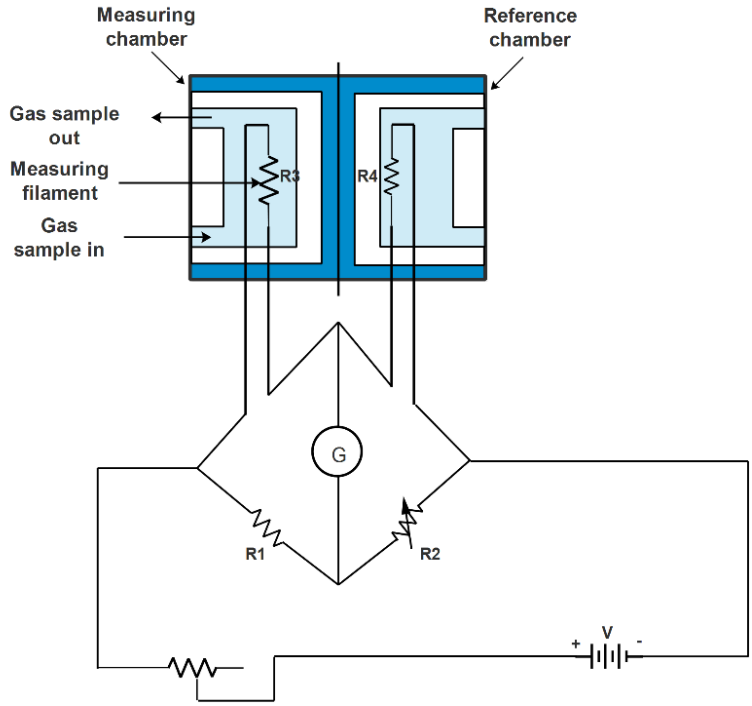

Fig. 1.8. Thermal conductivity type gas sensor.

1.3.2.3. Non-dispersive infrared sensors

Most gases have unique infrared (IR) absorption signatures in the 2–14 µm regions, and it is possible to determine the concentration of the detected gas by irradiating an infrared beam to the sample gas and measuring the strength of the infrared ray in the absorption wavelength range [94,95]. A simple non-dispersive infrared sensor consists of an IR light source, a sample compartment (of known optical length), an optical filter, and an IR detector, with its associated electronics as shown in Fig. 1.9.

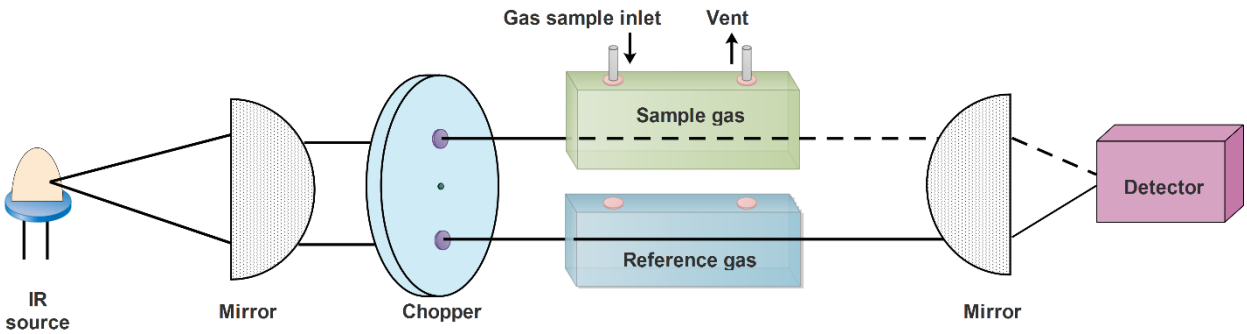

Fig 1.9. Non-dispersive infrared gas sensor.

1.3.3. Sensors based on gas sorption

1.3.3.1. Reactive-gate semiconductor device / Gas-FET / Chem-FET / ISFET (Ion-selective field-effect transistor)

The threshold voltage shift or drain current change of field-effect transistor (FET)-type gas sensors happens when they are exposed to the target gas [96]. These sensors employ a sensing material as a gate or channel. Figure 1.10 represents the schematic diagram. At the gate of the transistor, gas molecules are adsorbed, altering the resistance and current of the device. The sensor may be made very selective to a few gases by using various metals or coatings as the gate material. It minimises the power consumption of sensors due to their low thermal mass. These products are costly and offer a restricted user experience [97].

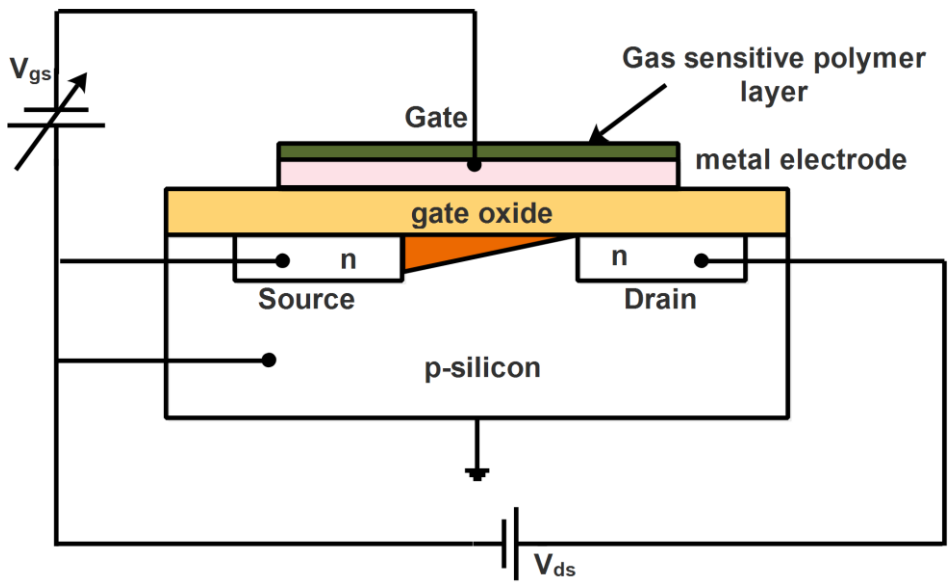

Fig. 1.10. Schematic diagram of a MOSFET and an ISFET structure.

(V_{gs} denotes gate-source voltage; V_{ds} denotes drain-source voltage)

1.3.3.2. Conductive polymer sensors

The electrical conductivity of polymers such as polyanilines and polythiophenes, used in conductive polymer-based sensors, varies as the polymers absorb particular gases (owing to charge transfer and swelling of the polymer). Despite several technical issues, such as temperature and humidity, baseline drift, and tuning features, Polymer sensors are receiving much attention from developers [98,99]. Figure 1.11 depicts an interdigitated conductive polymer sensor. The advantages of these sensors include operating at ambient temperature, a broad range of volatile organic chemicals, significant structural variations, and inexpensive cost.

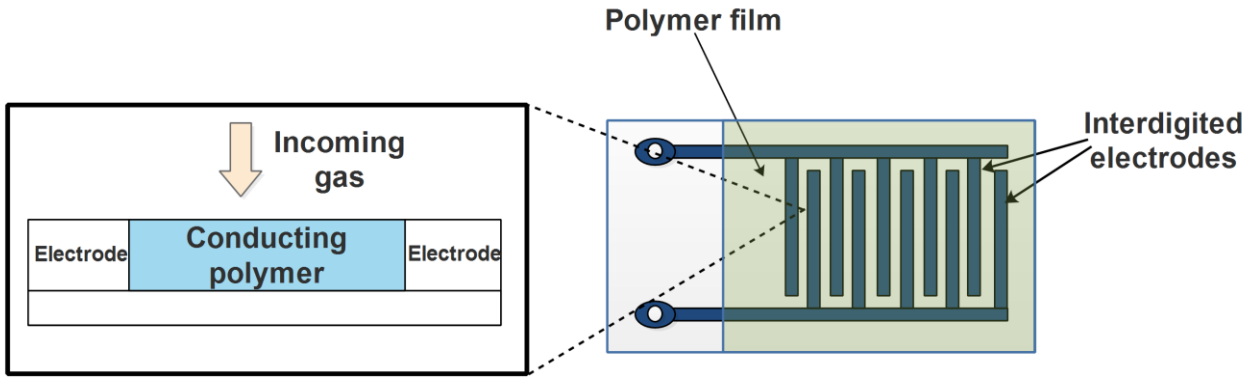

Fig. 1.11. Top plan view of the interdigitated polymer-based gas sensor.

1.3.3.3. Microbalances

A microbalance type gas sensor is based on the change in the resonant frequency of a quartz crystal upon mass deposition. The shift in frequency is susceptible and changes quickly due to a change in mass on the crystal surface. The shift in frequency can be measured upon gas adsorption, and the sensitivity of the sensor can be estimated. A quartz crystal microbalance can measure mass deposition as low as 0.1 nanograms.

1.3.4. Theory of QCM measurement

The use of a quartz crystal resonator for mass sensing was first realized in 1959 by a German physicist, G. Sauerbrey, who discovered that mass deposition on the resonator's surface leads to a decreased resonance frequency [100]. His work used quartz plate resonators as sensitive

microbalances for thin films. The main principle of the quartz crystal microbalance (QCM) is the piezoelectric phenomenon. A voltage forms on the crystal surfaces of a piezoelectric material in response to physical stress. Conversely, mechanical distortion results from the voltage applied across crystal surfaces. The cutting angle of the device substrate concerning the central crystallographic axis determines the device's oscillation and temperature behaviour. The AT-cut (35°15'), often used for QCMs, has exceptionally low-temperature dependence. The two sides oscillate in opposition to one another when AC voltage is supplied. The wavelength of the AC voltage precisely matches the plate thickness at resonance. Gravimetric or viscoelastic loading on the crystal surface is the fundamental determinant of oscillation frequency.

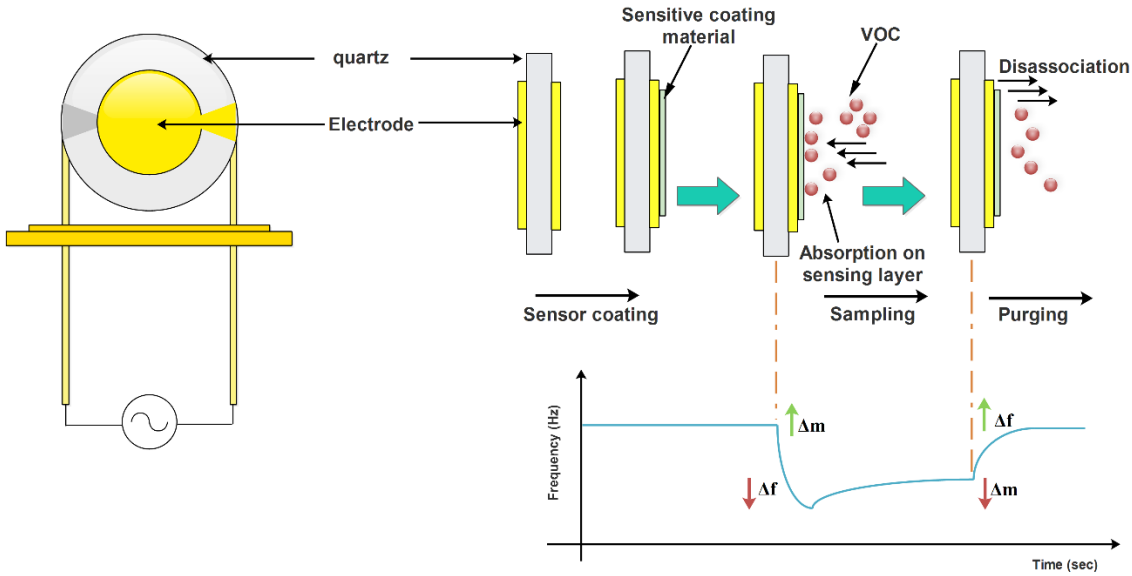

Fig. 1.12. The sensing mechanism of the QCM gas sensor.

In the QCM sensor, an AT-cut quartz crystal is inserted between either two gold or silver electrodes. According to the principle of piezoelectricity, when an alternating current is applied between the electrodes, the crystal oscillates at a resonant frequency depending on the crystal dimension, physical parameters and type of crystal cut. When a mass is applied to the crystal surface, the resonant frequency diminishes, which can be explained using Sauerbrey's equation (1.1).

$$\Delta f = \frac{2f_0^2}{\sqrt{\rho_q \mu_q}} \frac{\Delta m}{A} \qquad (1.1)$$

Where,

f_0– Resonant Frequency of the quartz crystal

Δf– Frequency change

Δm– Mass change

A –Piezoelectrically active crystal area

ρ_q– Density of the quartz crystal (2.649 g/cm^3)

μ_q– Shear Modulus of quartz (2.947×10^{11} g/cm.s^2)

The equation states the direct proportionality of the amount of mass deposited on the surface of the resonating crystal to the magnitude of change in frequency (Δf). The change in the frequency of the QCM determines the amount of the analyte deposited on the coating substance in ng/cm^2. For sensor characteristics studies, the relationship of Δf as a function of vapour concentration is monitored.

1.3.4.1. Sensing material for QCM sensor

The chemical sensitivity and selectivity of a QCM sensor are primarily determined by the materials used for sensing. The QCM sensors are sensing devices coated with compounds sensitive to the analyte being tested for. The Sauerbrey equation (1.1) demonstrates that the interaction of the coating with the analyte(s) of interest leads to a change in the mass and/or viscoelastic properties of the film, which in turn results in a change in the frequency or dissipation of the QCM sensor. Non-covalent, supramolecular, or intermolecular interactions, such as ion-ion, ion-dipole, dipole-dipole, hydrogen bonding, Van der Waals forces, and hydrophobic interactions, are primarily responsible for explaining the affinity of the target gas molecule towards the sensing material. Covalent interactions also play a role in this affinity. The "lock and key" model of host-guest interactions is the foundation of most interactions [101]. The host material must have a high affinity for adsorption on the target molecule for any of the approaches mentioned above to work. During the purging process, physical ties are swiftly removed, ensuring that the sensors may be used again. The complete sensing mechanism of the QCM gas sensor is depicted in Fig. 1.12.

1.3.4.2. Molecularly imprinted polymer (MIP)

A polymer prepared following the molecular imprinting method, which enables the formation of receptor sites in the form of cavities for a specific target molecule in the synthetic polymer matrix with an affinity for a "template" molecule of preference, is referred to as a molecularly imprinted polymer (MIP). The target molecule functions as a template around which interacting and cross-linking monomers are organised and co-polymerized to produce a polymer matrix. Once the template molecule has been removed, a molecular memory is imprinted within the polymer that is a perfect match for the molecules; as a result, the polymer becomes capable of selectively binding the target. Thus, sensors can recognise the template molecule in a manner that is selective and highly specific [102,103].

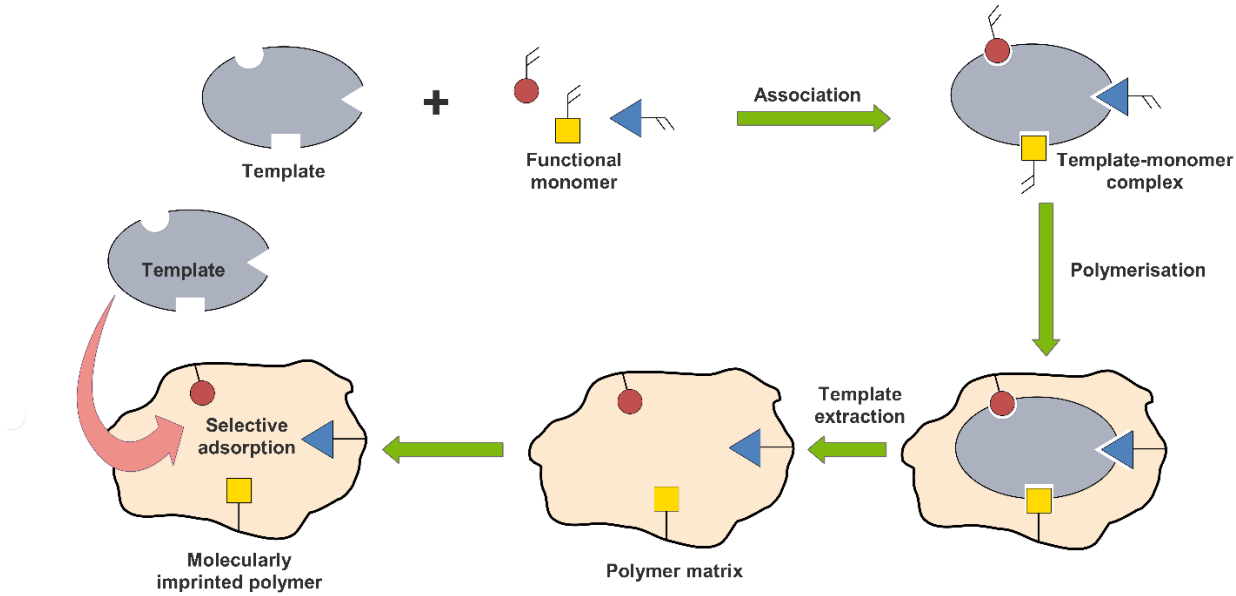

Fig. 1.13. The working principle of molecular imprinting technique.

These polymers have an affinity for the molecule they are intended to replace in various applications, including chemical separations, catalysis, and molecular sensors. After the template molecules have been removed, the cavities that correspond to the spatial arrangement of the template may be reconstructed; these cavities will then preferentially recognise the template molecules and their equivalents. Contacts between polymers and templates can take several forms,

the most prevalent of which are hydrogen bonds, Van der Waals (vdW) forces, and hydrophobic interactions. Thus, the QCM sensor coated with target "template" based MIP shows higher sensitivity, selectivity, and responsiveness towards the target molecule. The working principle of the molecular imprinting technique is illustrated in Fig. 1.13.

Fabrication of MIP sensor includes three stages

a. **Association:** In this step, the template molecule is mixed with a functional monomer, cross-linker, and initiator in a suitable solvent. Upon initiation of polymerization, the mixture forms a polymer complex with the template molecules through chemical bonding.
b. **Polymerization:** The polymerization step, including monomer, crosslinker and template molecules, is initiated using various reactions like thermal polymerization, photopolymerization, and electro-polymerization. The crosslinked monomers and the template molecule form a 3D porous polymer structure with recognition characteristics [104].
c. **Removal of the template:** To identify imprinted molecules with functional groups, template molecules are separated from polymers using an appropriate eluent, forming cavities with a three-dimensional structure that matches the template molecular size and shape [105,106].

The advantages and disadvantages of the gas sensors are illustrated in Fig. 1.14.

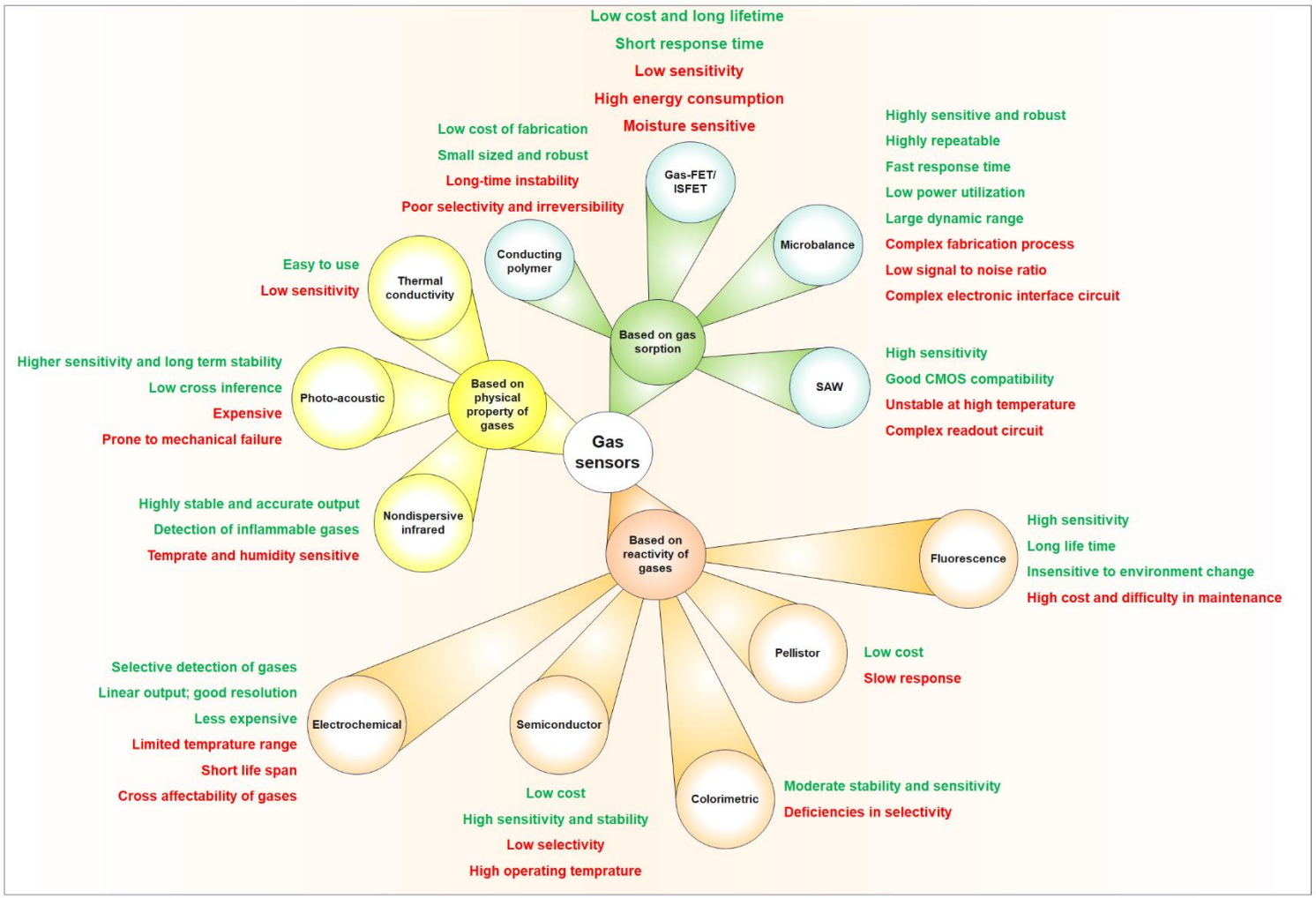

Fig. 1.14. Advantages and disadvantages of gas sensors.

1.5. Problem statement

Despite cardamom's high economic and medicinal values, there is a severe lack of proper post-harvest procedures and quality evaluation in the global market. Post-harvest production of cardamom is mainly based on age-old processes in India with minimal modern technology-based input [107]. The detailed stages for cultivation production steps are illustrated in Fig. 1.15. After harvest, mature capsules are manually removed off spikes. Following this, curing the capsules (having a moisture content of 70-80%) [108] takes place where the moisture content is effectively reduced to 10-12% to aid safe storage. Curing of the cardamom capsules takes place in a traditional Bhatti (furnace-based drying oven), which generally results in poor quality of the capsules due to the loss of volatile components of essential oil during the process [109] at high temperature. Various enhanced drying techniques were devised, resulting in higher quality; however, farmers are not yet assured of their worth because each system has its own set of faulty issues [110]. Apart from poor post-harvest techniques, the cardamom industry has some serious problems with grading the quality of capsules in local as well as global markets during export, trading through auction. No proper gradation or quality evaluation technique is available to date to categorise cardamom capsules for their spice value. To date, the capsule is graded according to the size of the pod, external colour and texture of the pod and quality of aroma tested by human volunteers. Awareness about the quality evaluation by price tag is still not in practice, therefore needs proper attention for the farmers and traders. Large cardamom is commercially available in commercial markets as '*Badadana*' (big capsules) and '*chotadana*' (small capsules), which necessarily do not signify the quality of the sample. The pod size and color may vary due to several reasons, including the cultivar type or the difference in post-harvesting processing. Due to lacunae in the procedure for quality assessment of large and small cardamon, without implementation of modern technology based devices the spice market economy mainly depends on human subjects till today [6]; and as a consequence India is passing through tough hurdles in competitive international market. Photographs taken by the author during field work along Darjeeling hills of Eastern Himalayan Biodiversity Hotspot presented in Fg.1.16 explained the current cultivation, postharvest, and processing by the local farmers.

Fig. 1.15. Detailed stages of production steps for Indian cardamom.

1.6. Motivation for the work

Different works of literature explained the presence of some VOCs responsible for the distinct aroma of cardamom. Depending on the concentration of these volatiles, i.e., landrace/variety-based volatile fingerprints, different cardamom varieties get their unique aroma scenario, directly affecting their commercial value. Changes in the aromatic volatile upon drying and storage of spices thus can be taken into consideration based on consumer opinion on the quality of dried spices.

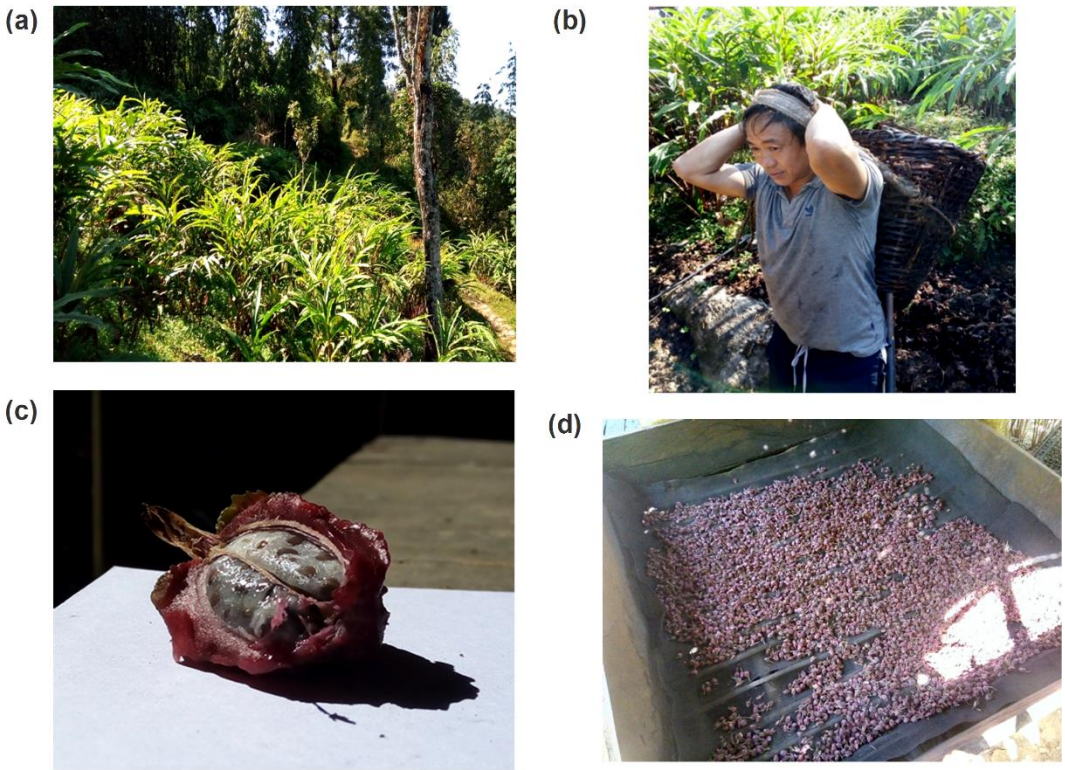

Fig. 1.16. Photographs taken during field visit to Lolegaon, Kalimpong of (a) large cardamom cultivation, (b) Harvesting of fruits by farmers, (c) Cardamom seed before drying, (d) Curing of cardamom in Bhatti.

Hence, spices' aroma profiles should be considered an appropriate benchmark to assess quality. Since no quality assessment criteria are present in the cardamom industry for commercialization, detecting volatiles in the aroma of cardamom is highly required. As discussed earlier, cardamom aroma is majorly composed of monoterpenes and sesquiterpenes. Table 1.5 lists different detection methods of monoterpenes reported in earlier research works.

Table 1.5. Detection of monoterpene by the different sensing processes.

Detection process	**Transducer**	**Sensing Materials**	**Monoterpenes Analyte**	**Refs.**
GC/SAW sensor	GC	Cyanopropyl phenyl polydimethylsiloxane fused silica capillary column	Linalool, α-pinene, benzaldehyde, benzyl methyl ether, 1,8-cineole, phenylacetaldehyde	[111]
HS-SPME	GC–MS	Carboxen-divinylbenzene-polydimethylsiloxane (CAR-DVB-PDMS) SPME fiber	α-pinene, β-pinene, benzaldehyde, linalool, β-myrcene, benzyl methyl ether, 1,8-cineole, α-Terpinolene	[111]
K-type MOS	MOS	Tungsten oxide impregnated with a small amount of platinum	1,4-cineole, 1,8-cineole, limonene, linalool, terpinene-4-ol, nerol, geraniol	[60]
MOS gas sensor	MOS	Alumina substrate-based electrode	Limonene	[112]
DNA-NT	FET	DNA-Carbon nano tube	Limonene, α-pinene, β-pinene	[113]
DNA-SWCNT	FET	DNA-Single-walled carbon nanotubes	Dimethyl-sulfone, isovaleric acid, α-pinene, β-pinene	[114]
MAA-MIP	QCM	Methacrylic acid	α-pinene, β-phellandrene, 3-carene, *cis*-thujopsene	[115]

PDMS-MIP	QCM	Polydimethylsiloxane	α-pinene, limonene, 1,8-cineole, β-pinene, terpinene, estragole	[116]
Molecularly imprinted sol-gel (MISG)	Glass slides electromagnetic field	Sol-gel Gold (Au) nano-urchins film	Limonene, *cis*-jasmone, α-pinene, γ-terpinene	[117]
MIP	Au substrate-based interdigit electrodes	Au nanoparticles conductive polymers	Limonene, geraniol	[118]

The above processes, like gas chromatography (GC), have a high-end, time, and power-consuming system. The metal oxide semiconductor (MOS) sensors are highly temperature-sensitive and require significant power consumption. Field-effect transistor (FET) sensors require low power but are complex electrode development. However, the molecularly imprinted polymer (MIP) is a vital sensing technique implemented for the selective detection of VOCs. The MIP fabrication steps are not so easy and are time-consuming. In contrast, quartz crystal microbalance (QCM) coated sensors are easy to fabricate and require fewer steps and time for fabrication. Due to such simplicity and ease of design, QCM sensors have been chosen.

There has been an increasing demand in the development of QCM sensor among researchers because it has high sensitivity and can be utilised at ambient temperature. Furthermore, the sensor operation is simple, quick, and may be monitored in real-time [119]. Several research studies employing quartz crystal microbalance (QCM) sensors have been done to evaluate the quality of various agricultural products. However, no research on the identification of volatile organic molecules in cardamom has been published as of yet.

Yamanaka et al. [120,121] developed eight QCM gas sensors using lipid and the GC stationary phase materials as the sensing layer for determining the aroma of apple, jasmine, and spices. Iqbal et al. [122] demonstrated selective adsorption of terpenes from fresh and dried rosemary, basil and sage using a QCM-based MIP layer. Likewise, the research conducted by Lieberzeit et al. [123] discussed the development of a molecularly imprinted layer for selective detection of terpenes and alcohols such as α-pinene, linalool, thymol, camphene, and estragole from odoriferous plants such

as basil and peppermint. Okur et al. [124] have reported discriminating six mint species by developing a QCM sensor array using 12 sensing layers including metal oxide nanoparticle dispersions, metal Organic Frame, and polymer films. To assess the quality of cinnamon samples, Toniolo et al.'s [125] introduced a variety of room-temperature ionic liquids (RTILs) coated QCM sensors for the detection of 31 volatile organic compounds (VOCs), including alcohols, phenols, aldehydes, esters, ketones, acids, amines, hydrocarbons, and terpenes.

Furthermore, QCM gas sensors have been used to detect the aroma of various fruits and food products. Natale et al. [126] developed metalloporphyrins coated eight QCM sensors to analyse the aromatic quality of multiple foods such as codfish, veal meat, tomato pulp, and red wine. Ali et al. [37,127,128] reported the sensitive adsorption of important volatiles of mangoes such as 3-carene, β-caryophyllene, and β-myrcene using QCM sensors. A similar study sensing a significant volatile in mango, Ocimene, was published by Ghatak et al. [38] using mustard oil as the sensor coating. Muñoz-Aguirre et al. [129] developed four QCM gas sensors for determining orange aroma and five QCM sensors for melon aroma using lipids and stationary GC phase material as the sensing surface. In another research, to restrict the premature rotting of fruits, Tolentino et al. [130] devised an ethylene sensor by drop-coating polyvinylpyrrolidone/$AgBF_4$ composite over a quartz crystal microbalance sensor. Wen et al. [131] have developed an ethyl cellulose coated QCM sensor to detect the changes in D-Limonene abundance due to *Bactrocera dorsalis* (Hendel) infestation in citrus fruits. Sharma et al. [33,34,132] extensively used QCM sensors to detect aroma characteristics in black tea like linalool, geraniol, and methyl salicylate. The author framed the present dissertation to improvise a modern and user-friendly sensing device using QCM sensors, which will be easily accessible for quality checks in the spice market.

1.7. Research questions

This thesis aims to find out the solutions to the following questions using a scientific approach regarding aromatic detection of cardamom given below:

Question 1: Is it possible to differentiate cardamom based on its aroma?

Question 2: Can the primary compounds responsible for the variation in aroma be identified?

Question 3: Is it possible to develop a low-cost portable sensing system for VOC identification of cardamom?

Question 4: Is it possible to detect the important volatiles of cardamom using QCM sensors from actual samples?

Question 5: Can a relationship between the intensity of the VOC sensed by the developed sensor be drawn with the actual content of the VOC in the sample?

1.8. Objectives and scope

The objectives of this thesis work can be summed up as follows:

i. Chemical characterization by Head-Space Microextraction guided Gas Chromatography-Mass Spectrometry (GCMS) for volatile organic constituents of Indian cardamom.
ii. Identification of important VOCs from headspace chromatogram of cardamom samples.
iii. Development of a low-cost, portable VOC sensing system based on QCM sensor.
iv. Selection of the sensor coating materials and studying its structural and morphological parameters.
v. Developing QCM sensors for the dominant VOCs in cardamom using different coating methods.
vi. Study the sensor characteristics (sensitivity, selectivity, repeatability, reproducibility, stability, electrical impedance, adsorption isotherm, etc.) of the developed sensors.
vii. Correlation of GCMS estimation with sensor output.

Given the above-mentioned objectives, the work has been divided into eight chapters. A brief chapter-wise organization of the thesis is presented below.

Chapter 1 introduces the importance of Indian cardamom in the Indian economic scenario. Moreover, details have been discussed regarding its origin, cultivars, and health benefits, pointing out the necessity for its quality evaluation. A detailed literature review emphasizing the volatiles present in different cultivars of cardamom has been discussed. A brief idea of different gas sensors has been elaborated, focusing on quartz crystal microbalance (QCM) sensors. The chapter concludes with the objective and scope of this research work.

Chapter 2 presents the overview of gas chromatography-mass spectrometry and discusses all essential experimental parameters used in this work. A detailed SPME-GCMS report of 24 (21 large; 3 small) cardamoms samples used in this work has been presented. A comprehensive study

has been done to correctly evaluate the VOCs responsible for the discrimination between the samples using principal component analysis (PCA), similarity percentage (SIMPER) test, one-way analysis of variance (ANOVA), etc. Finally, the influence of the headspace volatiles of the samples based on different physical parameters like altitude, pod weight, and curing method has been investigated. The major volatiles identified in this work has been further considered as the target VOC for the QCM sensors developed in the latter part of the thesis.

Chapter 3 presents the development stages of a portable and low-cost QCM sensor-based gas sensing device. The portable instrument rapidly identified cardamom volatile organic compounds (VOCs). The system is comprised of an 8284A oscillation circuit, a Teensy 3.2-based counter module, and a Raspberry Pi 4 with a 7-inch touch display for data monitoring and control. A customized Python-based graphical user interface was designed to facilitate the recording and storing of sensor data. Moreover, brief definitions of the different sensing parameters studied using this device have been illustrated in the latter part of this section.

Chapter 4 shows the development of a QCM sensor with the vegetable oil from olive (OLV-QCM) to detect a critical volatile organic compound, β-pinene, in Indian cardamom. The field emission scanning electron microscopy (FESEM) and Fourier-transform infrared spectroscopy (FTIR) study have been conducted to determine the surface morphology and chemical compositions of the fabricated QCM sensor coating. The sensitivity, reproducibility, repeatability, and reusability were studied for the developed sensor. The physical adsorption affinity of the sensor has been validated towards β-pinene applying Langmuir, Freundlich, and Langmuir-Freundlich isotherm models. GCMS correlation with the real sample has been presented in this chapter.

Chapter 5 discusses the fabrication of a rice-bran (RB-QCM) oil-coated QCM sensor for the detection of α-pinene in large and small cardamom. Different sensor characteristics like sensitivity, selectivity, repeatability, stability and humidity responses have been studied. The binding interaction between the sensitive coating material and α-pinene has been investigated using Ultraviolet-Visible (UV-Vis) spectroscopy and molecular docking studies. Furthermore, sensor surface morphology studies have been carried out by FTIR, Scanning electron microscopy (SEM),

and Atomic force microscopy (AFM). Finally, the performance of the developed sensors was verified with real samples and correlated with its GCMS headspace peak area percentages.

Chapter 6 contains the synthesis and fabrication steps for modified castor oil (QCM-Phe-CAS-Phe) based QCM sensor for the detection of 1,8-cineole in large cardamom. Detailed explanations regarding the selection of the coating material and its binding interaction have been given. The binding affinity between the sensitive coating material and 1,8-cineole has been studied using UV-Vis spectroscopy and GCMS headspace analysis. The sensor surface characteristics have been studied by FTIR, SEM, and AFM. Different sensor properties along with their performance with real samples have been carried out. Moreover, a mathematical model has been developed for the prediction of 1,8-cineole content in cardamom samples using the developed QCM-Phe-CAS-Phe sensor using Python programming language.

Chapter 7 presents a molecularly imprinted polymer (MIP) technique for the development of a QCM gas sensor (aTA-MIP-QCM) to detect α-terpinyl acetate in small cardamom. Here α-terpinyl acetate, Methacrylic Acid (MAA), Ethylene glycol dimethacrylate (EGDMA), Azobis(cyclohexanecarbonitrile) (ABCN) has been chosen as template molecule, functional monomer, crosslinker, and radical initiator respectively. Detailed sensor study along with the characterization of MIP material using FTIR, SEM, and Brunauer-Emmett-Teller (BET) has been discussed in this chapter. The sensor responses have been further studied using cardamom samples to obtain the correlation with the GCMS estimates.

Chapter 8 discusses the conclusion and future scope of the thesis. The merits and demerits of the sensors and recommendations are presented.

References

[1] M. Anbuchelvi, Import and Export of Small Cardamom in India, Shanlax International Journal of Arts, Science and Humanities. 7 (2019) 97–111. https://doi.org/10.34293/sijash.v7i1.561.

[2] K.P.P. Nair, The Agronomy and Economy of Cardamom (Elettaria cardamomum M.): The "Queen of Spices," in: Advances in Agronomy, Academic Press, 2006: pp. 179–471. https://doi.org/10.1016/S0065-2113(06)91004-9.

[3] M. Zakir, Review on Breeding Method and Achievements of Cardamom (Elettaria cardamomum Maton) and Future Prospects, International Journal of Research in Agriculture and Forestry. 6 (2019). https://www.semanticscholar.org/paper/Review-on-Breeding-Method-and-Achievements-of-and-Zakir/aa82b76903602cabaaa3ca9d555d486f83f1f8d3 (accessed July 1, 2022).

[4] D.G. Sharma, Traditional knowledge systems in large cardamom farming: biophysical and management diversity in Indian mountainous regions, Indian Journal of …. (2009). https://www.academia.edu/54103370/Traditional_knowledge_systems_in_large_cardamom_farming_biophysical_and_management_diversity_in_Indian_mountainous_regions (accessed July 17, 2022).

[5] V.K. Bisht, J.S. Negi, A.K. Bh, ari, R.C. Sundriyal, Amomum subulatum Roxb: Traditional, phytochemical and biological activities-An overview, AJAR. 6 (2011) 5386–5390. https://doi.org/10.5897/AJAR11.745.

[6] A.I. Singh, A.K. Pothula, Postharvest Processing of Large Cardamom in the Eastern Himalaya, Mred. 33 (2013) 453–462. https://doi.org/10.1659/MRD-JOURNAL-D-12-00069.1.

[7] P.N. Ravindran, K.J. Madhusoodanan, eds., Cardamom: The Genus Elettaria, 1st edition, Taylor and Francis, 2002.

[8] M. Snoussi, E. Noumi, N. Trabelsi, G. Flamini, A. Papetti, V. De Feo, Mentha spicata Essential Oil: Chemical Composition, Antioxidant and Antibacterial Activities against Planktonic and Biofilm Cultures of Vibrio spp. Strains, Molecules. 20 (2015) 14402–14424. https://doi.org/10.3390/molecules200814402.

[9] S. Ghosh, K. Ghosh, S. Karamakar, S. Prasad, N. Debabhuti, P. Sharma, B. Tudu, N. Bhattacharyya, R. Bandyopadhyay, Development of an IOT based robust architecture for environmental monitoring using UAV, in: 2019 IEEE 16th India Council International Conference (INDICON), 2019: pp. 1–4. https://doi.org/10.1109/INDICON47234.2019.9028987.

[10] K.N. Gurudutt, J.P. Naik, P. Srinivas, B. Ravindranath, Volatile Constituents of Large Cardamom (Amomum subulatum Roxb.), Flavour and Fragrance Journal. 11 (1996) 7–9. https://doi.org/10.1002/(SICI)1099-1026(199601)11:1<7::AID-FFJ542>3.0.CO;2-9.

[11] N. Gopalakrishnan, C.S. Narayanan, Supercritical carbon dioxide extraction of cardamom, J. Agric. Food Chem. 39 (1991) 1976–1978. https://doi.org/10.1021/jf00011a018.

[12] K. Madhusoodanan, K. Rao, Cardamom, in: Handbook of Herbs and Spices, 1st ed., Woodhead Publishing, Cambridge, UK, 2001: pp. 134-142.

[13] V. Parthasarathy, D. Prasath, Cardamom, in: Handbook of Herbs and Spices, 2nd ed., Woodhead Publishing, Cambridge, UK, 2012: pp. 132–167.

[14] K. Vijayan, K. Madhoosdanan, V. Radhakrishnan, P. Ravindran, Properties and end-uses of scardamom, CRC Press, 2002. https://doi.org/10.1201/9780203216637-17.

[15] R.G. Hamzaa, N. Osman, Using of Coffee and Cardamom Mixture to Ameliorate Oxidative Stress Induced in γ-irradiated Rats, Biochemistry and Analytical Biochemistry. 1 (2012) 2161–1009. https://doi.org/10.4172/2161-1009.1000113.

[16] A. ullah Khan, Q.J. Khan, A.H. Gilani, Pharmacological basis for the medicinal use of cardamom in asthma, Bangladesh Journal of Pharmacology. 6 (2011) 34–37. https://doi.org/10.3329/bjp.v6i1.8133.

[17] A. Saeed, B. Sultana, F. Anwar, M. Muhammad, K. Alkharfy, A.-H. Gilani, Antioxidant and Antimutagenic Potential of Seeds and Pods of Green Cardamom (Elettaria cardamomum), International Journal of Pharmacology. 10 (2014) 461–469. https://doi.org/10.3923/ijp.2014.461.469.

[18] N.M. Elguindy, G.A. Yacout, E.F. El Azab, Amelioration of DENA-induced oxidative stress in rat kidney and brain by the essential oil of Elettaria cardamomum, Beni-Suef University Journal of Basic and Applied Sciences. 7 (2018) 299–305. https://doi.org/10.1016/j.bjbas.2018.02.005.

[19] I. Das, A. Acharya, D.L. Berry, S. Sen, E. Williams, E. Permaul, A. Sengupta, S. Bhattacharya, T. Saha, Antioxidative effects of the spice cardamom against non-melanoma skin cancer by modulating nuclear factor erythroid-2-related factor 2 and NF-κB signalling pathways, Br J Nutr. 108 (2012) 984–997. https://doi.org/10.1017/S0007114511006283.

[20] A.H. Gilani, Q. Jabeen, A. Khan, A.J. Shah, Gut modulatory, blood pressure lowering, diuretic and sedative activities of cardamom, J Ethnopharmacol. 115 (2008) 463–472. https://doi.org/10.1016/j.jep.2007.10.015.

[21] M.M. Rahman, M.N. Alam, A. Ulla, F.A. Sumi, N. Subhan, T. Khan, B. Sikder, H. Hossain, H.M. Reza, M.A. Alam, Cardamom powder supplementation prevents obesity, improves glucose intolerance, inflammation and oxidative stress in liver of high carbohydrate high fat diet induced obese rats, Lipids Health Dis. 16 (2017) 151. https://doi.org/10.1186/s12944-017-0539-x.

[22] R. Sharma, Cardamom comfort, Dent Res J (Isfahan). 9 (2012) 237.

[23] S.N. Goyal, C. Sharma, U.B. Mahajan, C.R. Patil, Y.O. Agrawal, S. Kumari, D.S. Arya, S. Ojha, Protective Effects of Cardamom in Isoproterenol-Induced Myocardial Infarction in Rats, Int J Mol Sci. 16 (2015) 27457–27469. https://doi.org/10.3390/ijms161126040.

[24] M. Bhaswant, H. Poudyal, M.L. Mathai, L.C. Ward, P. Mouatt, L. Brown, Green and Black Cardamom in a Diet-Induced Rat Model of Metabolic Syndrome, Nutrients. 7 (2015) 7691–7707. https://doi.org/10.3390/nu7095360.

[25] G.M. Nitasha Bhat, N. Nayak, K. Vinodraj, N. Chandralekha, P. Mathai, J. Cherian, Comparison of the efficacy of cardamom (Elettaria cardamomum) with pioglitazone on dexamethasone-induced hepatic steatosis, dyslipidemia, and hyperglycemia in albino rats, J Adv Pharm Technol Res. 6 (2015) 136–140. https://doi.org/10.4103/2231-4040.157981.

[26] S. Kadiri, A. Unnisa, K. Sushmitha, A. Lokhande, R. Suthakaran, Antidepressant Activity of Cardamom oil by Marble Burying test in rats, Der Pharmacia Lettre. 8 (2016) 279–282. https://doi.org/10.13140/RG.2.2.29097.52327.

[27] K. Ashokkumar, S. Vellaikumar, M. Murugan, M.K. Dhanya, G. Ariharasutharsan, S. Aiswarya, M. Akilan, T.D. Warkentin, A. Karthikeyan, Essential Oil Profile Diversity in Cardamom Accessions From Southern India, Frontiers in Sustainable Food Systems. 5 (2021). https://www.frontiersin.org/article/10.3389/fsufs.2021.639619 (accessed March 25, 2022).

[28] K. Ashokkumar, M. Murugan, M.K. Dhanya, T.D. Warkentin, Botany, traditional uses, phytochemistry and biological activities of cardamom [Elettaria cardamomum (L.) Maton] - A critical review, J Ethnopharmacol. 246 (2020) 112244. https://doi.org/10.1016/j.jep.2019.112244.

[29] K. Ashokkumar, A. Pandian, M. Murugan, M.K. Dhanya, T. Sathyan, P. Sivakumar, S. Raj, T.D. Warkentin, Profiling bioactive flavonoids and carotenoids in select south Indian spices and nuts, Natural Product Research. 34 (2020) 1306–1310. https://doi.org/10.1080/14786419.2018.1557179.

[30] K. Ashokkumar, M. Murugan, M.K. Dhanya, T.D. Warkentin, Botany, traditional uses, phytochemistry and biological activities of cardamom [Elettaria cardamomum (L.) Maton] – A critical review, Journal of Ethnopharmacology. 246 (2020) 112244. https://doi.org/10.1016/j.jep.2019.112244.

[31] S.J.S. Kumara, E.V. Packiyasothy, E.R. Jansz, Some studies on the effect of maturity and storage on the chlorophyll content and essential oils of the cardamon fruit (Elettaria cardamomum), Journal of the Science of Food and Agriculture. 36 (1985) 491–498. https://doi.org/10.1002/jsfa.2740360611.

[32] K.P.A. Padmakumari Amma, P.N. Venugopalan Nair, I. Sasidharan, M. Priya Rani, Chemical composition, flavonoid - phenolic contents and radical scavenging activity of four major varieties of cardamom, International Journal of Biological and Medical Research. 1 (2010) 20–24.

[33] P. Sharma, A. Ghosh, B. Tudu, L.P. Bhuyan, P. Tamuly, N. Bhattacharyya, R. Bandyopadhyay, A. Chatterjee, Detection of linalool in black tea using a quartz crystal microbalance sensor, Sensors and Actuators B: Chemical. 190 (2014) 318–325. https://doi.org/10.1016/j.snb.2013.08.088.

[34] P. Sharma, A. Ghosh, B. Tudu, L.P. Bhuyan, P. Tamuly, N. Bhattacharyya, R. Bandyopadhyay, U. Das, A Quartz Crystal Microbalance Sensor for Detection of Geraniol in Black Tea, IEEE Sensors Journal. 15 (2015) 1178–1185. https://doi.org/10.1109/JSEN.2014.2359741.

[35] P. Sharma, A. Ghosh, B. Tudu, S. Sabhapondit, B.D. Baruah, P. Tamuly, N. Bhattacharyya, R. Bandyopadhyay, Monitoring the fermentation process of black tea using QCM sensor based electronic nose, Sensors and Actuators B: Chemical. 219 (2015) 146–157. https://doi.org/10.1016/j.snb.2015.05.013.

[36] I.D. Pradhan, B. De, Varietal variation of hexane soluble chemical components of Indian mango (Mangifera indica L.) fruit pulp, J Pharmacogn Phytochem. 8 (2019) 3193–3198.

[37] S.B. Ali, B. Ghatak, N. Debabhuti, P. Sharma, A. Ghosh, B. Tudu, N. Bhattacharya, R. Bandyopadhyay, Detection of β-caryophyllene in mango using a quartz crystal microbalance sensor, Sensors and Actuators B: Chemical. 255 (2018) 3064–3073. https://doi.org/10.1016/j.snb.2017.09.131.

[38] B. Ghatak, S.B. Ali, B. Tudu, P. Pramanik, S. Mukherji, R. Bandyopadhyay, Detecting Ocimene in mango using mustard oil based quartz crystal microbalance sensor, Sensors and Actuators B: Chemical. 284 (2019) 514–524. https://doi.org/10.1016/j.snb.2018.12.156.

[39] A. Alam, R.S. Majumdar, P. Alam, COMPARATIVE STUDY OF METABOLITES AND ANTIMICROBIAL ACTIVITIES OF ESSENTIAL OILS EXTRACTED FROM THREE AMOMUM SUBULATUM CULTIVARS: Isolation, chemical characterization, antimicrobial study of three Greater cardamom cultivars essential oils, Asian Journal of Pharmaceutical and Clinical Research. (2019) 219–223. https://doi.org/10.22159/ajpcr.2019.v12i6.33215.

[40] J. Pura Naik, L. Jagan Mohan Rao, T.M. Mohan Kumar, S.R. Sampathu, Chemical composition of the volatile oil from the pericarp (husk) of large cardamom (Amomum subulatum Roxb.), Flavour and Fragrance Journal. 19 (2004) 441–444. https://doi.org/10.1002/ffj.1336.

[41] G.O. Adegoke, L. Jagan Mohan Rao, N.B. Shankaracharya, A comparison of the essential oils of Aframomum daniellii (Hook. F.) K. Schum. and Amomum subulatum Roxb., Flavour and Fragrance Journal. 13 (1998) 349–352. https://doi.org/10.1002/(SICI)1099-1026(1998090)13:5<349::AID-FFJ758>3.0.CO;2-O.

[42] S. Eyob, M. Appelgren, J. Rohloff, A. Tsegaye, G. Messele, Traditional medicinal uses and essential oil composition of leaves and rhizomes of korarima (Aframomum corrorima (Braun) P.C.M. Jansen) from southern Ethiopia, South African Journal of Botany. 74 (2008) 181–185. https://doi.org/10.1016/j.sajb.2007.10.007.

[43] R. Tisserand, R. Young, Essential oil safety: a guide for health care professionals, 2014. http://public.ebookcentral.proquest.com/choice/publicfullrecord.aspx?p=1746613 (accessed April 2, 2022).

[44] D. Sadeh, N. Nitzan, D. Chaimovitsh, A. Shachter, M. Ghanim, N. Dudai, Interactive effects of genotype, seasonality and extraction method on chemical compositions and yield of essential oil from rosemary (Rosmarinus officinalis L.), Industrial Crops and Products. 138 (2019) 111419. https://doi.org/10.1016/j.indcrop.2019.05.068.

[45] I.P.S. Kapoor, B. Singh, G. Singh, C.S. De Heluani, M.P. De Lampasona, C.A.N. Catalan, Chemical Composition and Antioxidant Activity of Essential Oil and Oleoresins of Nutmeg (Myristica fragrans Houtt.) Fruits, International Journal of Food Properties. 16 (2013) 1059–1070. https://doi.org/10.1080/10942912.2011.576357.

[46] S. Sim, S.K. Tan, B. Kohlenberg, N.A. Braun, Amomum tsao-ko—Chinese Black Cardamom: Detailed Oil Composition and Comparison With Two Other Cardamom Species, Natural Product Communications. 14 (2019) 1934578X19857675. https://doi.org/10.1177/1934578X19857675.

[47] A. Alam, T. jawaid, P. Alam, In vitro antioxidant and anti-inflammatory activities of green cardamom essential oil and in silico molecular docking of its major bioactives, Journal of Taibah University for Science. 15 (2021) 757–768. https://doi.org/10.1080/16583655.2021.2002550.

[48] Abdullah, A. Asghar, M.S. Butt, M. Shahid, Q. Huang, Evaluating the antimicrobial potential of green cardamom essential oil focusing on quorum sensing inhibition of Chromobacterium violaceum, J Food Sci Technol. 54 (2017) 2306–2315. https://doi.org/10.1007/s13197-017-2668-7.

[49] Abdullah, A. Algburi, A. Asghar, Q. Huang, W. Mustfa, H.U. Javed, S. Zehm, M.L. Chikindas, Black cardamom essential oil prevents Escherichia coli O157:H7 and Salmonella Typhimurium JSG 1748 biofilm formation through inhibition of quorum sensing, J Food Sci Technol. 58 (2021) 3183–3191. https://doi.org/10.1007/s13197-020-04821-8.

[50] S. Ghosh, P. Bhattacharjee, S. Das, 1,8-cineol-rich Cardamom Seed (Elettaria cardamomum) Extracts Using Green Technologies and Conventional Extractions: Process Analysis, Phytochemical Characterization, and Food Application, Separation Science and Technology. 50 (2015) 1974–1985. https://doi.org/10.1080/01496395.2015.1016038.

[51] F.A. Santos, V.S.N. Rao, 1,8-Cineol, a Food Flavoring Agent, Prevents Ethanol-Induced Gastric Injury in Rats, Dig Dis Sci. 46 (2001) 331–337. https://doi.org/10.1023/A:1005604932760.

[52] S. Chowdhury, S. Kumar, Alpha-terpinyl acetate: A natural monoterpenoid from Elettaria cardamomum as multi-target directed ligand in Alzheimer's disease, Journal of Functional Foods. 68 (2020) 103892. https://doi.org/10.1016/j.jff.2020.103892.

[53] S.S. Husain, M. Ali, Analysis of volatile oil of the fruits of Elettaria cardamomum (L.) Maton and its antimicrobial activity., World Journal of Pharmacy and Pharmaceutical Sciences (WJPPS). 3 (2014) 1798–1808.

[54] A.K. Vijayan, N.K. Leela, M. Dhanalakshmi, H.J. Akshitha, R. Rahul, P. Utpala, K.N. Babu, Volatile oil composition of four popular varieties of large cardamom (Amomum subulatum Roxb.), Journal of Spices and Aromatic Crops. 26 (2017) 37–43. https://doi.org/10.25081/josac.2017.v26.i1.805.

[55] A.K. Bhandari, V. Bisht, J. Negi, M. Baunthiyal, 1, 8-cineole: A predominant component in the essential oil of large cardamom (Amomum subulatum Roxb.), Undefined. (2013). https://www.semanticscholar.org/paper/1%2C-8-cineole%3A-A-predominant-component-in-the-oil-of-Bhandari-Bisht/10a61436ca1b5f30930bc4bdb951c75742556548 (accessed April 25, 2022).

[56] R. Joshi, P. Sharma, V. Sharma, R. Prasad, R.K. Sud, A. Gulati, Analysis of the essential oil of large cardamom (Amomum subulatum Roxb.) growing in different agro-climatic zones of Himachal Pradesh, India, J Sci Food Agric. 93 (2013) 1303–1309. https://doi.org/10.1002/jsfa.5886.

[57] Syeda, R. Gilani, I. Shahid, M. Javed, S. Mehmud, R. Ahme, Antimicrobial Activities and Physico-Chemical Properties of the Essential Oil from Amomum Subulatum, International Journal of Applied Chemistry. 2 (2006) 81–86.

[58] V. Hajhashemi, A. Ghannadi, H. Jafarabadi, Black cumin seed essential oil, as a potent analgesic and antiinflammatory drug, Phytother Res. 18 (2004) 195–199. https://doi.org/10.1002/ptr.1390.

[59] A.T. San, D.C. Joyce, P.J. Hofman, A.J. Macnish, R.I. Webb, N.J. Matovic, C.M. Williams, J.J. De Voss, S.H. Wong, H.E. Smyth, Stable isotope dilution assay (SIDA) and HS-SPME-GCMS quantification of key aroma volatiles for fruit and sap of Australian mango cultivars, Food Chemistry. 221 (2017) 613–619. https://doi.org/10.1016/j.foodchem.2016.11.130.

[60] H. Komura, M. Sugimura, K. Onaga, H. Koda, Improved Application of Semiconducting Metal Oxides as a Detector for High-Resolution Gas Chromatography, in: Food Flavor, American Chemical Society, 2008: pp. 36–44. https://doi.org/10.1021/bk-2008-0988.ch003.

[61] L.-Y. Chen, D.-M. Wong, C.-Y. Fang, C.-I. Chiu, T.-I. Chou, C.-C. Wu, S.-W. Chiu, K.-T. Tang, Development of an electronic-nose system for fruit maturity and quality monitoring, in: 2018 IEEE International Conference on Applied System Invention (ICASI), 2018: pp. 1129–1130. https://doi.org/10.1109/ICASI.2018.8394481.

[62] A. Sanaeifar, S.S. Mohtasebi, M. Ghasemi-Varnamkhasti, H. Ahmadi, Application of MOS based electronic nose for the prediction of banana quality properties, Measurement. 82 (2016) 105–114. https://doi.org/10.1016/j.measurement.2015.12.041.

[63] N. Aghilinategh, M.J. Dalvand, A. Anvar, Detection of ripeness grades of berries using an electronic nose, Food Science & Nutrition. 8 (2020) 4919–4928. https://doi.org/10.1002/fsn3.1788.

[64] J. Wang, Y. Zhou, Electronic-nose technique: Potential for monitoring maturity and shelf life of tomatoes, New Zealand Journal of Agricultural Research. 50 (2007) 1219–1228. https://doi.org/10.1080/00288230709510405.

[65] V. Messina, P.G. Domínguez, A.M. Sancho, N. Walsöe de Reca, F. Carrari, G. Grigioni, Tomato Quality during Short-Term Storage Assessed by Colour and Electronic Nose, International Journal of Electrochemistry. 2012 (2012) e687429. https://doi.org/10.1155/2012/687429.

[66] F. De Cesare, S. Pantalei, E. Zampetti, A. Macagnano, Electronic nose and SPME techniques to monitor phenanthrene biodegradation in soil, Sensors and Actuators B: Chemical. 131 (2008) 63–70. https://doi.org/10.1016/j.snb.2007.12.012.

[67] F. De Cesare, E. Di Mattia, S. Pantalei, E. Zampetti, V. Vinciguerra, F. Canganella, A. Macagnano, Use of electronic nose technology to measure soil microbial activity through biogenic volatile organic compounds and gases release, Soil Biology and Biochemistry. 43 (2011) 2094–2107. https://doi.org/10.1016/j.soilbio.2011.06.009.

[68] J. Chen, J. Gu, R. Zhang, Y. Mao, S. Tian, Freshness Evaluation of Three Kinds of Meats Based on the Electronic Nose, Sensors (Basel). 19 (2019) 605. https://doi.org/10.3390/s19030605.

[69] X. Yang, W. Xie, C. Zhang, H. Wu, S. Li, L. Yang, Identification of Sensory Quality of Rapid Fermented Fish Using Electronic Nose, in: 2009 International Conference on Information Engineering and Computer Science, 2009: pp. 1–3. https://doi.org/10.1109/ICIECS.2009.5363781.

[70] N. Magan, A. Pavlou, I. Chrysanthakis, Milk-sense: a volatile sensing system recognises spoilage bacteria and yeasts in milk, Sensors and Actuators B: Chemical. 72 (2001) 28–34. https://doi.org/10.1016/S0925-4005(00)00621-3.

[71] J. Lozano, T. Arroyo, J.P. Santos, J.M. Cabellos, M.C. Horrillo, Electronic nose for wine ageing detection, Sensors and Actuators B: Chemical. 133 (2008) 180–186. https://doi.org/10.1016/j.snb.2008.02.011.

[72] B. Tudu, A. Jana, A. Metla, D. Ghosh, N. Bhattacharyya, R. Bandyopadhyay, Electronic nose for black tea quality evaluation by an incremental RBF network, Sensors and Actuators B: Chemical. 138 (2009) 90–95. https://doi.org/10.1016/j.snb.2009.02.025.

[73] M. Pardo, G. Niederjaufner, G. Benussi, E. Comini, G. Faglia, G. Sberveglieri, M. Holmberg, I. Lundstrom, Data preprocessing enhances the classification of different brands of Espresso coffee with an electronic nose, Sensors and Actuators B: Chemical. 69 (2000) 397–403. https://doi.org/10.1016/S0925-4005(00)00499-8.

[74] M. Righettoni, A. Amann, S.E. Pratsinis, Breath analysis by nanostructured metal oxides as chemo-resistive gas sensors, Materials Today. 18 (2015) 163–171. https://doi.org/10.1016/j.mattod.2014.08.017.

[75] J.-W. Yoon, J.-H. Lee, Toward breath analysis on a chip for disease diagnosis using semiconductor-based chemiresistors: recent progress and future perspectives, Lab on a Chip. 17 (2017) 3537–3557. https://doi.org/10.1039/C7LC00810D.

[76] K.M.M. Kabir, M.J. Baker, W.A. Donald, Micro- and nanoscale sensing of volatile organic compounds for early-stage cancer diagnosis, TrAC Trends in Analytical Chemistry. 153 (2022) 116655. https://doi.org/10.1016/j.trac.2022.116655.

[77] M. Rodríguez-Aguilar, L. Díaz de León-Martínez, P. Gorocica-Rosete, R. Pérez-Padilla, C.A. Domínguez-Reyes, J.A. Tenorio-Torres, O. Ornelas-Rebolledo, G. Mehta, B.N. Zamora-Mendoza, R. Flores-Ramírez, Application of chemoresistive gas sensors and chemometric analysis to differentiate the fingerprints of global volatile organic compounds from diseases. Preliminary results of COPD, lung cancer and breast cancer, Clinica Chimica Acta. 518 (2021) 83–92. https://doi.org/10.1016/j.cca.2021.03.016.

[78] L. Zhao, J. Qian, F. Tian, R. Liu, B. Liu, S. Zhang, M. Lu, A Weighted Discriminative Extreme Learning Machine Design for Lung Cancer Detection by an Electronic Nose System, IEEE Transactions on Instrumentation and Measurement. 70 (2021) 1–9. https://doi.org/10.1109/TIM.2021.3084312.

[79] J. Zhang, Y. Tian, Z. Luo, C. Qian, W. Li, Y. Duan, Breath volatile organic compound analysis: an emerging method for gastric cancer detection, J. Breath Res. 15 (2021) 044002. https://doi.org/10.1088/1752-7163/ac2cde.

[80] A.D. Wilson, Application of Electronic-Nose Technologies and VOC-Biomarkers for the Noninvasive Early Diagnosis of Gastrointestinal Diseases †, Sensors (Basel). 18 (2018) E2613. https://doi.org/10.3390/s18082613.

[81] L. Liu, T. Li, Z. Yi, F. Chi, Z. Lin, X. Zhang, K. Xu, Conductometric ozone sensor based on mesoporous ultrafine Co3O4 nanobricks, Sensors and Actuators B: Chemical. 297 (2019) 126815. https://doi.org/10.1016/j.snb.2019.126815.

[82] N. Chakraborty, S. Das, A. Hossain, D. Saha, S. Mondal, Poly aniline (PANI) loaded hierarchical Ti1−xSbxO2 rutile phase nanocubes for selective room temperature detection of benzene vapor, Sensors and Actuators B: Chemical. 347 (2021) 130622. https://doi.org/10.1016/j.snb.2021.130622.

[83] F. Harrou, A. Dairi, Y. Sun, F. Kadri, Detecting Abnormal Ozone Measurements With a Deep Learning-Based Strategy, IEEE Sensors Journal. 18 (2018) 7222–7232. https://doi.org/10.1109/JSEN.2018.2852001.

[84] E.L. Reber, L.G. Blackwood, A.J. Edwards, A.E. Egger, P.J. Petersen, Idaho Explosives Detection System: Development and Enhancements, Sens Imaging. 8 (2007) 121–130. https://doi.org/10.1007/s11220-007-0038-7.

[85] R. Rousier, S. Bouat, T. Bordy, H. Grateau, M. Darboux, J. Hue, G. Gaillard, S. Besnard, F. Veignal, P. Montméat, G. Lebrun, A. Larue, T-REX: A Portable Device to Detect and Identify Explosives Vapors, Procedia Engineering. 47 (2012) 390–393. https://doi.org/10.1016/j.proeng.2012.09.165.

[86] M. Ostafin, B. Nogaj, 14N-NQR based device for detection of explosives in landmines, Measurement. 40 (2007) 43–54. https://doi.org/10.1016/j.measurement.2006.04.003.

[87] S. Dong, B. Wang, Electrochemical Biosensing in Extreme Environment, Electroanalysis. 14 (2002) 7–16. https://doi.org/10.1002/1521-4109(200201)14:1<7::AID-ELAN7>3.0.CO;2-V.

[88] S. Andreescu, O.A. Sadik, Trends and challenges in biochemical sensors for clinical and environmental monitoring, Pure and Applied Chemistry. 76 (2004) 861–878. https://doi.org/10.1351/pac200476040861.

[89] P. D'Orazio, Biosensors in clinical chemistry, Clin Chim Acta. 334 (2003) 41–69. https://doi.org/10.1016/s0009-8981(03)00241-9.

[90] A. Sen, J.D. Albarella, J.R. Carey, P. Kim, W.B. McNamara, Low-cost colorimetric sensor for the quantitative detection of gaseous hydrogen sulfide, Sensors and Actuators B: Chemical. 134 (2008) 234–237. https://doi.org/10.1016/j.snb.2008.04.046.

[91] J. Shao, H. Lin, M. Yu, Z. Cai, H. Lin, Study on acetate ion recognition and sensing in aqueous media using a novel and simple colorimetric sensor and its analytical application, Talanta. 75 (2008) 551–555. https://doi.org/10.1016/j.talanta.2007.11.048.

[92] A. Tahirović, A. Copra, E. Omanović-Miklicanin, K. Kalcher, A chemiluminescence sensor for the determination of hydrogen peroxide, Talanta. 72 (2007) 1378–1385. https://doi.org/10.1016/j.talanta.2007.01.072.

[93] M. Kimura, J. Manaka, S. Satoh, S. Takano, N. Igarashi, K. Nagai, Application of the air-bridge microheater to gas detection, Sensors and Actuators B: Chemical. 25 (1995) 857–860. https://doi.org/10.1016/0925-4005(95)85189-5.

[94] F. López, J. de Frutos, Multispectral interference filters and their application to the design of compact non-dispersive infrared gas analysers for pollution control, Sensors and Actuators A: Physical. 37–38 (1993) 502–506. https://doi.org/10.1016/0924-4247(93)80086-V.

[95] T.-V. Dinh, I.-Y. Choi, Y.-S. Son, J.-C. Kim, A review on non-dispersive infrared gas sensors: Improvement of sensor detection limit and interference correction, Sensors and Actuators B: Chemical. 231 (2016) 529–538. https://doi.org/10.1016/j.snb.2016.03.040.

[96] S. Hong, M. Wu, Y. Hong, Y. Jeong, G. Jung, W. Shin, J. Park, D. Kim, D. Jang, J.-H. Lee, FET-type gas sensors: A review, Sensors and Actuators B: Chemical. 330 (2021) 129240. https://doi.org/10.1016/j.snb.2020.129240.

[97] K. Yokosawa, K. Saitoh, S. Nakano, Y. Goto, K. Tsukada, FET hydrogen-gas sensor with direct heating of catalytic metal, Sensors and Actuators B: Chemical. 130 (2008) 94–99. https://doi.org/10.1016/j.snb.2007.07.084.

[98] M. Kozłowski, S. Frąckowiak, Chemical sensors based on polymer composites, Sensors and Actuators B: Chemical. 109 (2005) 141–145. https://doi.org/10.1016/j.snb.2005.03.068.

[99] W. Zeng, M.Q. Zhang, M.Z. Rong, Q. Zheng, Conductive polymer composites as gas sensors with size-related molecular discrimination capability, Sensors and Actuators B: Chemical. 124 (2007) 118–126. https://doi.org/10.1016/j.snb.2006.12.021.

[100] G. Sauerbrey, The use of quarts oscillators for weighing thin layers and for microweighing, Zeitschrift Für Physik. 155 (1959) 206–222. https://doi.org/10.1007/BF01337937.

[101] J.-M. Lehn, Supramolecular Chemistry: Concepts and Perspectives, Wiley, 1995.

[102] G. Vasapollo, R.D. Sole, L. Mergola, M.R. Lazzoi, A. Scardino, S. Scorrano, G. Mele, Molecularly Imprinted Polymers: Present and Future Prospective, International Journal of Molecular Sciences. 12 (2011) 5908–5945. https://doi.org/10.3390/ijms12095908.

[103] W.J. Cheong, S.H. Yang, F. Ali, Molecular imprinted polymers for separation science: A review of reviews, Journal of Separation Science. 36 (2013) 609–628. https://doi.org/10.1002/jssc.201200784.

[104] C. Yu, K. Mosbach, Influence of mobile phase composition and cross-linking density on the enantiomeric recognition properties of molecularly imprinted polymers, J Chromatogr A. 888 (2000) 63–72. https://doi.org/10.1016/s0021-9673(00)00556-2.

[105] W.M. Mullett, E.P.C. Lai, Determination of Theophylline in Serum by Molecularly Imprinted Solid-Phase Extraction with Pulsed Elution, Anal. Chem. 70 (1998) 3636–3641. https://doi.org/10.1021/ac980264s.

[106] Boerje. Sellergren, Direct Drug Determination by Selective Sample Enrichment on an Imprinted Polymer, Anal. Chem. 66 (1994) 1578–1582. https://doi.org/10.1021/ac00081a036.

[107] Climate Change Impacts and Vulnerability in the Eastern Himalayas | HimalDoc, (n.d.). https://lib.icimod.org/record/26800 (accessed July 1, 2022).

[108] V.G. Rao, S. Mande, V.V.N. Kishore, Study of drying characteristics of large-cardamom, Biomass and Bioenergy. 20 (2001) 37–43. https://doi.org/10.1016/S0961-9534(00)00047-7.

[109] P.K. Rout, D. Sahoo, K.S. Jena, Y.R. Rao, Analysis of the Oil of Large Cardamom (Amomum subulatum Roxb.,) Growing in Sikkim, Journal of Essential Oil Research. 15 (2003) 265–266. https://doi.org/10.1080/10412905.2003.9712138.

[110] E. Sharma, R. Sharma, K.K. Singh, G. Sharma, A Boon for Mountain Populations, Mred. 20 (2000) 108–111. https://doi.org/10.1659/0276-4741(2000)020[0108:ABFMP]2.0.CO;2.

[111] S.Y. Oh, H.D. Shin, S.J. Kim, J. Hong, Rapid determination of floral aroma compounds of lilac blossom by fast gas chromatography combined with surface acoustic wave sensor, Journal of Chromatography A. 1183 (2008) 170–178. https://doi.org/10.1016/j.chroma.2008.01.024.

[112] M. Gancarz, J. Wawrzyniak, M. Gawrysiak-Witulska, D. Wiącek, A. Nawrocka, M. Tadla, R. Rusinek, Application of electronic nose with MOS sensors to prediction of rapeseed quality, Measurement. 103 (2017) 227–234. https://doi.org/10.1016/j.measurement.2017.02.042.

[113] N.J. Kybert, G.H. Han, M.B. Lerner, E.N. Dattoli, A. Esfandiar, A.T. Charlie Johnson, Scalable arrays of chemical vapor sensors based on DNA-decorated graphene, Nano Res. 7 (2014) 95–103. https://doi.org/10.1007/s12274-013-0376-9.

[114] S. Gaggiotti, S. Palmieri, F. Della Pelle, M. Sergi, A. Cichelli, M. Mascini, D. Compagnone, Piezoelectric peptide-hpDNA based electronic nose for the detection of terpenes; Evaluation of the aroma profile in different Cannabis sativa L. (hemp) samples, Sensors and Actuators B: Chemical. 308 (2020) 127697. https://doi.org/10.1016/j.snb.2020.127697.

[115] Z. Wang, W. Chen, S. Gu, J. Wang, Y. Wang, Discrimination of wood borers infested Platycladus orientalis trunks using quartz crystal microbalance gas sensor array, Sensors and Actuators B: Chemical. 309 (2020) 127767. https://doi.org/10.1016/j.snb.2020.127767.

[116] H.F. Hawari, N.M. Samsudin, A.Y. Md Shakaff, Supri.A. Ghani, M.N. Ahmad, Y. Wahab, U. Hashim, Development of Interdigitated Electrode Molecular Imprinted Polymer Sensor for Monitoring Alpha Pinene Emissions from Mango Fruit, Procedia Engineering. 53 (2013) 197–202. https://doi.org/10.1016/j.proeng.2013.02.026.

[117] B. Chen, C. Liu, L. Shang, H. Guo, J. Qin, L. Ge, C.J. Jing, C. Feng, K. Hayashi, Electric-field enhancement of molecularly imprinted sol–gel-coated Au nano-urchin sensors for vapor detection of plant biomarkers, J. Mater. Chem. C. 8 (2019) 262–269. https://doi.org/10.1039/C9TC05522C.

[118] J.-H. Jung, S.-P. Lee, Biomimetic MIP Terpene Sensors Adding Conductive Polymers, Journal of Sensor Science and Technology. 21 (2012) 345–351. https://doi.org/10.5369/JSST.2012.21.5.345.

[119] E. Casero, L. Vázquez, A.M. Parra-Alfambra, E. Lorenzo, AFM, SECM and QCM as useful analytical tools in the characterization of enzyme-based bioanalytical platforms, Analyst. 135 (2010) 1878–1903. https://doi.org/10.1039/C0AN00120A.

[120] T. Yamanaka, R. Matsumoto, T. Nakamoto, Study of odor blender using solenoid valves controlled by delta–sigma modulation method for odor recorder, Sensors and Actuators B: Chemical. 87 (2002) 457–463. https://doi.org/10.1016/S0925-4005(02)00300-3.

[121] T. Yamanaka, R. Matsumoto, T. Nakamoto, Study of recording apple flavor using odor recorder with five components, Sensors and Actuators B: Chemical. 89 (2003) 112–119. https://doi.org/10.1016/S0925-4005(02)00451-3.

[122] N. Iqbal, G. Mustafa, A. Rehman, A. Biedermann, B. Najafi, P.A. Lieberzeit, F.L. Dickert, QCM-Arrays for Sensing Terpenes in Fresh and Dried Herbs via Bio-Mimetic MIP Layers, Sensors. 10 (2010) 6361–6376. https://doi.org/10.3390/s100706361.

[123] P.A. Lieberzeit, A. Rehman, N. Iqbal, B. Najafi, F.L. Dickert, QCM sensor array for monitoring terpene emissions from odoriferous plants, Monatsh Chem. 140 (2009) 947–952. https://doi.org/10.1007/s00706-009-0141-7.

[124] S. Okur, M. Sarheed, R. Huber, Z. Zhang, L. Heinke, A. Kanbar, C. Wöll, P. Nick, U. Lemmer, Identification of Mint Scents Using a QCM Based E-Nose, Chemosensors. 9 (2021) 31. https://doi.org/10.3390/chemosensors9020031.

[125] R. Toniolo, A. Pizzariello, N. Dossi, S. Lorenzon, O. Abollino, G. Bontempelli, Room Temperature Ionic Liquids As Useful Overlayers for Estimating Food Quality from Their Odor Analysis by Quartz Crystal Microbalance Measurements, Anal. Chem. 85 (2013) 7241–7247. https://doi.org/10.1021/ac401151m.

[126] C. Di Natale, A. Macagnano, F. Davide, A. D'Amico, R. Paolesse, T. Boschi, M. Faccio, G. Ferri, An electronic nose for food analysis, Sensors and Actuators B: Chemical. 44 (1997) 521–526. https://doi.org/10.1016/S0925-4005(97)00175-5.

[127] S.B. Ali, B. Ghatak, S.D. Gupta, N. Debabhuti, P. Chakraborty, P. Sharma, A. Ghosh, B. Tudu, S. Mitra, M.P. Sarkar, N. Bhattacharyya, R. Bandyopadhyay, Detection of 3-Carene in mango using a quartz crystal microbalance sensor, Sensors and Actuators B: Chemical. 230 (2016) 791–800. https://doi.org/10.1016/j.snb.2016.03.005.

[128] S.B. Ali, B. Ghatak, N. Debabhuti, S. Pal, prolay sharma, B. Tudu, N. Bhattacharyya, R. Bandyopadhyay, Determination of β -Myrcene Volatile in Mango by Quartz Crystal Microbalance Sensor, IEEE Sensors Journal. 19 (2019) 893–900. https://doi.org/10.1109/JSEN.2018.2879539.

[129] S. Muñoz-Aguirre, A. Yoshino, T. Nakamoto, T. Moriizumi, Odor approximation of fruit flavors using a QCM odor sensing system, Sensors and Actuators B: Chemical. 123 (2007) 1101–1106. https://doi.org/10.1016/j.snb.2006.11.025.

[130] M.A.K.P. Tolentino, D.R.B. Albano, F.B. Sevilla, Piezoelectric sensor for ethylene based on silver(I)/polymer composite, Sensors and Actuators B: Chemical. 254 (2018) 299–306. https://doi.org/10.1016/j.snb.2017.07.015.

[131] T. Wen, M. Sang, M. Wang, L. Han, Z. Gong, X. Tang, X. Long, H. Xiong, H. Peng, Rapid detection of d-limonene emanating from citrus infestation by Bactrocera dorsalis (Hendel) using a developed gas-sensing system based on QCM sensors coated with ethyl cellulose, Sensors and Actuators B: Chemical. 328 (2021) 129048. https://doi.org/10.1016/j.snb.2020.129048.

[132] P. Sharma, B. Tudu, L.P. Bhuyan, P. Tamuly, N. Bhattacharyya, R. Bandyopadhyay, Detection of Methyl Salicylate in Black Tea Using a Quartz Crystal Microbalance Sensor, IEEE Sensors Journal. 16 (2016) 5160–5166. https://doi.org/10.1109/JSEN.2016.2564978.

Chapter 2

Determination of volatile organic compounds (VOCs) from Indian cardamom using GCMS analysis

2.1. Introduction

Cardamom being highly aromatic, the quality, economic value, and desirability of this spice depends on its aroma. Yet, plenty of research has been conducted to unveil the volatile constituents of large and small cardamom. However, most of the researches are concentrated on the volatilome of seed due to its direct commercial value. The outcome of this literature reveals that large cardamom contains many volatile organic compounds responsible for its flavour and essences. In most of the literature, researchers have concentrated on the large cardamom's total volatile contents. Their experimental approach involves the extraction of volatile essential oil using the hydro distillation technique, followed by their analysis in GC-FID or GC-MS [1–5]. As the hydro distillation technique involves boiling spices at a very high temperature, it allows all the volatile organic compounds present in the spices to come into the essential oil fraction. Many compounds having minimal volatility can be detected in this process [6]. Qualitatively, the volatiles of large cardamom and small cardamom are similar except for some unique volatiles like terpinyl acetate, geranyl acetate, linalyl acetate, citral, neral, and linalool [7]. Considering this, we have tried to investigate the HS volatilome of large and small cardamoms at normal atmospheric temperature (25^{o} - 27^{o}C) and attempted to categorise samples based on their aroma profile, which could be an essential factor in determining the quality and market value of cardamoms.

As a vast fraction of these VOCs has a very high boiling point, i.e. higher than room temperature and vaporisation enthalpy, many of them could not contribute significantly to the fragrance of this spice at normal temperatures [6]. Thus, it is essential to correctly figure out the VOCs responsible for forming the headspace aroma of cardamom. This becomes beneficial for the proper identification of VOCs using QCM gas sensors. Concerning these limitations of the hydro distillation technique, we have opted for another approach to analyse only those volatiles present in the headspace of the sample; more preciously, that **volatiles contribute to the development of aroma of large cardamom and small cardamom at normal temperature**. We have used the solid-phase microextraction technique (SPME) to adsorb only the headspace volatiles (HSVs) and consider them in our study. The available compounds in the headspace were correlated with the fabricated QCM sensors to validate the sensor performance properly. To date, no research article has been published exploring the HSVs or headspace volatilome of cardamom; thus, this study will provide proper insight into the aroma profile of cardamom in the Indian context.

2.2. Study of volatile components using GCMS

2.2.1. Principle of gas chromatography

The technique of gas chromatography (GC) separates analytes from a mixture by passing a mobile gas phase through a stationary sorbent. The function of a gas chromatograph is as follows: Through the injection port, column, and detector, a steady supply of inert carrier gas (such as helium; mobile phase) flows. The flow rate of the carrier gas is carefully controlled to maintain constant retention durations and prevent detector drift and noise. The sample is typically injected into the 15 to 30 m long capillary column using an injection port. Capillary column was made with liquid mobile phase coated with a high-temperature resistant, inert solid support (the stationary phase).

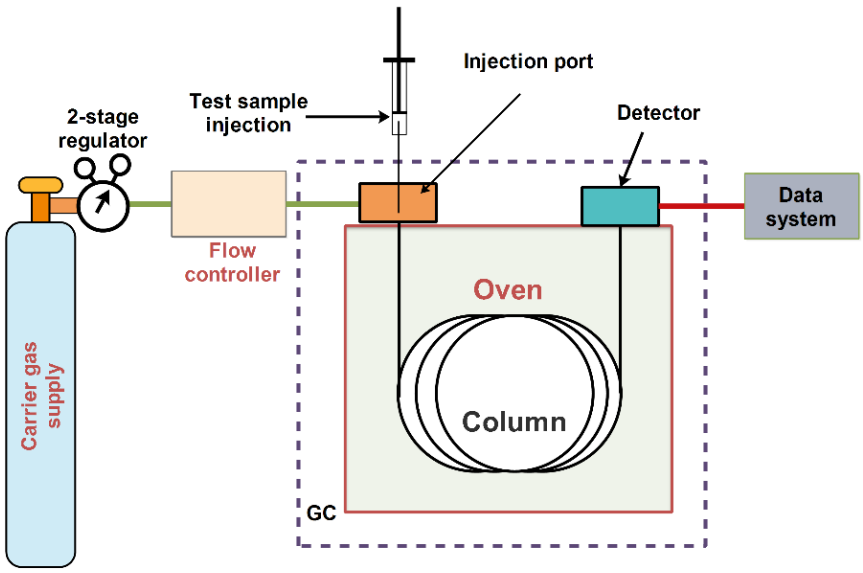

Fig. 2.1. Diagram of a gas chromatogram.

The "analytes" present in the mixture are separated according to the relative interaction of each analyte with the stationary phases regarding the specific mobile phase. The profile of the analytes separation of analytes is achieved by the differential partitioning ability of molecules in the stationary phase and mobile phase. The sample and carrier gas then pass through a detector. This device creates an electrical signal based on the retention of each molecule within the column (determined by the partition coefficient of each analyte) and expressed in terms of retention time

(RT). From this, a data system or integrator constructs a graph (the written analysis record). Fig. 2.1. describes the schematic of the GC process.

2.2.2. Mass spectrometry (MS)

MS analysis is a technique that identifies substances by ionising molecules into a vacuum chamber, accelerating them through a magnetic field, breaking the molecules into charged fragments and producing an unstable ion. A spectral plot displays the mass/charge ratio of the charged particle. Reference data is compared from the molecular mass and the fragments' mass to determine the specimen's identity. Each substance's mass spectrum is unique. Providing that the interpretation of the output correctly determines the parent mass, MS identification is conclusive. Block diagram of the working principle of mass spectrometer is shown in Fig. 2.2.

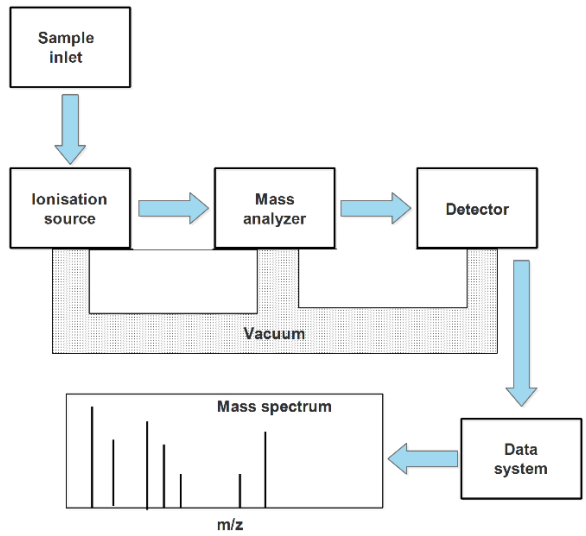

Fig. 2.2. Block diagram of the working principle of mass spectrometer.

2.2.3. Sample preparation

Despite its high separation power, some GC studies need sample preparation before injection. With gas chromatography, i) the analyte(s) are moved into a solvent phase (typically organic) for liquid injection or ii) into the vapour phase for introduction as headspace (generally through a sample loop or gas-tight syringe). Analytes must be volatile enough to traverse the instrument's inlet and column; ideally, the matrix interferences must also be volatile. The fundamental goal of sample preparation is to ensure that the above conditions are met.

2.2.3.1. Solvent Extraction

Solvent extraction techniques use non-polar or polar solvents depending on the hydrophobicity or hydrophilicity of the molecules. For hydrophobic compounds, the solvent that is immiscible with water is usually used to extract the target compound. On the other hand, for hydrophilic target compounds, polar solvent, typically water and methanol, is used for extraction. Sometimes, a mixture of solvent systems is used to increase the solubility of the target molecules. Ideally, the target compound is extracted selectively using a solvent with high solubility. The extraction of semi-volatile chemicals from water is often conducted using solvents with different polarities according to eluotropic series, such as dichloromethane, carbon tetrachloride, ethyl acetate, diethyl ether, and hexane.

2.2.3.2. Solid-phase microextraction (SPME)

Solid-phase microextraction (SPME) is a novel and sensitive solvent-free technique for sample preparation. SPME is a method that incorporates a fiber needle attachment which adsorbs analytes directly from the vapour phase over the liquid samples in a closed environment, i.e., exposed to the headspace vapours from liquid or solid samples. The coated fiber remains inside of protective needle and is attached to a holder that functions as a needle.

After being exposed to a sample, the analytes in the fiber partition into the sample headspace until an equilibrium is reached. The coating on the fiber adsorbs headspace VOCs from the sample. Desorption and analysis of the fiber are carried out in a gas chromatography (GC) apparatus after the fiber has been removed for a predetermined period. The adsorbed analytes are then thermally desorbed in GC for further identification. In addition to environmental, biological, and pharmaceutical samples, SPME are currently used to analyse food and beverage products, flavours and aromas, forensics and toxicology, and product testing.

2.2.4. Different Methods for Identification of HSVs

Identification and confirmation of the volatile organic compounds can be made in two ways. Firstly, HSVs can be identified tentatively by their unique mass fragmentation pattern after

comparing them with the National Institute of Standards and Technology (NIST search 2.3, 2017) database.

The co-chromatography by comparing retention time (RT) with the authentic compounds is also an acceptable approach to identifying a compound in GC. In this method, analytical standards should be run in the identical condition to the program in which the samples were analysed, and the retention time of each standard should be recorded. In the subsequent step, compounds can be identified accurately by comparing each standard's retention time with the compounds.

Alongside the co-chromatogram approach, retention index-based approaches are also used when standards are unavailable. In this approach, compounds are identified with the help of a mixture of n-alkanes series (C_8 - C_{40}) by comparing the experimental retention index (RI, also known as Kovats Index) of each compound with the values available in the NIST MS libraries. RI of specific compound(s) can be calculated for a particular program according to the equation (2.1)

$$RI = 100 \times \frac{T_X - T_n}{T_{n+1} - T_n} \quad (2.1)$$

T_n and T_{n+1} are retention times of n-alkanes (C_8 - C_{40}) eluting immediately before and after the desired compound.

T_x is the retention time of the desired compound "x".

2.3. Extraction of volatile flavour components (VFC) of large and small cardamom samples using SPME-guided GCMS

2.3.1. Procurement of sample

Twenty-four different cardamom samples (three small and 21 large) were procured from Spices Board India, Gangtok (Ministry of Commerce and Industry, Government of India), Indian Cardamom Research Institute (ICRI), Karnataka, and Institute of Bioresources & Sustainable Development (IBSD), Manipur throughout the course of this research work. The details of the samples are tabulated in Table 2.1.

Table 2.1. Details of cardamom samples (Cardamom samples with known cultivars are demarcated with *; cardamom samples purchased from market are marked with **)

Sample name	**Cultivars/ Commercial brand**	**Curing process**	**Location**	**Altitude (m)**	**Average wt. from at least three Pod Weight (g)**
LC1**	-		East Sikkim	-	1.23
LC2**	-		East Sikkim	-	0.89
LC3**	-		Sikkim	-	1.15
LC4**	Spice Jet		-	-	0.92
LC5**	Nepal Top JJ		-	-	0.64
LC6**	Pure and Sure		-	--	1.13
LC7**	Victory JJ		-	-	0.94
LC8*	Varlangey	Old Bhatti	Kalimpong	1000	1.08
LC9*	Varlangey	Old Bhatti	Kalimpong	1248	0.84
LC10*	Sawney	Modified Bhatti	North Sikkim	-	1.01
LC11*	Ramsey Chibey	New Bhatti	West Sikkim	1311	0.75
LC12*	Varlangey	Electric Dryer	West Sikkim	-	1.32
LC13*	Ramla	Old Bhatti	North Sikkim	1720	0.95
LC14*	Sawney	Old Bhatti	South Sikkim	1083	1.16
LC15**	JK		-	-	0.99
LC16*	Ramsey	Old Bhatti	East Sikkim	1322	1.11
LC17*	Sawney	New Bhatti	East Sikkim	-	1.13
LC18*	Varlangey	New Bhatti	Kalimpong	900	1.04

LC19*	Varlangey	New Bhatti	Kalimpong	1312	1.50
LC20*	Seremna	Old Bhatti	East Sikkim	1237	1.61
LC21*	-	Old Bhatti	Meghalaya	1396	1.0
SC1*	ICRI-1	Old Bhatti	Karnataka	-	0.16
SC2*	ICRI-2	Old Bhatti	Karnataka	-	0.28
SC3*	ICRI-3	Old Bhatti	Karnataka	-	0.37

2.3.2. Sample Preparation and extraction

After collecting the samples, cardamom seeds were adequately taken from the pod and weighed. 1.0 g seed of each sample was crushed using a mortar and pestle. The ground samples were sealed in a 10 mL Agilent gas-tight Teflon coated crimper vial for 10 minutes for headspace generation. The samples were handled by wearing disposable gloves, and the grinding equipment was washed thoroughly with double distilled water every time after use to prevent sample contamination. The schematic diagram of sample preparation and extraction using SPME fiber is shown in Fig. 2.3.

The absorption of VFCs was optimised by joining a 1 cm 50/30 µm divinylbenzene/ carboxen/ polydimethylsiloxane [(DVB/CAR/PDMS); (Supelco, USA) stable flexTM, 24 Ga SPME fiber with manual assembly holder (Supelco, USA)] with the vials containing the samples.

2.3.3 Specification and programme for SPME-GCMS analysis

GC-MS Specification: GC-MS analysis was performed using Thermo Fisher Trace 1300 (Thermo scientific, Milan- Italy) connected to a triple quadrupole mass spectrometer (Thermo MS-TSQ 9000)

Column: Wall-coated open tubular column (WCOT), TG-5 MS (30 m × 0.25 mm × 0.25 µm), a 10 m Dura guard capillary column.

Carrier gas: Helium (He) (purity > 99.99%) at flow rate of 1 mL/min.

Front Inlet temp: 250 ºC

Column Oven temperature program:

The column temperature was first maintained at 60 ºC for 1 min and then ramped to 120 ºC at a rate of 4 ºC min^{-1}. Then the temperature was again ramped to 230 ºC at a rate of 15 ºC min^{-1} and finally kept fixed for 3 min.

Total Runtime: 26.33 minutes

MS ion Source: 220 ºC

MS transfer line temperature: 250 ºC

Electron Energy: 70 eV (vacuum pressure: 2.21 e-0.5 torr)

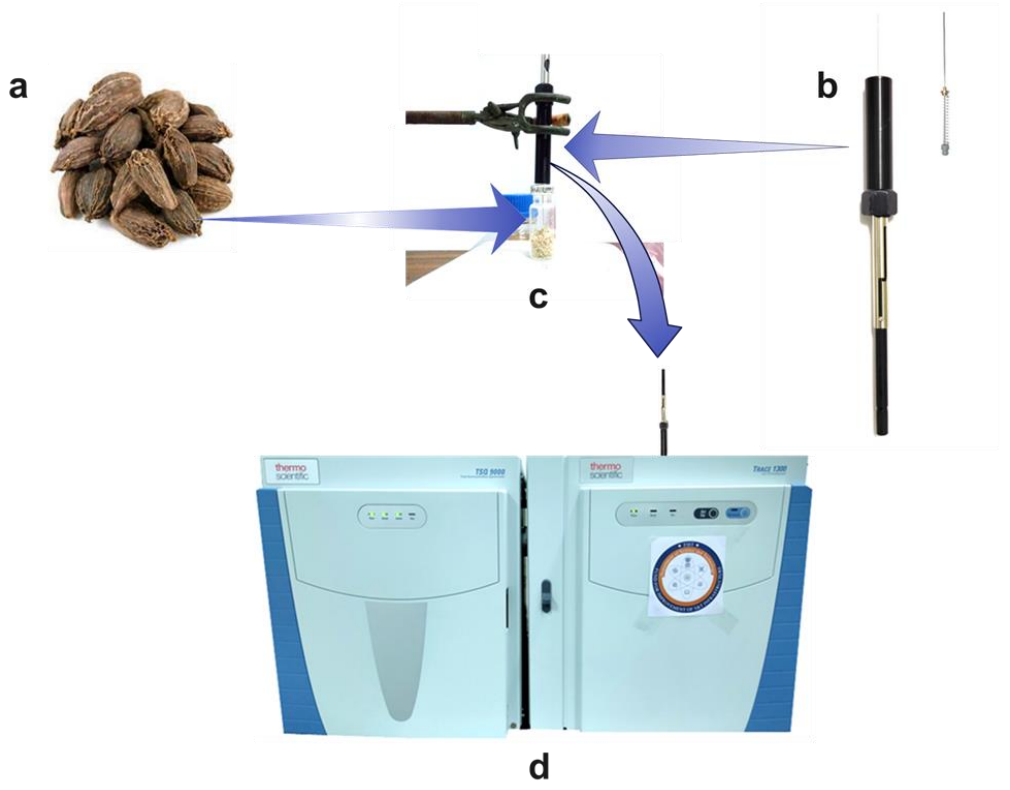

Fig. 2.3. Schematic diagram of sample preparation, headspace sampling and HSV analysis procedure. a) Large cardamom sample; b) SPME fiber and holder; c) headspace sampling and d) injection of adsorbed volatiles in GC-MS.

2.3.4. Determination of volatile flavor compound (VFC) of cardamom samples

The major VOCs in the aroma profiles of the twenty-one large cardamom samples obtained from GC-MS analysis are listed in Table 2.2. A total of 35 VOCs can be identified from the chromatograms of the large cardamom samples and quantified from the percentage of peak areas. Similarly, the GCMS estimates of the small cardamom samples are tabulated in Table 2.3.

2.4 Results and discussions

2.4.1 Comparison with existing literature

As described earlier in the literature, most of the publications on the volatilome of large cardamom dealt with all the volatiles present in their respective essential oil. We have screened ten original research articles that explored the total volatilome of around 23 varieties of Indian large cardamoms *(Ammomum subulatum)*[1,2,4,5,8–12]. Their findings varied considerably, and they could detect 12-50 volatiles based on the cardamom variety, while 15-34 (n=18) volatiles were most frequent according to those studies. In every single case, 1,8-cineole or eucalyptol was the most dominant compound having a 37.36% - 84.40% peak area of total ion chromatogram. However, in most cases, 1,8-cineole content ranged between 50% - 75% (n=21). According to the available literature, large cardamom predominantly contains monoterpenes (81.84% - 88.58%); however, 4.64% - 9.42% of sesquiterpenes are also present in this spice. In our investigation, we analysed 21 large cardamom samples by SPME-guided-GCMS, and we detected a total of 35 HSVs (number of HSVs ranging from 20-33), of which 33 are monoterpene and 2 are sesquiterpene (trace quantity) in general. Unlike essential oils, in the HSV fraction, the relative amount of 1,8-cineole is more consistent (70%-85%) and edged on the higher side. Detailed illustration and comparison of the total number of VOCs and 1,8-cineole content in available literature (essential oils) and present investigation (HSVs) are pictured as a frequency distribution in Fig. 2.4.

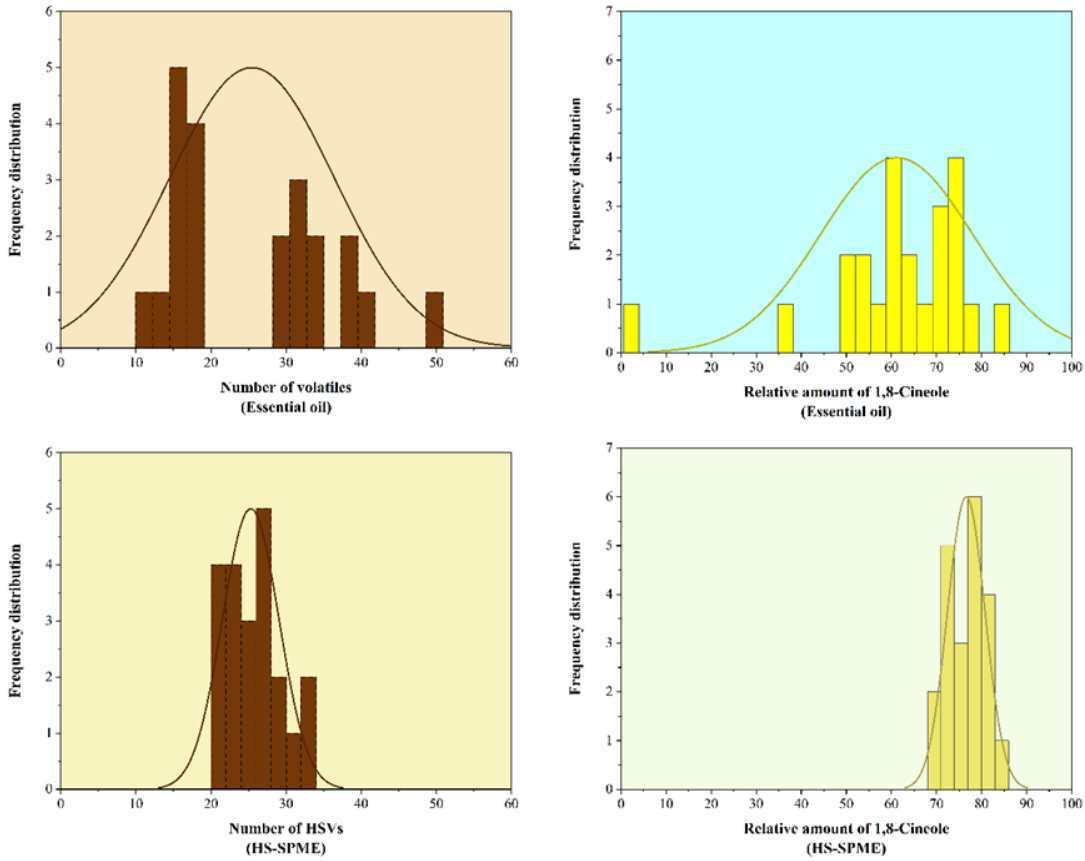

Fig. 2.4. Frequency distribution plot to compare the total number VOCs and 1,8-cineole content in available literature (essential oils) and present investigation (HSVs).

2.4.2. Variances of HS volatilome between large cardamom samples

Twenty-one large cardamom samples, some with known cultivar detail (n=12) and some purchased from the market (n=9) (as mentioned in Table 2.1), have been procured and screened for their headspace volatile (HSV) compositions. A total of 35 common HSVs have been identified from the HS of these samples, which are shown in Table 2.1. These HSVs vary considerably between samples, which are annotated as relative amounts in Table 2.1, and based on this variability of headspace volatile, and every sample secures a unique volatile fingerprint. Using this unique volatile fingerprint of each sample, a similarity dissimilarity index was developed following the Euclidian algorithm (Fig. 2.5). **The result suggests significant differences between considered large cardamom samples based on HS volatilome. Based on these findings, QCM sensors have been developed to detect the significant volatiles in the HSV of cardamom.**

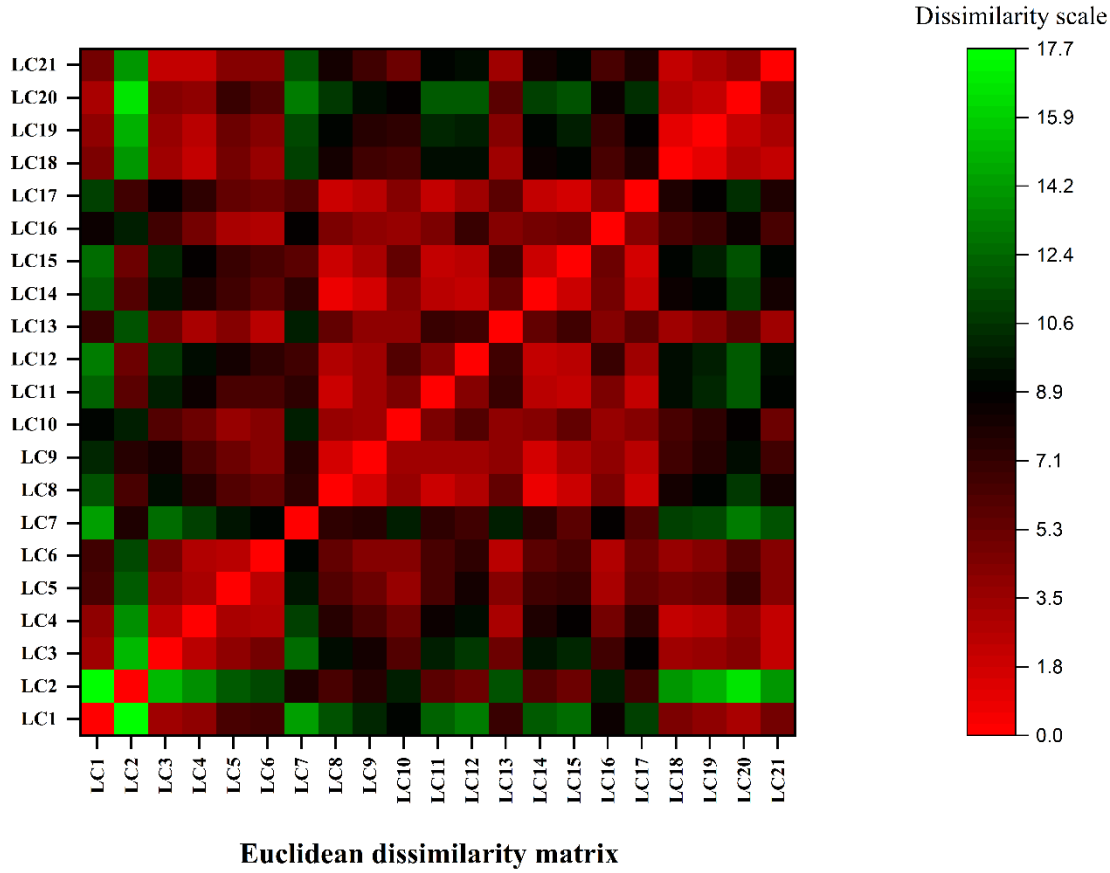

Fig. 2.5. Euclidian similarity dissimilarity indices between large cardamom depending on entire headspace volatilome.

Among the 35 HSVs, 15 volatiles, i.e., 3-Thujene, α-pinene, Camphene, Sabinene, β-Pinene, β-Myrcene, α-Phellandrene, o-Cymene, Limonene, 1,8-cineole, γ-Terpinene, Sabinene hydrate, cis-β-Terpineol, Terpinen-4-ol, and α-Terpineol are found in all samples of large cardamom irrespective of the cultivars and commercial sources **(Fig. 2.6)**. In all samples, **1,8-cineole or eucalyptol is the most dominant compound having 70%-85% area of the total ion chromatogram of the HSVs.** Besides 1,8-cineole, α-pinene (1.84%-9.87%), β-pinene (0.58%-9.16%), Limonene (4.07%-8.24%), Sabinene (0.53%-5.12%) and β-Myrcene (0.02%-1.86%) are other major compounds in certain samples.

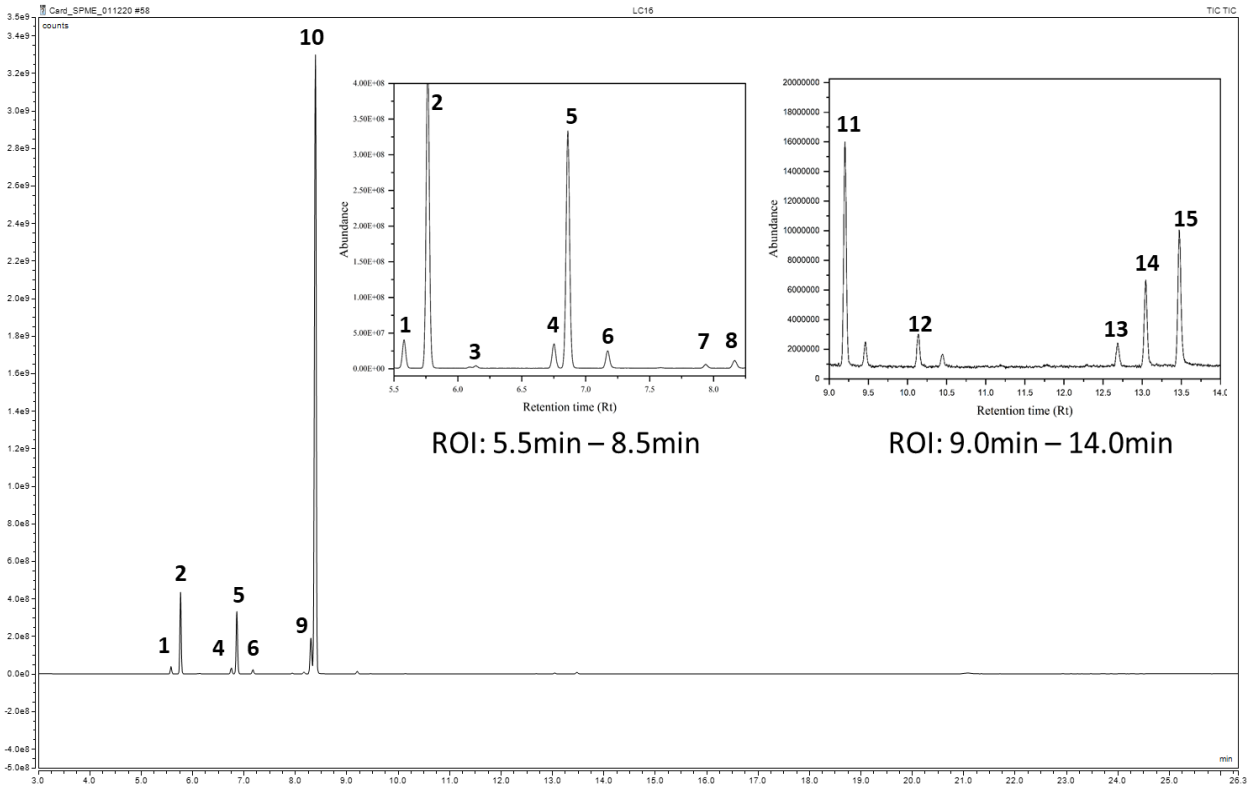

Fig. 2.6. GC-MS chromatogram of large cardamom sample. Fifteen HSVs in all large cardamom samples are represented here with numeric codes 1-15.

(1. 3-Thujene; 2. α-Pinene; 3. Camphene; 4. Sabinene; 5. β-Pinene; 6. β-Myrcene; 7. α-Phellandrene; 8. o-Cymene; 9. Limonene; 10. 1,8-cineole; 11. ϒ-Terpinene; 12. Sabinene hydrate; 13. cis-β-Terpineol; 14. Terpinen-4-ol; 15. α-Terpineol)

The remaining 29 HSVs were detected in very trace quantity and had less than 1% area of the total ion chromatogram. One-way analysis of variance was performed (ANOVA) to understand the major volatiles' variance, assuming the variance between the samples is identical. It was found that the variances between the samples are significantly different for 1,8-cineole (ANOVA (20,42), F=266.4, p=7.65E-38), α-pinene (ANOVA (20,42), F=198.1, p=3.57E-35), β-pinene(ANOVA (20,42), F=383.9, p=3.83E-41), Limonene (ANOVA (20,42), F=60.83, p=1.05E-24), Sabinene (ANOVA (20,42), F=335.2, p=6.47E-40), β-Myrcene (ANOVA (20,42), F=105, p=1.66E-29). Variation of these HSVs among the individual samples was analysed using post hoc Tukey's test and represented in Fig. 2.7.

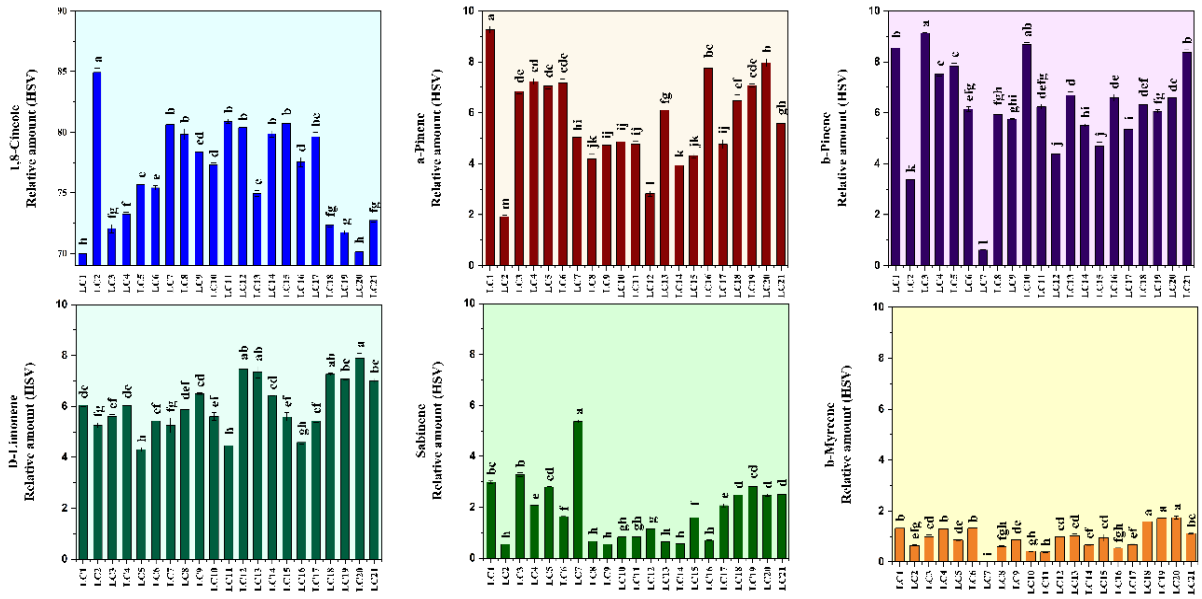

Fig. 2.7. Variation of the most dominant HSVs among the individual samples using post hoc Tukey's test.

Despite having considerable HSV diversity, only a few major volatiles dominate primarily to contribute to the aroma quality or aroma specificity of different large cardamom varieties. To compare the HSVs among the samples, the relative amount of each volatile was subjected to principal component analysis (PCA) (following variance-covariance matrix). From the PCA analysis, we narrowed our focus to a few volatiles based on which the considered samples showed maximum variability. The HSVs that have maximum influence on PC1 (81.1%) and PC2 (9.8%) are represented in Fig. 2.8 (a) and (b). The PCA score plot reveals that there are some variations between considered samples. In a broader sense, the score plot shows two primary groups, one that resides on the positive axis of PC1 (n=10) [influenced by 3-Thujene, α-pinene, Sabinene, β-Pinene, β-Myrcene, and Limonene] and the other that is present in the negative axis of PC1 (n=7) [influenced by 1,8-cineole]. In the scoring plot, LC2 and LC7 occupy a completely distinct position in the negative axis of PC1. The remaining two samples, i.e., LC10 and LC16, were found to be located in the neutral region concerning PC1. Besides this proximate analysis, detailed multivariate studies have been done (using the critical volatiles attained from PC1) to find out how the geography, physical form, and post-harvest curing processes influence the aroma profile of selected large cardamom cultivars.

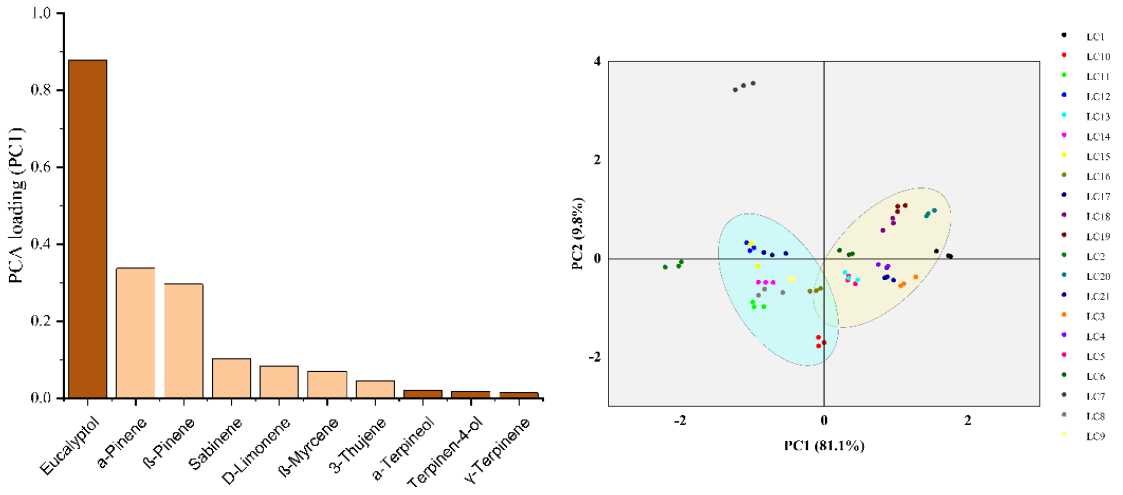

Fig. 2.8. Loading plot (a) and Score plot (b) obtained from principal component analysis (PCA).

Following this, the SIMPER test was performed using the Bray-Curtis algorithm to identify the HSVs, based on which maximum dissimilarities between the cardamom varieties occur, and it was found that **1,8-cineole, α-pinene, and β-pinene are three major volatiles that secures the maximum** average dissimilarity score, followed by Sabinene, limonene, and β-Myrcene (Fig. 2.9). The SIMPER outcome also revealed that the first three volatiles are responsible for nearly 70% cumulative Bray-Curtis dissimilarity between samples. **This is one of the primary reasons behind our selection of 1,8-cineole, α-pinene, and β-pinene for the QCM sensor development.**

Table 2.2. GCMS relative peak area estimates of large cardamom.

HSVs	LC1	LC2	LC3	LC4	LC5	LC6	LC7	LC8	LC9	LC10	LC11	LC12	LC13	LC14	LC15	LC16	LC17	LC18	LC19	LC20	LC21
3-Thujene	0.78 ± 0.02	0.14 ± 0	0.55 ± 0.02	0.76 ± 0.02	0.58 ± 0.01	0.79 ± 0.03	0.35 ± 0.02	0.4 ± 0.02	0.45 ± 0.01	0.47 ± 0.02	0.39 ± 0.02	0.26 ± 0.02	0.51 ± 0.01	0.4 ± 0.01	0.35 ± 0.05	0.75 ± 0.04	0.36 ± 0.02	0.83 ± 0.06	1.02 ± 0.05	0.99 ± 0.04	0.72 ± 0.03
α-pinene	9.26 ± 0.23	1.93 ± 0.09	6.84 ± 0.17	7.23 ± 0.21	7.05 ± 0.19	7.17 ± 0.28	5.04 ± 0.02	4.2 ± 0.34	4.73 ± 0.05	4.87 ± 0.35	4.76 ± 0.21	2.83 ± 0.19	6.11 ± 0.02	3.95 ± 0.14	4.32 ± 0.17	7.76 ± 0.3	4.77 ± 0.31	6.49 ± 0.4	7.08 ± 0.11	7.97 ± 0.29	5.58 ± 0.18
d-Camphene	0.05 ± 0.01	-	0.04 ± 0.01	0.04 ± 0	0.04 ± 0.01	0.04 ± 0	0.06 ± 0	0.02 ± 0	0.03 ± 0.01	0.03 ± 0	0.02 ± 0	0.01 ± 0	0.02 ± 0	0.02 ± 0	0.02 ± 0	0.03 ± 0	0.02 ± 0	0.04 ± 0	0.05 ± 0.01	0.05 ± 0.01	0.04 ± 0
Camphene	0.11 ± 0.01	0.05 ± 0.01	0.08 ± 0	0.09 ± 0.01	0.08 ± 0	0.1 ± 0.01	1.01 ± 0.05	0.05 ± 0.01	0.06 ± 0	0.07 ± 0.01	0.05 ± 0.01	0.03 ± 0	0.05 ± 0.01	0.04 ± 0	0.04 ± 0	0.08 ± 0.01	0.04 ± 0	0.1 ± 0.01	0.1 ± 0.01	0.11 ± 0	0.1 ± 0.01
Sabinene	2.99 ± 0.1	0.55 ± 0.02	3.28 ± 0.14	2.09 ± 0.02	2.8 ± 0.03	1.64 ± 0.03	5.37 ± 0.1	0.67 ± 0.07	0.55 ± 0.01	0.83 ± 0.03	0.84 ± 0.06	1.15 ± 0.02	0.65 ± 0.03	0.56 ± 0	1.6 ± 0.41	0.71 ± 0.03	2.07 ± 0.11	2.49 ± 0.06	2.81 ± 0.18	2.48 ± 0.1	2.5 ± 0.16
ß-Pinene	8.55 ± 0.28	3.38 ± 0.11	9.14 ± 0.03	7.53 ± 0.15	7.85 ± 0.19	6.15 ± 0.17	0.61 ± 0.03	5.94 ± 0.25	5.76 ± 0.05	8.68 ± 0.16	6.24 ± 0.18	4.38 ± 0.18	6.69 ± 0.25	5.51 ± 0.12	4.7 ± 0.26	6.6 ± 0.24	5.36 ± 0.24	6.33 ± 0.14	6.06 ± 0.11	6.6 ± 0.04	8.38 ± 0.19
ß-Myrcene	1.33 ± 0.07	0.63 ± 0.08	1 ± 0.12	1.3 ± 0.05	0.86 ± 0.04	1.33 ± 0.02	0.02 ± 0	0.61 ± 0.05	0.87 ± 0.03	0.43 ± 0.03	0.4 ± 0.04	0.99 ± 0.04	1.04 ± 0.11	0.7 ± 0.01	0.95 ± 0.25	0.55 ± 0.03	0.69 ± 0.04	1.59 ± 0.02	1.72 ± 0.04	1.75 ± 0.11	1.12 ± 0.03
α-Phellandrene	0.02 ± 0.01	0.03 ± 0.01	0.02 ± 0.01	0.04 ± 0.01	0.01 ± 0	0.05 ± 0.01	0.09 ± 0.01	0.03 ± 0	0.06 ± 0.01	0.02 ± 0.01	0.02 ± 0.01	0.03 ± 0.01	0.04 ± 0	0.03 ± 0.01	0.01 ± 0	0.02 ± 0	0.01 ± 0	0.05 ± 0.01	0.05 ± 0.01	0.07 ± 0	0.04 ± 0.01

α-Terpinolene	0.04 ± 0	0.16 ± 0.02	0.05 ± 0.01	0.27 ± 0.02	0.05 ± 0.01	0.37 ± 0.01	-	0.15 ± 0.02	0.28 ± 0.01	0.06 ± 0	0.05 ± 0.01	0.15 ± 0	0.24 ± 0.02	0.14 ± 0	0.05 ± 0.01	0.12 ± 0	0.02 ± 0	0.34 ± 0.03	0.41 ± 0.06	0.29 ± 0.01	0.26 ± 0.05
o-Cymene	0.16 ± 0.02	0.23 ± 0.02	0.33 ± 0.05	0.22 ± 0.01	0.12 ± 0.01	0.25 ± 0.01	0.39 ± 0.01	0.51 ± 0.06	0.38 ± 0.02	0.48 ± 0.36	0.48 ± 0.03	0.28 ± 0.01	0.35 ± 0.03	0.31 ± 0.01	0.15 ± 0.03	0.26 ± 0.01	0.25 ± 0.01	0.24 ± 0.01	0.1 ± 0.01	0.16 ± 0.02	0.16 ± 0.01
Limonene	6.05 ± 0.1	5.27 ± 0.18	5.6 ± 0.15	6.04 ± 0.11	4.31 ± 0.13	5.43 ± 0.09	5.26 ± 0.51	5.88 ± 0.29	6.5 ± 0.08	5.61 ± 0.27	4.47 ± 0.35	7.47 ± 0.25	7.35 ± 0.39	6.43 ± 0.02	5.59 ± 0.3	4.59 ± 0.12	5.44 ± 0.12	7.27 ± 0.08	7.09 ± 0.09	7.9 ± 0.34	7 ± 0.17
1,8-cineole	69.99 ± 0.46	84.94 ± 0.62	72.05 ± 0.62	73.26 ± 0.27	75.68 ± 0.21	75.41 ± 0.34	80.64 ± 0.63	79.84 ± 0.78	78.37 ± 0.18	77.32 ± 0.27	80.91 ± 0.33	80.39 ± 0.21	74.96 ± 0.42	79.86 ± 0.46	80.74 ± 0.33	77.55 ± 0.68	79.63 ± 0.66	72.36 ± 0.32	71.75 ± 0.26	70.14 ± 0.36	72.73 ± 0.24
α-Terpinene	-	-	-	0.11 ± 0.05	-	0.1 ± 0.03	0.02 ± 0.00	0.13 ± 0.03	0.16 ± 0.03	-	-	0.11 ± 0.01	0.17 ± 0.06	0.09 ± 0.01	0.1 ± 0.02	-	0.17 ± 0.04	0.1 ± 0.02	0.11 ± 0.04	-	-
ß-Ocimene	0.06 ± 0.01	0.08 ± 0.01	0.03 ± 0.01	0.06 ± 0	0.03 ± 0	0.07 ± 0.01	-	0.04 ± 0.01	0.06 ± 0.01	0.03 ± 0.01	0.02 ± 0	0.07 ± 0.01	0.09 ± 0.05	0.03 ± 0	0.07 ± 0.03	0.02 ± 0	0.06 ± 0.02	0.08 ± 0.02	0.12 ± 0.01	0.08 ± 0	0.03 ± 0
γ-Terpinene	0.11 ± 0.01	0.82 ± 0.08	0.12 ± 0.02	0.54 ± 0.02	0.12 ± 0.01	0.67 ± 0.01	0.38 ± 0.03	0.53 ± 0.07	0.85 ± 0.05	0.24 ± 0.02	0.23 ± 0.02	0.58 ± 0.04	0.75 ± 0.15	0.55 ± 0.01	0.17 ± 0.07	0.38 ± 0.03	0.2 ± 0.04	0.65 ± 0.06	0.73 ± 0.09	0.08 ± 0.01	0.43 ± 0.07
Sabinene hydrate	0.26 ± 0.04	0.17 ± 0.03	0.35 ± 0.08	0.07 ± 0.01	0.23 ± 0.02	0.03 ± 0.01	0.05 ± 0.01	0.06 ± 0.02	0.04 ± 0	0.06 ± 0.01	0.1 ± 0.01	0.1 ± 0.01	0.06 ± 0.02	0.12 ± 0.01	0.46 ± 0.24	0.04 ± 0	0.48 ± 0.13	0.27 ± 0.03	0.18 ± 0.03	0.53 ± 0.01	0.3 ± 0.02
γ-Terpinolene	0.02 ± 0	0.16 ± 0.03	0.03 ± 0.01	0.09 ± 0.01	0.02 ± 0	0.11 ± 0.01	-	0.1 ± 0.01	0.15 ± 0.01	0.06 ± 0	0.05 ± 0.01	0.1 ± 0.01	0.12 ± 0.03	0.1 ± 0.01	0.04 ± 0.02	0.06 ± 0	0.02 ± 0	0.14 ± 0.02	0.16 ± 0.02	0.24 ± 0.03	0.1 ± 0.02
cis-b-Terpineol	0.04 ± 0.01	0.07 ± 0.01	0.06 ± 0.02	0.02 ± 0	0.04 ± 0	0.02 ± 0	0.04 ± 0.03	0.04 ± 0	0.03 ± 0	0.05 ± 0.01	0.06 ± 0.01	0.05 ± 0.01	0.04 ± 0.01	0.06 ± 0.01	0.11 ± 0.05	0.03 ± 0.01	0.08 ± 0.02	0.05 ± 0.01	0.04 ± 0.02	0.11 ± 0.01	0.06 ± 0.02

6-Camponenol	-	0.02 ± 0.00	-	-	-	-	-	-	0.01 ± 0	0.01 ± 0	-	0.02 ± 0.01	0.01 ± 0	0.01 ± 0	-	-	-	-	-	-	-
α-Campholenal	-	0.02 ± 0.01	0.02 ± 0.01	-	-	-	-	0.01 ± 0	-	-	0.02 ± 0.01	0.01 ± 0	0.01 ± 0	0.01 ± 0	0.01 ± 0.01	-	0.01 ± 0	-	-	0.03 ± 0.01	0.03 ± 0.01
Limonene oxide	-	-	-	-	-	-	-	-	-	-	0.03 ± 0.01	-	0.01 ± 0.00	-	0.01 ± 0.01	-	-	-	-	0.01 ± 0.01	0.02 ± 0
Isopinocarveol	-	0.02 ± 0.01	0.02 ± 0.01	-	-	-	-	0.01 ± 0	0.01 ± 0.01	0.02 ± 0	-	0.01 ± 0	-	0.02 ± 0	0.01 ± 0.00	-	0.01 ± 0	0.03 ± 0.01	-	0.01 ± 0	0.02 ± 0.01
Isopulegol	-	-	-	-	-	-	-	-	-	-	-	-	-	-	0.01 ± 0	-	-	-	-	-	-
Pinocarvone/ Sabinone	0.02 ± 0.02	-	0.02 ± 0	-	-	-	-	-	-	0.03 ± 0	0.03 ± 0.01	0.01 ± 0	0.01 ± 0.00	0.01 ± 0	0.01 ± 0.01	-	0.01 ± 0.01	0.06 ± 0.02	0.06 ± 0.01	0.01 ± 0	0.01 ± 0
d-Terpineol	0.03 ± 0.01	0.11 ± 0.03	0.03 ± 0.01	0.03 ± 0.01	0.03 ± 0.01	0.02 ± 0	0.06 ± 0.02	0.06 ± 0.02	0.06 ± 0.01	0.04 ± 0	0.07 ± 0.02	0.09 ± 0.01	0.06 ± 0.02	0.1 ± 0.02	0.06 ± 0.06	0.05 ± 0.01	0.04 ± 0.01	-	-	0.05 ± 0.02	0.05 ± 0.01
Terpinen-4-ol	0.03 ± 0.01	0.47 ± 0.07	0.03 ± 0.01	0.12 ± 0.01	0.02 ± 0	0.15 ± 0.02	0.23 ± 0.04	0.29 ± 0.05	0.27 ± 0.03	0.19 ± 0.02	0.2 ± 0.01	0.29 ± 0.03	0.3 ± 0.07	0.29 ± 0.03	0.05 ± 0.05	0.16 ± 0.02	0.04 ± 0.01	0.08 ± 0.01	0.12 ± 0.01	0.05 ± 0.01	0.03 ± 0.01
Dill ether	-	-	-	-	-	-	-	-	-	-	-	-	-	-	0.01 ± 0.00	-	0.25 ± 0.06	-	-	-	-
α-Terpineol	0.18 ± 0.03	0.79 ± 0.16	0.2 ± 0.07	0.16 ± 0.02	0.13 ± 0.03	0.17 ± 0.01	0.36 ± 0.06	0.46 ± 0.1	0.4 ± 0.06	0.24 ± 0.02	0.39 ± 0.02	0.59 ± 0.05	0.4 ± 0.1	0.62 ± 0.07	0.43 ± 0.24	0.27 ± 0.03	0.01 ± 0	0.38 ± 0.03	0.4 ± 0.01	0.34 ± 0.06	0.34 ± 0.06

Myrtenal	-	-	0.05 ± 0.06	-	-	-	-	0.01 ± 0.00	-	0.02 ± 0	0.03 ± 0	-	-	0.02 ± 0	0.01 ± 0.00	-	0.01 ± 0.01	-	-	-	-
exo-2-Hydroxycineole	0.01 ± 0	0.02 ± 0.01	-	-	-	-	0.01 ± 0	0.01 ± 0.01	0.01 ± 0	0.01 ± 0	0.01 ± 0	0.01 ± 0.01	0.01 ± 0	0.01 ± 0	0.01 ± 0	-	-	0.01 ± 0.00	-	0.01 ± 0.01	0.01 ± 0
Bicyclosesquiphellandrene	-	0.02 ± 0.01	0.15 ± 0.15	0.01 ± 0.00	-	-	0.01 ± 0.01	-	-	-	0.01 ± 0	-	-	0.01 ± 0	-	-	-	-	-	-	-
α-Terpinyl acetate	-	-	-	-	-	-	-	-	-	-	-	-	0.01 ± 0	-	0.01 ± 0	-	-	-	-	-	-
b-Selinene	-	-	-	-	-	-	0.03 ± 0.01	0.02 ± 0	0.01 ± 0	0.02 ± 0.01	0.02 ± 0	0.04 ± 0.01	0.02 ± 0.01	0.05 ± 0.01	0.02 ± 0.01	0.01 ± 0	0.01 ± 0	-	-	-	-
Bicyclogarmacrene	-	-	-	-	-	-	-	-	-	-	-	0.02 ± 0.02	0.01 ± 0	0.01 ± 0	0.01 ± 0.00	-	-	-	-	-	-
Nerolidol	-	-	-	-	-	-	-	0.01 ± 0	-	0.01 ± 0	0.01 ± 0	-	0.01 ± 0	0.01 ± 0.01	0.01 ± 0.00	-	-	0.05 ± 0.03	0.03 ± 0.03	0.01 ± 0.01	0.02 ± 0

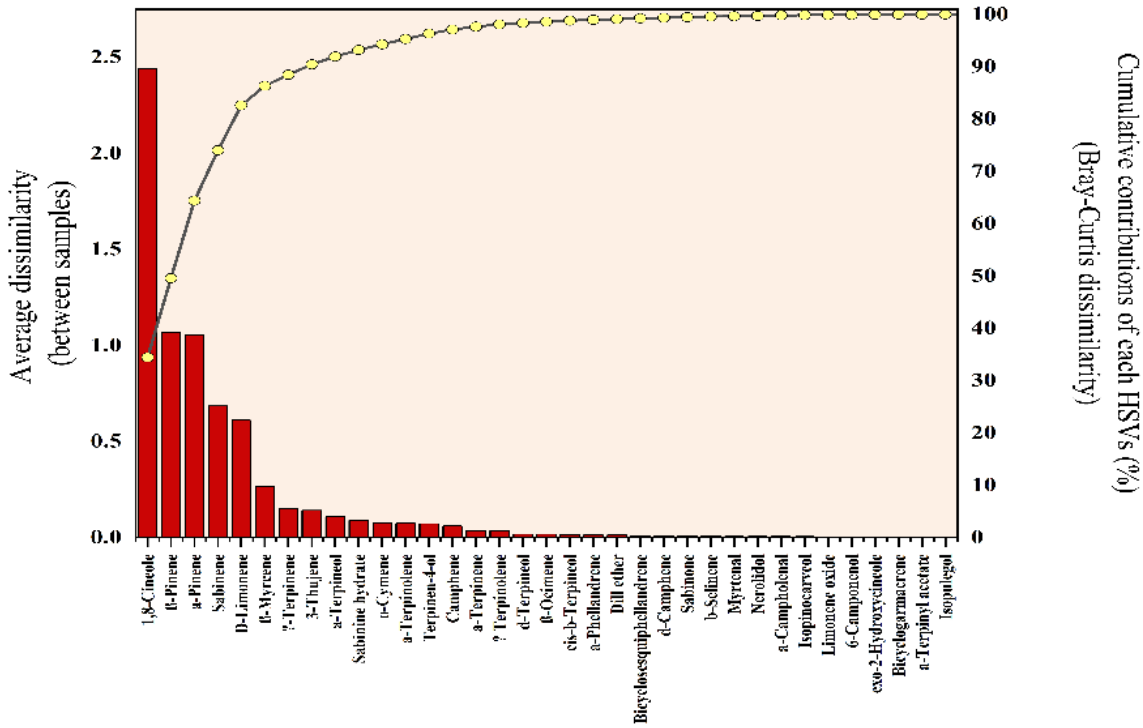

Fig. 2.9. Screening of key volatiles that causes maximum dissimilarity between cardamom varieties using SIMPER analysis and Bray-Curtis dissimilarity index.

2.4.3. Influence of physical characters, geographical parameters and processing method

A total of twelve known cultivars of large cardamom samples have been included in our study, which is given in table 2.1. These twelve samples were procured from different altitudes of West Bengal and Sikkim, India, ranging from 900 m -1720 m. As altitude is one of the important factors that regulate the microclimate of a geographical area, altitudes of those regions (where that particular cardamom variety has been cultivated) are considered in our study as representative of geographical factors. This wide range of altitudes is categorised into three classes, i.e., **low altitude (n=3), mid-altitude (n=3), and high altitude (n=6)**. One-way multivariate analysis of variance (MANOVA) was performed to assess the volatilome's dependency on the altitude of microclimate. It was found that the HSV profile of large cardamom significantly depends on the altitude at which the sample is cultivated (Wilk's lambda $_{(df1\ 34,\ df2\ 34)}$ =0.01447, F= 7.313, p=3.947E-8). However, post hoc analysis suggests that the HSV profiles of the lower altitude samples are not significantly different from the mid-altitude samples. On the contrary, volatilome of high-altitude samples is significantly different from the low-altitude (MANOVA, p=0.016013) and mid-altitude

(MANOVA, p=0.00089808) samples. We have also assessed whether the pod size or weight has some influence on the aroma profile of large cardamom. We measured the weight of these 12 known cultivars, ranging from 0.747 to 1.611 g. For the multivariate study, these 12 cultivars have been categorized in three categories, i.e., small-sized (<1 g) (n=3), medium-sized (1-1.25 g) (n=6) and large-sized (1.25 g<) (n=3). Significant differences in the HSV profile were observed between the samples with different pod weights and sizes (Wilk's lambda $_{(df1\ 34,\ df2\ 34)}$ =0.006788, F= 11.44, p= 2.919E-11). Post hoc analysis revealed that each category is significantly different from the other two categories [Small-Medium (MANOVA, p=0.0035688); Medium-Large (MANOVA, p= 0.017069); Small-Large (MANOVA, p=0. 0.12504)]. An important factor determining a spice's quality is its post-harvest-curing method. The twelve samples considered in this section have gone through three different curing methods, i.e., old Bhatti curing, modified Bhatti curing, and electric dryer-based curing. It was found that the HSV fingerprints of large cardamoms depend on the curing process (Wilk's lambda $_{(df1\ 34,\ df2\ 34)}$ = 0.004616, F= 13.72, p=3.989E-11), and it was also observed that the HSVs of cardamom samples processed in old Bhatti is statistically different from modified Bhatti cured (MANOVA, p=1.26E-07) and electrically dried (MANOVA, p=0.0065149) samples.

Alongside one-way MANOVA, linear discriminant analysis was also performed to evaluate whether the HSV constituents (selected from PCA) and their relative amount in the HS are adequate to categorise the selected samples into their respective altitude, pod size, and processing method. Using linear discriminant analysis (LDA), these twelve samples (n= 12×3) (using 10 HSVs selected from PC1) can be categorised accurately, to some extent. Confusion matrices (Jackknified) obtained from LDA suggest that depending on the HSV constituents, cultivars can be classified into accurate pod sizes (accuracy 83.33%)), altitude at which a specific sample is cultivated (accuracy 91.67%) and the post harvesting processing methods (accuracy 91.67%) (Fig. 2.10).

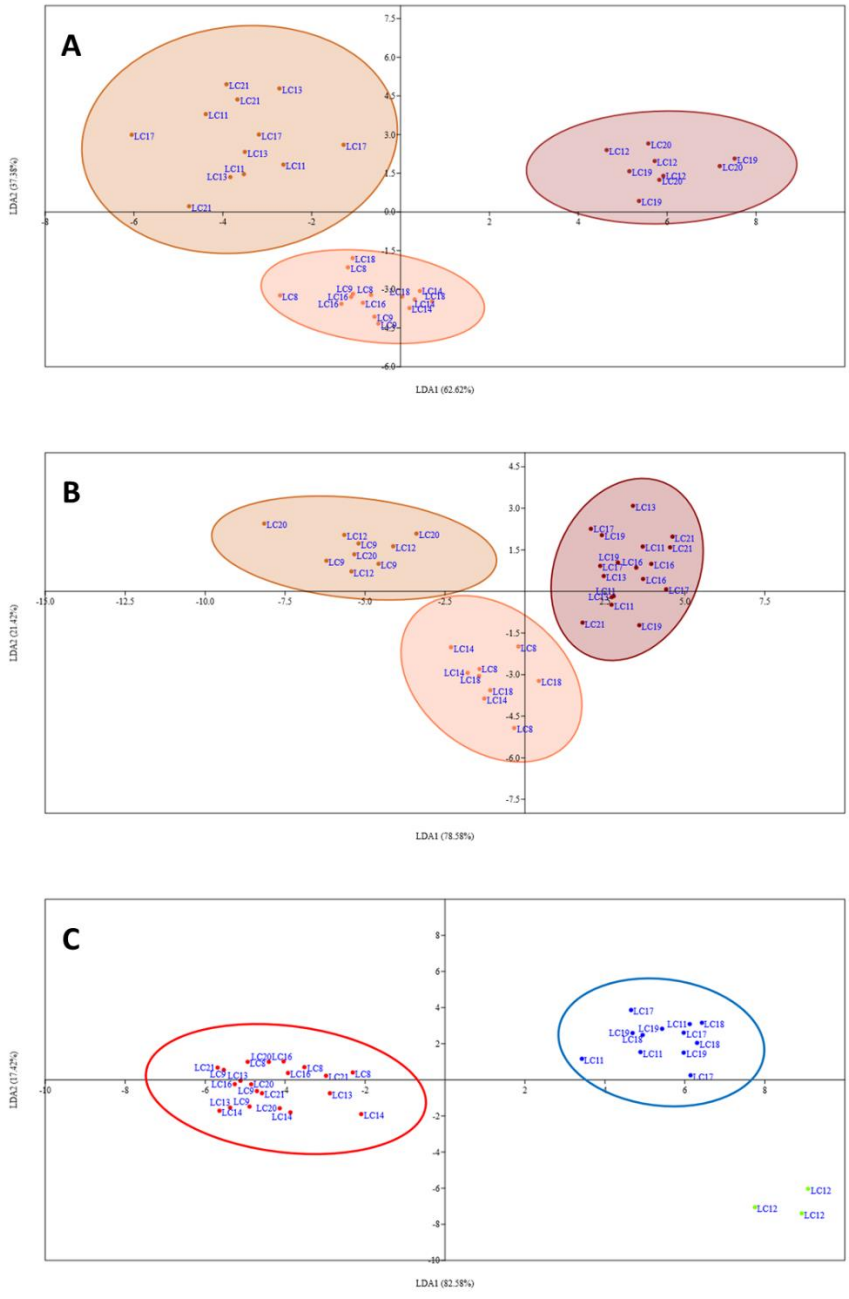

Fig. 2.10. Supervised linear discriminant analysis of twelve varieties of large cardamom based on their pod (a) weight, (b) geo-climate of cultivation, (c) post-harvest processing method.

2.4.4. Variances of HS volatilome between small cardamom samples

As mentioned earlier, due to some unique volatiles, small cardamoms have an entirely different aroma from large cardamom. Headspace volatilomes of small cardamoms were also analysed using SPME-guided GC-MS analysis (Fig. 2.11), revealing the presence of seven significant HSVs with varying quantities as tabulated in Table 2.3.

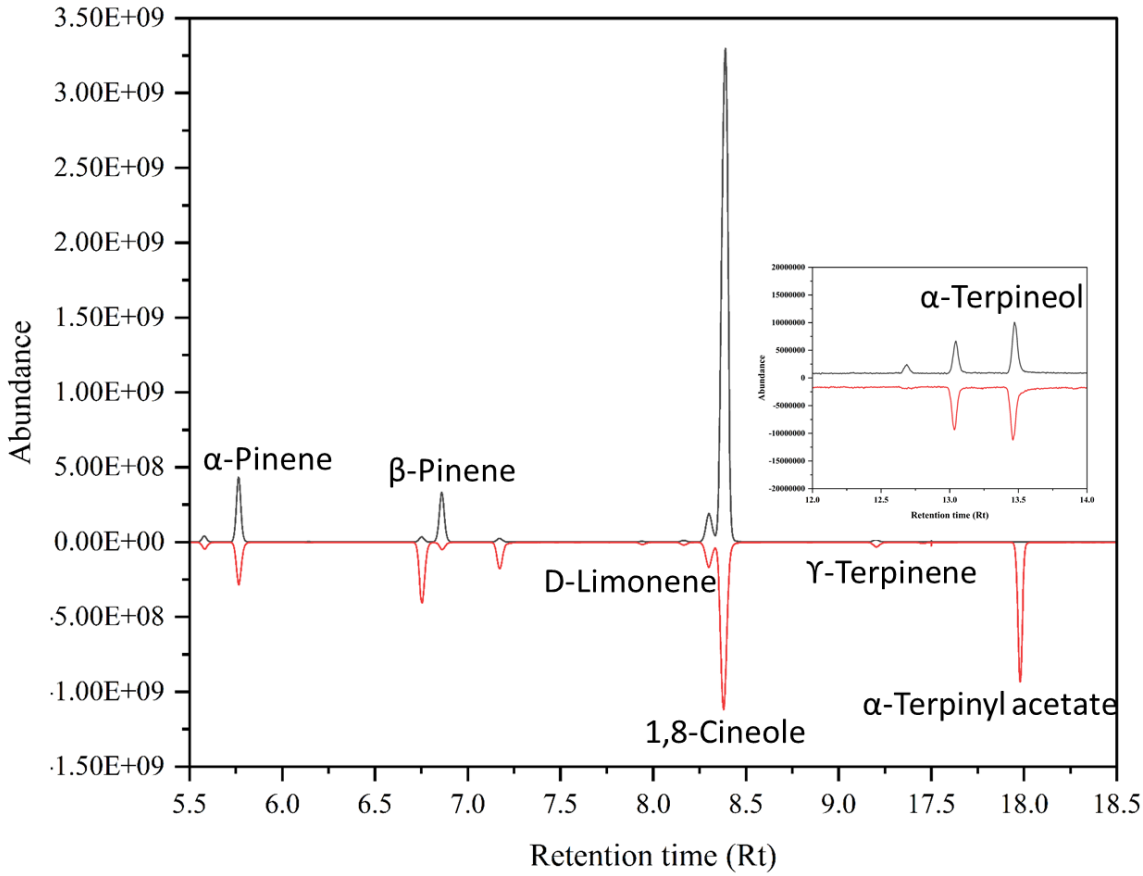

Fig. 2.11. Comparison between large cardamom and small cardamom chromatogram showing considerable variation in HSV profile.

Table 2.3. GCMS relative peak area estimates in small cardamom

VOCs	GCMS relative peak area (%)		
	SC1	**SC2**	**SC3**
α-Pinene	12.54 ± 0.30	11.92 ± 0.39	11.10 ± 0.70
β-Pinene	2.07 ± 0.087	2.05 ± 0.11	1.89 ± 0.07
Limonene	8.95 ± 0.10	8.07 ± 0.11	7.51 ± 0.25
1,8-cineole	62.66 ± 1.23	61.50 ± 3.61	50.63 ± 1.84
γ-Terpinene	0.88 ± 0.03	1.11 ± 0.02	1.39 ± 0.04
α-Terpineol	0.136 ± 0.00	0.32 ± 0.13	0.47 ± 0.07
α-Terpinyl acetate	12.75 ± 0.91	15.00 ± 3.59	27.25 ± 1.86

A principal component analysis has been performed to determine the significant HSVs, based on maximum discrimination between two aromas. The score plot suggests that based on HSVs, small cardamom and large cardamom varieties form two distinct clusters at the negative and positive axes of PC1 (89.4%), respectively. PCA loading plot reveals that 1,8-cineole and α-Terpinyl acetate are the two major HSVs based on this; large and small cardamom varieties are mostly segregated (Fig. 2.12). The PCA score plot and loading plot suggest that **α-terpinyl acetate is one of the essential characteristics HSVs that determine the aroma of small cardamom.**

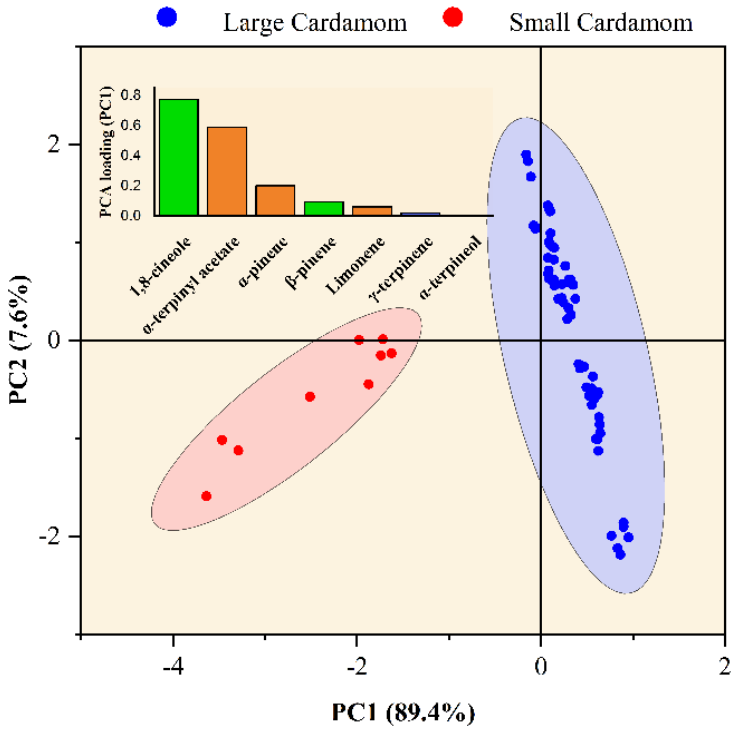

Fig. 2.12. PCA score plot and loading plot of the major HSVs present in large and small cardamom.

In a subsequent analysis, we have screened the key HSV(s), based on which the small cardamom varieties are distinct from each other, using PCA analysis. Expectedly, α-terpinyl acetate and 1,8-cineole are the two major HSV(s) that influence maximum discrimination between selected small cardamom varieties (Fig. 2.13). Based on the HSV's loading, three clusters were formed on three distinct regions of the PCA score plot (Fig. 2.14). In addition to PCA, the SIMPER test was also performed to identify the HSVs that are present in small cardamoms based on maximum discrimination. SIMPER result validates the PCA result as it also annotated α-terpinyl acetate and 1,8-cineole as the principal volatiles, based on nearly 80% Bray-Curtis dissimilarity between the samples present (Fig. 2.14).

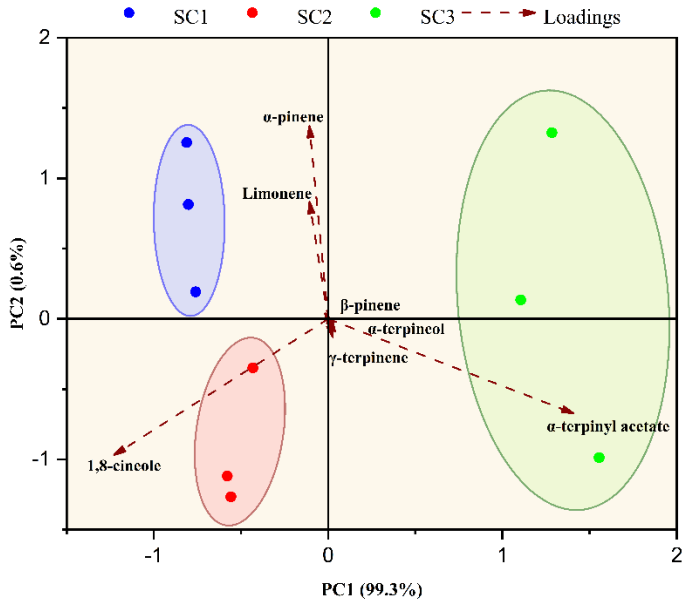

Fig. 2.13. PCA biplot that represents the variation among varieties based on their HSV profile.

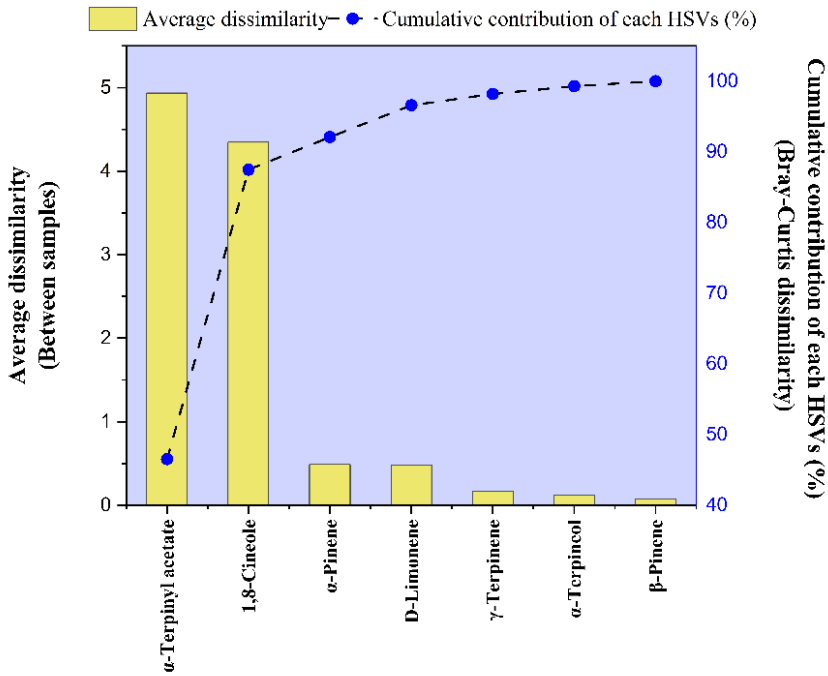

Fig. 2.14. Screening of key volatiles that causes maximum dissimilarity between small cardamom varieties using SIMPER analysis and Bray-Curtis dissimilarity index.

2.5. Conclusion

The aroma of both large and small cardamom varieties varies considerably based on their headspace volatiles. Though the volatiles is shared between the varieties of large cardamom, as well as in the case of small cardamom, their relative proportion in the headspace fraction determines their unique fragrance. **1,8-cineole, being the most abundant HSV**, has the highest impact on the development of the aroma of large cardamom, which is distinct between varieties. Additionally, to some extent, **two other monoterpenes, i.e., α-pinene and β-pinene, have also varied between varieties.** This implies that the aroma of the large cardamom variety strongly depends on these three mentioned HSVs. Besides, 1,8-cineole is also determined to be the most variable volatile that is influenced by the post-harvesting processing method, agro-climatic zone and size of the large cardamom. The relative proportion of α-Pinene and β-Pinene, though not that much diverse like 1,8-cineole, varied based on the agroclimatic zone and size of the pod, respectively. On the other hand, **small cardamom has an entirely distinct unique aroma owing to the presence of α-terpinyl acetate** and based on their relative proportion in the headspace, alongside 1,8-cineole, small cardamom varieties are different. Based on the above investigations, **it was decided to consider these four HSVs for developing four different sensors, which can qualitatively and quantitatively determine this volatiles present in the headspace of both large and small cardamom, to discriminate them based on varieties, qualities and thus for commercial values.**

References

[1] A.K. Bhandari, V. Bisht, J. Negi, M. Baunthiyal, 1, 8-cineole: A predominant component in the essential oil of large cardamom (Amomum subulatum Roxb.), Undefined. (2013). https://www.semanticscholar.org/paper/1%2C-8-cineole%3A-A-predominant-component-in-the-oil-of-Bhandari-Bisht/10a61436ca1b5f30930bc4bdb951c75742556548 (accessed March 27, 2022).

[2] K.N. Gurudutt, J.P. Naik, P. Srinivas, B. Ravindranath, Volatile constituents of large cardamom (Amomum subulatum Roxb.), Flavour and Fragrance Journal. 11 (1996) 7–9. https://doi.org/10.1002/(sici)1099-1026(199601)11:1<7::aid-ffj542>3.0.co;2-9.

[3] M. Jabbar, H. Ghorbaniparvar, Determination of Volatile Components in Black Cardamom with Gas Chromatography-Mass Spectrometry and Chemometric Resolution, International Journal of Engineering Research & Technology. 3 (2014).

[4] R. Joshi, P. Sharma, V. Sharma, R. Prasad, R.K. Sud, A. Gulati, Analysis of the essential oil of large cardamom (Amomum subulatum Roxb.) growing in different agro-climatic zones of Himachal Pradesh, India, Journal of the Science of Food and Agriculture. 93 (2013) 1303–1309. https://doi.org/10.1002/jsfa.5886.

[5] P.K. Rout, D. Sahoo, K.S. Jena, Y.R. Rao, Analysis of the Oil of Large Cardamom (Amomum subulatum Roxb.,) Growing in Sikkim, Journal of Essential Oil Research. 15 (2003) 265–266. https://doi.org/10.1080/10412905.2003.9712138.

[6] X. Wang, Y. Wu, H. Zhu, H. Zhang, J. Xu, Q. Fu, M. Bao, J. Zhang, Headspace Volatiles and Endogenous Extracts of Prunus mume Cultivars with Different Aroma Types, Molecules. 26 (2021) 7256. https://doi.org/10.3390/molecules26237256.

[7] K. Ashokkumar, S. Vellaikumar, M. Murugan, M.K. Dhanya, G. Ariharasutharsan, S. Aiswarya, M. Akilan, T.D. Warkentin, A. Karthikeyan, Essential Oil Profile Diversity in Cardamom Accessions From Southern India, Frontiers in Sustainable Food Systems. 5 (2021). https://www.frontiersin.org/article/10.3389/fsufs.2021.639619 (accessed March 27, 2022).

[8] M. Jabbar, H. Ghorbaniparvar, Determination of Volatile Components in Black Cardamom with Gas Chromatography-Mass Spectrometry and Chemometric Resolution, International Journal of Engineering Research & Technology. 3 (2014). https://www.ijert.org/research/determination-of-volatile-components-in-black-cardamom-with-gas-chromatography-mass-spectrometry-and-chemometric-resolution-IJERTV3IS110914.pdf, https://www.ijert.org/determination-of-volatile-components-in-black-cardamom-with-gas-chromatography-mass-spectrometry-and-chemometric-resolution (accessed March 27, 2022).

[9] A. Vijayan, N. Leela, M. Dhanalakshmi, H.J. Akshitha, R. Rahul, P. Utpala, K.N. Babu, Volatile oil composition of four popular varieties of large cardamom (Amomum subulatum Roxb.), (2017). https://doi.org/10.25081/JOSAC.2017.V26.I1.805.

[10] R.A. Kaskoos, S.R. Mir, R. Kapoor, Mohd. Ali, Essential Oil Composition of the Fruits of Amomum subulatum Roxb, Journal of Essential Oil Bearing Plants. 11 (2008) 184–187. https://doi.org/10.1080/0972060X.2008.10643617.

[11] G.O. Adegoke, L. Jagan Mohan Rao, N.B. Shankaracharya, A comparison of the essential oils of Aframomum daniellii (Hook. F.) K. Schum. and Amomum subulatum Roxb., Flavour and Fragrance Journal. 13 (1998) 349–352. https://doi.org/10.1002/(SICI)1099-1026(1998090)13:5<349::AID-FFJ758>3.0.CO;2-O.

[12] P. Satyal, N.S. Dosoky, B.L. Kincer, W.N. Setzer, Chemical Compositions and Biological Activities of Amomum subulatum Essential Oils from Nepal, Natural Product Communications. 7 (2012) 1934578X1200700935. https://doi.org/10.1177/1934578X1200700935.

Chapter 3

Development of a portable volatile organic compound detection system using QCM sensor

Content of the this chapter is based on the following publication:

N. Debabhuti, A. Sengupta, P. Sharma, R. Sen, B. Tudu, R. Bandyopadhyay, Development of the Data Acquisition System and GUI for QCM Sensor Based System, Social Science Research Network, Rochester, NY, 2020.

3.1. Introduction

Olfaction is one of the essential attributes of the human sensing system used to differentiate between aromatic materials. Proper aroma analysis is necessary to get an overview of the quality of a product. Cardamom is an aromatic spice and one of the essential spice crops in the Indian market. Being highly aromatic, the presence of volatile organic compounds (VOCs) in cardamom is critical for determining the quality and grade. The Indian cardamom is still graded and classified mostly by human expertise. However, the process is laborious, and the precision may be degraded due to human error [1]. Apart from this manual procedure, other analytical, chemical, and gas chromatographic procedures were employed to determine the presence of VOCs in various spice crops [2–5]. These classical methods are also analogous to the manual process, which is time-consuming and requires qualified personnel to operate. As a result, these traditional techniques are unsuitable for field and small-scale industrial applications.

Table 3.1. Portable gas sensing devices

Devises/Gas sensing system	**Sensing Technology**	**Data acquisition**	**Area of application**	**Ref.**
Packed food quality monitoring metal-oxide field-effect transistor (MOSFET) gas sensor array based alarming communicative device.	Intrinsically conducting polymer and metal oxide conductivity gas sensors, MOSFET gas sensors.	RFID tag integrated with gas sensor for data communication and alarming purposes.	Industrial packed food self-life monitoring.	[6]
Integrated and portable semiconductor-type multiple gas detection modules.	Chemiresistive gas sensors on a micro-electro-mechanical-systems (MEMS)-based sensor.	Data transmission through an ESP32 to Android app that displays the sensor data.	Multiple gas sensing	[7]
A miniaturized portable low-cost and low-power VOC analysis system based on GC × GC device.	Photo-ionization detector (PID) sensors based.	Compact RIO computer (cRIO, National Instruments) platform.	VOC's	[8]

Kiwi fruit odour sensing surface acoustic wave (SAW) gas sensor array system.	Thermal desorption–gas chromatography-mass spectrometry (TD-GC-MS) system, gold interdigital transducers, and SAW sensor.	Data recording via Arduino and computer-based display.	Detection of kiwi ripening stages.	[9]

Even if the analytical processes provide consistent data, portability and response time are critical characteristics to consider when performing real-time VOC detection. The real-time portable gas detection equipment may address the drawbacks of manual and conventional techniques. Table 3.1 lists various developed portable real-time gas detecting systems based on a literature review. Some of the portable gadgets produced have been used for food quality detection, which is very beneficial in the food sector. The devices that employ MOS technology [10] for gas detection utilize more power. MOS sensors' repeatability and temperature sensitivity make them unsuitable for single odour recognition. The MOS-based warning system may indicate only the presence and absence of harmful gases. The system could not quantify the real-time gas emitted by the tested sample. A portable GC was designed to lower the cost of traditional GC devices. For sensing and data collection, a photo-ionization detector and a computer were employed [8]. The sensor was appropriate for detecting multiple VOCs; however, the results were impacted by humidity. As a result of the humidity impact and the need for an additional power source for a portable device, real-field sensing and data collecting were challenging. This portable equipment is solely appropriate for laboratory and industrial applications. Another multi-gas detecting system uses a chemoresistive sensor for gas sensing, which is difficult to build. The gadget was divided into two parts: one for gas detection and the other for data collecting through an Android app [6]. A wi-fi communication device was used to link these two parts. The device proved effective for long-distance gas detection, but an internet connection may provide a barrier for real-time data collecting. The thermal desorption gas chromatography-mass spectrometry system has a disadvantage in size and cost [9]. The inclusion of gold interdigital transducers and a surface acoustic wave sensor made the device more sophisticated and costly and a separate computer-handled data presentation. As a result, a portable device with an onboard gas sensor, data collection, and a self-powered system is essential for real-field specific gas detection.

Given the above drawbacks, developing a portable VOC detection system would be beneficial for product quality analysis in the spice industry. So, our focus is to develop a system with a Raspberry pi 4-based data-acquisition complete package portable system. The system is validated for detecting cardamom VOCs, which are not yet being developed as per our survey.

The developed system was solely used for the purpose of fabrication and sensor performance analysis to detect α-pinene, β-pinene, 1,8-cineole, and α-terpinyl acetate VOCs discussed in the following chapters.

3.2. Overview of the portable gas sensing unit

The developed system consists of three major blocks: the QCM sensor chamber, the hardware interface, and the software module. The sensor chamber houses the QCM sensor required for the olfaction of the VOC. The hardware interface module cum measurement circuit consists of different electronic interfaces, its power supply, and microcontrollers for the execution of various sequential operations as well for data acquisition of the experimental data. The responsibility of the software module is the execution of sequence control steps for operating the hardware interface module and recording their measurements. A user interface block has been developed for proper monitoring and development of sensors and for processing, presentation, and analysis of the measured data. The block diagram for the developed sensing system is depicted in Fig 3.1.

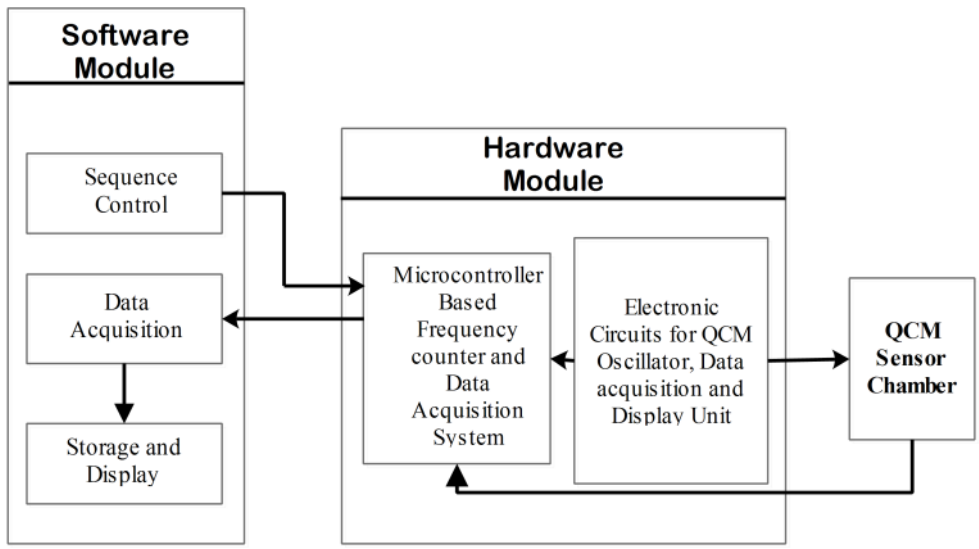

Fig. 3.1. Block diagram of the developed sensing system.

3.2.1. QCM sensor chamber

The sensor chamber block consists of a 100 mL airtight Teflon-made chamber as shown in Fig. 3.2 for placing the QCM sensors during experiments. The sensor chamber is attached to a three-way valve for proper sampling and purging processes. The other end of the sensor chamber is connected to a 12 V suction pump through a two-way valve to purge ambient air through the air inlet to the sensor chamber. The QCM sensor is attached to a holder placed on a sensor circuit board which is then connected to the oscillator circuit module.

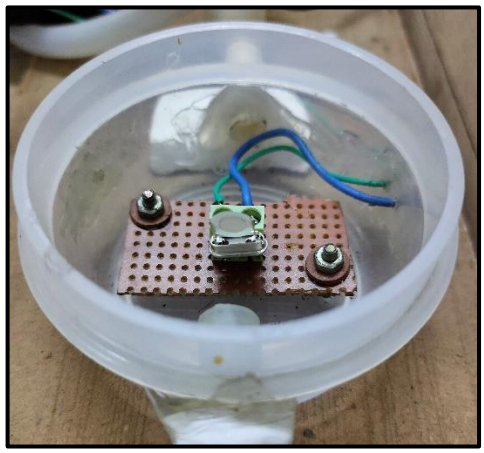

Fig. 3.2. Photograph of the sensor chamber with QCM sensor.

3.2.2. Hardware interface module cum measurement circuit

3.2.2.1. Power supply

A commercial power bank with a capacity of 20000 mAh and an output voltage capacity of 5V was employed as a power source for this device. Since the oscillator circuit, Raspberry Pi, Teensy 3.2, and the Arduino modules were operated at a voltage of 5 V, and it was attached to the power bank via a USB power cable. The power bank offered adequate backup for up to 3 days required for field usage.

3.2.2.2. Frequency oscillator module

The QCM sensor oscillation frequencies are produced by the 8284A IC, which is a high-performance CMOS clock generator-driver. Fig. 3.3 depicts the oscillator module's circuit design. The crystal leads are linked to the pins 16 (X1) and 17 (X2) of the IC through the OSC_IN

connection port. For stability, two series resistances R1 and R2, are selected as 510 Ω and linked across the leads of the quartz crystal. In order to protect the circuit from surges during power ON/OFF, two capacitors C1 and C2 of 33 pf and 100 pf are supplied. The oscillator output is provided at PIN 12 as a square wave with a frequency equal to the crystal's resonance frequency. Through connector port OSC_OUT, this pin is attached to the frequency counter module. To maintain output voltage fluctuations, the IC 8284 is powered by a 5V controlled power source supplied by a commercial power bank and an LM7805 voltage regulator IC.

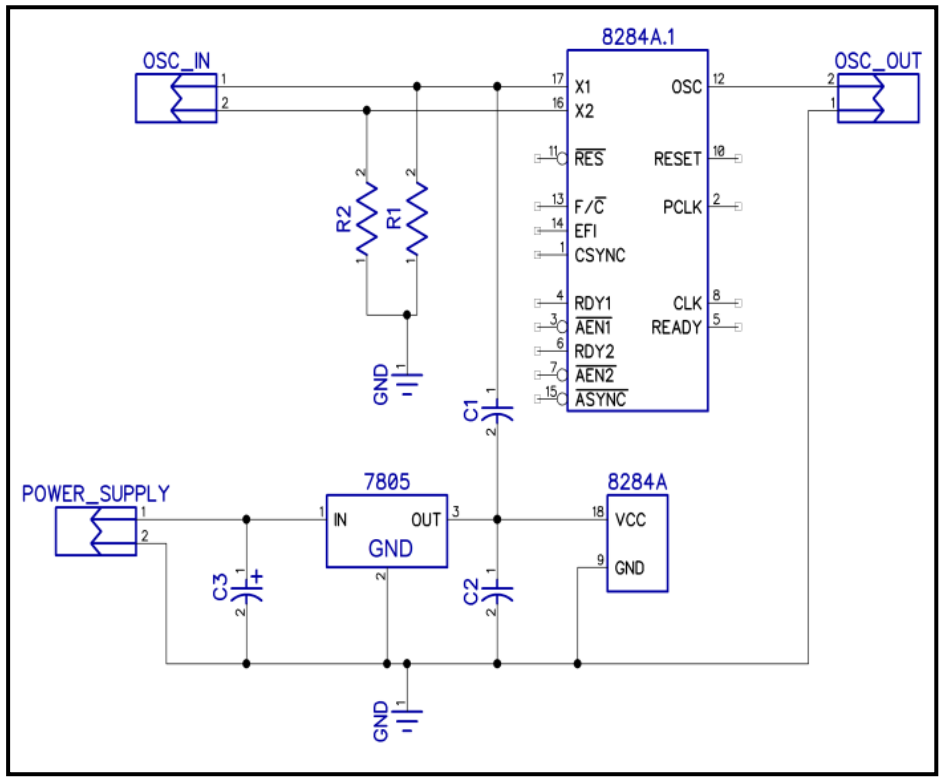

Fig. 3.3. Circuit diagram of the oscillator module.

3.2.2.3. Microcontroller-based frequency counter

A frequency counter is an effective tool for correctly counting the frequency of the QCM sensor and for conducting subsequent measurements. The frequency counter was developed using the Teensy 3.2 development board (PJRC, USA), which features an MK20DX256VLH7 processor with an ARM Cortex M4 core operating at 72 MHz. The frequency produced by the 10 MHz QCM sensor was calculated using two counter/timers. A 16-bit Low Power Timer (LPTMR) is utilised to monitor the number of times a leading edge is detected, while an interval timer is employed to

maintain a set interval (gate width). When the interval timer exceeds the gate width, an interrupt is generated, which terminates the pulse counting. The gate pulse with a duration of one second is used to calculate the output frequency in Hertz (Hz). Thus, the created system's frequency measurement of the QCM sensor has a resolution of 1 second. The LPTMR's input port is linked to the OSC_OUT pin of the frequency oscillator circuit on Teensy 3.2. The gate pulse was kept at one second. Fig. 3.4 illustrates the counting mechanism.

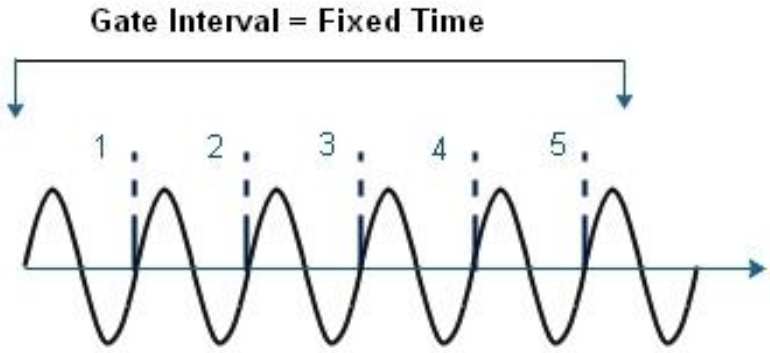

Fig. 3.4. Frequency counter mechanism using MK20DX256VLH7 chip.

3.2.2.4. Data acquisition unit

The data acquisition unit comprises Raspberry Pi 4, a low-cost single-board computer. The primary reason for using the Raspberry pi 4 is its Linux kernel operating system, so the entire system becomes a standalone system with its operating system. The oscillation frequency of the sensor generated by the counter module was sent to Raspberry Pi 4. A buffer system using Arduino nano (Arduino SRL, Strambiano, Italy) has been utilized to properly synchronise the data from the counter module to the data acquisition system. The frequency generated per second was transferred to the buffer unit as a packet of data through serial communication. Finally, the data were sent to Raspberry Pi 4 through a serial USB connection from the buffer unit. The data were stored in real-time for further analysis and post-processing.

3.2.2.5. Graphical user interface and display unit

The frequency deviation of the sensor was monitored and displayed from Raspberry Pi 4 through a 7” capacitive touch screen display using an HDMI connection. A custom python program-based graphical user interface (GUI) for sensor data collection was programmed using the Tkinter toolkit,

enabling the raspberry pi to properly control and monitor the sensing phenomenon like sensitivity, selectivity, and repeatability. The real-time data after being received by the Raspberry pi were stored adequately in .csv format for later reference, as well as generated a real-time sensing graph for monitoring of the data.

3.2.3. Software module

Fig. 3.5. depicts the user interface for the data acquisition of the developed system. The data acquisition software's main interface consisted of five sections: (a) real-time sensor response display, (b) sampling parameter input, (c) sensor response status display, (d) control stages for different acquisitions, and (e) file name and directory input area. The obtained QCM sensor graph was displayed in the response display area. The sampling parameter setup box used the drop-down menu to enter the user-defined concentration (ppm). The directory and file name input section were created to allow users to pick or update the saving location for sensor data and the input sensor and gas name. The 'Sampling start/stop' button was used to initialise the sampling and store the sensor data. The status display section was used to show the software's current state, including initial frequency, current frequency, and final deviation.

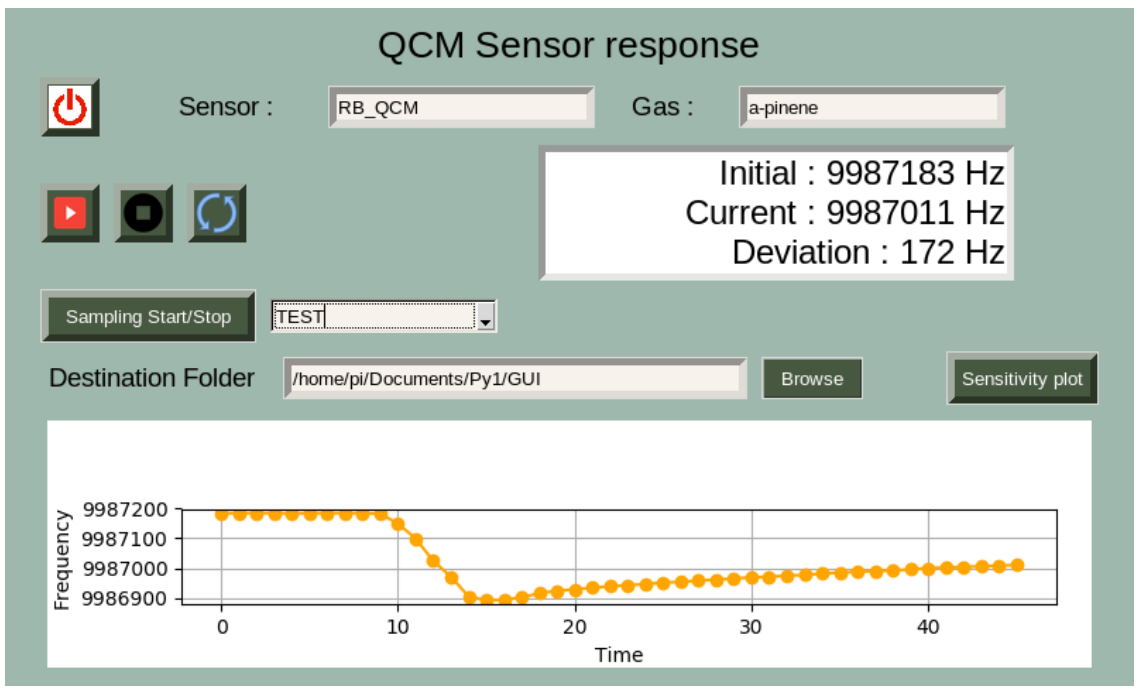

Fig. 3.5. User interface for the data acquisition of the sensing system.

3.2.3.1. Data processing and measurement module

The pre-sampling step is the initial standby stage, during which the QCM sensor oscillates at its original frequency, ultimately utilized as the initial frequency after the gas is introduced. This step is an infinite loop that continues reading the initial frequency of the QCM sensor and displaying it on the GUI until the user drives the whole system into the sampling state when the gas is injected into the gas chamber.

The user initiates the sampling stage while exposing the VOC to the sensor. At each instance, the frequency deviation of the sensor is read and recorded. The deviation from the initial stage frequency (initial frequency from the pre-sampling stage) is displayed as a real-time graph in the GUI. The real-time frequency deviation plot gives an overview of the sensitivity of the sensor to the exposed VOC. While the sampling stop is initiated system's algorithm was designed to account for the storage of final frequency and total frequency deviation. The complete algorithm for the operation is illustrated in Fig. 3.6.

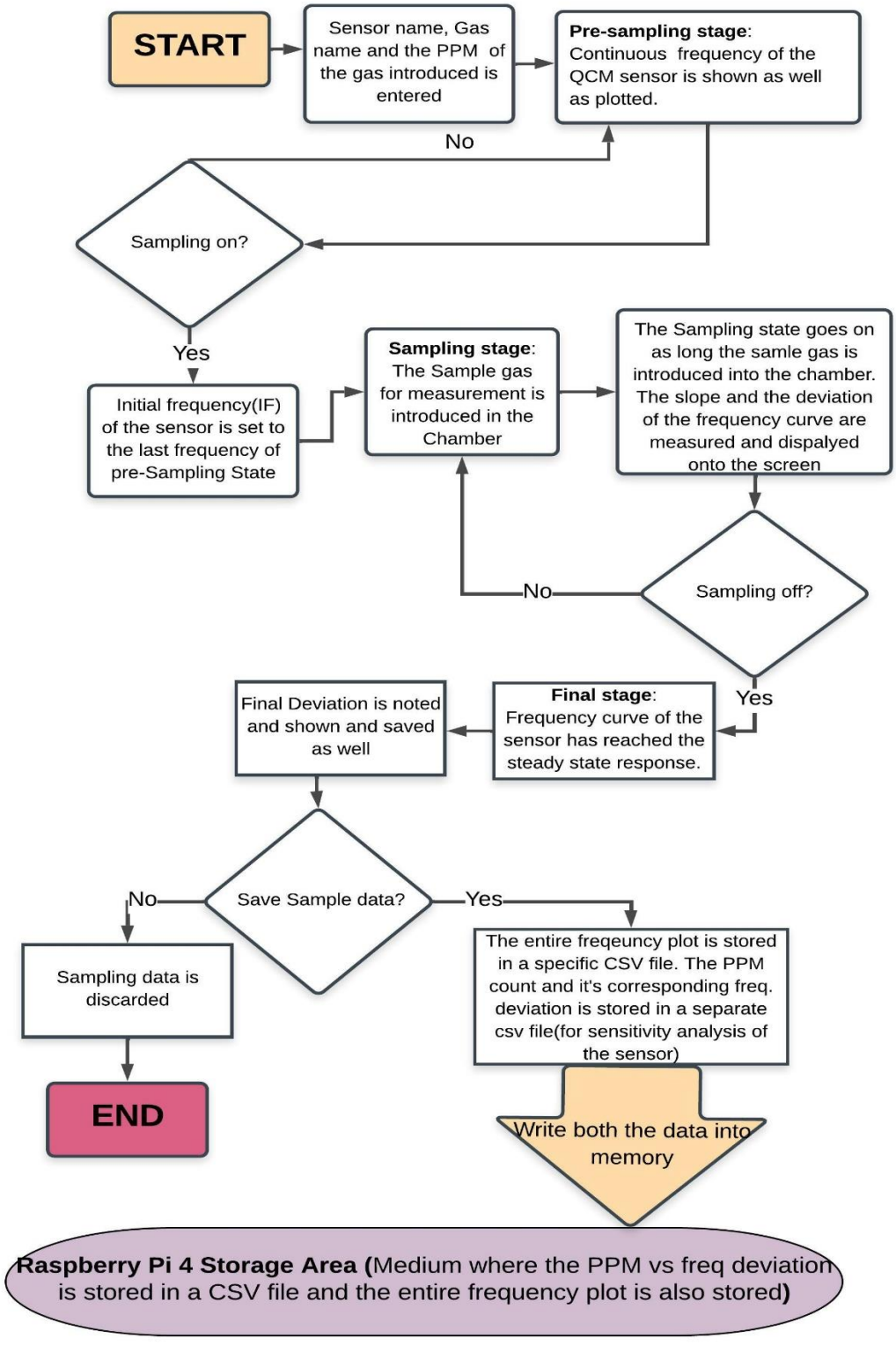

Fig. 3.6. The detailed algorithm of the data acquisition and processing module of the developed system.

3.3. Mechanical design/packaging of the developed portable gas sensing unit

As illustrated in Fig. 3.7, a custom casing has been developed to accommodate all of the components as well as a sensor chamber. All of the hardware components, i.e., the computing parts (Raspberry Pi4, Teensy 3.2), the touch interface, and the power bank, are placed in a compact, portable format. It is ensured that the system can work on the go and can be used even, uninterrupted, without an external power source.

The components are packaged inside a wooden frame with the touch interface on the side to take the necessary inputs and display the data recorded. A valve-controlled opening is placed on the top to allow the inflow of gases from the sample to be tested. An inlet is provided to allow the entry of fresh air, which aids in the purging of the sensor. Along with it, an outlet from the sensor chamber is also provided with the purpose of passing out the gas that was present during the testing phase. This configuration makes for a robust system, allowing the proper exchange of gases at required intervals and in turn, aiding in its portability. The schematic diagram of the system is given in Fig. 3.8.

Fig. 3.7. The developed portable gas sensing system.

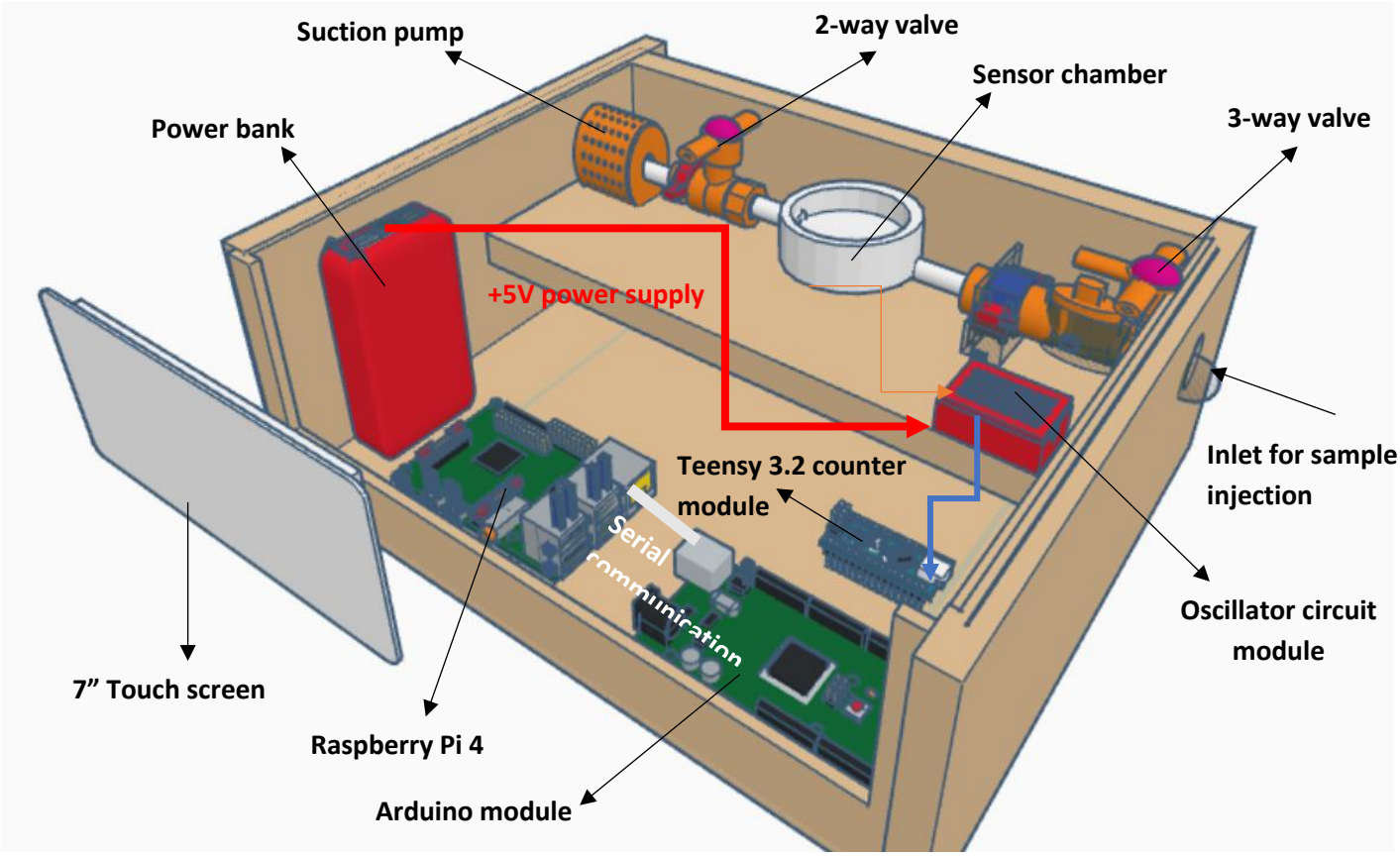

Fig. 3.8. Schematic diagram of the developed portable gas sensing system.

3.4. Conclusion

The development and working modules of a low-cost, compact and portable VOC detection system and data acquisition system based on QCM gas sensors have been discussed. The developed system is equipped with suitable hardware, and electrical components for the gas sensing mechanism and a touch screen operated GUI interface for superior operation and data outputs. The developed interface is capable of controlling different modes of QCM-based gas sensing mechanism along with its suitable data storage. Moreover, the developed system is powered by a 5V power bank which aids in its portability. Different QCM sensors can be fabricated for sensing distinct VOC and can be accurately used in the developed system.

References

[1] E.V. Malhotra, M. Kamalapriya, S. Bansal, D.P.S. Meena, A. Agrawal, Improved protocol for micropropagation of genetically uniform plants of commercially important cardamom (Elettaria cardamomum Maton), In Vitro Cell.Dev.Biol.-Plant. 57 (2021) 409–417. https://doi.org/10.1007/s11627-020-10131-7.

[2] M.J. George, P.B. Njobeh, S. Gbashi, G.O. Adegoke, I.A. Dubery, N.E. Madala, Rapid Screening of Volatile Organic Compounds from Aframomum danielli Seeds Using Headspace Solid Phase Microextraction Coupled to Gas Chromatography Mass Spectrometry, Int J Anal Chem. 2018 (2018) 8976304. https://doi.org/10.1155/2018/8976304.

[3] M.A. Farag, N. Hegazi, E. Dokhalahy, A.R. Khattab, Chemometrics based GC-MS aroma profiling for revealing freshness, origin and roasting indices in saffron spice and its adulteration, Food Chem. 331 (2020) 127358. https://doi.org/10.1016/j.foodchem.2020.127358.

[4] A.R. Bilia, G. Flamini, V. Taglioli, I. Morelli, F.F. Vincieri, GC–MS analysis of essential oil of some commercial Fennel teas, Food Chemistry. 76 (2002) 307–310. https://doi.org/10.1016/S0308-8146(01)00277-1.

[5] H.H. Jeleń, A. Gracka, Analysis of black pepper volatiles by solid phase microextraction-gas chromatography: A comparison of terpenes profiles with hydrodistillation, J Chromatogr A. 1418 (2015) 200–209. https://doi.org/10.1016/j.chroma.2015.09.065.

[6] J.-H. Suh, I. Cho, K. Kang, S.-J. Kweon, M. Lee, H.-J. Yoo, I. Park, Fully integrated and portable semiconductor-type multi-gas sensing module for IoT applications, Sensors and Actuators B: Chemical. 265 (2018) 660–667. https://doi.org/10.1016/j.snb.2018.03.099.

[7] R. Suzuki, T. Emura, Y. Tokura, N. Kawamura, Y. Hori, A Quartz Crystal Microbalance Based Portable Gas Sensing Platform for On-Demand Human Breath Monitoring, IEEE Access. 8 (2020) 146166–146171. https://doi.org/10.1109/ACCESS.2020.3013857.

[8] X. Pang, H. Nan, J. Zhong, D. Ye, M.D. Shaw, A.C. Lewis, Low-cost photoionization sensors as detectors in GC × GC systems designed for ambient VOC measurements, Sci Total Environ. 664 (2019) 771–779. https://doi.org/10.1016/j.scitotenv.2019.01.348.

[9] T.-Y. Yen, D.-J. Yao, Detection of the Freshness of Kiwifruit with a TD-GC-MS and a Gas-sensing Array Based on the Surface-acoustic-wave Technique, IEEE Trans Nanobioscience. PP (2021). https://doi.org/10.1109/TNB.2021.3094505.

[10] S. Matindoust, M. Baghaei-Nejad, Z. Zou, L.-R. Zheng, Food quality and safety monitoring using gas sensor array in intelligent packaging, Sensor Review. 36 (2016) 169–183. https://doi.org/10.1108/SR-07-2015-0115.

Chapter 4

A study of vegetable oil modified QCM sensor to detect β-pinene in Indian cardamom

Content of the this chapter is based on the following publication:

N. Debabhuti, S. Mukherjee, S. Neogi, P. Sharma, U.H. Sk, S. Maiti, M.P. Sarkar, B. Tudu, N. Bhattacharyya, R. Bandyopadhyay, A study of vegetable oil modified QCM sensor to detect β-pinene in Indian cardamom, Talanta. 236 (2022) 122837.

4.1. Introduction

As discussed in Chapter 2, the **HSV profile of cardamom by GCMS revealed several VOCs; it was statistically proved that 1,8-cineole is the primary compound that influences the characteristic smell of that particular landrace/variety of large cardamom. In addition, α-pinene and β-pinene are the other two critical monoterpenes of large cardamom that affect the aroma quality. In contrast, quantitative variations of α-terpinyl acetate in small cardamom represent the principal component of aroma quality. Moreover, α-pinene, β-pinene, 1,8-cineole, limonene, and others also play a crucial role in fragrance in different varieties depending on other environmental and climatic factors.** Therefore, in these succeeding chapters, based on these target molecules [**β-pinene, α-pinene, 1,8-cineole and α-terpinyl acetate**] of large & small cardamom, different types of sensors were developed, fabricated and experimentally tested for their best-suited performance and experimental results were subsequently validated for selection of best-manufactured sensor for its marketable quality. The following subsections were arranged accordingly.

4.1.1. Development of QCM sensor for β-pinene

β-pinene is a bicyclic (one six-membered ring along with a highly reactive four-membered ring) monoterpene hydrocarbon [3] with an exocyclic double bond and plays a crucial role in its quality. It is a colourless liquid in physical appearance and insoluble in water. Due to its woody-green pine-like odour, β-pinene is used in flavour and fragrance products. The compound β-pinene is also found in several other spices, including fruits like rosemary, nutmeg, cumin, and mangoes [4–7]. Thus, developing sensors for detecting β-pinene may be beneficial for evaluating the quality of agricultural products and spices. Previously reported literature on the detection of monoterpenes by various sensing processes is presented in Chapter 1, Table 1.1.

For the detection of β-pinene in Indian cardamom, an olive oil-coated QCM sensor was fabricated. Triglycerides with different fatty acid compositions constitute the majority of oils. Since monoterpenes are hydrophobic, olive oil was used as the coating material [8]. A QCM sensor coated in mustard oil was previously reported to detect ocimene in mango [9]. In other research works, castor oil-based polymer-coated sensors and linseed oil–styrene-divinylbenzene copolymer coated QCM sensors for the detection of aliphatic amines (methylamine, ethylamine, tert-butylamine, diethylamine, triethylamine, and ammonia) and volatile aromatic hydrocarbons (o-

xylene, benzene, ethylbenzene, toluene, cresol, etc.) were reported [10,11]. The sensitivity, selectivity, repeatability, reproducibility, and reusability of the β-pinene sensor were tested with olive oil and with similar vegetable oils like castor, linseed, and sunflower. The results are included in this work.

The β-pinene is considered as one of the key markers in distinguishing different varieties of cardamom. This study focuses on applying the olive oil-coated QCM (OLV-QCM) sensor as a component of an electronic nose for the qualitative gradation of Indian cardamom. Therefore, the OLV-QCM sensor prepared by the natural vegetable oil from olive may be helpful and safe for the agro and food processing industry.

4.2. Experimental

4.2.1. Chemicals and materials

Ten MHz AT-cut piezoelectric quartz crystals measuring 8 mm diameter, crammed between two gold electrodes of 5 mm diameter, were obtained from Andhra Electronics, Andhra Pradesh, India. The essential oils of cardamom - α-pinene, γ-terpinene, α-terpineol, β-pinene, and olive, linseed, castor, and sunflower oils were purchased from Sigma-Aldrich, Germany. 1,8-cineole was procured from Alfa Aesar, USA. α-terpinyl acetate was acquired from TCI, Tokyo, Japan. Solvent n-hexane was purchased from Merck India Ltd. All the chemicals were of analytical grade (>95% pure). The cardamom samples were collected from Spices Board India, Gangtok (Ministry of Commerce and Industry, Government of India). Deionised water from Millipore™ was used throughout the experiment.

4.2.2. QCM sensor fabrication

The 10 MHz QCM sensors were appropriately washed with ethanol and then with deionised water. Then four QCM sensors (OLV-QCM, CAST-QCM, LSEED-QCM, SUNF-QCM) were prepared with four different oil coatings viz olive (OLV), castor (CAST), linseed (LSEED), and sunflower (SUNF). The sensing film was developed by a homogeneous deposition of the oil solutions with an ultrasonic nebuliser [12]. The coating solution was ultrasonically vibrated to form aerosol and was channelised with the help of compressed air upon the coating unit. After that, the prepared

sensor was kept in a vacuum desiccator for 24 h for proper drying before use. The complete coating mechanism is shown in Fig. 4.1.

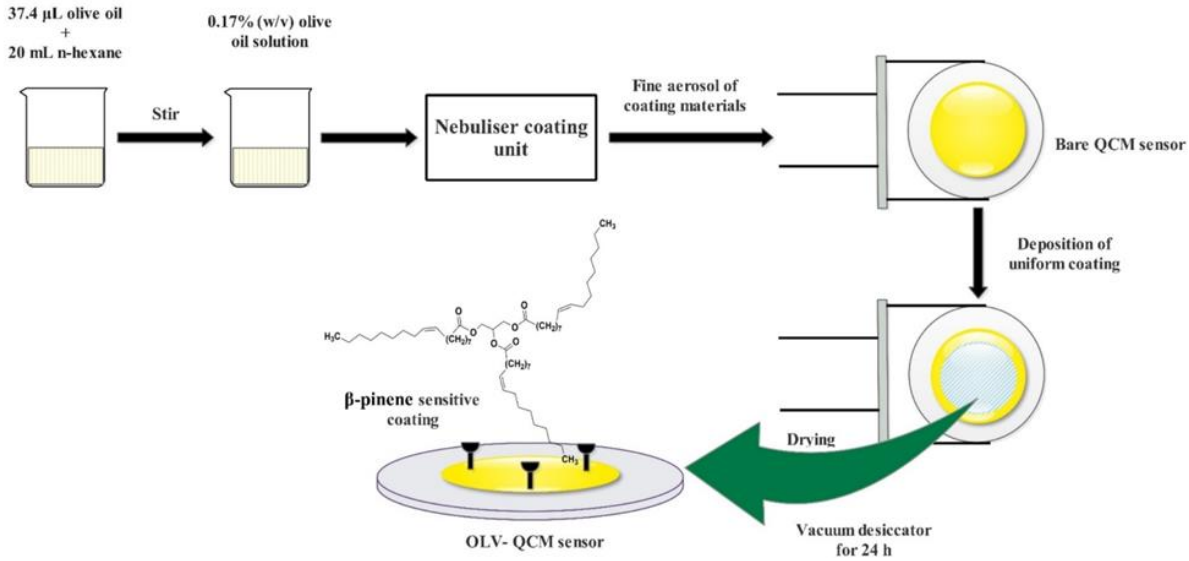

Fig. 4.1. OLV-QCM sensor fabrication mechanism.

The optimum concentration for the olive oil coating was determined as 0.17% (w/v) solution (~37 µL of analytical grade olive oil in 20 mL n-hexane). The sensor prepared with this concentration of olive oil exhibited better performance (Fig. 4.2.) than the other fabricated sensors.

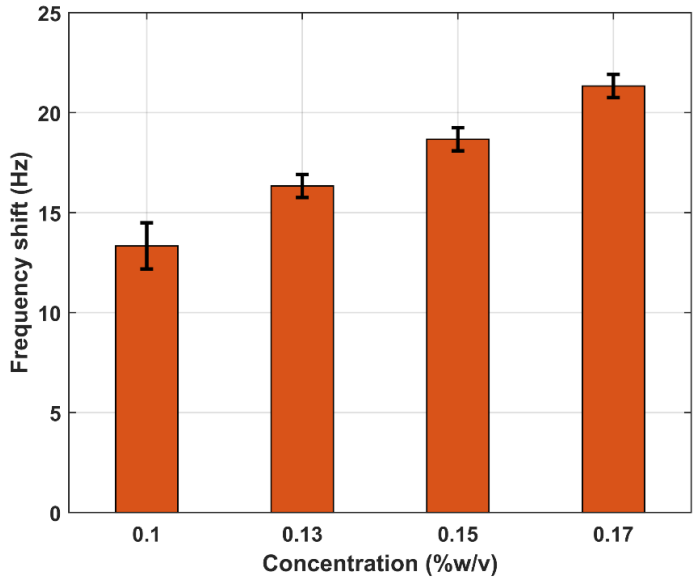

Fig. 4.2. Response profile of OLV-QCM sensor for different concentrations of olive oil exposed to 100 ppm of β-pinene VOC (27 ± 1) ºC.

4.2.3. Sensor measurement setup

The portable QCM-based sensing system and measurement setup were developed to monitor its sensitivity, selectivity, reproducibility, and long-term stability, as discussed in Chapter 3. For the experimental purpose, the developed QCM sensors were mounted on a holder, placed inside a 100 mL Teflon chamber, and kept isolated from the other electronic components used in this study. The electrical excitation was supplied to the sensors through the mounting base which is connected to the signal processing unit. The temperature of the Teflon chamber was maintained at (27 ± 1) ºC during the study, and the sensor temperature was kept as same as that of the Teflon chamber. As the electronic interface was kept separately outside the Teflon chamber, there was no effect of temperature on the sensor surface due to this. The Teflon chamber is made airtight to avoid any leakage of the incoming VOCs, and the studies were performed at standard atmospheric pressure. The studies were performed at a controlled temperature of (27 ± 1) ºC and normal atmospheric pressure. The RH was 67.7%, and the effect of humidity was considered the same since the experimental conditions were kept constant throughout.

The surrounding laboratory air was used as the base gas of the test VOCs and was applied to purge the test VOCs after the sampling phase throughout the experiment. No carrier gas has been separately applied. An automatic syringe pump (Unigenetics Instruments Pvt. Ltd. India, NE-1000) was used to inject the gas samples inside the sensor chamber. Different values of relative humidity (RH) required for the experiment were generated using Omron NE-U17 ultrasonic nebuliser and monitored using a digital hygrometer HTC-1. Also, the test VOCs of cardamoms like α-terpinyl acetate, α-terpineol,1,8-cineole, α-pinene, and β-pinene were injected inside the sample chamber in specific concentrations (10-1000ppm) using a syringe pump, maintaining a fixed flow rate of 2 mL/sec to achieve a uniform and constant inflow of VOC.

In addition, an array-based arrangement comprising eight sensors was used to study the sensors' reproducibility based on the dynamic headspace sampling method [13].

4.2.4. Volatile organic compounds preparation

The β-pinene, 1,8-cineole, α-terpinyl acetate, α-pinene, α-terpineol, and γ-terpinene were prepared to be injected into the sensor chamber to evaluate the sensor properties. Five mL of each liquid analyte was poured into a clean Petri dish, weighed, and then placed inside a sealed 10 L desiccator

for 24 h to obtain the saturated volatile at the headspace. The saturated concentration of the volatile (ppm) attained in the desiccator was measured by determining the mass change of the analyte and using equation (4.1) [14]

$$C = \frac{22.4\rho TV_S}{273MV} \times 1000 \quad (4.1)$$

where C is the saturation concentration in ppm, ρ is the density of each liquid analyte (gm mL^{-1}), T is the testing temperature (K), V_S is the volume of each liquid analyte evaporated (µL, calculated according to the change in weight), M is the molecular weight of each VOC (gm mol^{-1}), V is the volume of the desiccator (L).

When the headspace reached saturation, the required concentration of VOC samples was drawn in a 60 mL syringe and injected inside the sensor chamber using an automatic syringe pump, generating various concentration levels of static headspace. The required volume (V_2) for generating a particular concentration was determined using the equation (4.2):

$$V_1S_1 = V_2S_2 \quad (4.2)$$

where S_1 is the required concentration inside the sample chamber (ppm), V_1 is the volume of the sample chamber (mL), S_2 is the concentration of the gaseous VOC in the desiccator (ppm), V_2 is the volume required to inject inside the sample chamber (mL).

4.2.5. Cardamom sample preparation for the study of OLV-QCM sensor

Six different samples (three small and three large) of cardamom, marked as SC-1, SC-2, SC-3, LC-1, LC-2, and LC-3, were collected to study the developed sensor. 25 gm of crushed seeds from each cardamom sample was kept in a 250 mL desiccator for approximately 50 mins. to generate enough headspace. 50 mL of the headspace generated from the samples were injected within the sensor chamber,

4.2.6. Extraction and determination of volatile flavour compound (VFC) of cardamom samples using SPME and GC-MS technique

The detailed sample preparation, extraction and determination procedures of VOCs from cardamom have been discussed in Chapter 2, section 2.3.2 and 2.3.3. The relative quantity of each volatile was obtained by dividing the area of a target compound (obtained from total ion

chromatogram; TIC) with the total TIC area of all selected compounds and expressed as the relative abundance of each molecule. A total of six HSVs were chosen for further studies in this chapter. The relative abundance of this volatiles in the headspace of six cardamom samples is listed in Table 4.1.

Table 4.1. The OLV-QCM sensor response with GC-MS results

VOC	The % peak area of samples					
	SC-1	**SC-2**	**SC-3**	**LC-1**	**LC-2**	**LC-3**
α-pinene	13.49 ± 0.78	12.97 ± 0.42	12.01 ± 0.78	10.49 ± 0.23	2.09 ± 0.09	7.73 ± 0.12
β-pinene	2.35 ± 0.04	2.24 ± 0.11	2.04 ± 0.09	9.69 ± 0.32	3.80 ± 0.28	10.32 ± 0.11
1,8-cineole	67.37 ± 2.21	66.9 ± 3.84	54.45 ± 1.33	79.34 ± 0.39	92.32 ± 0.09	81.35 ± 0.15
γ-terpinene	0.95 ± 0.06	1.21 ± 0.01	1.50 ± 0.05	0.29 ± 0.04	0.89 ± 0.09	0.39 ± 0.08
α-terpineol	0.15 ± 0.01	0.35 ± 0.14	0.52 ± 0.07	0.17 ± 0.04	0.88 ± 0.19	0.20 ± 0.08
α-terpinyl acetate	13.72 ± 1.22	16.32 ± 3.93	29.46 ± 1.95	0	0	0

4.3. Results and discussion

4.3.1. Study of the surface area of the oils using HyperChem 8.0

The surface area has a significant impact on adsorption due to the surface phenomena [15]. In general, a greater surface area represents higher physical adsorption. Non-polar oils can form lipophilic assemblies, making them an excellent choice for sensing lipophilic β-pinene. The largest surface area will more likely promote more substantial hydrophobic contact, combined with other elements impacting this interaction. Later in section 4.3.7, the adsorption isotherm experiments are also included. So, using HyperChem 8.0 software, the computational simulation was done to

determine the van der Waals surface area to obtain an overview. The lowest energy conformation was chosen as allowed by Austin Method (AM1) with Polak-Ribierre and RMS gradient 0.01 kcal/ (Åmol). For each oil (olive, castor, linseed, and sunflower), the fatty acid with the highest concentration was selected, and the associated surface area ($Å^2$) was calculated. Oleic acid in olive oil and ricinoleic acid in castor oil had more significant surface areas than the other combinations, according to the data shown in Table 4.2. As a result, they may be more sensitive to the target volatile by providing the most significant area for the necessary physical adsorption.

Table 4.2. The calculated surface area of fatty acid chain in different oil by HyperChem 8.0

Name of the oil	**Fatty acid chain**	**Surface Area ($Å^2$)**
Olive oil	Oleic acid	407.35
Castor oil	Ricinoleic acid	409.43
Linseed oil	Linoleic acid	392.53
Sunflower oil	Linolenic acid	398.05

4.3.2. Study of the sensing properties of OLV-QCM sensor

The objective of the sensitivity study was to assess how the frequency of the developed OLV-QCM sensor would vary in response to the controlled administration of β-pinene. The QCM sensors developed from sunflower, linseed, and castor oil were labelled SUNF-QCM, LSEED-QCM, and CAST-QCM, respectively. Following exposure to 10-1000 ppm of β-pinene vapour, the developed sensors were examined using the corresponding sensitivity plots. Figure 4.3 displays the sensitivity charts for the four developed sensors. Evaluating the OLV-QCM sensor to the other sensors, it can be seen that it exhibited greater sensitivity to β-pinene VOC.

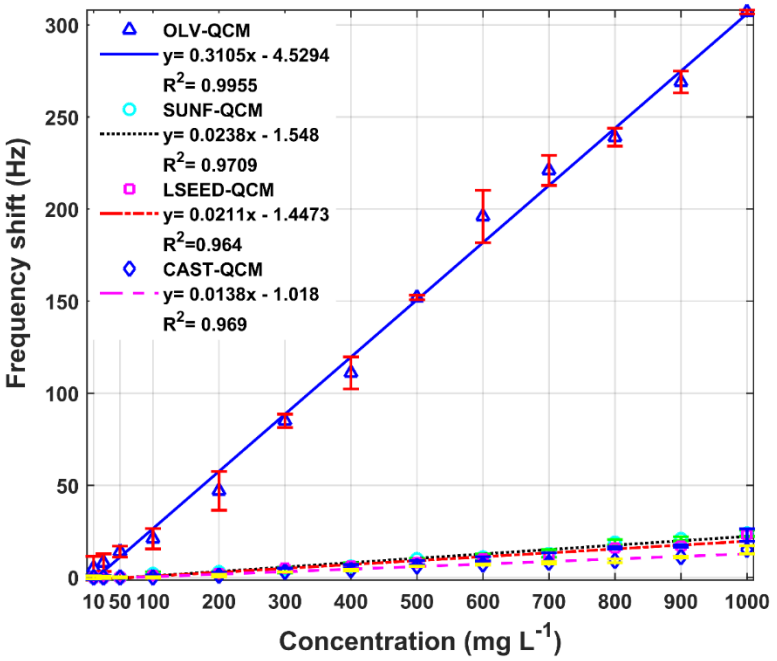

Fig. 4.3. The sensitivity of OLV-QCM, SUNF-QCM, LSEED-QCM, and CAST-QCM sensor to β-pinene vapour at 10–1000 ppm concentration operated at (27 ± 1) °C, RH=67.70%, and standard atmospheric pressure.

Each molecule of vegetable oil used for this study has three esterified analogues of separate long-chained fatty acids to one glycerol molecule. Therefore, the configuration of the long hydrophobic chains in each fatty acid is the determining element in the binding interaction between the oils and β-pinene. The exocyclic olefinic double bond of β-pinene is only available to interact with the fatty acid chains in oils. Oleic acid has a double bond at its 9^{th} carbon atom that may be involved in forming a non-covalent bond with β-pinene. The unsaturated double bond, in this case, exists in cis-configuration. As a result, the accessible exocyclic olefinic double bond of β-pinene immediately interacts with the π -bond present in each oleic acid chain via π-π interaction, as seen in Fig. 4.4. Oleic acid also has a greater surface area, which facilitates in the adsorption of β-pinene. Table 4.3 shows the essential constituent of olive oil [16].

Table 4.3. Composition of oils

	Castor oil	**Linseed oil**	**Sunflower oil**	**Olive oil**
Palmitic acid (C16:0)	0.5-1.0%	7%	5%	7.5-20%
Stearic acid (C18:0)	0.5-1.0%	3.4-4.6%	6%	0.5-5%
Oleic acid (C18:1)	2-6%	18.5-22.5%	30%	55-83%
Ricinoleic acid (12-OH-C18:1)	85-95%	Not present	Not present	Not present
Linoleic acid (C18:2)	1-5%	14-17%	59%	3.5-21%
Linolenic acid (C18:3)	Trace	52-55%	Trace	0-1.5%

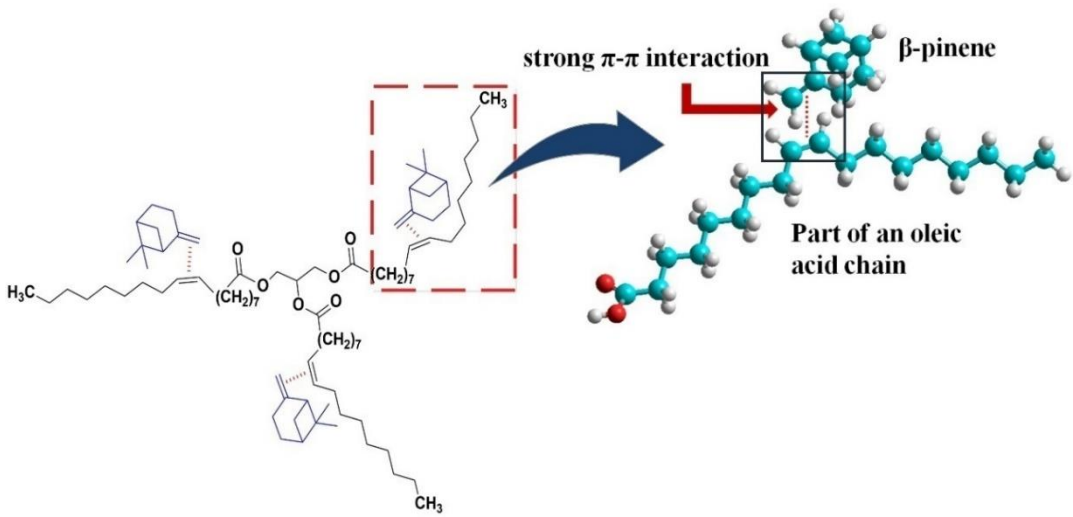

Fig. 4.4. Interaction mechanism of olive oil with β-pinene. (Red- O atom, Blue- C atom, and white-H atom).

Ricinoleic acid is the primary fatty acid in castor oil, and it has hydrophilicity due to a polar hydroxyl (-OH) group at its 12th carbon atom, which repels β-pinene. As a result, although having the largest surface area, ricinoleic acid scarcely binds to the volatile β-pinene (as studied using HyperChem 8.0 in Section 4.3.1). The omega-6 linoleic acid and omega-3 -linolenic acid found in sunflower oil and linseed oil are the most prevalent fatty acids in these oils. Due to the possibility

of shared interaction between the π-bond of β-pinene and the two double bonds of the chain with a kink in an overlapping electron cloud, linoleic acid, which is doubly unsaturated linoleic acid (non-conjugated, cis-configuration), produces weak π-π interactions. However, different interactions with two individual β-pinene molecules may not be possible because of a steric hindrance at the adjacent positions.

Linolenic acid in linseed oil is also triply unsaturated (non-conjugated, cis-configuration). As a result, linseed oil with a typical structure of twisted fatty acid chains cannot interact adequately with β-pinene, explaining the poor sensitivity ratings of the respective sensors. The chemical structures of the oils mentioned above are illustrated in Fig. 4.5(a-c), and 3D examples of the corresponding essential properties of the oil structures impacting β-pinene adsorption are depicted in Fig. 4.6.(a-c).

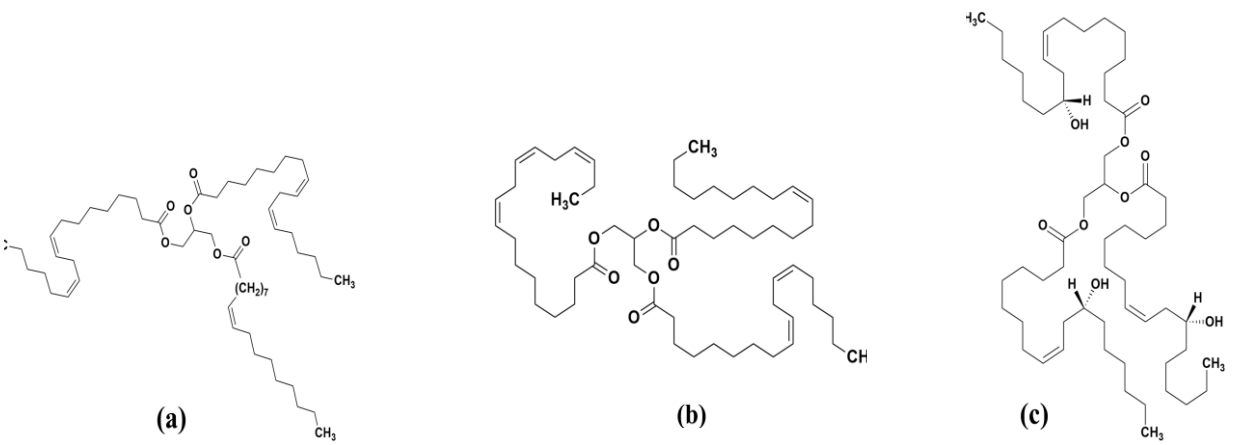

Fig. 4.5. Structures of (a) Sunflower oil, (b) Linseed oil, (c) Castor oil.

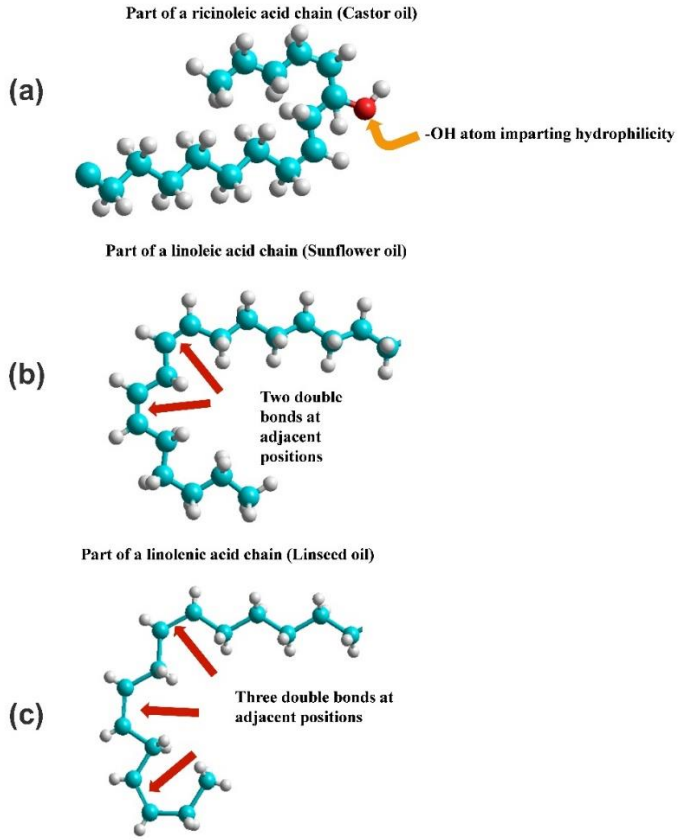

Fig. 4.6. Possible structural features of(a) castor oil, (b) sunflower oil, and (c) linseed oil-coated QCM sensor affecting the sensitivity towards β-pinene. (Red- O atom, Blue- C atom, and white-H atom).

The target and the competent VOCs were prepared considering ambient air as the medium. It was essential to analyse the OLV-QCM sensor in response to the ambient air. Using a syringe, air volume ranging from 10 to 50 mL was injected into the sensor chamber. Figure 4.7 illustrates the response of the OLV-QCM sensor. Thus, it can be concluded that the responses of the OLV-QCM sensor are caused by the applied VOCs and not by the surrounding air.

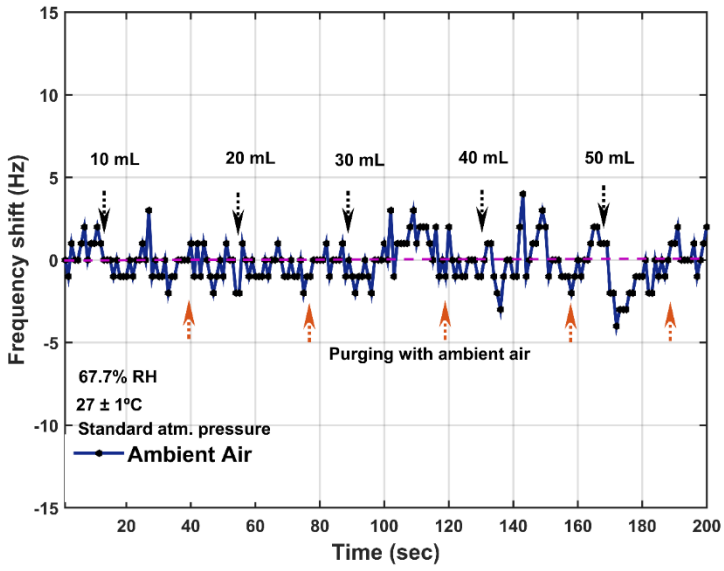

Fig. 4.7. Response of the OLV-QCM sensor towards the different volumes of ambient air studied at (27 ± 1) °C, RH= 67.70%, and standard atmospheric pressure.

When varied amounts of β-pinene were introduced into the OLV-QCM sensor, the frequency (Δf) altered from its baseline resonant frequency. The sensor response was evaluated three times. Fig. 4.8(a) illustrates the frequency shift caused by the injection of 1000 ppm of β-pinene VOC. Until the introduction of the target VOC, the oscillation frequency of the developed sensor remained uniform and steady for 16 seconds. The solid red arrow indicates the injection of the sample, after which the sensor response showed a significant decline in response to 412 Hz in 17 seconds, then steadily climbed till it attained a saturated response of 335 Hz in 36 seconds. The black arrow represents the commencement of purging the sensor chamber with ambient air, where the sensor response gradually recovers to the initial baseline, indicating the reversibility of the fabricated sensor.

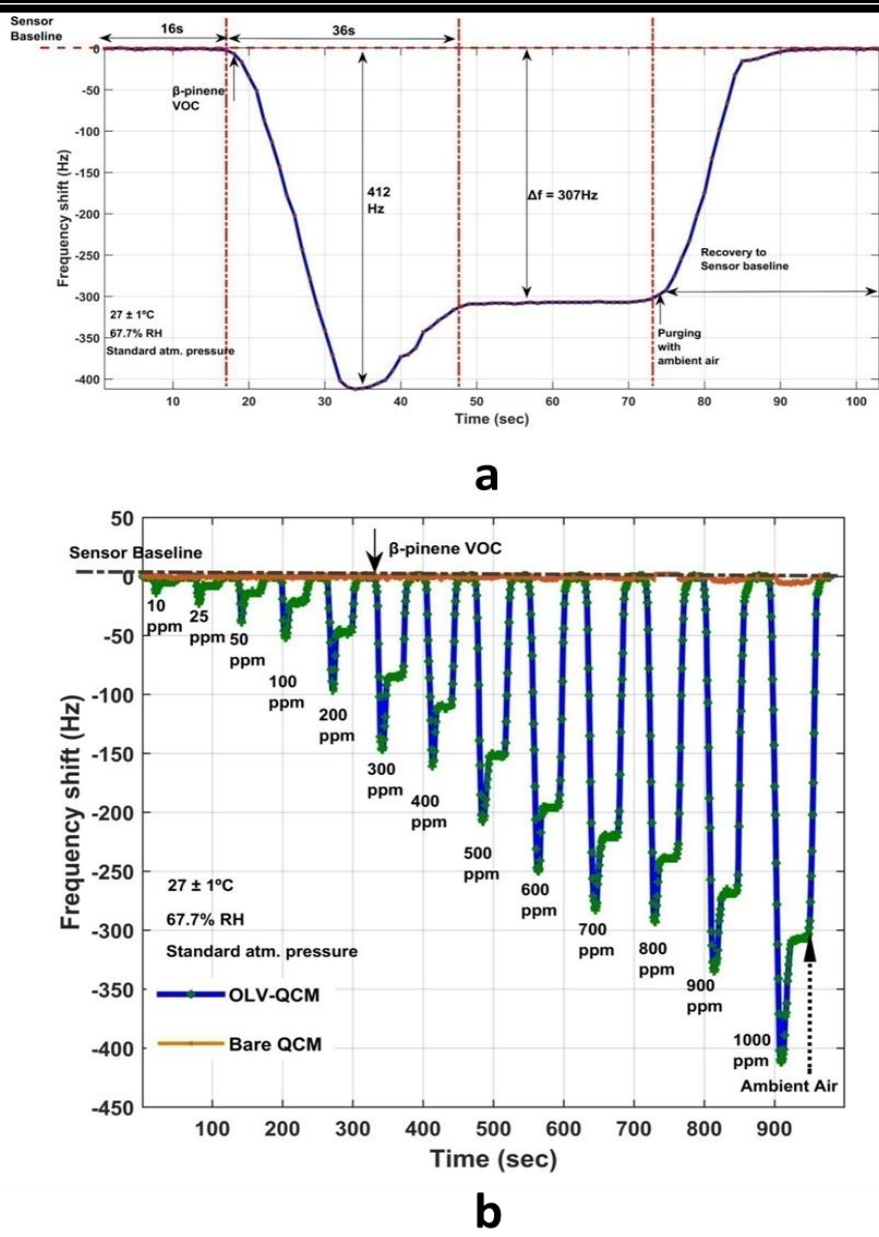

Fig. 4.8. Complete OLV-QCM sensor response profile (a) for 1000 ppm of β-pinene (b) at different concentrations of VOC ranging between 10 -1000 ppm at (27 ± 1) ºC, 67.7% RH and standard atmospheric pressure.

The sensor frequency response profile due to the injection of 10 – 1000 ppm of β-pinene VOC at 67.7% RH is shown in Fig. 4.8(b). It can be noticed that the shape of the sensor response graph remains identical, while the time to reach the saturation state for different concentrations of β-pinene is different. The sensor response reacts promptly to the ambient air led to the desorption of the analyte from the sensor surface resulting in the frequency shift to reach the original sensor

baseline without any noticeable drift. It is also evident from Fig. 4.8(b) that the frequency deviation of the developed sensor increases with the increasing concentration of injected VOC. The OLV-QCM sensor responses with the different concentrations of VOC are shown in Fig. 4.3 and can be approximated by equation (4.3)

$$y\,(Hz) = 0.3105\,\left(\frac{Hz}{ppm}\right)x - 4.5294 \qquad (4.3)$$

The sensor shows the sensitivity of 0.3105 Hz/ppm, *y* indicates the shift in frequency of the OLV-QCM sensor for the different injected concentrations of β-pinene in Hz, and *x* is the concentration of β-pinene VOC in ppm. The correlation value, R^2, was obtained as 0.9979. The R^2 measures the degree of linearity, and R denotes the regression coefficient. The standard error estimate (σ_{est}) was calculated using equation (4.4), which measures the average of the difference between the actual values of sensor deviation to that of the approximated values from the linear equation (4.4).

$$\sigma_{est} = \frac{\sqrt{(\hat{y}-y)^2}}{(n-2)} \qquad (4.4)$$

where, $\hat{y}$ = approximated value, *y* = actual value, and *n* is the number of samples considered for the plot. The limit of detection (LOD) was calculated as 5.57 ppm using equation (4.5).

$$\text{LOD} = 3(S_{y/x})/m \qquad (4.5)$$

$S_{y/x}$ denotes the standard deviation of the regression line, and *m* is the slope of the sensor characteristics equation.

Also, the limit of quantitation (LOQ) was calculated to be 18.59 ppm from following equation (4.6).

$$\text{LOQ} = 10(S_{y/x})/m \qquad (4.6)$$

4.3.3. Study of the binding interaction of OLV-QCM sensor with β-pinene using UV-Visible spectroscopy

The π-π interaction between the coating layer of the OLV-QCM sensor and β-pinene, as stated in Section 3.2, has been validated using UV-Visible spectroscopy work (Shimadzu double beam spectrophotometer, serial no. A116351). For the experiment, a 0.2% (v/v) concentration of olive oil was dissolved in n-hexane. Even though the medium of interaction in sensor performance is gaseous, it is liquid in UV-vis spectrometers. The spectroscopic experiment was conducted to analyse the π-stacking effect in various media.

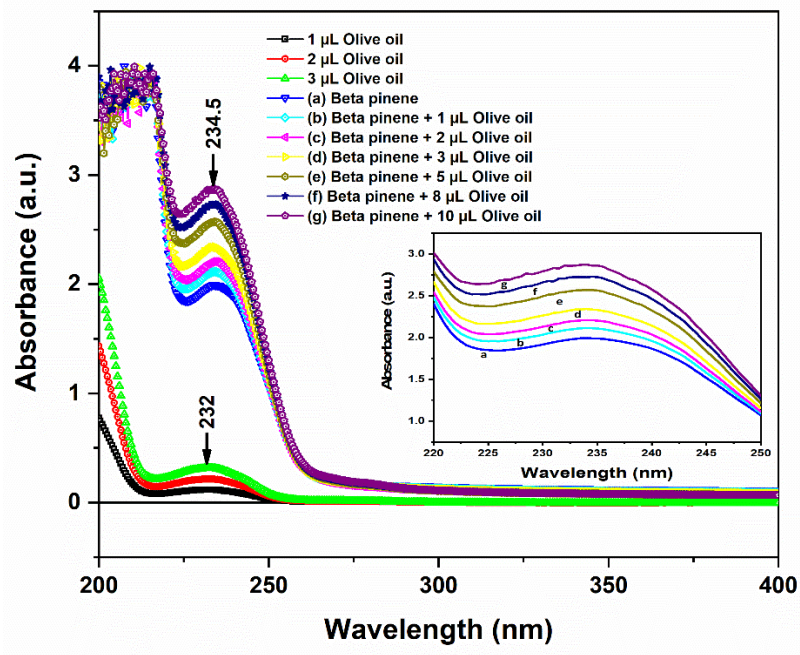

Fig. 4.9. The UV-vis absorption spectra for π-π interaction between olive oil and β-pinene.

The UV-vis absorption spectra illustrated in Fig. 4.9 were taken in the wavelength range of 200-400 nm (UV region) as no significant peak was obtained in the spectra's visible region (400-800 nm). After carrying out the baseline correction with the solvent n-hexane, three subsequent spectra were recorded with the gradual addition of 1µL of 0.2% (v/v) olive oil solution in the solvent and three tiny hump-like peaks (black, red, and green lines) at around 232 nm of wavelength were obtained. The sharp peak (blue line) at a wavelength of 234.5 nm was acquired with only β-pinene in the medium because of its exocyclic double bond as the chromophore [17]. Then six successive peaks (cyan to purple lines) at the same wavelength emerged when 1µL of the same olive oil solution was added to the medium with β-pinene. The β-pinene peak exhibited a hyperchromic

shift, increasing the intensity upon adding olive oil solution. Clearly, the absorbance value showed an additive property, as shown in the inset of Fig. 4, by magnifying the peak area at the wavelength region of 220-250 nm from the complete peak profile. This happens when there is an incorporation of auxochrome, some moiety that causes enhancement in intensity because of a rise in the number of π-π* transitions. Here it occurred because of a separate engagement of the exocyclic π-bond of β-pinene by interacting with the olefinic π-bond in the oleic acid chain [18]. The schematic diagram of the incorporation of olive oil in small batches causing an elevation in the number of π-π* transitions has been elucidated in Fig. 4.10. Therefore, this experimental study confirms the presence of a π-π stacking which attaches the volatile target β-pinene with the adsorbent olive oil on the OLV-QCM sensor.

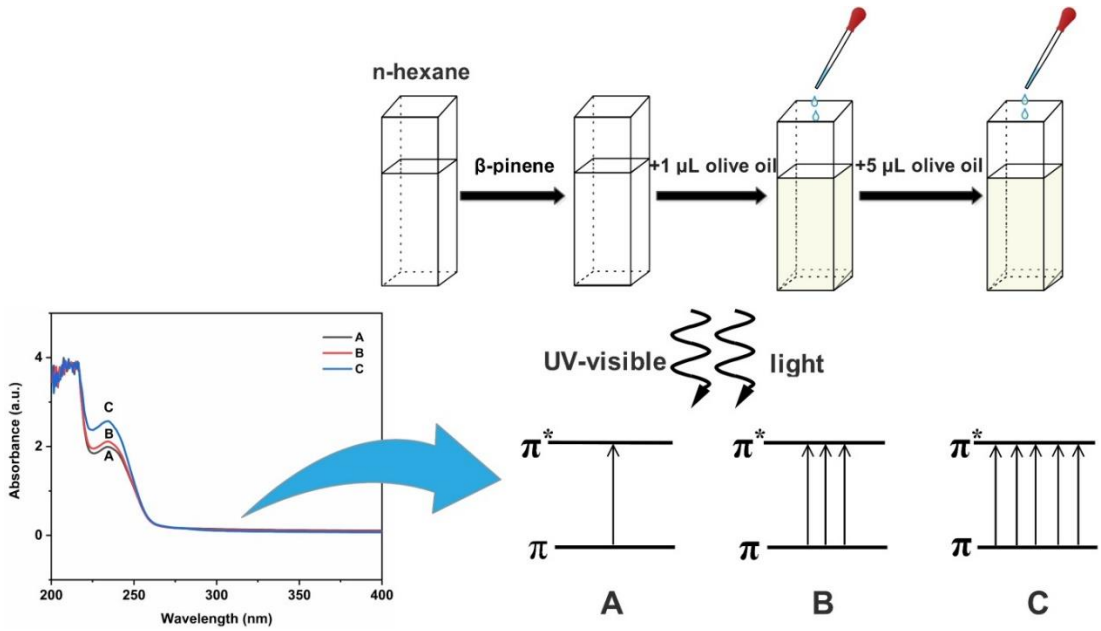

Fig. 4.10. The schematic diagram of the increase in the number of π-π* transitions due to the interaction between olive oil and β-pinene.

4.3.4. Fourier transform infrared spectroscopy (FTIR) Analysis

Olive oil is mainly composed of triacylglycerols with free fatty acids in a small amount [19]. Triacylglycerols are esterified analogues of three long-chained fatty acids (saturated and unsaturated) to one glycerol molecule [20]. The significant fatty acids present in olive oil are presented in Table 4.3. FTIR spectra (Shimadzu FTIR spectrometer (IR Prestige)) of olive oil in Fig. 4.11 reveal the presence of the functional groups and bonds required for the specified interaction of olive oil with β-pinene.

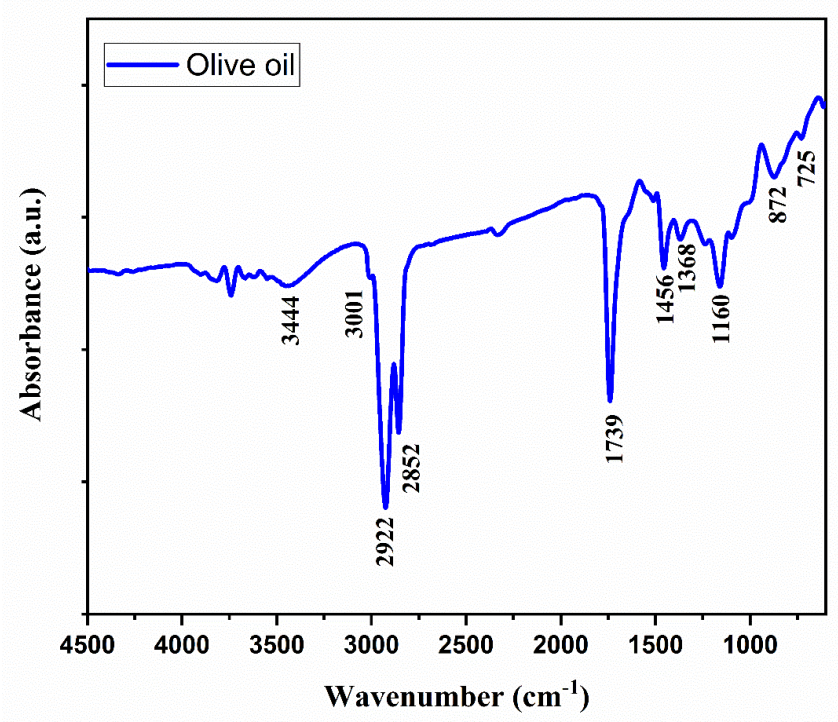

Fig. 4.11. FTIR spectra of the olive oil coating material.

The band around 2922 cm^{-1} and 2852 cm^{-1} arises due to symmetric and asymmetric -C-H stretching vibration of the methylene (-CH2) groups. A tiny shoulder at 3001 cm^{-1} appears due to the stretching vibration of the cis-olefinic double bonds (C=C) [21]. The sharp dip at 1739 cm^{-1} signifies the triglyceride's ester carbonyl group (-O-C=O). A small peak at about 1456 cm^{-1} can be assigned to the -CH2 and methyl (-CH3) aliphatic groups [22]. A hump of nominal intensity at 1368 cm-1 is evaluated as the bending vibration of the $-CH_2$ groups. The peaks at 1160 cm^{-1} and 725 cm^{-1} can be accredited to C-O stretching and overlaying two different vibrations (rocking vibration of the methylene groups and out-of-plane vibration of cis-disubstituted C=C groups), respectively. The wagging of =CH2 moieties can cause the minor shoulders at 872 cm^{-1}, and the broad hump at 3444 cm^{-1} appeared for O-H stretching of the carboxylic groups of the free fatty acids. Thus, the results of FTIR spectra justify the composition of olive oil used for coating the decorated sensor, as mentioned in Table 4.3

4.3.5. Field Emission Scanning Electron Microscope (FESEM) Analysis

Figure 4.12 represents the FESEM micrographs (FESEM: Zeiss Microscopy, ΣIGMA) of (a) without and (b-d) with olive oil film coated on the surface of the OLV-QCM sensor. Fig. 4.12(a)

and (b) demonstrates the difference in the surface morphology of the OLV-QCM sensor surface. Fig. 4.12(b) suggests uniform deposition of olive oil on the surface of the gold electrode. Magnified pictures of the coating are presented in Fig. 4.12(c,d). The rough texture of the top surface of the olive oil-coated thin film is prominent in these images. Such a typical surface feature facilitates the adsorption of target VOC molecules, which are probably encapsulated in lock and key mode via different non-covalent bonds such as hydrogen bonds, van der Waals attracting forces, and hydrogen bonds [23].

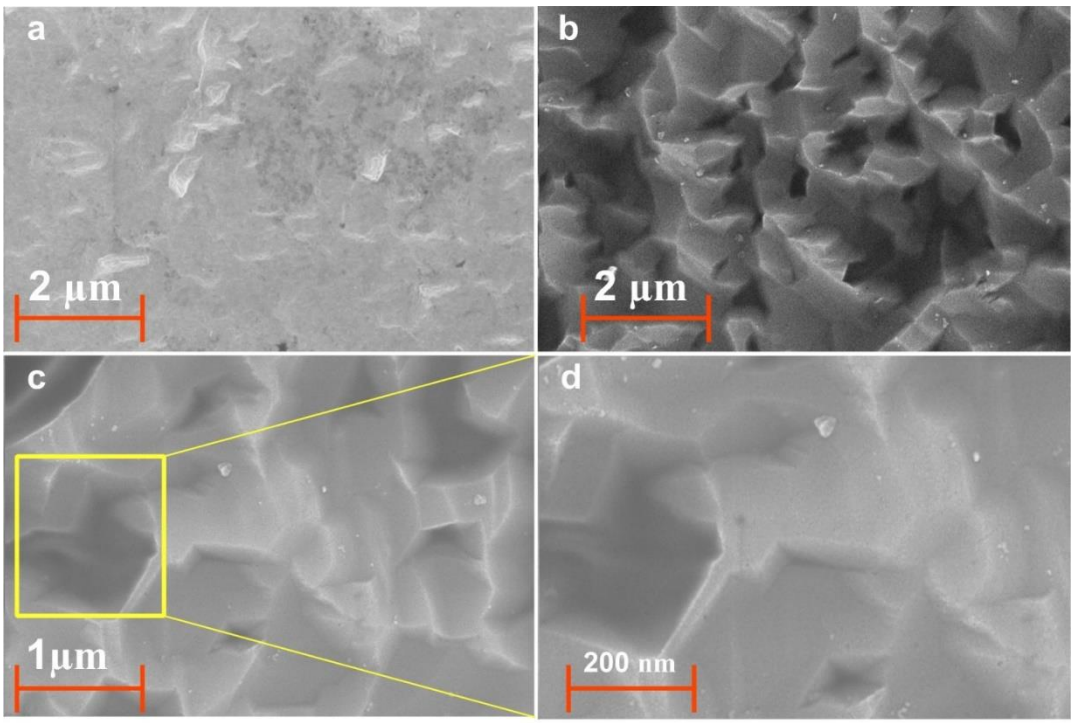

Fig. 4.12. FESEM images of (a) blank QCM sensor; (b) olive oil coated QCM sensor; (c-d) magnified version of the coated film on OLV-QCM sensor at 1µm and 200 nm, respectively.

4.3.6. Study of the selectivity characteristics of OLV-QCM sensor

The selectivity of the fabricated OLV-QCM sensor was studied to evaluate the sensor performance to detect the targeted β-pinene VOC from a pool of mixed-VOCs, as in the case of cardamom samples. The sensor was tested in the presence of other monoterpene volatiles that influences the aroma of six cardamom samples such as 1,8-cineole, α-pinene, α-terpinyl acetate, α-terpineol, and γ-terpinene. as mentioned in Table 4.1

Table 4.4. Selective calculation of the developed sensor

Concentration (ppm)	Selectivity ($S_{Volatile}$ in %)					
	β-pinene	**α-terpinyl acetate**	**1,8-cineole**	**α-pinene**	**γ-terpinene**	**α-terpineol**
10	83.33	0	16.66	0	0	0
25	72.72	0	27.27	0	0	0
50	63.63	0	27.27	9.09	0	0
100	52.5	2.5	27.5	12.5	0	5
200	56.62	3.44	21.83	13.79	0	6.89
300	61.60	2.89	15.21	12.31	0.72	7.24
400	61.32	4.97	14.36	11.04	1.10	7.18
500	65.23	4.72	12.44	9.44	1.28	6.86
600	64.26	4.59	12.13	10.16	1.96	6.88
700	61.55	4.73	14.20	10.86	2.50	6.12
800	59.45	4.72	14.17	10.94	3.48	7.21
900	57.48	4.70	15.17	11.53	3.20	7.90
1000	57.71	5.07	14.84	11.09	3.19	8.08

The selectivity of each volatile was calculated using equation (4.7) for concentrations ranging from 10-1000 ppm and tabulated in Table 4.4.

$$S_{Volatile} = \frac{R_{Volatile}}{\sum_{i=1}^{n} R_i} \times 100\% \quad (4.7)$$

Here, $S_{volatile}$ denotes the selectivity obtained for a particular VOC for the developed sensor; $R_{volatile}$ is the respective sensor response for any particular concentration of volatile; n is the total number of competent VOCs; R_i is the sensor output for other VOCs.

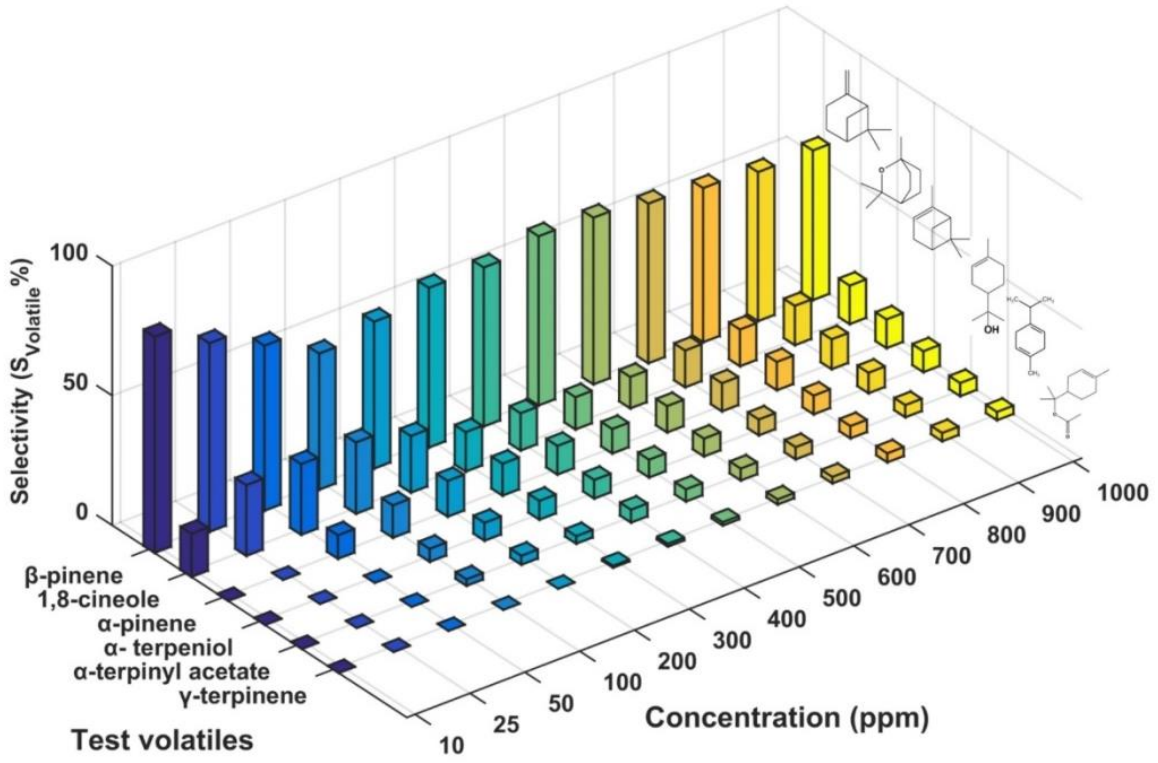

Fig. 4.13. Bar plot diagram of % selectivity of the OLV-QCM sensor for β-pinene,1,8-cineole, α-pinene, α-terpineol, α-terpinyl acetate, and γ-terpinene VOCs at 10-1000 ppm.

Figure 4.13 shows the structures of β-pinene and its competing volatiles and the bar plots of the % selectivity of OLV-QCM sensor for β-pinene, α-pinene, 1,8-cineole, α-terpinyl acetate, α-terpineol, and γ-terpinene as obtained from Table 4.4. The developed sensor revealed selective behaviour at higher and lower concentration range towards β-pinene with a selectivity percentage of 57.70% at 1000 ppm and 83.33% at 10 ppm.

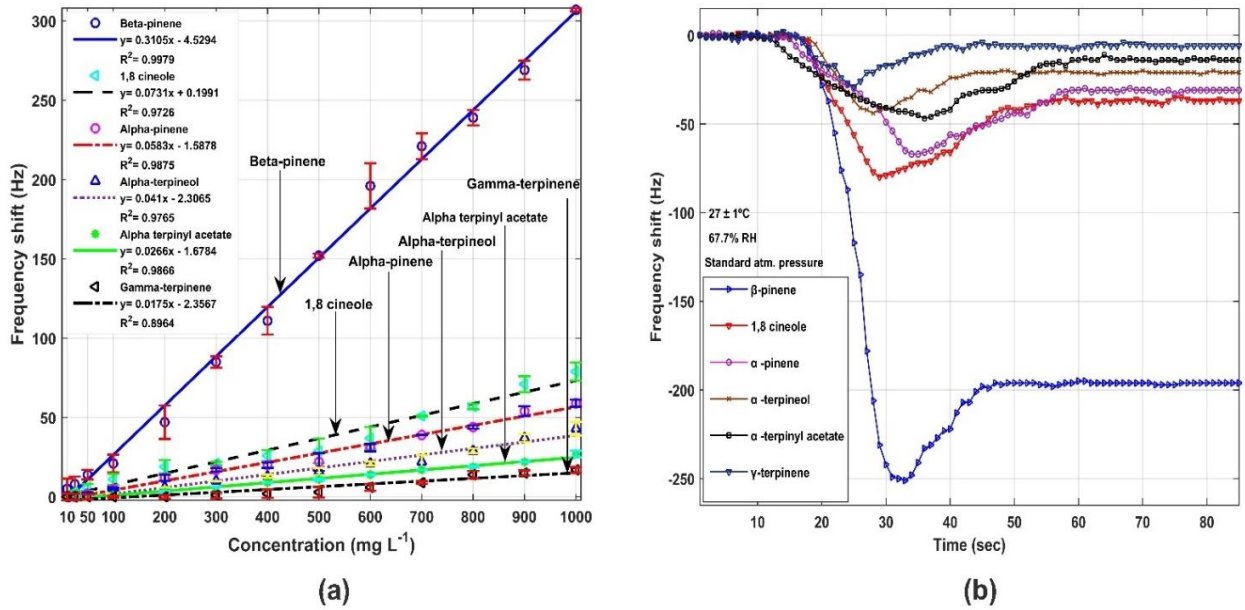

Fig. 4.14 (a). Characteristics OLV-QCM sensor responses towards β-pinene and other competing VOCs ranging between 10-1000 ppm, (b) OLV-QCM sensor response pattern for 600 ppm of β-pinene, 1,8-cineole, α-terpinyl acetate, α-pinene, α-terpineol, and γ-terpinene at (27 ± 1) ºC, 67.7% RH and standard atmospheric pressure.

The average value of the sensor responses for three consecutive sampling stages for each concentration of VOC was considered to calculate the sensitivity. The developed OLV-QCM sensor was tested with other dominating volatiles in cardamom viz. α-pinene, 1,8-cineole, α-terpinyl acetate, α-terpineol, and γ-terpinene keeping all the experimental procedures and calculations constant. The corresponding sensitivity plots of the fabricated OLV-QCM sensor with error bars were plotted as shown in Fig. 4.14(a) after exposure to β-pinene and other dominating volatiles in cardamom. **It was observed that the developed sensor shows higher sensitivity towards β-pinene as compared to other VOCs.** The sensitivity comparison of the interfering VOCs towards OLV-QCM is demonstrated in the bar plot in Fig. 4.15. The sensor responses of the OLV-QCM sensor during controlled exposure to 600 ppm of all the dominating VOCs used in this study are shown in Fig. 4.14(b). It is quite understandable from the frequency shift that the sensor showed a higher frequency shift towards β-pinene compared to the other competing volatiles in this study.

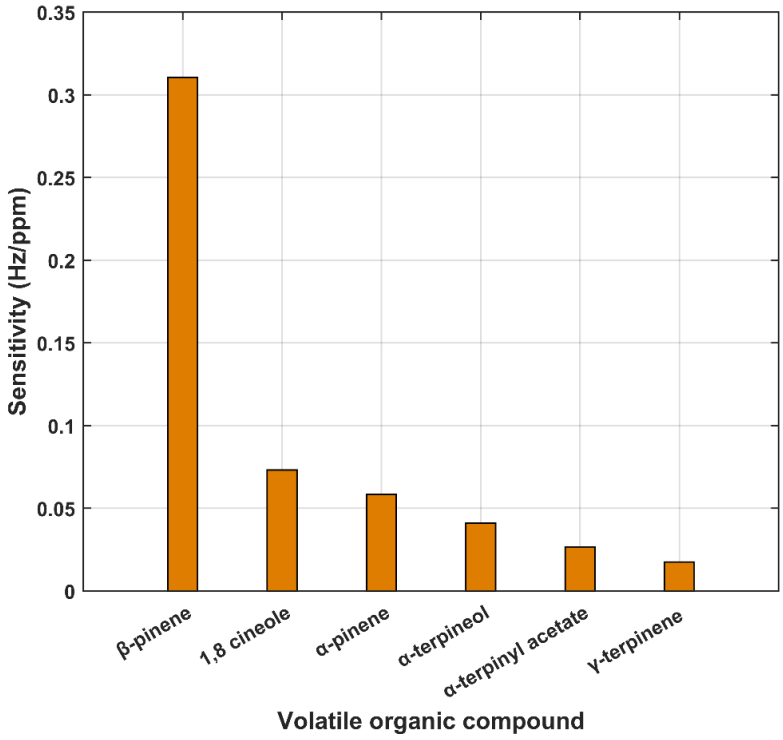

Fig. 4.15. Sensitivity comparison of the interfering VOCs in cardamom towards OLV-QCM sensor.

From the structures of the volatile provided in Fig. 4.3, β-pinene is a bicyclic alkene with an **exocyclic double bond.** Clearly, except for β-pinene, the other volatiles possess **endocyclic** π-bond or no π-bond at all. Endocyclic double bonds usually are constrained to form π interaction with a long fatty acid chain. With a higher number of exposed surfaces, the exocyclic double bond is more prone than the corresponding endo one to π-π interaction, to long-range interaction for which the OLV-QCM sensor shows the highest average selectivity towards β-pinene.

On the other hand, 1,8-cineole has an oxygen atom as its only reactive site, and it can bind with the π-bond of the oleic acid chain with its lone pair of electrons. Since lone pair-π interaction is much stronger than π-π interaction, the results should have reflected the same. However, the presence of a polar oxygen atom obstructs the interaction with the long, non-polar hydrocarbon chain. Besides, the high electronegativity of the O atom decreases its nucleophilic character to some extent explaining why 1,8-cineole ends up being in the second position in terms of selectivity, as observed in Fig. 4.14(a). Among the other competent volatiles, α-pinene is the structural isomer of β-pinene, and it has a similar structure with an endocyclic double bond.

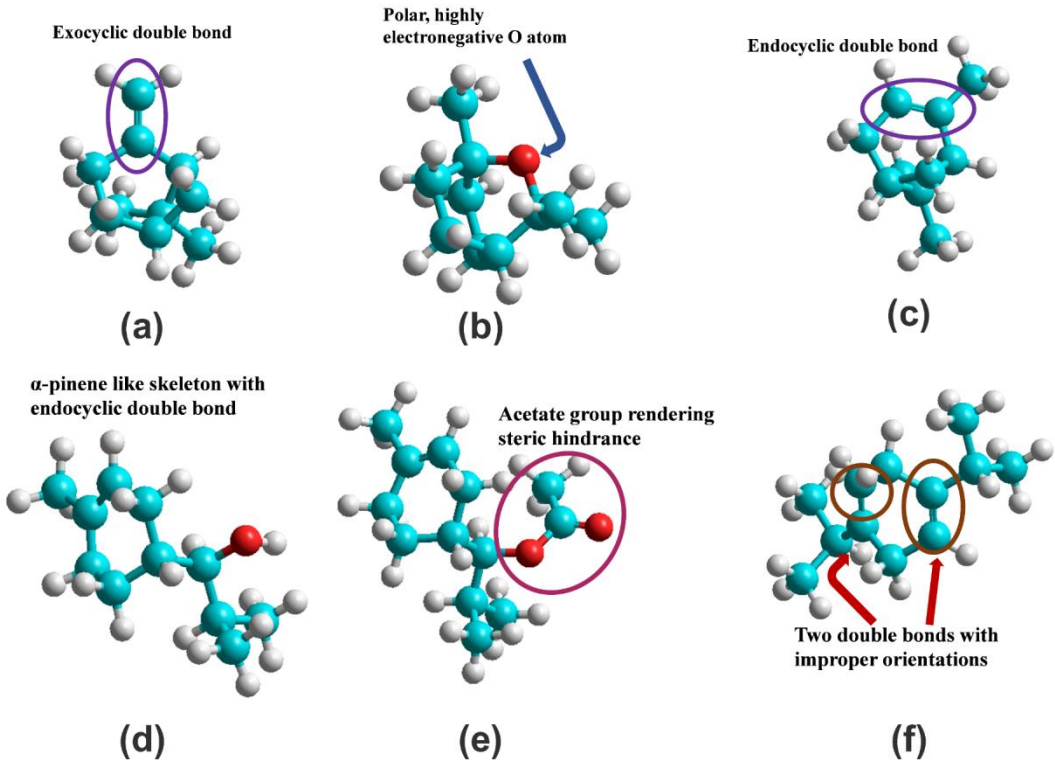

Fig. 4.16. Probable structural characteristics of the VOCs affecting the selectivity of OLV-QCM sensor towards (a) β-pinene, (b) 1,8-cineole, (c) α-pinene, (d) α-terpineol, (e) α-terpinyl acetate, and (f) γ-terpinene. (Red- O atom, Blue- C atom, and white-H atom).

Therefore, it may form feeble π-π interaction with the oleic acid chain, showing the third most selectivity (%) of the much alike decorated sensor towards α-pinene. The skeletal structures of α-terpineol and α-pinene are similar. In comparison, the orientation of the -CH_3 groups is different, and an extra polar hydroxyl (-OH) group is present in α-terpineol. Therefore, in terms of selectivity (%), it appears precisely after α-pinene. Furthermore, α-terpinyl acetate, being the corresponding ester of α-terpineol possesses an acetate group instead of the -OH group, which renders steric hindrance making the interaction with the oleic acid even weaker. Because of not having proper orientations of the two double bonds present in γ-terpinene, it cannot get attached with the double bond in oleic acid suitably even after having the required reactivity present faces very low selectivity responded by the OLV-QCM sensor. The interaction of the OLV-QCM sensor with the interfering VOCs is shown in Fig. 4.16.

Referring to different research reports and the results of the SPME-GCMS analysis of the six cardamom samples shown in Table 4.1, it is evident that 1,8-cineole occupied the maximum

abundance in cardamom. **However, the average selectivity of the OLV-QCM sensor showed higher selectivity for β-pinene (62.88%) compared to 1,8-cineole (17.93%). The cross-sensitive interference due to 1,8-cineole thus contributed to minor inaccuracy in the sensor output.** The other interfering VOCs like α-pinene, α-terpineol, α- terpinyl acetate, and γ-terpinene merely had cross-sensitive behaviour due to their low selectivity towards the OLV-QCM sensor. However, detecting the presence of β-pinene in other samples with dissimilar abundance in the interfering VOCs may lead to improper cross-sensitive behaviour and require further investigation.

4.3.7. Equilibrium analysis of OLV-QCM sensor

Adsorption isotherm correlates the equilibrium concentration of bound and free guests to a specific concentration region. Hence the interaction model between β-pinene molecules and the olive oil-coated QCM sensor was developed based on Langmuir, Freundlich, and Langmuir-Freundlich isotherm models [24] illustrated in Fig. 4.17. The linear relationship of the model is satisfied by using the following equations:

Langmuir: $\Delta m = \frac{\Delta m_{max}\,[C]}{K_D + C}$ (4.8)

Freundlich: $\Delta m = \Delta m_{max}[C]^{1/n}$ (4.9)

Langmuir- Freundlich: $\Delta m = \frac{\Delta m_{max}[C]^{1/n}}{K_D + [C]^{1/n}}$ (4.10)

where Δm is the change of mass on a unit surface area of the electrode of the QCM sensor (μg/cm^2); C is the β-pinene vapour concentration (μg/mL); K_D is the constant of reverse equilibrium (mL/μg); $1/n$ is the index of heterogeneity of Freundlich isotherm; max subscript represents the maximum.

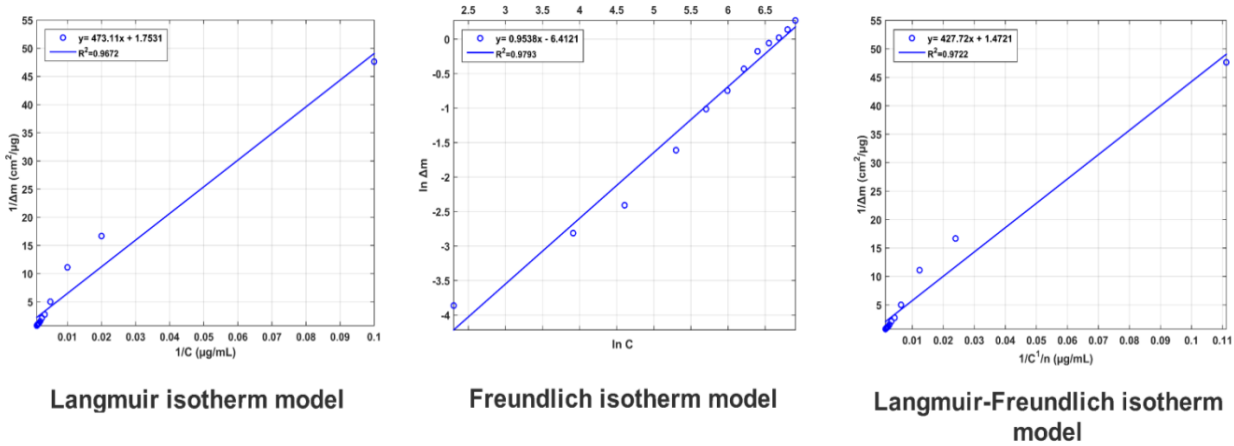

Fig. 4.17. Isotherm models for the equilibrium analysis on the sensor coating surface.

The Langmuir model evaluates the homogeneous uni-layered physical adsorption affinity bond of the olive oil coated film for β-pinene VOC connected to a particular constant value. The study of the Freundlich isotherm model relates to the heterogeneous binding affinity of the coated oil surface denoted by the heterogeneity factor *1/n*, and this model is applicable for single-layered physisorption. On the other hand, the Langmuir-Freundlich model shows the non-uniform attribute of coated oil and is suitable for recounting the adsorption isotherms' saturation conduct in high adsorption regions. It is observed that the linearity of the Freundlich equation is better than that of Langmuir and Langmuir–Freundlich equations for all coating instants. The Freundlich isotherm is the best-fitted model, according to the $R^2 = 0.9793$ correlation coefficient and $y = 0.9538x - 6.4121$ linear data shows the interlinkage between the β-pinene molecules and the olive oil coated QCM sensors. The isotherms model analysis is given in Table 4.5, which conveys the nature of active binding sites towards β-pinene VOC to be heterogeneous distribution on the OLV- QCM sensor.

Table 4.5. Langmuir, Freundlich and Langmuir-Freundlich isotherm constants for OLV-QCM sensor.

Langmuir		**Freundlich**		**Langmuir-Freundlich**	
Δm_{max}	0.570	Δm_{max}	0.0016	Δm_{max}	0.68
K_A (µg/mL)$^{-1}$	0.0037	1/n	0.9538	K_A (µg/mL)$^{-1}$	0.0034
K_D (µg/mL)	269.67	R^2	0.9793	K_D (µg/mL)	290.85
R^2	0.9672			1/n	0.9538
				R^2	0.9722

4.3.8. Study of the effect of relative humidity on the sensor response

The applied VOCs in the sensor chamber were delivered by ambient air. The impact of the OLV-QCM sensor performance parameters owing to the changeable humid conditions was thus essential. For higher values, humid air in aerosol was injected, and the humidity was measured using a Digital Hygrometer HTC-1. Significantly more little humidity (RH) values were obtained using a dehumidifier. Fig. 4.18(a) represents the frequency variations of the fabricated QCM sensor upon stabilising at varying RH. After injection of ambient air, altering the RH from 45 to 85%, the frequency shifts fluctuated between 1 and 5 Hz. This may be explained by the fact that many hydrophilic carboxyl acid groups of various long-chained fatty acids found in olive oil interact with the polar water molecules, enhancing the frequency shift [25]. Here the extent of interaction is relatively low due to the sizeable hydrophobic hydrocarbon moiety in long-chained fatty acids like oleic acid, palmitic acid, stearic acid, and low loading of the material [25]. As a result, the change in frequency is minimal, and the change in relative humidity is most likely caused by the practically saturated adsorption of H_2O molecules at greater humidity.

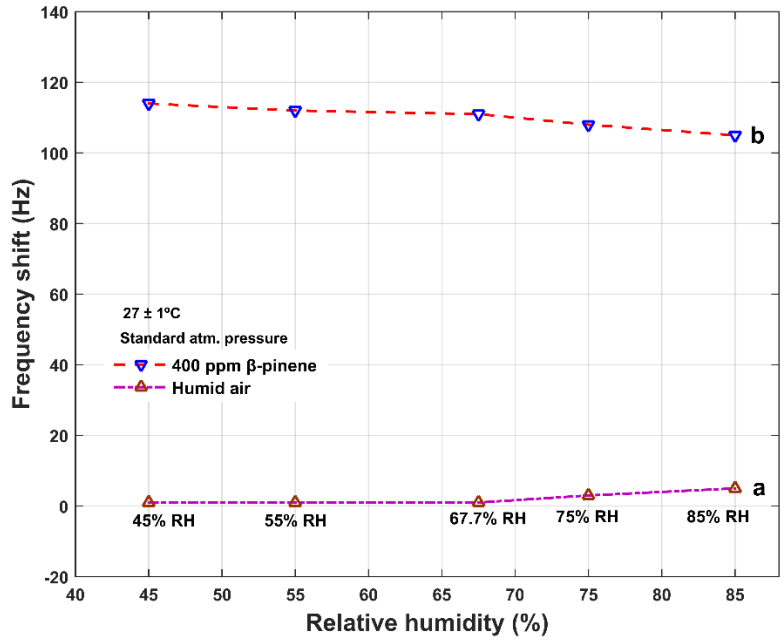

Fig. 4.18. Response profile of OLV-QCM sensor (a) towards ambient air, (b) for 400 ppm of β-pinene at the different relative humidity (%), at (27 ± 1) ºC, and standard atmospheric pressure.

The effect of relative humidity on the OLV-QCM sensor characteristics on the injection of β-pinene aroma is illustrated in Fig. 4.18(b). 400 ppm of β-pinene VOC at various relative humidity of 45, 55, 67.5, 75, and 85% were injected into the sensor chamber. The sensor responses recorded were 114, 112, 111, 108, and 105 Hz, respectively. A slight decreasing trend in sensor adsorption is observed towards β-pinene with increasing humidity. This is because the hydrophobic interaction between β-pinene and oleic acid molecules of olive oil gets slightly hindered with increased humidity in the air. So, this confirms the negligible effect of the sensor performance due to ambient humidity of 67.7%.

4.3.9. Study of the reusability of the OLV–QCM sensor

The reusability of the OLV–QCM sensor was tested with 400 ppm of β-pinene once a week for six months. Fig. 4.19 shows weekly sensor responses. The study demonstrates that sensor output decreases by 1.80% after four weeks. After 24 weeks, the declining trend reached 18.01%. After 14 weeks, sensor responses varied by 10.81%. Therefore, the sensor may be used for up to 14 weeks without any significant reduction of sensitivity.

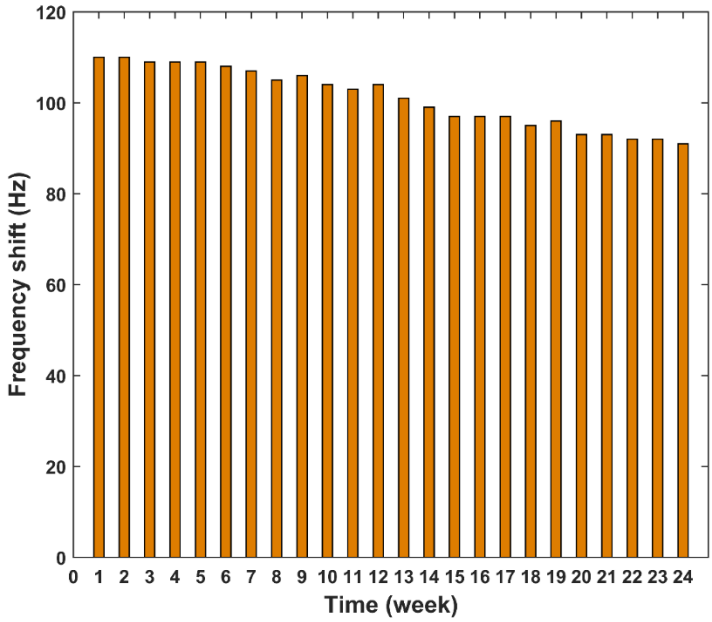

Fig. 4.19. Bar plot representation of reusability of the OLV-QCM sensor on application of 400 ppm of β-pinene measured at (27 ± 1)°C, RH= 67.70%, and standard atmospheric pressure.

4.3.10. Study of the repeatability and reproducibility

The β-pinene VOC ranging from 10-1000 ppm were injected into the sensor chamber. The relative standard deviations of the values obtained using equation (4.11) are presented in Table 4.6.

$$R_{P,D} = (1 - RSD) \times 100\% \quad (4.11)$$

where *RSD* denotes the relative standard deviation.

The repeatability study helped to determine the sensor performance to generate similar responses for repeated sensing applications. The OLV-QCM sensor was repeatedly sampled (n=4) with 200 ppm of β-pinene vapour, as shown in Fig. 4.20. The sensor frequency profile maintained the same shape and amplitude for each repeated instance of VOC injection and recovered its initial baseline during the purging condition. The average frequency shift of the OLV-QCM sensor for four consecutive repetitions at 200 ppm was calculated as 48.25 ± 1.25 Hz. The maximum of repeatability R_P was calculated as 99.44% for 1000 ppm of the target VOC. The repeatability gradually increased with the rise in concentrations (in ppm) of β-pinene VOC. The study, therefore, confirms greater chances to recreate favourably similar sensor data output at higher concentrations

of VOCs. The average percentage of repeatability of the sensor was calculated as 95.14%, confirming the ability to generate repeated responses efficiently.

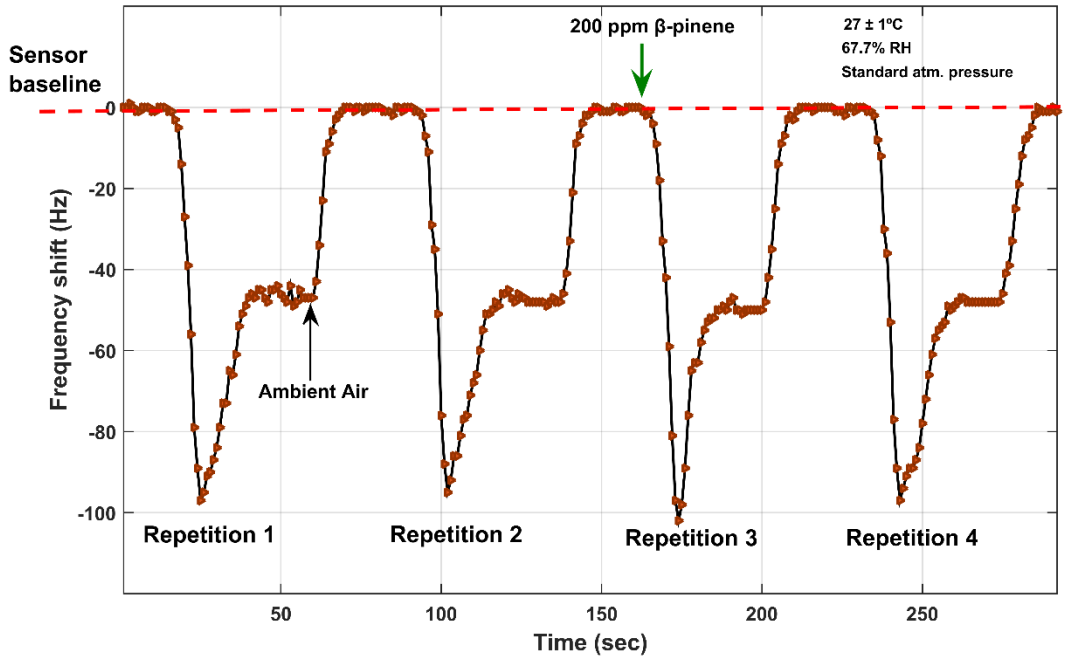

Fig. 4.20. Repeatability profile of OLV-QCM sensor towards 200 ppm of β-pinene at (27 ± 1) ºC, 67.7% RH, and standard atmospheric pressure.

Table 4.6. Repeatability and Reproducibility measurement with the 95% confidence interval.

Concentration (ppm)	Repeatability		Reproducibility	
	R_P (%)	CI	R_D (%)	CI
10	77.47	± 0.94	73.80	± 0.97
25	84.81	± 1.26	79.14	± 1.22
50	91.67	± 1.26	79.82	± 1.94
100	93.25	± 1.47	90.82	± 1.40
200	97.39	± 1.23	94.74	± 1.71
300	98.03	± 1.67	97.36	± 1.57
400	98.88	± 1.23	98.61	± 1.07

500	99.02	± 1.46	98.67	± 1.43
600	99.11	± 1.69	98.97	± 1.38
700	99.17	± 1.78	98.87	± 1.73
800	99.20	± 1.87	99.20	± 1.33
900	99.37	± 1.67	99.15	± 1.57
1000	99.44	± 1.67	99.24	± 1.63

CI-confidence interval.

The reproducibility of the sensor preparation unit was also studied. Eight OLV-QCM sensors were fabricated using the same unit and placed inside the 300 mL sensor chamber. The sensor array was then exposed to 10-1000 ppm of β-pinene aroma, keeping the same experimental conditions. The developed sensors OLV-QCM-1to OLV-QCM-8 exhibited an average sensitivity value of 0.3128 ± 0.0017 Hz/ppm in the 0.3105 – 0.3154 Hz/ppm range. The average LOD and LOQ for the eight reproducible OLV-QCM sensors were observed as 5.54 ± 0.031 Hz and 18.45 ± 0.104 Hz, respectively. The detailed sensor parameters of each reproduced sensor are presented in Table 4.7. *RSD* was obtained through all the sensor frequency outputs corresponding to each concentration of VOC to calculate R_D using equation (4.11). The average reproducibility was found as 93% for the complete range of input volatiles. The maximum reproducibility value was recorded at 99.24% for 1000 ppm, whereas the lowest value of 73.80% was calculated at 10 ppm. The reproducibility values follow the same trend as repeatability and gradually increase with the increased concentration of β-pinene aroma. The 95% confidence interval values of different concentrations of VOC indicate that the response values have very few variations, and the sensor data are precise for repeated use. Hence, the existing system can fabricate OLV-QCM sensors with high reproducibility.

Table 4.7. Comparison of Sensitivity, LOD, and LOQ of OLV-QCM eight sensors

OLV-QCM Sensors	**Sensitivity (Hz/ppm)**	**LOD (ppm)**	**LOQ (ppm)**
QCM-1	0.311	5.578	18.594
QCM-2	0.314	5.513	18.375
QCM-3	0.313	5.543	18.475
QCM-4	0.311	5.575	18.582
QCM-5	0.314	5.509	18.364
QCM-6	0.313	5.534	18.446
QCM-7	0.312	5.551	18.505
QCM-8	0.315	5.492	18.305

4.3.11. Sensing properties of OLV-QCM sensor with cardamom samples

The OLV-QCM sensor was tested with three varieties of small cardamom, namely SC-1, SC-2, SC-3, and three large cardamom varieties, LC-1, LC-2, and LC-3. Three sniffs of the sensor were taken for each cardamom sample. Fig. 4.21(a) shows the average OLV-QCM sensor responses for each of the samples. The OLV-QCM sensor responses were scatter plotted for evaluated GC-MS peak area of β-pinene with obtained $R^2 = 0.98$ as shown in Fig. 4.21(b).

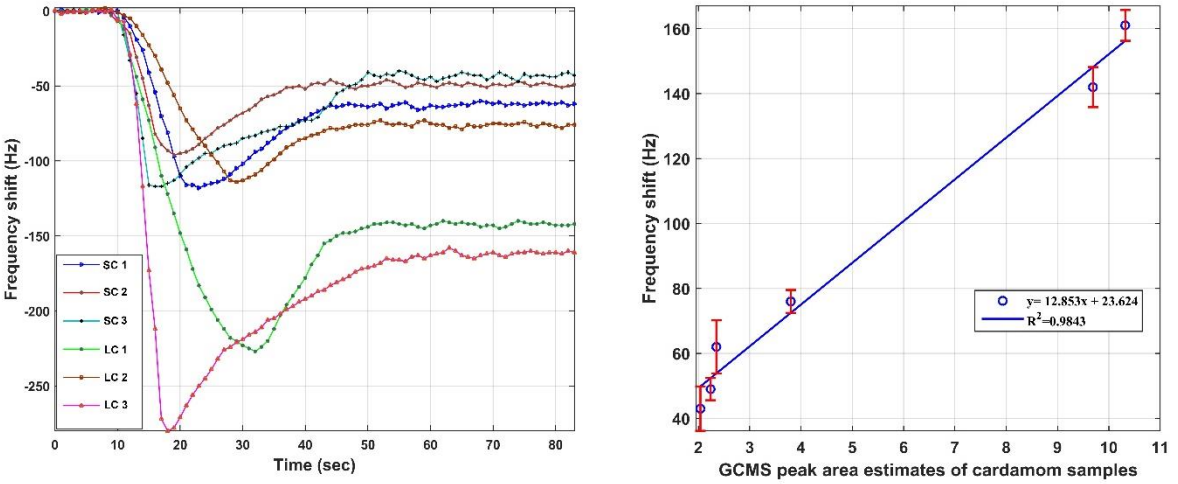

Fig. 4.21. (a) OLV-QCM sensor frequency response towards different cardamom samples, (b) Scatter plot for GC-MS estimates, and OLV-QCM response.

It can be observed that the volatile that was injected produces distinct frequency profiles maintaining different deviations from the initial responses. Moreover, the frequency graphs show quick sensing characteristics of the incoming aroma at 12 secs and reach the saturation state at around 50 secs, proving the uniform and swift sensing behaviour of the OLV-QCM sensor.

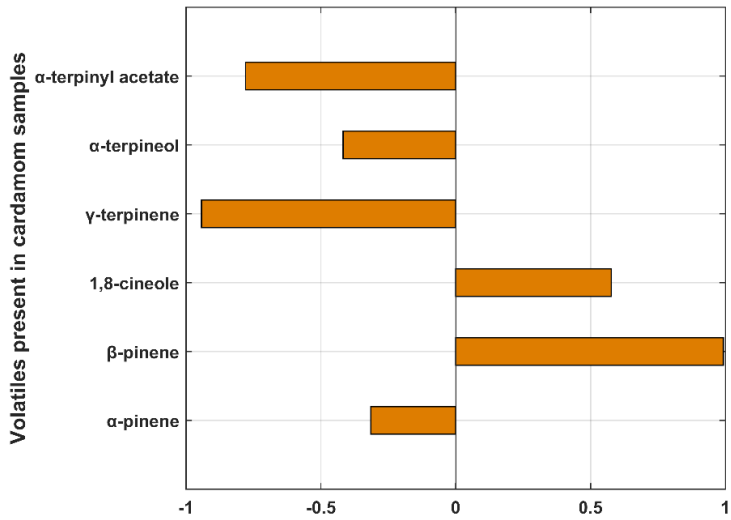

Fig. 4.22. Bar diagram illustrating the correlation between the sensor output and relative abundance of β-pinene in selected small and large cardamom samples

Table 4.8 shows the relative quantity of β-pinene in six cardamom samples and their corresponding QCM sensor output. The correlation factor for β-pinene was 0.992, the highest among the other

volatiles in cardamom (Fig. 4.22). **The high accuracy in measurement obtained from the scatter plot demonstrates the OLV-QCM sensor efficiency to be highly sensitive to the β-pinene aroma in cardamom.**

Table 4.8. GC-MS and OLV-QCM sensor response for β- pinene.

Sample	GC-MS estimates of β-pinene (%)	OLV- QCM frequency shift (Hz)	Correlation with QCM response
SC-1	2.35	62	-0.315
SC-2	2.24	49	0.992
SC-3	2.04	43	0.577
LC-1	9.69	142	-0.942
LC-2	3.8	76	-0.417
LC-3	10.32	161	-0.779

4.4. Conclusion

The development of an olive oil-coated QCM sensor for the detection of β-pinene in cardamom has been discussed in this present work. The developed sensor shows high sensitivity towards β-pinene with a sensitivity of 0.3105 Hz/ ppm with R^2 = 0.9979. Furthermore, the sensor is adequately selective towards β-pinene in the presence of other dominant VOCs present in the cardamoms. The average reproducibility and repeatability of the OLV-QCM sensor have been calculated to be 93% and 95.14% within a 95% confidence interval. Additionally, the fabricated sensor exhibits prompt recovery, long-term stability, and minimal humidity effect at 67.7% RH. The developed sensor has been tested with six cardamom samples both large and small), and its responses show effective results with a correlation factor of 0.992 with the β-pinene estimates from GC-MS analysis. The proper identification and quantification of β-pinene can pave a new path for quality analysis of cardamom samples based on aroma-sensitive array-based E-nose. Unlike hazardous chemicals, the natural product olive oil is used in this study to develop a sensor suitable for the food processing industry. A simple sensor design convention has been implemented that is easy to develop and cost-effective, which may benefit the practical deployment of the sensor in the agro and food industry.

References

[1] M. Balakrishnan, G.S.V. Raghavan, V.V. Sreenarayanan, R. Viswanathan, Batch Drying Kinetics of Cardamom in a Two-Dimensional Spouted Bed, Drying Technology. 29 (2011) 1283–1290. https://doi.org/10.1080/07373937.2011.591714.

[2] J. Olivero-Verbel, T. González-Cervera, J. Güette-Fernandez, B. Jaramillo-Colorado, E. Stashenko, Chemical composition and antioxidant activity of essential oils isolated from Colombian plants., Revista Brasileira de Farmacognosia. 20 (2010) 568–574.

[3] G.O. Adegoke, L. Jagan Mohan Rao, N.B. Shankaracharya, A comparison of the essential oils of Aframomum daniellii (Hook. F.) K. Schum. and Amomum subulatum Roxb., Flavour and Fragrance Journal. 13 (1998) 349–352. https://doi.org/10.1002/(SICI)1099-1026(1998090)13:5<349::AID-FFJ758>3.0.CO;2-O.

[4] S. Eyob, M. Appelgren, J. Rohloff, A. Tsegaye, G. Messele, Traditional medicinal uses and essential oil composition of leaves and rhizomes of korarima (Aframomum corrorima (Braun) P.C.M. Jansen) from southern Ethiopia, South African Journal of Botany. 74 (2008) 181–185. https://doi.org/10.1016/j.sajb.2007.10.007.

[5] D. Sadeh, N. Nitzan, D. Chaimovitsh, A. Shachter, M. Ghanim, N. Dudai, Interactive effects of genotype, seasonality and extraction method on chemical compositions and yield of essential oil from rosemary (Rosmarinus officinalis L.), Industrial Crops and Products. 138 (2019) 111419. https://doi.org/10.1016/j.indcrop.2019.05.068.

[6] R. Tisserand, R. Young, Essential oil safety: a guide for health care professionals, 2014. http://public.ebookcentral.proquest.com/choice/publicfullrecord.aspx?p=1746613 (accessed April 2, 2022).

[7] I.P.S. Kapoor, B. Singh, G. Singh, C.S. De Heluani, M.P. De Lampasona, C.A.N. Catalan, Chemical Composition and Antioxidant Activity of Essential Oil and Oleoresins of Nutmeg (Myristica fragrans Houtt.) Fruits, International Journal of Food Properties. 16 (2013) 1059–1070. https://doi.org/10.1080/10942912.2011.576357.

[8] Y. Xia, R.C. Larock, Vegetable oil-based polymeric materials: synthesis, properties, and applications, Green Chem. 12 (2010) 1893–1909. https://doi.org/10.1039/C0GC00264J.

[9] Karumbaiah.N. Chappanda, O. Shekhah, O. Yassine, S.P. Patole, M. Eddaoudi, K.N. Salama, The quest for highly sensitive QCM humidity sensors: The coating of CNT/MOF composite sensing films as case study, Sensors and Actuators B: Chemical. 257 (2018) 609–619. https://doi.org/10.1016/j.snb.2017.10.189.

[10] Department of Oil & Paint Technology, Harcourt Butler Technological Institute (HBTI) Kanpur-208002 (UP), India, F. Habib, M. Bajpai, Department of Oil & Paint Technology, Harcourt Butler Technological Institute (HBTI) Kanpur-208002 (UP), India, Synthesis and Characterization of Acrylated Epoxidized Soybean Oil for UV-Cured Coatings, ChChT. 5 (2011) 317–326. https://doi.org/10.23939/chcht05.03.317.

[11] R. Das, S. Pradhan, S. Biswas, P. Sharma, A. Ghosh, R. Bandyopadhyay, P. Pramanik, Aliphatic amines vapours detection by quartz crystal microbalance sensor, Sensors and Actuators B: Chemical. 198 (2014) 94–101. https://doi.org/10.1016/j.snb.2014.03.020.

[12] S.B. Ali, B. Ghatak, N. Debabhuti, P. Sharma, A. Ghosh, B. Tudu, N. Bhattacharya, R. Bandyopadhyay, Detection of β-caryophyllene in mango using a quartz crystal microbalance sensor, Sensors and Actuators B: Chemical. 255 (2018) 3064–3073. https://doi.org/10.1016/j.snb.2017.09.131.

[13] B. Chen, C. Liu, L. Shang, H. Guo, J. Qin, L. Ge, C.J. Jing, C. Feng, K. Hayashi, Electric-field enhancement of molecularly imprinted sol–gel-coated Au nano-urchin sensors for vapor detection of plant biomarkers, J. Mater. Chem. C. 8 (2019) 262–269. https://doi.org/10.1039/C9TC05522C.

[14] N. Debabhuti, S. Neogi, S. Mukherjee, A. Dhar, P. Sharma, R.L. Vekariya, M.P. Sarkar, B. Tudu, N. Bhattacharyya, R. Bandyopadhyay, Mohd. Muddassir, Development of QCM sensor to detect α-terpinyl acetate in cardamom, Sensors and Actuators A: Physical. 319 (2021) 112521. https://doi.org/10.1016/j.sna.2020.112521.

[15] D. Zhang, Y. Sun, Y. Zhang, Fabrication and characterisation of layer-by-layer nano self-assembled ZnO nanorods/carbon nanotube film sensor for ethanol gas sensing application at room temperature, J Mater Sci: Mater Electron. 26 (2015) 7445–7451. https://doi.org/10.1007/s10854-015-3378-4.

[16] D.M. Ruthven, Adsorption (Chemical Engineering), in: R.A. Meyers (Ed.), Encyclopedia of Physical Science and Technology (Third Edition), Academic Press, New York, 2003: pp. 251–271. https://doi.org/10.1016/B0-12-227410-5/00013-2.

[17] FoodData Central, (n.d.). https://fdc.nal.usda.gov/fdc-app.html#/food-details/171413/nutrients (accessed April 2, 2022).

[18] W. Kemp, Energy and the Electromagnetic Spectrum, in: W. Kemp (Ed.), Organic Spectroscopy, Macmillan Education UK, London, 1991: pp. 1–17. https://doi.org/10.1007/978-1-349-15203-2_1.

[19] H. Wijnja, J.J. Pignatello, K. Malekani, Formation of pi-pi complexes between phenanthrene and model pi-acceptor humic subunits, J Environ Qual. 33 (2004) 265–275. https://doi.org/10.2134/jeq2004.2650.

[20] D. Boskou, Olive Oil: Chemistry and Technology, Second Edition, 2nd ed., AOCS Publishing, New York, 2006. https://doi.org/10.4324/9781003040217.

[21] A.H. Lichtenstein, Fats and Oils, in: Encyclopedia of Human Nutrition, Elsevier, 2013: pp. 201–208. https://doi.org/10.1016/B978-0-12-375083-9.00097-0.

[22] M. Poiana, G. Mousdis, E. Alexa, D. Moigradean, M. Negrea, C. Mateescu, Application of FTIR spectroscopy to assess the olive oil adulteration, Journal of Agroalimentary Processes and Technologies. 18 (2012) 277–282.

[23] A. Rohman, Y.B.C. Man, Fourier transform infrared (FTIR) spectroscopy for analysis of extra virgin olive oil adulterated with palm oil, Food Research International. 43 (2010) 886–892. https://doi.org/10.1016/j.foodres.2009.12.006.

[24] Y. Li, Y. Liu, J. Liu, J. Liu, H. Tang, C. Cao, D. Zhao, Y. Ding, Molecularly imprinted polymer decorated nanoporous gold for highly selective and sensitive electrochemical sensors, Sci Rep. 5 (2015) 7699. https://doi.org/10.1038/srep07699.

[25] B. Mumyakmaz, A. Özmen, M.A. Ebeoğlu, C. Taşaltın, İ. Gürol, A study on the development of a compensation method for humidity effect in QCM sensor responses, Sensors and Actuators B: Chemical. 147 (2010) 277–282. https://doi.org/10.1016/j.snb.2010.03.019.

Chapter 5

Development of rice bran oil modified QCM sensor to detect α-pinene in Indian cardamom

5.1. Introduction

α-pinene is a bicyclic monoterpene hydrocarbon and is found in the headspace of several spices and fruits like rosemary, clove, black pepper, mangoes [1–4], and also different types of cardamom. It is generally hydrophobic and insoluble in water and less soluble in alcohol. α-pinene has a natural fresh pine-like smell; that's why it is used as an odour and fragrance agent. α-pinene has a therapeutical property against upper respiratory tract infection [5]. As discussed in Chapter 2, it was found that 1,8-cineole, α-pinene, and β-pinene are the three major volatiles responsible for dissimilarities in the HSV profile between the cardamom varieties.

Detection of α-pinene was done by different sensors and sensing materials developed by other research groups like solid-state sensors [6], chemical sensors [7], molecularly imprinted polymer-based sensors [8], and localised surface plasmon resonance sensors [9]. The biological, polymers, and nanoparticles were used for coating, which has some inappropriate issues. It cannot show good repeatability, reproducibility, stability, and reusability per the benchmark. Fabrication of sensors is also very complex using those materials. Rashmita et al. reported a linseed oil-coated QCM sensor for VOC detection [10], and the presence of β-ocimene in mango was also established by a mustard oil-coated QCM sensor [11]. This coating material is readily available, inexpensive, and easy to coat. From the previous chapter, it was concluded that the olive oil-coated QCM sensor works well. Therefore, in this chapter, a rice bran, oil-coated QCM sensor for the detection of α-pinene was fabricated.

5.2. Experimental

5.2.1. QCM sensor fabrication

The fabrication steps of the sensor are identical, as discussed in Chapter 4, section 4.2.2. Five solutions of different vegetable oils, namely rice bran (RB), soybean (SOY), groundnut (GN), castor (CAS), and coconut (COC), were prepared for this study with 0.2% (w/v) concentration by dissolving in n-hexane. All the authentic volatile compounds and experimental materials were purchased as discussed in Chapter 4, Section 4.2.1. Limonene was supplied from Sigma-Aldrich, Germany. The detailed experimental condition was maintained as discussed in Chapter 4, section 4.2.3. The sensor was rinsed with ethanol and deionised water for 15 minutes, followed by drying in the oven at 60 ^{o}C for 30 minutes. The sensors were fabricated using an ultrasonic nebuliser [12].

Moreover, the loading of the sensors was maintained at 5500 Hz in real-time using the developed gas sensing unit addressed in Chapter 3. The developed sensors (RB-QCM, SOY-QCM, GN-QCM, CAS-QCM, COC-QCM) were kept in a vacuum desiccator for 24h for proper stabilisation before the experiment.

The detailed sensor fabrication parameters of the five sensors have been given in Table 5.1. It was noticed that the fundamental frequencies of the sensors were around 10 MHz before coating. The frequency changes observed due to the mass deposited on the silver electrodes have been evaluated using the Sauerbrey equation [13].

Table 5.1. Detailed sensor fabrication parameters

QCM sensor	**Initial frequency (Hz)**	**Frequency shift (Hz)**	**Mass of coating surface (ng)**
RB-QCM	9992912	5514	11837
SOY-QCM	9992890	5500	11807
GN-QCM	9992560	5537	11888
CAS-QCM	9993277	5619	12062
COC-QCM	9992895	5639	12106

5.2.2. Measurement setup and sensor measurements

The details of the measurement setup have been discussed in Chapter 3. Furthermore, an identical sensor measurement protocol has been followed, as mentioned in Chapter 4, section 4.2.3.

5.2.3. Measurement of electrical impedance

The stability and accuracy of the QCM sensor response depend on the measurement of two critical factors, namely the dissipation factor (D-factor) and resonant frequency of the crystal [14–16]. The D-factor can be calculated as the inverse of the quality factor (Q-factor) of the sensor responses ($D = Q^{-1}$). The Q-factor of the sensor estimates the rigidity of the adsorbing film on the sensor surface. The study of Q-factor in this study has been carried out using a precision impedance analyser (E4990A, Keysight) and adaptor (16047E, Keysight) connected to the sensor chamber of the developed system. The conductance and susceptance spectrum of the bare QCM sensor using this measurement setup is shown in Fig 5.1.

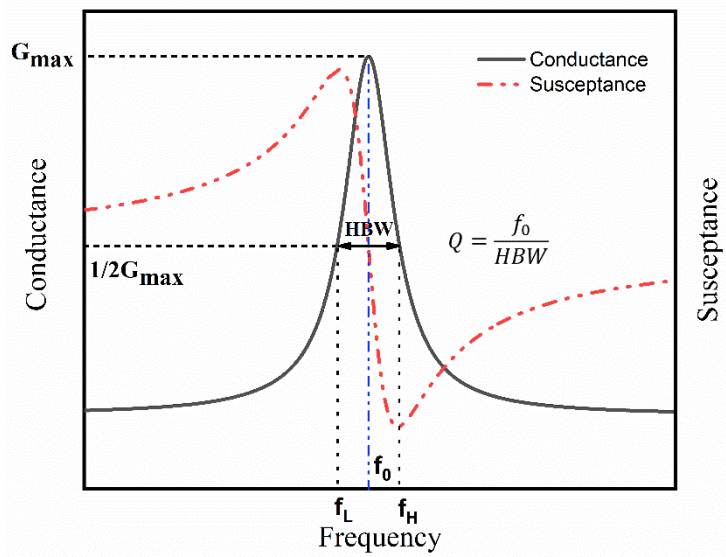

Fig. 5.1. The conductance and susceptance spectrum of 10 MHz bare QCM sensor.

The maximum conductance (G_{max}) was obtained at the resonant frequency (f_0) of the QCM sensor. Finally, the Q-factor can be calculated as the ratio of the resonant frequency (f_0) to the half bandwidth (HBW) of the conductance spectrum [17]. Proper determination of the Q-factor is an essential parameter for the estimation of the stability, energy loss, and frequency noise in micro/ nano-electromechanical systems (MEMS/NEMS) [18]. Moreover, the equivalent circuit

parameters of the bare crystal were obtained by fitting the admittance spectrum with Butterworth-Van Dyke (BVD) mode [19], as shown in Table 5.2.

Table 5.2. Resonant parameters of the bare QCM

Sensor	f (Hz)	R (ohm)	L (mH)	C (fF)	C0 (pF)	Q
Bare QCM	9993332	12	8.76	28.92	11.2	45081

5.2.4. Volatile organic compounds preparation

The VOCs like 1,8-cineole, α-terpinyl acetate, limonene, α-pinene, β-pinene, α-terpineol, and γ-terpinene were prepared inside 10 L desiccators for the experimental study. The VOCs attained saturation and the respective concentration were determined from their mass change following the protocol as mentioned by Zhang et.al. [20]. The saturated concentration of the volatiles was drawn using a 60 mL glass syringe attached to an automatic syringe pump for uniform injection into the sensor chamber. Different concentrations of the VOCs (10-1000 ppm) were generated for this study using the procedure discussed in Chapter 4, Section 4.2.4.

5.2.5. Cardamom sample preparation for the study of RB-QCM sensor

Nine cardamom samples (three small and six large) were selected and labelled as SC_1, SC_2, SC_3, LC_1, LC_2, LC_3, LC_4, LC_5, and LC_6 was collected to estimate the VOCs for the study of the developed sensors. The sample preparation steps were followed, as mentioned in Chapter 4, section 4.2.5. The responses were recorded and correlated with GC-MS results.

5.2.6. Extraction and determination of volatile flavour compound (VFC) of cardamom samples using SPME and GC-MS technique

The details of the extraction and determination of VOCs from cardamom have been discussed in Chapter 2, sections 2.3.2 and 2.3.3. The major VOCs found in the aroma signatures of the nine varieties of both large and small cardamom samples obtained from GC-MS analysis are listed in Table 5.3. Seven major VOCs were identified in the chromatograms of cardamom samples. Each cardamom sample includes varying amounts of α-pinene. It was found to be more prevalent in

small cardamom samples than in large cardamom samples. **As a result, α-pinene was chosen as a marker compound for aroma quality assessment, and a sensor was fabricated.**

Table 5.3. GC-MS results of the test cardamom samples

VOC	**The % peak area of samples**								
	SC_1	**SC_2**	**SC_3**	**LC_1**	**LC_2**	**LC_3**	**LC_4**	**LC_5**	**LC_6**
α-pinene	**12.54 ± 0.30**	**11.92 ± 0.4**	**11.10 ± 0.7**	**9.82 ± 0.23**	**1.98 ± 0.08**	**7.27 ± 0.12**	**7.63 ± 0.2**	**7.47 ± 0.3**	**7.56 ± 0.3**
β-pinene	2.07 ± 0.86	2.05 ± 0.11	1.89 ± 0.07	9.07 ± 0.3	3.60 ± 0.28	9.71 ± 0.09	7.94 ± 0.12	8.25 ± 0.18	6.48 ± 0.17
Limonene	8.95 ± 0.1	8.07 ± 0.11	7.51 ± 0.25	6.40 ± 0.11	5.4 ± 0.21	6.17 ± 0.58	6.37 ± 0.11	4.53 ± 0.13	5.7 ± 0.08
1,8-cineole	62.66 ± 1.23	61.5 ± 3.61	50.36 ± 1.18	74.26 ± 0.39	87.34 ± 0.12	76.28 ± 0.7	77.36 ± 0.37	79.59 ± 0.26	79.42 ± 0.39
γ-terpinene	0.88 ± 0.03	1.11 ± 0.02	1.39 ± 0.04	0.28 ± 0.03	0.84 ± 0.08	0.37 ± 0.08	0.56 ± 0.02	0.11 ± 0.15	0.7 ± 0.01
α-terpineol	0.14 ± 0.005	0.32 ± 0.14	0.47 ± 0.07	0.16 ± 0.04	0.66 ± 0.43	0.19 ± 0.08	0.12 ± 0.03	0.11 ± 0.03	0.14 ± 0.01
α-terpinyl acetate	12.75 ± 0.91	15 ± 3.59	27.25 ± 1.86	0	0	0	0	0	0

5.3. Results and discussion

5.3.1. Selection of coating oil for sensor of α-pinene

5.3.1.1. Study of the sensing properties of RB-QCM sensor

In this study, the performance of the five-vegetable oil-coated sensors (RB-QCM, SOY-QCM, GN-QCM, CAS-QCM, COC-QCM) towards α-pinene was evaluated. Initially, the sensors were exposed to different concentrations (10-1000 ppm) of the saturated headspace of α-pinene. The sensitivity of the different sensors was based on the different oil coatings on the sensor layer and the mass of the incoming volatiles adsorbed on them. The sensitivity plots of the sensors were depicted in Fig. 5.2. It can be observed from the sensitivity calculation that RB-QCM showed maximum acceptance towards different concentrations of α-pinene. The chemical composition of the rice bran (RB) oil escalated the sensing behavior towards α-pinene in comparison to the other oils in the study which has been further investigated.

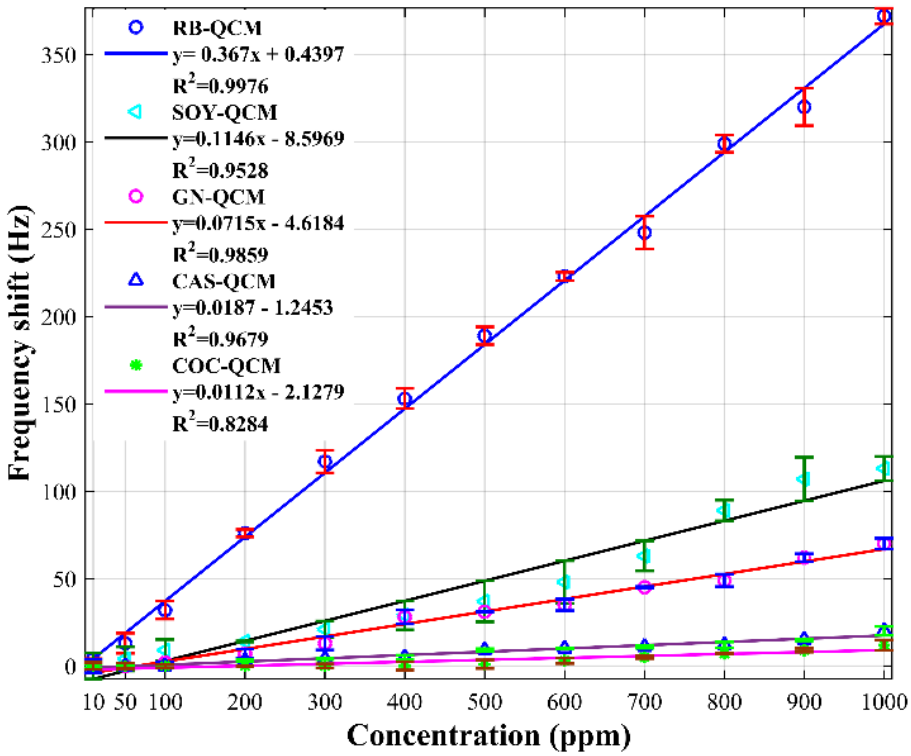

Fig. 5.2. The sensitivity of RB-QCM, SOY-QCM, GN-QCM, CAST-QCM, and COC-QCM sensor to α-pinene vapour at 10–1000 ppm concentration operated at (27 ± 1) °C, RH=67.70%, and standard atmospheric pressure.

For the selection of oil for sensor fabrication following oil was analysed to investigate the fatty acid content (Table 5.4). The primary fatty acids, which constitute at least 10% of the total fatty acid content of that specific oil, are taken into consideration for further study.

Table 5.4. Composition of vegetable oils

Fatty acids	Rice bran oil	Groundnut oil	Olive oil	Castor oil	Coconut oil
Lauric acid (C12:0)	Trace	Trace	Trace	Trace	47.7%
Myristic acid (C14:0)	Trace	Trace	Trace	Trace	19.9%
Oleic acid (C18:1)	41.4%	55.27%	66.08%	Trace	Trace
Ricinoleic acid (12-OH-C18:1)	Trace	Trace	Trace	95%	Trace
Linoleic acid (C18:2)	34.9%	24.27%	12.97%	Trace	Trace

**Trace = <10%*

Sensing volatile gaseous compounds by sensor coating material is accomplished by reversible physical adsorption mechanism, which ensures efficient sensing and indorses accurate recovery to baseline. Due to the hydrophobic nature of α-pinene tends to interact with the long alkyl chains in the rice bran oil [21]. Van der walls interaction between two molecules is considered the leading driving force behind the physisorption mechanism, and the strength of the interaction is proportional to the molecular surfaces present in two interacting candidates. The molecular surface area of each fatty acid and their binding energy with α-pinene was simulated using HyperChem8.0 software following Chapter 4, section 4.3.1, and tabulated in Table 5.5.

Table 5.5. The calculated surface area of fatty acid chain in different oil and its binding energy with α-pinene by HyperChem 8.0

Coating material	Surface area ($Å^2$)	FA- α-pinene binding energy (kcal/mol)
Linoleic acid	413.127	-8.568
Oleic acid	422.749	-0.503
Ricinoleic acid	422.141	-0.305

Myristic acid	345.671	-0.14
Lauric acid	300.54	-0.372

Oleic acid (422.749 Å^2), ricinoleic acid (422.141 Å^2) and linoleic acid (413.127 Å^2) are present in rice bran oil, groundnut oil, olive oil, and castor oil (in different proportions) have highest surface area than lauric acid (300.54 Å^2) and myristic acid (345.671 Å^2) present in coconut oil. The presence of a small-sized fatty acyl chain, as shown in Fig. 5.3(a-b), accounts for the low surface area of these fatty acids. This low surface area of lauric acid and myristic acid could be the possible reason behind the minor sensitivity of α-pinene towards coconut oil-coated sensors.

The remaining three fatty acids are naturally unsaturated and have more or less similar molecular surface areas. The principal component of castor oil, i.e., ricinoleic acid, though has a pleasing molecular surface area, the hydrophilic hydroxyl group present in the 12th carbon atom makes the molecule less hydrophobic, which lessens the possibility of α-pinene-ricinoleic acid interaction (Figure 5.3(c)).

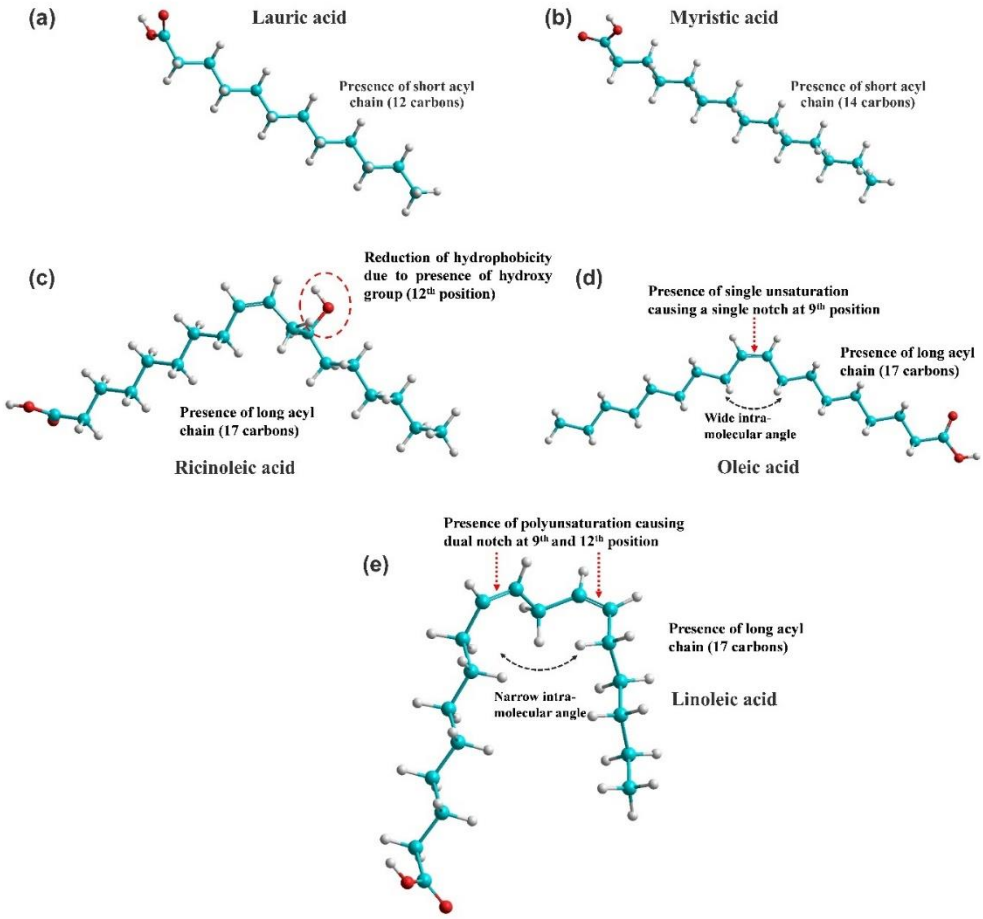

Fig. 5.3. The structural characteristics of (a) lauric acid, (b) myristic acid, (c) ricinoleic acid, (d) oleic acid, and (e) linoleic acid.

The last two fatty acids, i.e., oleic and linoleic acid, both have eighteen carbon-long acyl chains but are based on the degree of unsaturation, and they differ from each other as shown in Figure 5.3(d-e). Each unsaturation creates an angle of 30 degrees that eventually folds the fatty acyl chain to some extent [22]. Oleic acid has an unsaturation in its 9^{th} carbon atom, which creates a single hinge on the fatty acyl chain, but linoleic acid is a polyunsaturated fatty acid with two unsaturation in its 9^{th} and 12^{th} position. The presence of two consecutive unsaturation gives a "U" shaped orientation to linoleic acid, with two segments, i.e., C_1-C_9 and C_{13}-C_{18}, parallel to each other (4 to 4.5 angstrom apart). **This "U" shaped structural orientation causes aggregation of atoms and owing to this, α-pinene can interact with the atoms in both parallel segments. Fig. 5.3 depicts the 3D representations of the essential properties of the oil structures that impact the adsorption of α-pinene.**

Thus, the structural orientation of linoleic acid positively influences Van der Waals (vdW) interactions between linoleic acid and α-pinene, which is the probable reason behind the linoleic acid-rich rice bran oil's sensitivity towards α-pinene (Fig. 5.4).

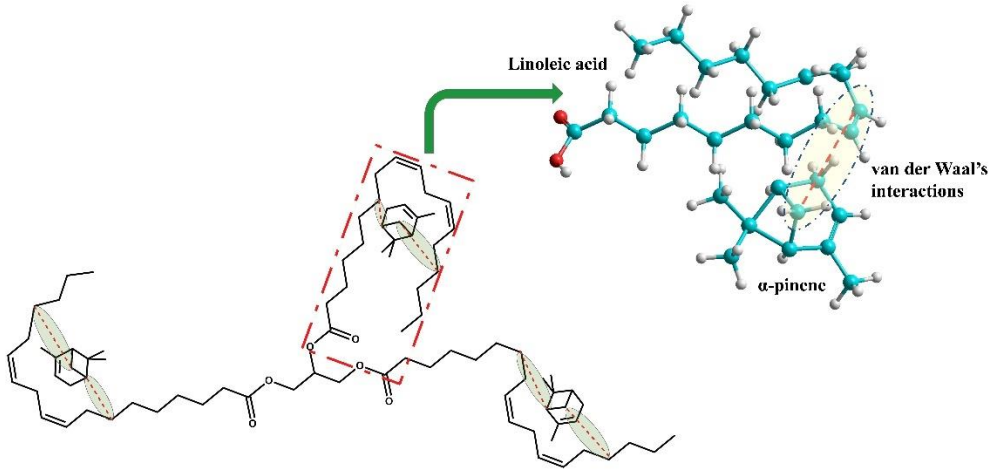

Fig. 5.4. Probable interaction of linoleic acid with α-pinene VOC.

To validate the hypothesis the linoleic acid is the principal component in oil that is involved in α-pinene sensing, we performed Pearson's correlation coefficient analysis (r). In the study, significant fatty acid concentrations in different oils were considered as an independent variable, and α-pinene sensing frequency was considered as the dependent variable for each concentration. The correlation was performed for each concentration (10-1000 ppm) of α-pinene, and the resultant model fitted with our hypothesis. It was observed that α-pinene sensitivity was increased with increasing linoleic acid concentration in different oils with r = 0.79-0.94. Contrariwise, similar results were not observed in the case of other fatty acids present, as shown in Fig. 5.5.

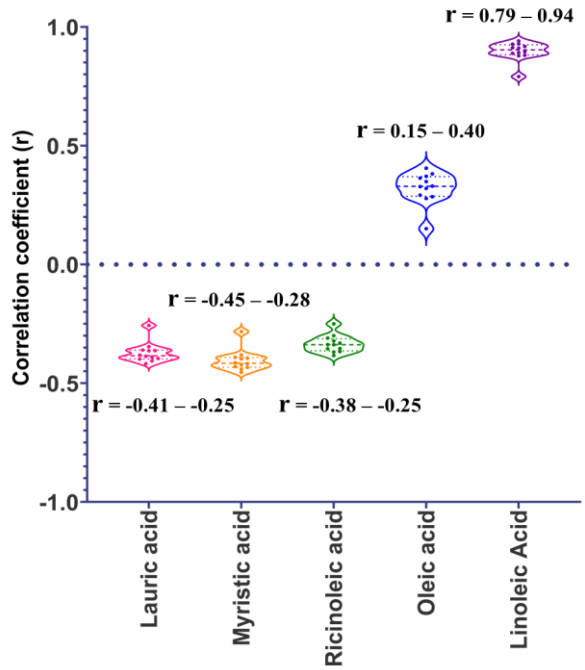

Fig. 5.5. Pearson's correlation coefficient analysis of major fatty acids and α-pinene sensing response.

Fig. 5.6(a) demonstrates the RB-QCM response curve upon injection of 1000 ppm of α-pinene VOC into the sensor chamber. Before the introduction of the VOC, the sensor frequency remained consistent and constant for 15 seconds. Upon injection, the sensor frequency decreased rapidly, reaching 433 Hz within 9 s. After that, the sensor frequency increased slowly and finally attained a saturation state at 372 Hz. During purging of the sensor with ambient air (indicated by an arrow in Fig. 5.6(b)) the sensor frequency progressively climbed till it met the sensor baseline. Thus, the sensor profile showed good reversibility with negligible drift. The response (t_{res}) and the recovery (t_{recov}) time of the sensor were calculated as the time taken to reach 90% of the initial frequency shift during sampling and purging of the VOC, respectively [23]. The t_{res} and t_{recov} of the RB-QCM sensor towards 1000 ppm of α-pinene were evaluated as 6 and 11 s, respectively.

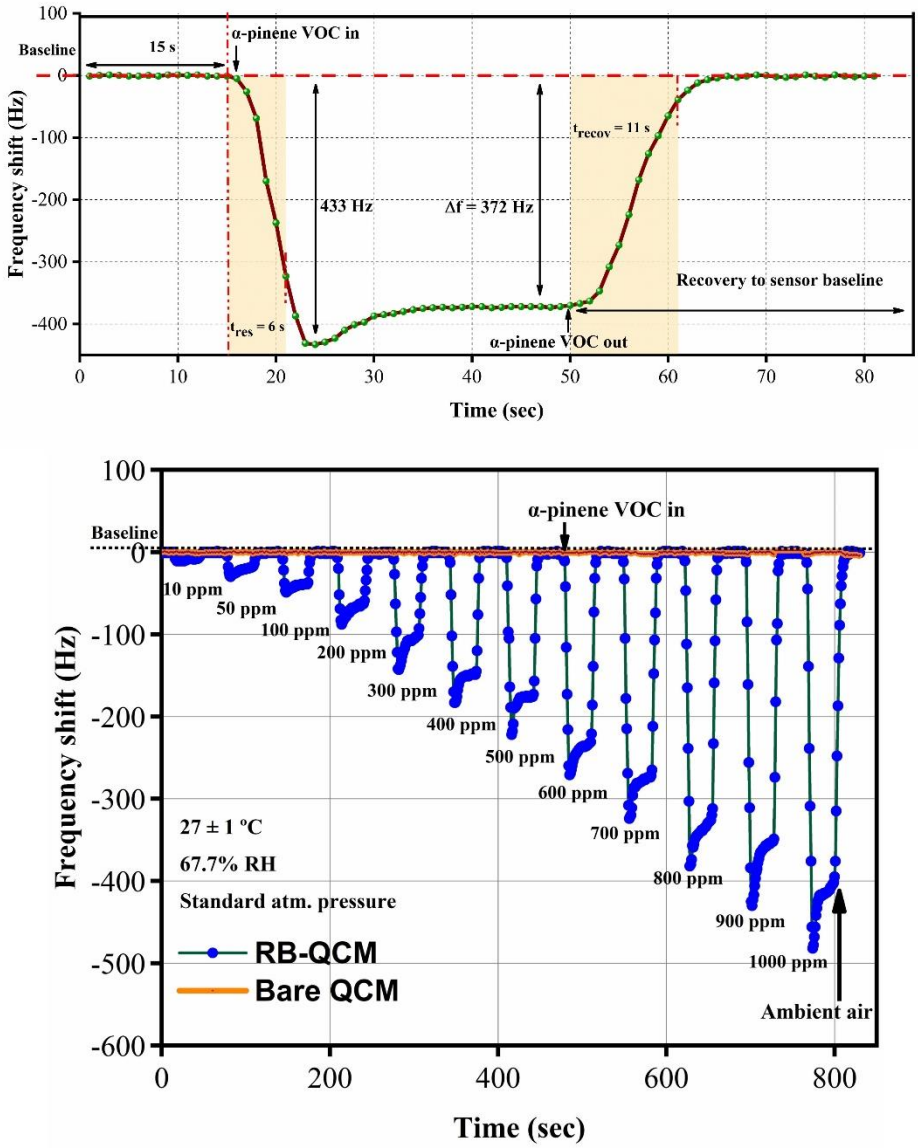

Fig. 5.6. Complete RB-QCM sensor response profile (a) for 1000 ppm of α-pinene (b) at different concentrations of α-pinene VOC ranging between 10 -1000 ppm at (27 ± 1) ºC, 67.7% RH and standard atmospheric pressure.

The characteristic responses for the RB-QCM sensor compared to the bare QCM sensor for corresponding α-pinene VOC concentration for 10-1000 ppm have been displayed in Fig. 5.6(b). It was visible that the bare QCM showed no frequency changes due to the unavailability of the sensing layer. However, in the case of the RB-QCM sensor, the response curves showed identical properties, with increasing frequency shift for increasing input volatile concentrations following Sauerbrey's equation [24]. Moreover, it can be noticed that the time for attaining the saturation state varied for different concentrations of α-pinene. All the sensor responses attained the initial baseline during the purging process without showing any drift. The curve fitting function of the

frequency shifts at saturation state for a varied concentration of α-pinene is calculated as $\Delta f = 0.367x + 0.4397$, where Δf was the frequency response at saturation state (Hz), x was the α-pinene concentration (ppm). The sensitivity of the RB-QCM sensor was calculated as 0.367 Hz/ppm, along with a correlation coefficient, $R^2 = 0.9976$. The standard error estimate (σ_{est}) of the sensor was evaluated as 6.47 Hz, which estimates the average value of the error generated between the exact output and approximated output derived from the characteristics equation of the sensor [12]. The limit of detection (LOD) and limit of quantification (LOQ) of the sensor was estimated as 4.71 Hz and 15.73 Hz, respectively [12].

5.3.2. Optimisation of the RB-QCM sensor loading

The optimal loading of the fabricated RB-QCM sensor was determined using electrical impedance and respective frequency shifts towards α-pinene VOC. Five RB-QCM sensors (RB-QCM_3500, RB-QCM_4500, RB-QCM_5500, RB-QCM_6500, RB-QCM_7500) were fabricated with rice bran oil having loadings ranging from 3500-7500 Hz, respectively.

Fig. 5.7(a) shows the conductance spectra of the developed RB-QCM sensors with different sensor loading. It is evident that with increasing loading, the sensor conductance peak gradually left-shifted due to a decrease in sensor resonant frequency. Moreover, a reduction of conductance spectra can be observed as the loading increases from 3500 Hz to 7500 Hz. The Q-factor parameters of the sensors were calculated using an automated analysis function of the impedance analyser and listed in Table 5.6. It is seen that the obtained Q factors decreased along with the broadening of conductance spectrum bandwidth with higher loading of the coating materials.

Table 5.6 Estimation of Q-factor of RB-QCM sensor based on loading

RB-QCM	**Sensor loading (Hz)**				
	3500	**4500**	**5500**	**6500**	**7500**
Q factor	15676	15587	9961	7218	5725

The five sensors were exposed to 200 ppm α-pinene VOC, and the frequency shifts were measured accordingly. The frequency loading of the sensors and their respective responses were normalised

(0,1) and were plotted in Fig. 5.7(b). Initially, the sensor responses were positively impacted by increasing loading. However, after a particular frequency (5500 Hz), the sensor responses decline and finally reach saturation at 7500 Hz. While sensor responses improved as loading increased, the drop in Q-factor at higher loading likely results in sensor response instability [25]. Based on these experimental results, the appropriate loading frequency for this research has been set at 5500 Hz.

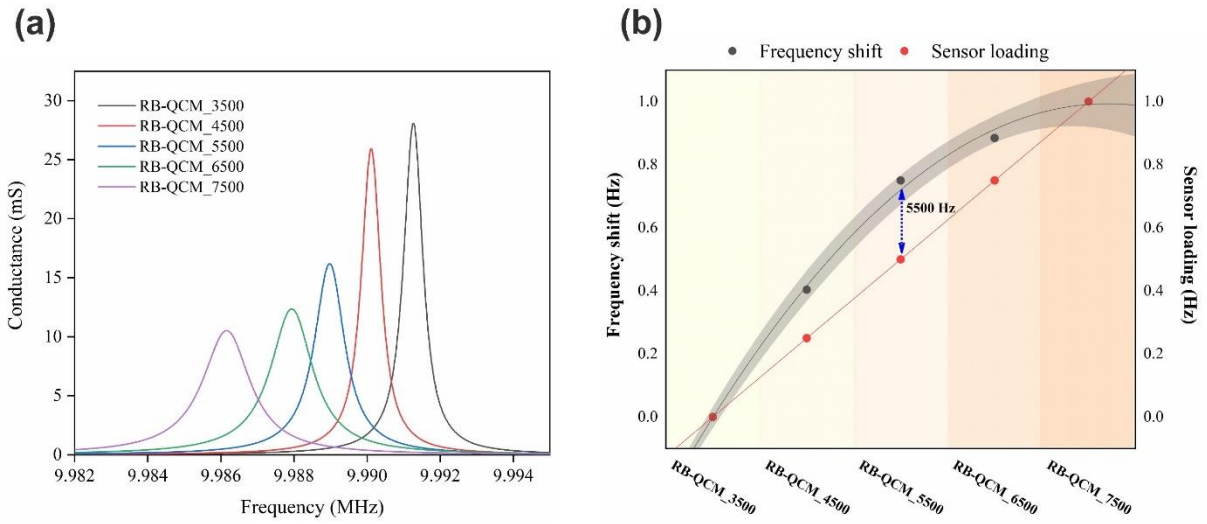

Fig. 5.7. (a) Conductance spectra; (b) Normalised (0,1) frequency loading and their respective sensor response for 200 ppm α-pinene with different sensor loadings (3500-7500 Hz).

5.3.3. Study of the binding interaction of RB-QCM sensor with α-pinene using UV-Visible spectroscopy

In the present study, the weak reversible molecular interaction between RB oil and α-pinene has been authenticated with the help of UV-Visible spectroscopy (Shimadzu double beam spectrophotometer, serial no. A116351) in five different steps. To perform the experiments, 0.1% (v/v), 0.2% (v/v), 0.3% (v/v) and 0.4% (v/v) solutions of α-pinene and rice bran oil were prepared by dissolving the respective molecules in n-hexane. In the first experiment, the absorbance of different concentrations of RB oil was monitored in the UV range, and the results are given in Fig. 5.8(a), which shows a distinct absorbance pattern containing three peaks with the absorption maxima at 230-232 nm. In the next experiment, the absorbance pattern of different concentrations of α-pinene was investigated, and the resultant absorbance appeared as a single sharp peak with absorption maxima of 228-232 nm (Fig. 5.8(b)). In the subsequent step, absorbance of 0.4% RB

(v/v) mixed with 0.1% (v/v), 0.2% (v/v), 0.3% (v/v) and 0.4% (v/v) α-pinene in 1:1 ratio was recorded. In this experiment, the resulting spectrogram revealed a decreased absorbance of α-pinene, possibly due to the presence of RB in the medium (Fig. 5.8(c)). To validate the third observation, we conducted our fourth experiment, where we recorded the absorbance of 0.1% (v/v), 0.2% (v/v), 0.3% (v/v) and 0.4% (v/v) alpha pinene first, followed by the addition of 50 uL of 0.4% (v/v) RB in each α-pinene solution and the absorption spectra was rerecorded. Supplementation of α-pinene with the RB significantly reduced the absorption intensity of the sole α-pinene standard (Fig. 5.8(d)). In addition to the prementioned experiments, we further investigated the interaction between α-pinene and RB by monitoring the kinetic change of absorbance of α-pinene at 330 nm, solely and in the presence of RB, as shown in Fig. 5.8(e). It was found that in the presence of RB, the absorbance of α-pinene at 330 nm gradually decreases over a period of 5 mins, which was not observed, while the absorption kinetics of α-pinene was recorded solely.

The experimental outcome hints toward the interaction between RB (sensor coating material) and α-pinene (target molecule). In the second experiment, free α-pinene molecules in the solution caused the absorption of UV light at its maximum potential, but in the subsequent two experiments, the addition of RB in the medium caused the reduction of absorption strength, which is possibly due to the formation of RB-α-pinene complex and reduction of free α-pinene molecule in the solution. In the last experiment, the experimental outcome suggests that the interaction between two selected molecules increases over time and eventually saturates to a certain point resulting in the decreasing trend of absorbance. During the whole-time scale, the absorbance of the solution fluctuated following a decreasing trend, which imitates the establishment of a very weak interaction between two molecules. Therefore, this experimental study confirms the presence of a very weak non-covalent hydrophobic interaction between the target volatile α-pinene with the adsorbent rice bran oil on the RB-QCM sensor. However, it is not possible to settle down the nature of the interaction established between two molecules.

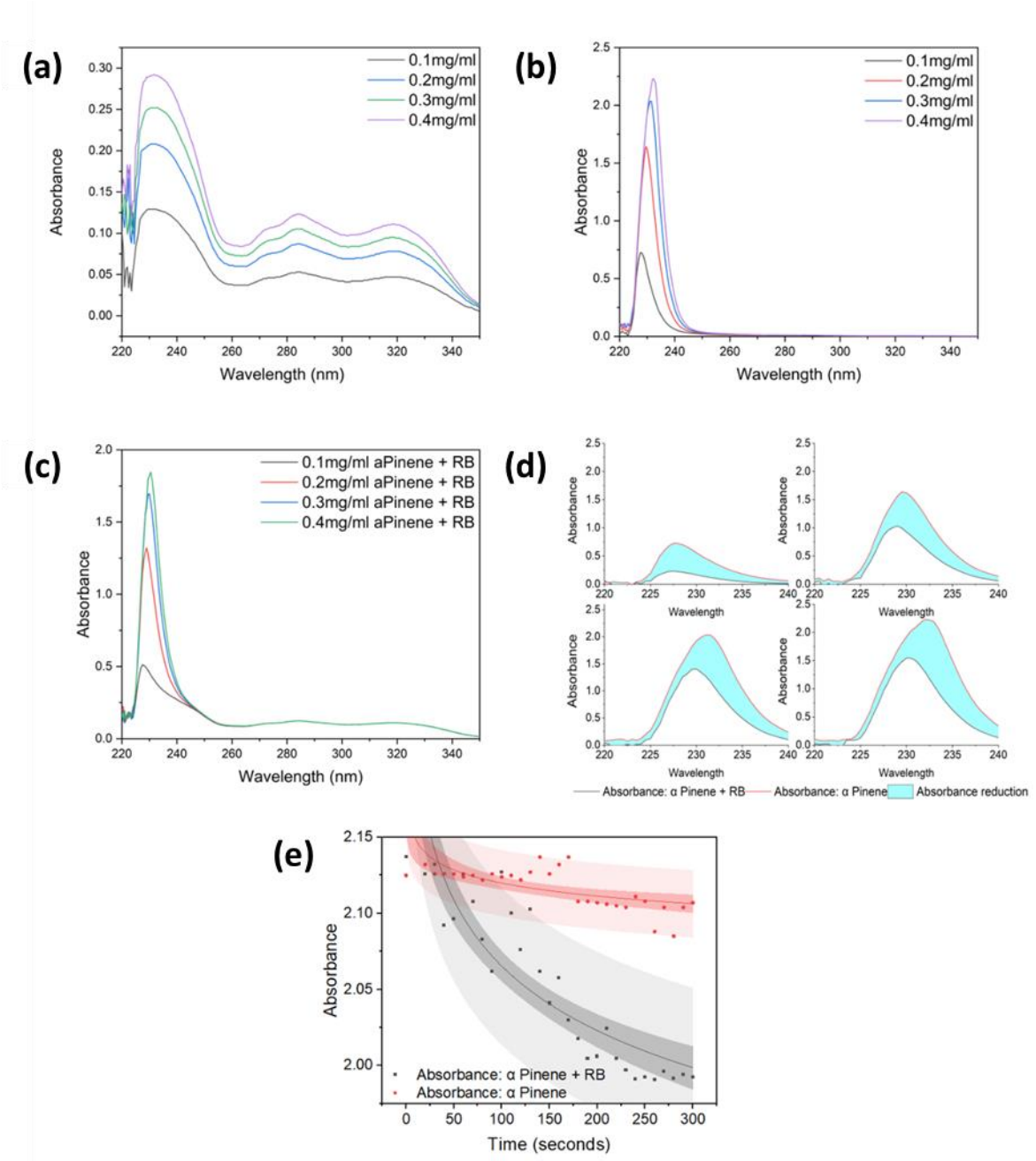

Fig. 5.8. The UV–vis absorption spectra for the interaction between rice bran oil and α-pinene. a) UV-Vis spectrum of rice bran oil in different concentrations (0.1-0.4 mg/mL); b)) UV-Vis spectrum of α-pinene in different concentrations(0.1-0.4 mg/mL); c-d) Suppression of absorbance maxima of 0.1-0.4 mg/mL α-pinene in the presence of rice bran oil (RB) in comparison with Fig. 5.8b; e) Time dependent change of the absorbance (at 232 nm) of α-pinene in the presence and absence of RB oil.

5.3.4. Sensor surface characterisation

The SEM images (SEM: ZEISS, EVO-18, special edition, Germany) of the coated QCM sensor in comparison to the bare crystal have been shown in Fig. 5.9. The difference in morphology of the sensor surface can be visualised in Fig. 5.9(a) and (b). The average porosity of the coating surface was calculated to be 3.3% (± 0.2%) using the particle analysis approach (ImageJ software version 1.8.0_172). It can be seen that the fabricated sensor possesses an uneven surface. Moreover, the nebulisation coating generated a uniform morphological behaviour throughout the sensor surface. The presence of rough and non-uniform indentation increases the sensor surface area, which enhances the adsorption site of the target VOC through different non-covalent bonds [26], which is shown in Fig. 5.9(c) and (d).

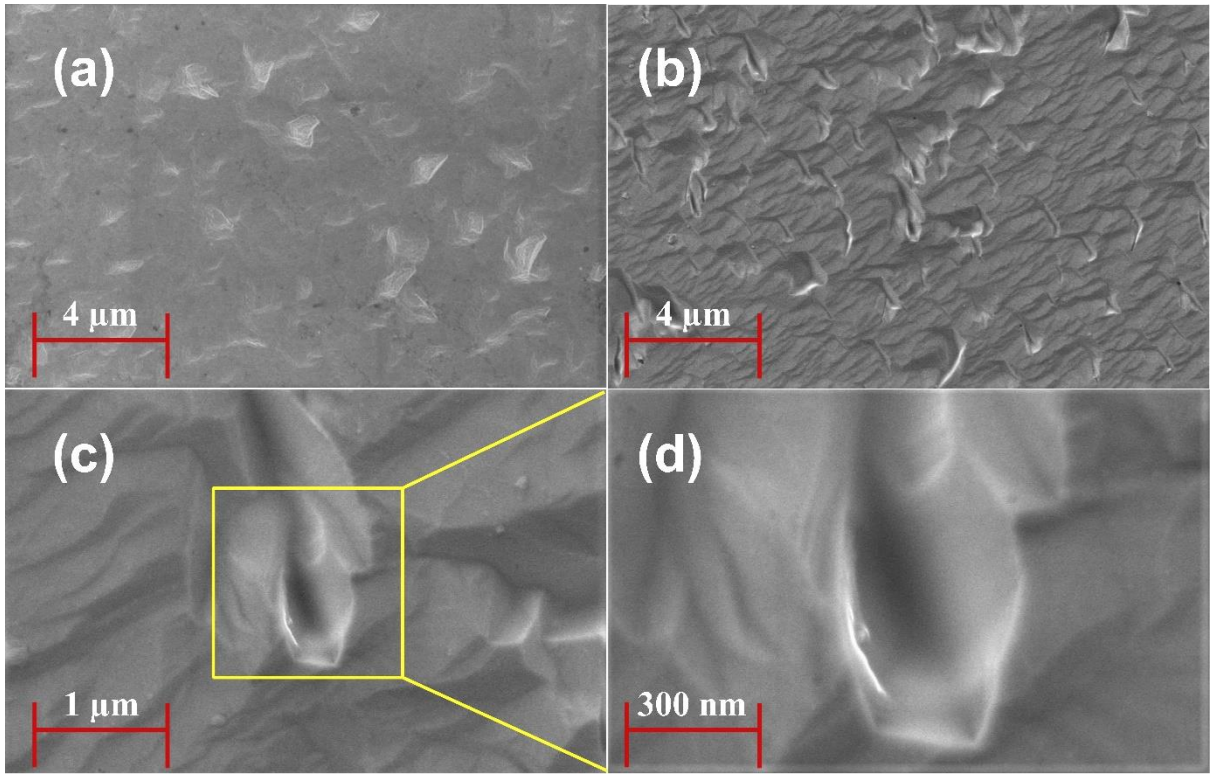

Fig. 5.9. SEM micrograph of (a) blank QCM sensor; (b) rice bran oil coated QCM sensor; (c-d) magnified version of the coated film on RB-QCM sensor at 1µm and 300 nm, respectively.

The AFM imaging (AFM: Agilent technologies/ Keysight technologies, Model no. Pico5500) of the RB-QCM sensor surface was conducted in contact mode to investigate the surface topology, morphology, and roughness of the sensing film. Fig. 5.10(a) and (b) represents the AFM images and their 3D visualisation of the sensor surface. The cross-sectional overview of Fig. 5.10(a) is

shown in Fig. 5.10(c) and (d). The mean height of the surface was determined as 0.68 µm. The distinct surface topography of the rice bran oil coating can be visualised as a rugged and uneven rough surface. Moreover, the oil-based film confirms uniform and homogeneous deposition of the oil on the quartz crystal surface. The AFM analyses were based upon an area of 100 × 100 μm^2 of the AFM image. The root mean square (RMS) roughness was calculated to be 435.3 nm along with a surface area of 10588 μm^2. Thus, the increase in the surface area certainly helps to bind the target molecule properly as size and symmetry matching play a determining role in the lock & key mechanism of the sorption process.

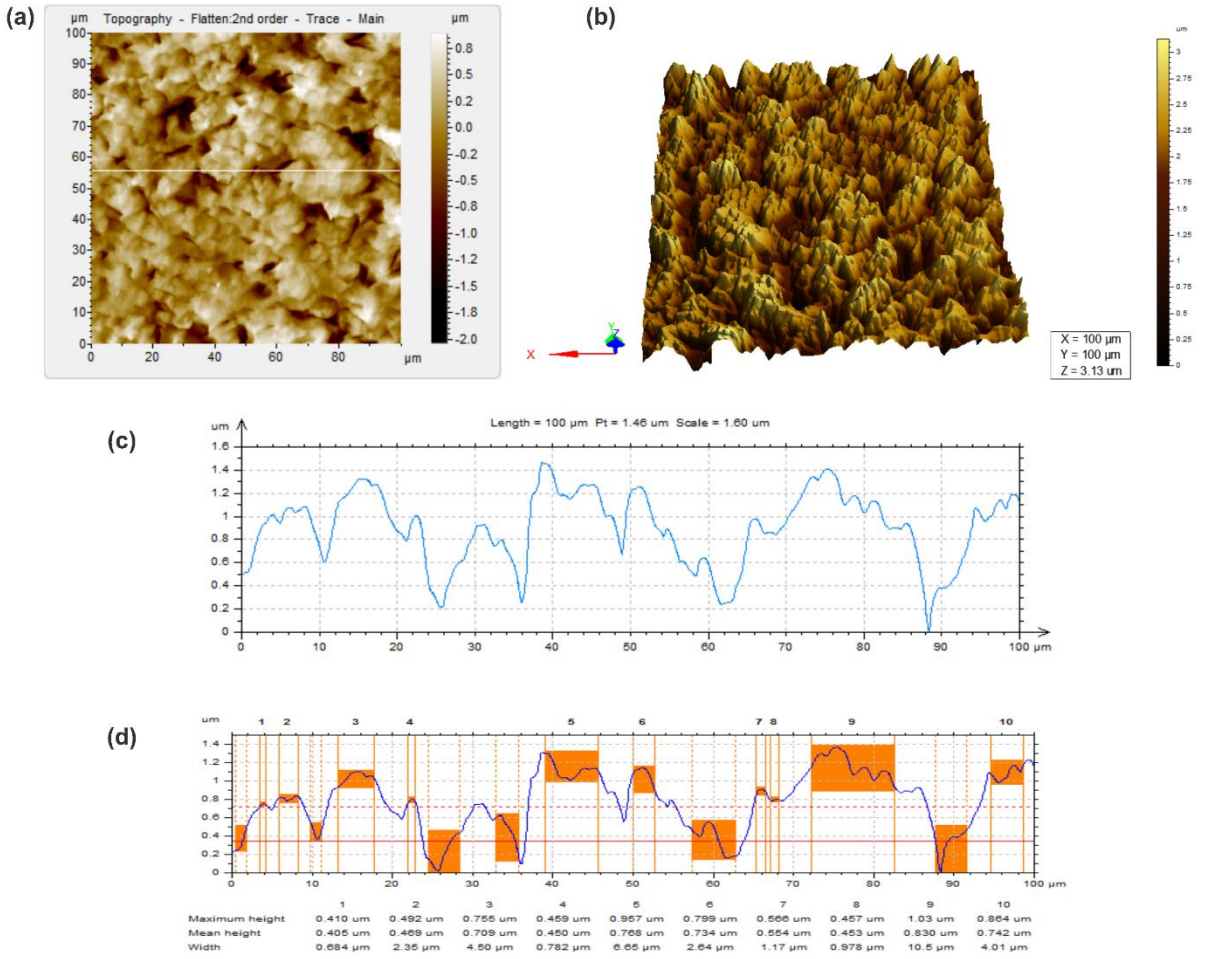

Fig. 5.10. AFM images of RB-QCM sensor surface (a) Topography flattened; (b) 3D view; (c) profile curve; (d) step height measurement.

The FTIR spectrum of rice bran oil (Shimadzu FTIR spectrometer (IR Prestige)) in Fig. 5.11 shows the existence of the functional groups and bonds necessary for the RB oil and α-pinene interaction.

The transmission peak at 3009 cm^{-1} can be noticed due to the stretching vibration peak of C=C and the significant presence of linoleic and linoleic acyl groups. The peaks at 2924 and 2859 cm^{-1} are caused by the symmetric and asymmetric stretching vibrations of the methylene (-CH2) groups. The presence of carbonyl groups (-O-C=O) in esterified fatty acids and glycerol was attributed to the peak at 1709 cm^{-1}. The peak at 1455 cm^{-1} occurred to the asymmetric vibrations of the CH_2 and CH_3 groups. The peaks at 1280 cm^{-1} may be attributed to C-C(=O)-C vibration of the carbonyl group [12,27]. The FTIR spectrogram thus confirms the presence of unsaturated fatty acids that may be responsible for physical interaction with α-pinene.

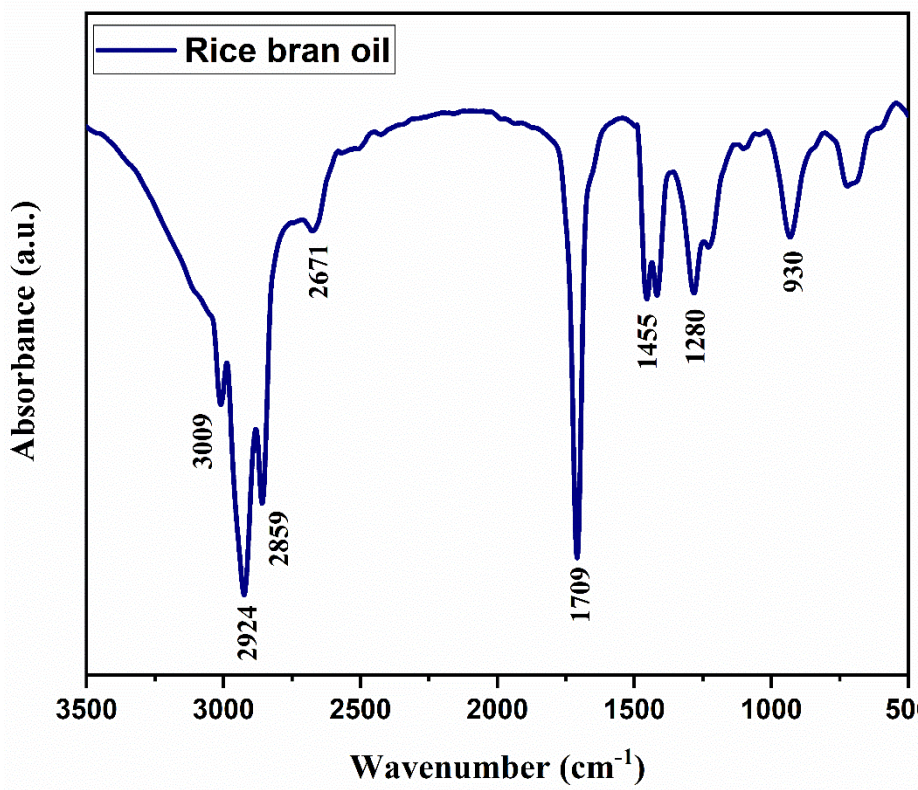

Fig. 5.11. FTIR spectra of the rice bran oil coating material.

5.3.5. Study of the selectivity characteristics of RB-QCM sensor

We have investigated the selectivity of the developed RB-QCM sensor to evaluate how effectively it could identify α-pinene in the presence of other volatiles in real samples. The developed sensor response was studied in the presence of other volatiles at concentrations ranging from 10 to 1000 ppm present in the cardamom samples, such as 1,8-cineole, β-pinene, α-terpinyl acetate, α-terpineol, limonene, and γ-terpinene as mentioned from our GC-MS analysis. The sensitivity was calculated using the average sensor response across three sample stages for each concentration of VOC. Fig. 5.12(a) shows the sensitivity graphs of the RB-QCM sensor following exposure to α-pinene and other dominant volatiles in cardamom. The developed sensor was shown to be more sensitive to α-pinene than other VOCs.

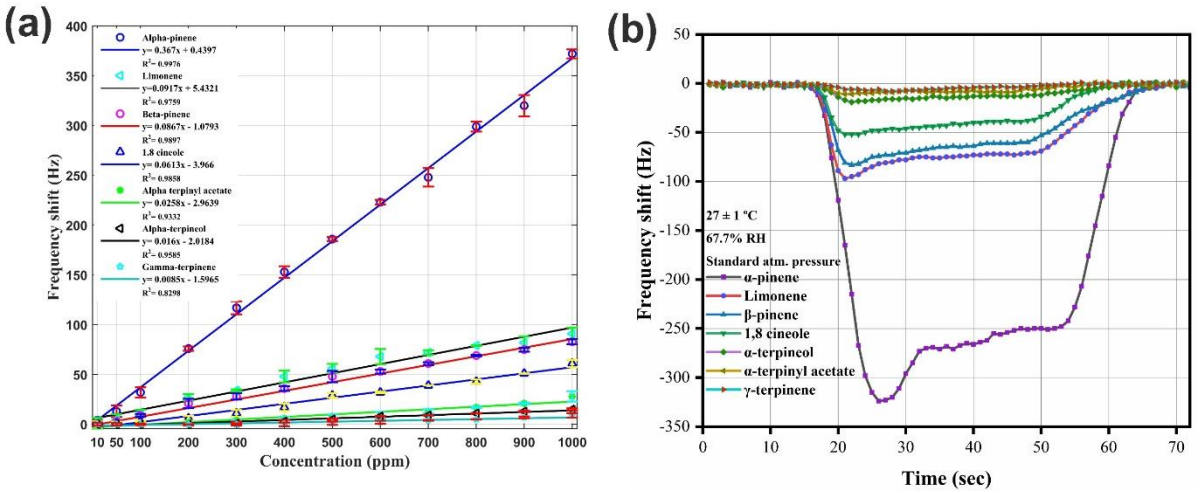

Fig. 5.12 (a). Characteristics RB-QCM sensor responses towards β-pinene and other competing VOCs ranging between 10-1000 ppm; (b) RB-QCM sensor response pattern for 700 ppm of β-pinene, 1,8-cineole, α-terpinyl acetate, α-pinene, limonene, α-terpineol, and γ-terpinene at (27 ± 1) ºC, 67.7% RH and standard atmospheric pressure.

The bar plot in Fig. 5.13 shows the competing VOCs' sensitivity to RB-QCM. Fig. 5.12(b) shows the RB-QCM sensor responses during controlled exposure to 700 ppm of the dominant VOCs employed in this work. The sensor demonstrated a high-frequency shift towards α-pinene at higher and lower concentrations (80% at ten ppm; 56.44% at 1000 ppm) relative to the other volatiles in our investigation, which has been further studied.

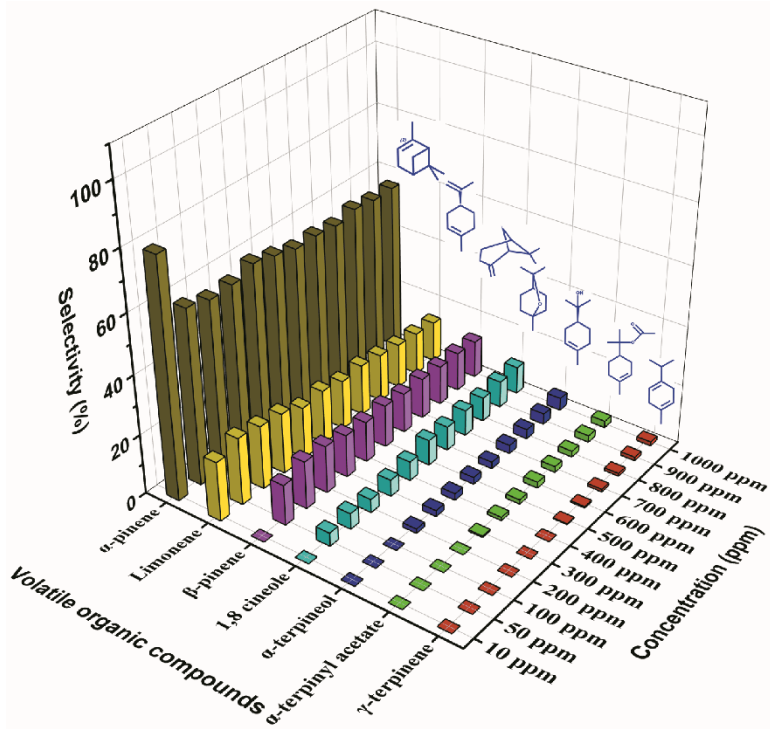

Fig. 5.13. Bar plot diagram of % selectivity of the RB-QCM sensor for β-pinene,1,8-cineole, α-pinene, limonene, α-terpineol, α-terpinyl acetate, and γ-terpinene VOCs at 10-1000 ppm.

The corresponding selectivity (%) results are calculated as discussed in Chapter 4, section 4.3.6 and are tabulated in Table 5.7.

All the volatile molecules considered in our study are nonpolar and lipophilic with varying degrees of hydrophobicity and vapour pressure (Table. 5.8), which is the possible reason behind the varying range of sensitivity of different monoterpenes toward rice bran oil coated on RB-QCM sensor. As both the coating material and target volatiles were hydrophobic, the most suitable interaction that could be possible between them was hydrophobic interactions, and previous literature also suggests that monoterpenes have a strong affinity toward oils [28]. Additionally, as we are dealing with surface interaction between two molecules and the building block of the sensitivity is adsorption, the vapour pressure of the candidate volatiles may play some vital role in the adsorption of volatiles as suggested in previous works of literature [26]. In our study, α-pinene showed the most promising sensitivity towards RB-QCM. α-pinene is a bicyclic monoterpene alkane containing a four-member and a six-member ring without any functional groups, which makes the molecule highly nonpolar and hydrophobic (log kow: 4.83) compared to other studied monoterpenes, and it can be assumed that is the primary reason behind the superior interaction

between α-pinene and RB-QCM sensor. The next two volatiles were followed by α-pinene, limonene, and β-pinene, which occupied the second and third positions in terms of sensitivity.

Table 5.7. Selectivity (%) of RB-QCM sensor.

Concentration (ppm)	**Selectivity (%)**						
	α-pinene	**Limonene**	**β-pinene**	**1,8-cineole**	**α-terpineol**	**α-terpinyl acetate**	**γ-terpinene**
10	80.00	20.00	0.00	0.00	0.00	0.00	0.00
50	59.09	22.73	13.64	4.55	0.00	0.00	0.00
100	57.14	21.43	16.07	5.36	0.00	0.00	0.00
200	57.58	20.45	15.91	4.55	1.52	0.00	0.00
300	60.00	17.44	14.36	5.64	2.05	0.51	0.00
400	58.17	18.25	13.69	6.46	2.28	1.14	0.00
500	56.25	16.67	14.29	8.63	2.38	1.49	0.30
600	56.46	17.22	13.42	8.10	2.28	2.03	0.51
700	55.61	16.14	13.68	8.74	2.91	2.02	0.90
800	57.17	15.11	13.19	8.22	3.25	2.10	0.96
900	56.24	14.41	13.18	8.96	3.69	2.28	1.23
1000	56.45	13.81	12.59	9.26	4.25	2.28	1.37

This is also because of their hydrophobic nature (log kow limonene: 4.57; β-pinene: 4.16), which is caused by the lack of polar molecules or any functional groups in their structure. In our experiment, 1,8-cineole, which is a bicyclic ether, held the fourth position despite lower hydrophobicity (log kow: 2.74) due to the presence of -O- in its ring structure than the remaining three volatiles. This imparity is probably because of the higher vapour pressure of 1,8-cineole than the other three molecules, which allowed more molecules of 1,8-cineole to get adsorbed on the QCM surface than remaining volatiles resulting in higher sensitivity than the rests. The following two molecules, i.e., α-terpinyl acetate and α-terpineol, are less hydrophobic (log kow: α-terpinyl acetate: 3.96; α-terpineol: 3.2) than the first three molecules due to the presence of (CH_3COO-) and (OH-) respectively, which significantly reduce the chance of hydrophobic interaction between these two molecules and RB-QCM. Finally, γ-terpinene showed minor sensitivity toward RB-QCM even if it is more hydrophobic than β-pinene (log kow: 4.36) and has higher vapour pressure than α-terpinyl acetate and α-terpineol.

Nevertheless, unlike α- pinene, β-pinene, and 1,8-cineole, γ-terpinene is a monocyclic terpene and doesn't possess an exocyclic four-membered ring, which makes the ring relatively planner in its geometrically optimised state. This absence of functional binding site and planner structure could be a cause behind the abhorrence between γ-terpinene and linoleic acid present on QCM. To further validate our proximate assumptions, we have performed in silico computational studies, which have been discussed in the later section of the article.

Table 5.8. Hydrophobicity and vapor pressure of the VOCs

Volatiles	**Octanol/water partition coefficient (log kow)**	**Vapour pressure (mmHg at 298K)**
α-pinene	4.83	4.5
Limonene	4.57	1.99
β-pinene	4.16	2.93
1,8-cineole	2.74	1.9
α- terpinyl acetate	3.96	0.04
Terpineol	3.2	0.02
γ-terpinene	4.36	1.09

Concerning earlier literature and the SPME-GCMS analysis of the nine cardamom samples reported in Table 5.3, it is clear that 1,8-cineole was one of the most abundant constituents of cardamom. However, the average selectivity of the RB-QCM sensor indicated a greater affinity for α-pinene (59.17%) than for 1,8-cineole (6.53%). The second most selective volatile, limonene (17.80%), has much lower selectivity concerning α-pinene and occupies a minor area in the chromatogram of cardamom volatile headspace. The obtained result indicates that the fabricated sensor can effectively detect the presence of α-pinene in cardamom samples, lowering the cross-sensitivity that may occur due to the other volatiles in cardamom aroma. The other volatiles has lower selectivity probability and thus may result in minute cross-sensitivity. Detecting α-pinene in other samples with differing abundances of interfering VOCs may lead to erroneous cross-sensitivity and requires additional findings.

5.3.6. Study of the sensing mechanism of RB-QCM sensor using AutoDock tools

Binding interactions between the linoleic acid and candidate monoterpenes were predicted using in silico molecular docking approach. Three-dimensional structures of linoleic acid and candidate volatiles were collected from NIST online library in SDF format. In a subsequent step, SDF files were converted into PDB and then into PDBQT format using Openbabel v3.1.1. Molecular docking was performed using the Autodock suite to predict the binding energies between linoleic acid and concerned volatiles. Linoleic acid was chosen as a receptor or macromolecule to perform the analysis. On the other hand, individual volatile was demarcated as a ligand for each computational trial. Firstly, a grid box was drawn using Autogrid 4.0 to cover the whole linoleic acid and trialled volatile. The same grid parameter was maintained for each computational trial. After setting the grid parameter, docking was performed following Lamarckian GA 4.2 algorithm using Autodock 4.0. The output conformations of each volatile were screened for their root mean square deviation (RMSD) values, and the conformation with the lowest RMSD value was considered the best docking conformation. The estimated free energy of binding (ΔG) is positively influenced by the final intermolecular energy (vdW, Hydrogen bond) and negatively impacted by the presence of torsions in the volatile molecule(s). In the molecular docking, the α-pinene-linoleic acid complex obtained the best docking score, i.e., the highest binding energy compared to other candidate monoterpenes (Table 5.9).

Furthermore, to visualise the binding interactions between linoleic acid and concerned volatiles, PyMOL was used. In the lowest RMSD state, the four-carbon cyclic ring of α-Pinene serves as the leading site that interacts with linoleic acid via vdW interaction (Fig. 5.14). Five vdW contact points were found between α-pinene and linoleic acid. **In addition, α-pinene is the most hydrophobic molecule based on the hydrophobic index (log kow). Thus, the volatile can interact with the lipophilic linoleic acid more quickly than the other concerning monoterpenes in Table 5.9.**

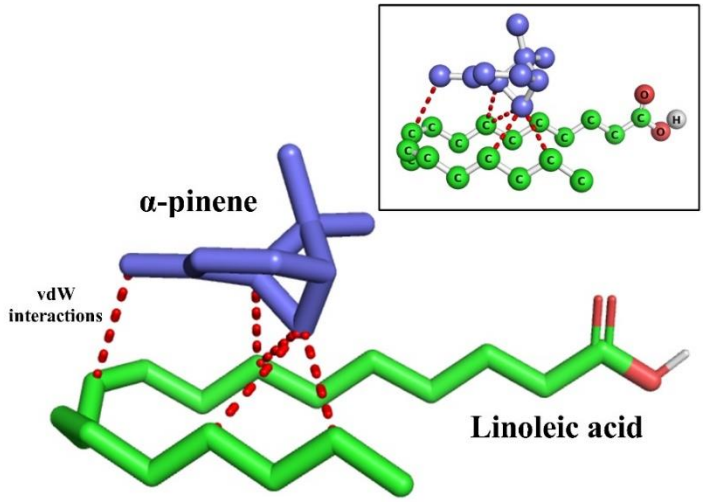

Fig. 5.14. Van der Waal's interactions between α-pinene and linoleic acid in the lowest RMSD docked state.

Conversely, other volatile candidates that are involved in the study are significantly less hydrophobic in nature (Table 5.9), which reduces their potential to involve in the hydrophobic interactions. Besides hydrophobicity, the binding energy of the best-docked state of other monoterpenes isn't optimal for vdW interactions (Fig. 5.15).

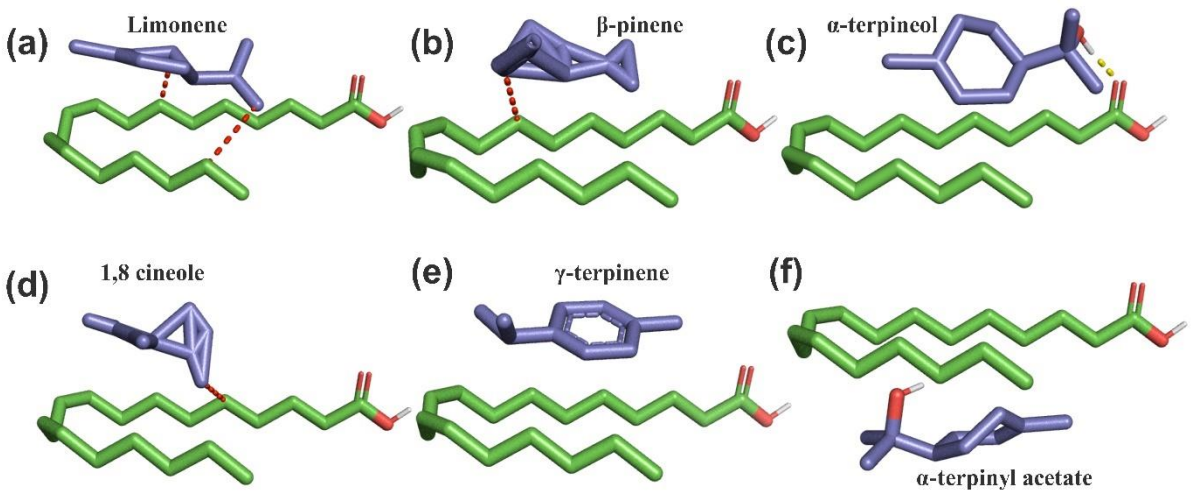

Fig. 5.15. Binding interactions between linoleic acid and other dominant volatiles.

Apart from α-pinene, β-pinene and 1,8-cineole are also bicyclic terpenes containing six-member and four-member rings. In the case of 1,8-cineole, the four-membered ring includes an oxygen atom that slackens the strength of hydrophobic interaction between 1,8-cineole and linoleic acid, which results in the establishment of a single vdW point of contact between 1,8-cineole and linoleic acid. Similarly, in the lowest RMSD state, the four-membered ring of β-pinene did not orient towards linoleic acid. The orientation does not ensure the adequate available surface area to make strong vdW contact with the linoleic acid; consequently, a single vdW point of contact was formed during the computational analysis. Other concerned components like γ-terpinene, α-terpinyl acetate, α-terpineol, and limonene are monocyclic, but the twisted structure of limonene in its lowest RMSD, docked state, permits it to make a couple of vdW contact with linoleic acid. An unfavourable interaction between α-terpineol and linoleic acid was observed during the computational study, as the hydroxyl (-OH) group of the former molecule established an H-bond with the carbonyl oxygen of the carboxyl group (-COOH) of linoleic acid (Fig. 5.15).

Table 5.9. Molecular docking results of the interaction between linoleic acid and major VOCs in cardamom.

Monoterpenes	Binding free energy (Kcal/mol)	Torsional free energy (Kcal/mol)	Number of interaction(s)
α-pinene	-2.46	0	5
Limonene	-2.39	0.3	2
β-pinene	-2.37	0.3	1
α-terpineol	-2.37	0.6	1
1,8-cineole	-2.31	0.3	1
γ-terpinene	-2.19	0.3	0
α- terpinyl acetate	-2.1	0.6	0

5.3.7. Equilibrium analysis of RB-QCM sensor

Adsorption isotherm illustrates the relationship between the equilibrium concentrations of bound and free gas molecules across a given concentration range. Our present study investigated the interaction between α-pinene and RB-coated QCM sensors using Langmuir, Freundlich, and Langmuir-Freundlich isotherm models [29,30]. The details of the analysis have been discussed in Chapter 4, section 4.3.7. The isotherm models are depicted in Fig. 5.16.

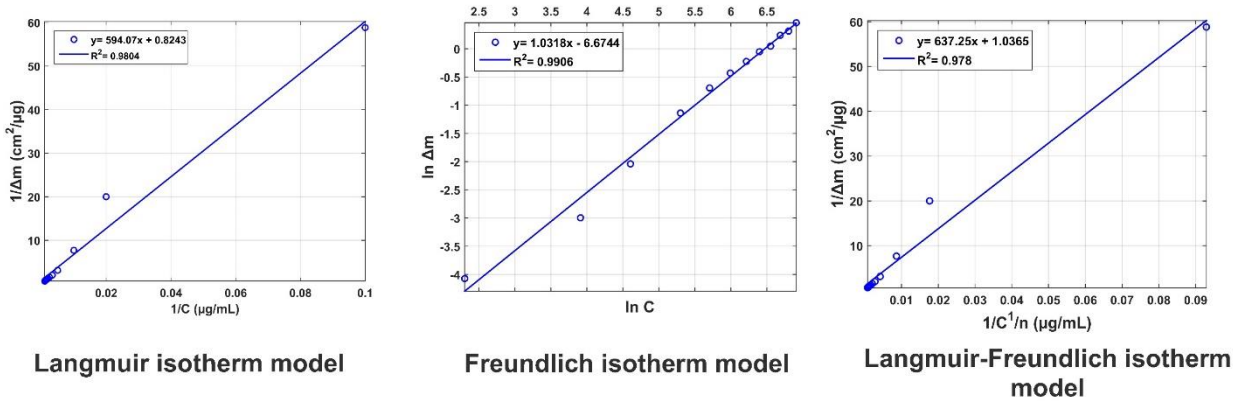

Fig. 5.16. Isotherm models for the equilibrium analysis on the sensor coating surface.

Our present investigation found that the interaction between α-pinene and RB QCM surface fitted most accurately with Freundlich isotherm, based on correlation coefficient of 0.9906 and linearity y = 1.0318x - 6.6744, than other isotherms like Langmuir, and Langmuir Freundlich models. Evaluating the outcomes, it can be presumed that α-pinene molecules have heterogeneous binding sites when bound to the RB-coated QCM sensor. The results of the different isotherm analyses between α-pinene and RB QCM surface are given in Table 5.10.

Table 5.10. Langmuir, Freundlich and Langmuir-Freundlich isotherm constants for RB-QCM sensor.

Langmuir		**Freundlich**		**Langmuir-Freundlich**	
Δm_{max}	1.213	Δm_{max}	0.0098	Δm_{max}	0.96
K_A (µg/mL)$^{-1}$	0.0013	1/n	1.032	K_A (µg/mL)$^{-1}$	0.0016
K_D (µg/mL)	720.60	R^2	0.9976	K_D (µg/mL)	611.766
R^2	0.9804			1/n	1.032
				R^2	0.978

5.3.8 Study of the gas sensing properties of RB-QCM sensor

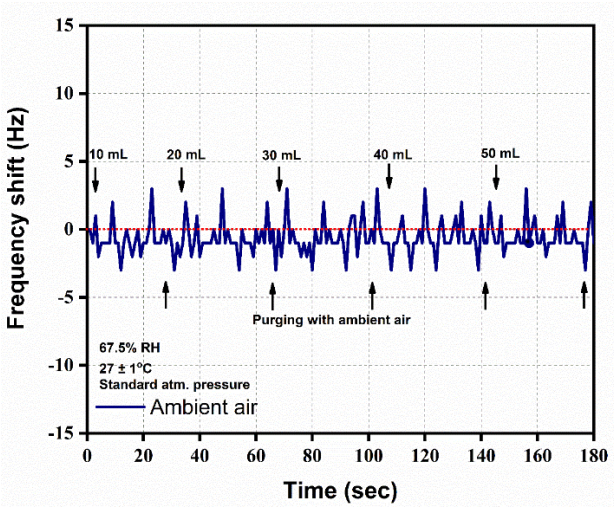

Fig. 5.17. Response of the RB-QCM sensor towards different volumes (10-50 mL) of ambient air studied at (27 ± 1) °C, RH= 67.70%, and standard atmospheric pressure.

The ambient air was used to prepare the different concentrations of VOCs and used as a medium for sampling. Thus, the sensor performance towards ambient air needs to be validated. Fig. 5.17 illustrates the RB-QCM sensor showed no frequency shift due to different amounts (10-50 mL) of incoming ambient air injected into the sensor chamber. Thus, the RB-QCM sensor responses are attributable to applied VOCs, not ambient air.

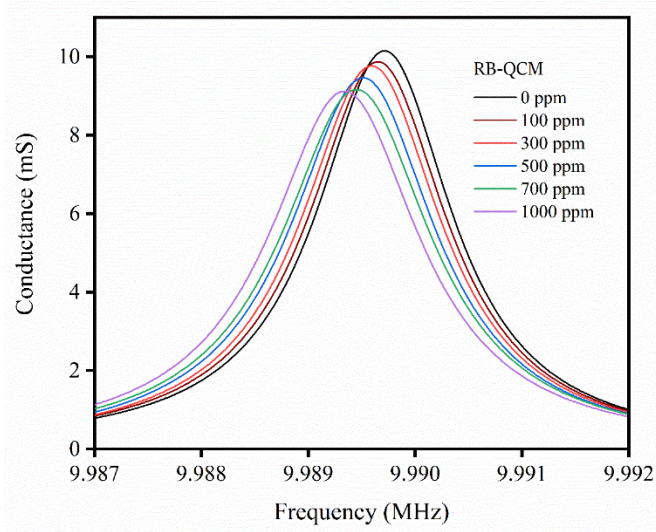

Fig. 5.18. Conductance spectrum of RB-QCM sensor towards different concentrations of α-pinene.

The conductance spectra of the RB-QCM sensor were studied for varied concentrations (100-1000 ppm) of α-pinene VOC, as shown in Fig. 5.18. The resonance frequencies followed a decreasing trend with an increasing concentration of α-pinene. The corresponding conductance spectra showed the left shift corresponding with the growing frequency shift due to the sensitivity of the sensor. Moreover, the Q-factor gradually decreases, corresponding to the increasing concentration due to the viscoelastic nature of the prepared sensing film [31]. The change in Q-factor corresponding to each concentration of α-pinene has been illustrated in Fig. 5.19.

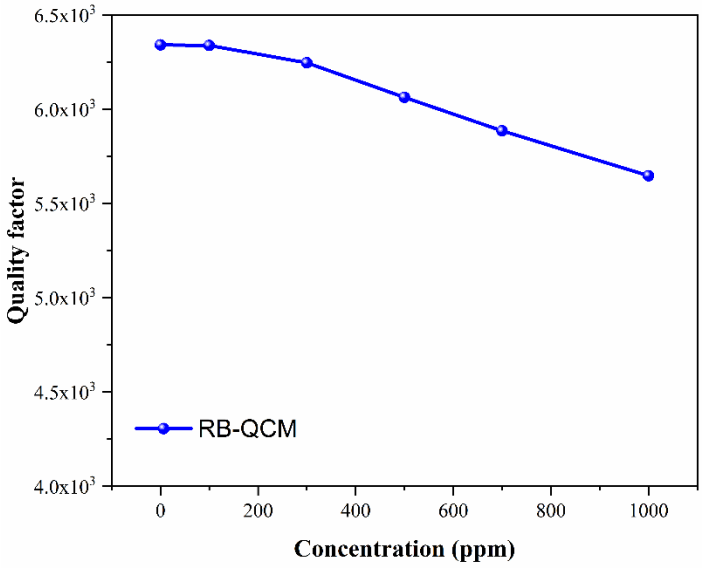

Fig. 5.19. Variation in the quality factor of RB-QCM sensor towards different concentrations of α-pinene.

The repeatability of a sensor is an important performance metric to evaluate its capacity to produce consistent results throughout a wide range of repeated sensing applications. The repeatability of the RB-QCM sensor was assessed at different concentrations (10 – 1000 ppm) of α-pinene at similar experimental conditions. The repeatability percentage (R_p) was calculated based on the relative standard deviation (RSD) for four consecutive samplings, as discussed in Chapter 4 and tabulated in Table 5.11.

Table 5.11. Repeatability measurement (n = 4) of RB-QCM sensor for 10-1000 ppm of α-pinene.

Concentration (ppm)	**Repeatability (n=4)**		
	Frequency shift (Hz)	**R_P (%)**	**CI**
10	4 ± 0.82	79.59	± 0.80
50	11.5 ± 1.29	88.77	± 1.27
100	34 ± 2.16	93.65	± 2.12
200	75.5 ± 2.08	97.24	± 2.04

300	117.75 ± 1.71	98.55	± 1.67
400	153.75 ± 2.22	98.56	± 2.17
500	187.5 ± 2.38	98.73	± 2.33
600	224.25 ± 2.22	99.01	± 2.17
700	250.75 ± 2.22	99.12	± 2.17
800	297 ± 2.38	99.20	± 2.33
900	321.25 ± 2.50	99.22	± 2.45
1000	371.25 ± 2.50	99.33	± 2.45

Fig. 5.20. shows the performance of the as-prepared sensor in the presence of 300, 600, and 900 ppm of α-pinene followed by proper purging with ambient air. The average sensor responses for different concentrations of α-pinene were obtained as 117.75 ± 1.71 Hz (300 ppm), 224.25 ± 2.22 Hz (600 ppm), and 321.25 ± 2.50 Hz (900 ppm), respectively. It was further observed that the repeatability increased with increasing concentration of α-pinene, with average repeatability of 95.91%. Moreover, the response pattern showed a similar shape with negligible variation in frequency shift at its saturation, which indicates the efficiency of the sensor for generating repeated responses.

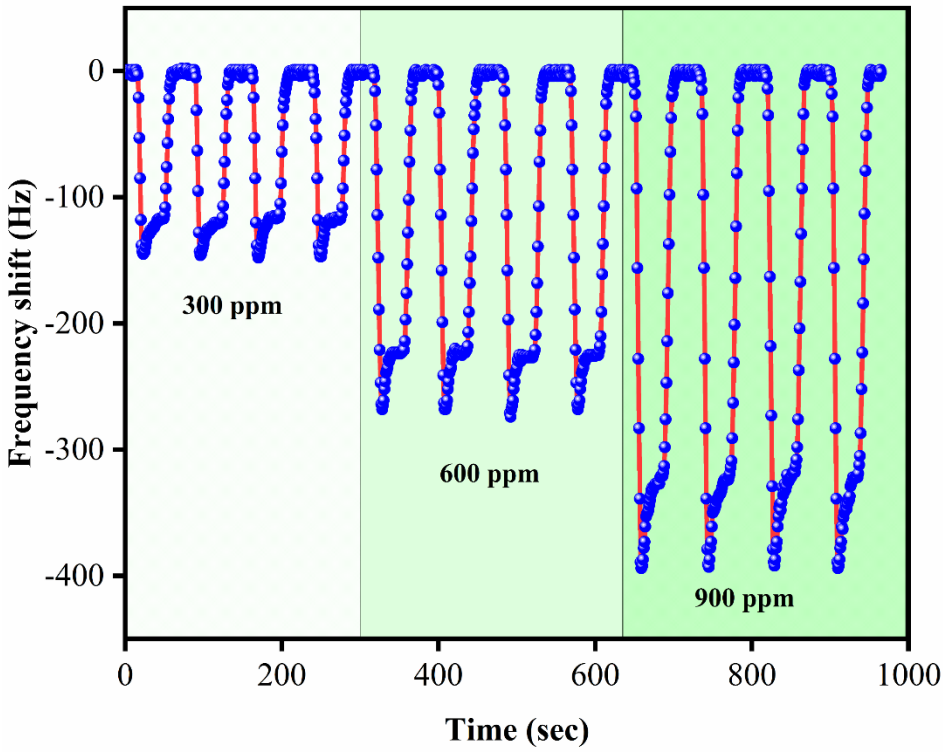

Fig. 5.20. Repeatability profile of RB-QCM sensor towards 300, 600, and 900 ppm of α-pinene at (27 ± 1) ºC, 67.7% RH, and standard atmospheric pressure.

The sensor responses for different humidity (45-85% RH) were studied by generating respective humid conditions [12]. The frequency shifts of the RB-QCM sensor in response to different humid conditions were represented in Fig. 5.21(a). The sensor showed no detectable frequency shift (0-1 Hz) in the range of 45-65% RH. This may be explained by the presence of hydrophobic long-chained fatty acids (dominantly linoleic acid) present on the sensor surface, which don't have any natural hygroscopic property. However, a negligible shift was observed when exposed to a higher humid environment, i.e., 4 Hz (75% RH) and 6 Hz (85% RH). This is possibly due to the formation of glitter on oily sensor surfaces owing to the deposition of moisture at higher humidity. The RB-QCM sensor was further tested with 800 ppm of α-pinene in different humid conditions (45-85% RH), as illustrated in Fig. 5.21(b). The frequency shifts were 310 Hz (45% RH), 309 Hz (55% RH), 307 Hz (67.5% RH), 303 Hz (75% RH), 299 Hz (85% RH). With increased humidity, a minimal decrease in sensor adsorption towards α-pinene was noticed as the hydrophobic interaction between the α-pinene and linoleic acid was significantly affected. This may be explained by the emergence of hydrophilic moisture glitter on the sensor surface in the higher humid condition, which interfered with the formation of hydrophobic interactions between α-

pinene and the sensor surface. This validates that the sensor performance has a minimal influence on the ambient humidity.

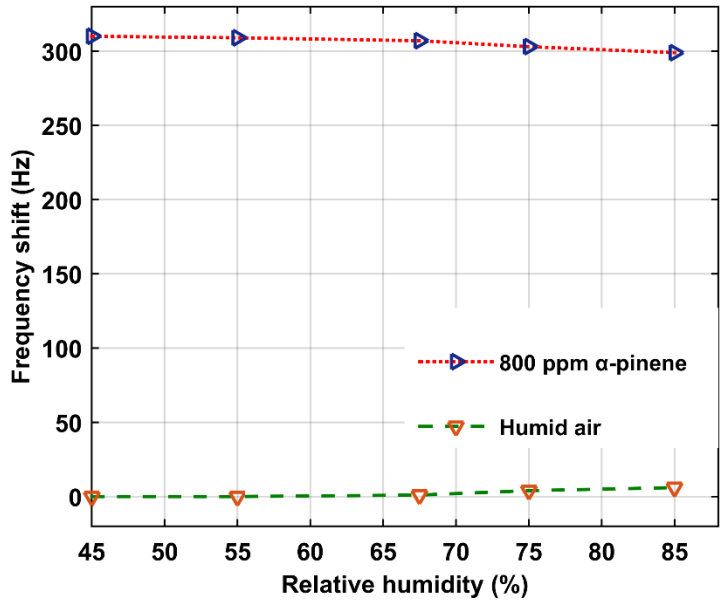

Fig. 5.21. Response profile of RB-QCM sensor (a) towards ambient air, (b) for 800 ppm of β-pinene at the different relative humidity (%), at (27 ± 1) ºC, and standard atmospheric pressure.

Stability refers to the ability of a sensor to maintain a steady output value over time in an ambient, experimental condition. Depending on the period, the short- and long-term stability of a sensor can be measured. To evaluate the short-term stability, the RB-QCM sensor was attached to the sensor chamber and the frequency changes were monitored for 200 secs as illustrated in Fig. 5.22. The coefficient of variation (CV) measures the fluctuations in sensor readings (f_{sensor}) by using equation (5.1) [32]

$$CV = \frac{S_{f\,sensor}}{\overline{f_{sensor}}} \times 100\% \qquad (5.1)$$

where $S_{fsensor}$ and $\overline{f_{sensor}}$ denotes the standard deviation and mean of f_{sensor}, respectively.

The as-fabricated sensor showed a CV of 0.000005454%, which determines its efficient short-term stability.

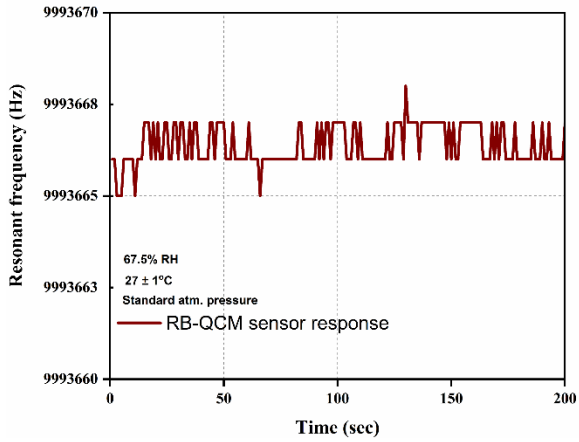

Fig. 5.22. Short-term stability of RB-QCM sensor.

The long-term stability of the RB-QCM sensor was determined by measuring its responsiveness to a fixed 400 ppm of α-pinene at an interval of 10 days for three months after fabrication. As illustrated in Fig. 5.23, the sensor responses at saturation after injection of α-pinene were 153.25 ± 1.26 Hz (10 days), 150.75 ± 0.96 Hz (20 days), 148.25 ± 1.26 Hz (30 days), 147 ± 1.41 Hz (40 days), 143 ± 1.83 Hz (50 days), 140 ± 1.83 Hz (60 days), 134.25 ± 2.22 Hz (70 days), 131 ± 2.16 Hz (80 days), and 117.75 ± 2.99 Hz (90 days), respectively. According to the study, the developed sensor output decreased by 3.58% after 30 days. The response eventually declined to 23.41% at the end of the study. Moreover, degradation of the sensor output was calculated to be around 8.94 % after 60 days from the original observation. Therefore, the sensor can be utilised for that period without incurring a substantial loss in sensitivity.

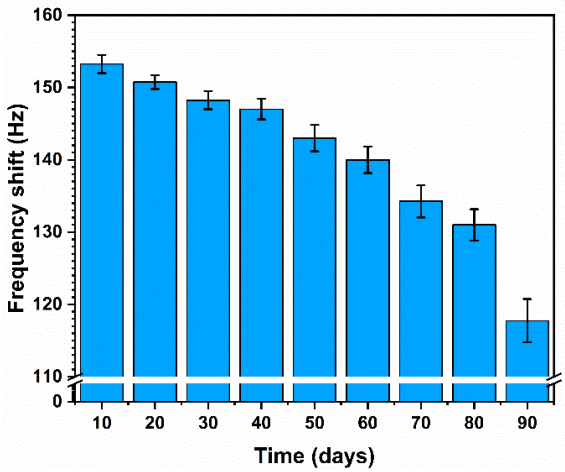

Fig. 5.23. Bar plot representation of long-term stability of the RB-QCM sensor on the application of 400 ppm of α-pinene.

5.3.9. Study of the RB-QCM sensor performance with cardamom samples

The RB-QCM sensor was tested with three small cardamom types, SC_1, SC_2, and SC_3, as well as six large cardamom kinds, LC_1, LC_2, LC_3, LC_4, LC_5, and LC_6. For each cardamom sample, three sniffs of the sensor were obtained. The average RB-QCM sensor responses for each sample are shown in Fig. 5.24(a).

Table 5.12. Correlation with the RB-QCM sensor response with GC-MS response of cardamom samples.

VOC	**The % peak area of samples**									
	SC_1	**SC_2**	**SC_3**	**LC_1**	**LC_2**	**LC_3**	**LC_4**	**LC_5**	**LC_6**	**Correlation with QCM response**
α-pinene	12.54 ± 0.30	11.92 ± 0.4	11.10 ± 0.7	9.82 ± 0.23	1.98 ± 0.08	7.27 ± 0.12	7.63 ± 0.2	7.47 ± 0.3	7.56 ± 0.3	0.987
β-pinene	2.07 ± 0.86	2.05 ± 0.11	1.89 ± 0.07	9.07 ± 0.3	3.60 ± 0.28	9.71 ± 0.09	7.94 ± 0.12	8.25 ± 0.18	6.48 ± 0.17	-0.353
Limonene	8.95 ± 0.1	8.07 ± 0.11	7.51 ± 0.25	6.40 ± 0.11	5.4 ± 0.21	6.17 ± 0.58	6.37 ± 0.11	4.53 ± 0.13	5.7 ± 0.08	0.8
1,8-cineole	62.66 ± 1.23	61.5 ± 3.61	50.36 ± 1.18	74.26 ± 0.39	87.34 ± 0.12	76.28 ± 0.7	77.36 ± 0.37	79.59 ± 0.26	79.42 ± 0.39	-0.813
γ-terpinene	0.88 ± 0.03	1.11 ± 0.02	1.39 ± 0.04	0.28 ± 0.03	0.84 ± 0.08	0.37 ± 0.08	0.56 ± 0.02	0.11 ± 0.15	0.7 ± 0.01	0.33
α-terpineol	0.14 ± 0.005	0.32 ± 0.14	0.47 ± 0.07	0.16 ± 0.04	0.66 ± 0.43	0.19 ± 0.08	0.12 ± 0.03	0.11 ± 0.03	0.14 ± 0.01	-0.462
α-terpinyl acetate	12.75 ± 0.91	15 ± 3.59	27.25 ± 1.86	0	0	0	0	0	0	0.63

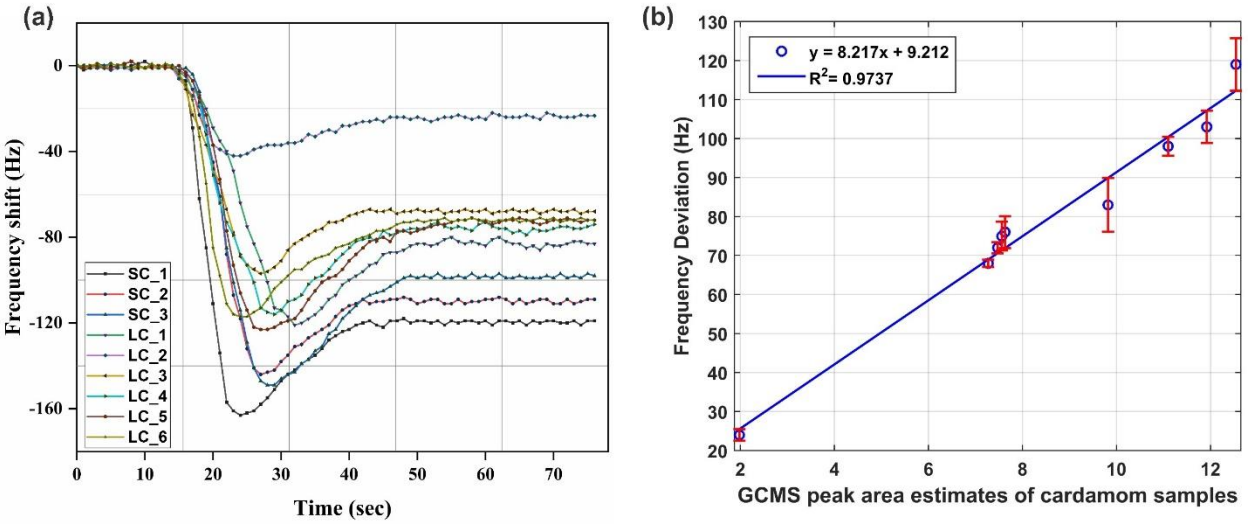

Fig. 5.24.(a) RB-QCM sensor responses; (b) scatter plot of sensor responses and GCMS estimates of cardamom samples.

The aroma of the samples that were injected causes various frequency profiles. Furthermore, the frequency graphs show rapid sensing characteristics of the incoming smell at 15 seconds and approach saturation at roughly 45 secs, demonstrating uniform and speedy sensing behaviour of the RB-QCM sensor. The correlation factor of each VOC in nine cardamom samples with their matching QCM sensor output is shown in Table 5.12. The correlation factor for α-pinene was found to be 0.987, the highest among the other volatiles in cardamom, as seen in the bar graphs in Fig. 5.25.

5.13. GC-MS and RB-QCM sensor response for α-pinene.

Sample	**GC-MS estimates of α-pinene**	**RB-QCM frequency shift (Hz)**
SC_1	12.54	119
SC_2	11.92	103
SC_3	11.1	98
LC_1	9.82	83
LC_2	1.98	24
LC_3	7.27	68

LC_4	7.63	76
LC_5	7.47	72
LC_6	7.56	75

Table 5.13. shows the QCM sensor responses from the investigated samples and the associated GC-MS estimate of α-pinene. The curve fit of the scatter plot for the sensor responses with estimated GC-MS peak region of α-pinene was y = 8.217x + 9.212 with R^2 = 0.97 is given in Fig. 5.24(b). The scatter plot's precision in measuring reveals the efficacy of the RB-QCM sensor in being very sensitive to the α-pinene fragrance contained in cardamom.

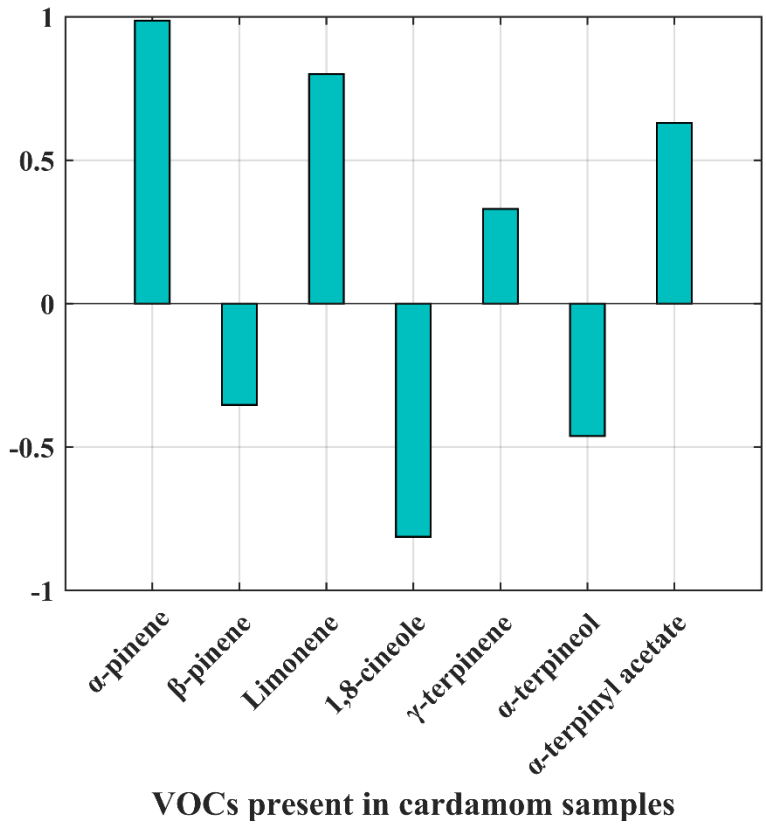

Fig. 5.25. Bar plot representation of the correlation factor between important VOCs in cardamom with its RB-QCM sensor outputs.

5.5. Conclusion

This chapter addresses the development of a rice bran oil-coated QCM sensor for detecting α-pinene in cardamom. **The sensor was intended to be sensitive to α-pinene, measuring 0.367 Hz/ppm and having an R^2 of 0.9976.** Furthermore, even in the presence of other main VOCs present in cardamom, the sensor is adequately selective for α-pinene. Again, at 67.7 %RH, the developed sensor exhibits quick recovery, long-term stability, short-term stability, little humidity impact, and 95.91% average repeatability. **Through Van der Waal's interaction, the rough, uneven surface of the sensor coating increases the area for α-pinene adsorption**. A GC-MS technique was used to validate the interaction between the nine cardamom samples, and the results indicated a correlation of 0.987 with the α-pinene estimates and QCM responses.

References

[1] NS. Dosoky, P. Satyal, L.M. Barata, JKR da Silva, W.N. Setzer, Volatiles of Black Pepper Fruits (Piper nigrum L.), Molecules. 24 (2019) 4244. https://doi.org/10.3390/molecules24234244.

[2] M.E. Maldonado-Celis, E.M. Yahia, R. Bedoya, P. Landázuri, N. Loango, J. Aguillón, B. Restrepo, J.C. Guerrero Ospina, Chemical Composition of Mango (Mangifera indica L.) Fruit: Nutritional and Phytochemical Compounds, Frontiers in Plant Science. 10 (2019). https://www.frontiersin.org/article/10.3389/fpls.2019.01073 (accessed April 2, 2022).

[3] M. Muchalal, J. Crouzet, Volatile Components of Clove Essential Oil (Eugenia caryophyllus Spreng): Neutral Fraction, Agricultural and Biological Chemistry. 49 (1985) 1583–1589. https://doi.org/10.1080/00021369.1985.10866947.

[4] C. Tschiggerl, F. Bucar, Investigation of the Volatile Fraction of Rosemary Infusion Extracts, Sci Pharm. 78 (2010) 483–492. https://doi.org/10.3797/scipharm.1004-23.

[5] B. Salehi, S. Upadhyay, I. Erdogan Orhan, A. Kumar Jugran, S. LD. Jayaweera, D. A. Dias, F. Sharopov, Y. Taheri, N. Martins, N. Baghalpour, W. C. Cho, J. Sharifi-Rad, Therapeutic Potential of α- and β-Pinene: A Miracle Gift of Nature, Biomolecules. 9 (2019) 738. https://doi.org/10.3390/biom9110738.

[6] H.F. Hawari, N.M. Samsudin, A.Y. Md Shakaff, Supri.A. Ghani, M.N. Ahmad, Y. Wahab, U. Hashim, Development of Interdigitated Electrode Molecular Imprinted Polymer Sensor for Monitoring Alpha Pinene Emissions from Mango Fruit, Procedia Engineering. 53 (2013) 197–202. https://doi.org/10.1016/j.proeng.2013.02.026.

[7] K.A. Weerakoon, J.H. Shu, M.-K. Park, B.A. Chin, Polyaniline Sensors for Early Detection of Insect Infestation, ECS J. Solid State Sci. Technol. 1 (2012) Q100. https://doi.org/10.1149/2.014205jss.

[8] B. Chen, C. Liu, X. Sun, K. Hayashi, Molecularly imprinted polymer coated Au nanoparticle sensor for α-pinene vapor detection, in: 2013 IEEE SENSORS, 2013: pp. 1–4. https://doi.org/10.1109/ICSENS.2013.6688152.

[9] B. Chen, C. Liu, Y. Xie, P. Jia, K. Hayashi, Localized Surface Plasmon Resonance Gas Sensor Based on Molecularly Imprinted Polymer Coated Au Nano-Island Films: Influence of Nanostructure on Sensing Characteristics, IEEE Sensors Journal. 16 (2016) 3532–3540. https://doi.org/10.1109/JSEN.2016.2536629.

[10] R. Das, S. Pradhan, S. Biswas, P. Sharma, A. Ghosh, R. Bandyopadhyay, P. Pramanik, Aliphatic amines vapours detection by quartz crystal microbalance sensor, Sensors and Actuators B: Chemical. 198 (2014) 94–101. https://doi.org/10.1016/j.snb.2014.03.020.

[11] B. Ghatak, S.B. Ali, N. Debabhuti, P. Sharma, A. Ghosh, B. Tudu, R. Bandyopadhyay, N. Bhattacharya, Discrimination of Tomatoes Based on Lycopene Using Cyclic Voltammetry, Sensor Letters. 15 (2017) 827–836. https://doi.org/10.1166/sl.2017.3884.

[12] N. Debabhuti, S. Mukherjee, S. Neogi, P. Sharma, U.H. Sk, S. Maiti, M.P. Sarkar, B. Tudu, N. Bhattacharyya, R. Bandyopadhyay, A study of vegetable oil modified QCM sensor to detect β-pinene in Indian cardamom, Talanta. 236 (2022) 122837. https://doi.org/10.1016/j.talanta.2021.122837.

[13] G. Sauerbrey, Verwendung von Schwingquarzen zur Wägung dünner Schichten und zur Mikrowägung, Z. Physik. 155 (1959) 206–222. https://doi.org/10.1007/BF01337937.

[14] M.C. Dixon, Quartz Crystal Microbalance with Dissipation Monitoring: Enabling Real-Time Characterisation of Biological Materials and Their Interactions, J Biomol Tech. 19 (2008) 151–158.

[15] D. Johannsmann, I. Reviakine, R.P. Richter, Dissipation in Films of Adsorbed Nanospheres Studied by Quartz Crystal Microbalance (QCM), Anal. Chem. 81 (2009) 8167–8176. https://doi.org/10.1021/ac901381z.

[16] X. Ding, X. Chen, X. Chen, X. Zhao, N. Li, A QCM humidity sensor based on fullerene/graphene oxide nanocomposites with high quality factor, Sensors and Actuators, B: Chemical. 266 (2018) 534–542. https://doi.org/10.1016/j.snb.2018.03.143.

[17] X. Li, X. Chen, Y. Yao, N. Li, X. Chen, X. Bi, Multi-Walled Carbon Nanotubes/Graphene Oxide Composites for Humidity Sensing, IEEE Sensors Journal. 13 (2013) 4749–4756. https://doi.org/10.1109/JSEN.2013.2273615.

[18] K. Triyana, A. Rianjanu, D.B. Nugroho, A.H. As'ari, A. Kusumaatmaja, R. Roto, R. Suryana, H.S. Wasisto, A highly sensitive safrole sensor based on polyvinyl acetate (PVAc) nanofiber-coated QCM, Scientific Reports. 9 (2019) 1–12. https://doi.org/10.1038/s41598-019-51851-0.

[19] T. Nan, Y. Hui, M. Rinaldi, N.X. Sun, Self-Biased 215MHz Magnetoelectric NEMS Resonator for Ultra-Sensitive DC Magnetic Field Detection, Sci Rep. 3 (2013) 1985. https://doi.org/10.1038/srep01985.

[20] D. Zhang, Y. Sun, Y. Zhang, Fabrication and characterisation of layer-by-layer nano self-assembled ZnO nanorods/carbon nanotube film sensor for ethanol gas sensing application at room temperature, J Mater Sci: Mater Electron. 26 (2015) 7445–7451. https://doi.org/10.1007/s10854-015-3378-4.

[21] A. Zielińska, N.R. Ferreira, A. Durazzo, M. Lucarini, N. Cicero, S.E. Mamouni, A.M. Silva, I. Nowak, A. Santini, E.B. Souto, Development and Optimisation of Alpha-Pinene-Loaded Solid Lipid Nanoparticles (SLN) Using Experimental Factorial Design and Dispersion Analysis, Molecules. 24 (2019) 2683. https://doi.org/10.3390/molecules24152683.

[22] H.F. Lodish, Molecular Cell Biology, 4th ed., W.H. Freeman, New York, U.S.A, 2000. https://www.academia.edu/10355171/Molecular_Cell_Biology_5th_ed_Lodish_et_al (accessed April 2, 2022).

[23] K. Triyana, A. Rianjanu, D.B. Nugroho, A.H. As'ari, A. Kusumaatmaja, R. Roto, R. Suryana, H.S. Wasisto, A highly sensitive safrole sensor based on polyvinyl acetate (PVAc) nanofiber-coated QCM, Scientific Reports. 9 (2019) 1–12. https://doi.org/10.1038/s41598-019-51851-0.

[24] G. Sauerbrey, The use of quarts oscillators for weighing thin layers and for microweighing, Zeitschrift Für Physik. 155 (1959) 206–222. https://doi.org/10.1007/BF01337937.

[25] Y. Yao, X. Chen, X. Li, X. Chen, N. Li, Investigation of the stability of QCM humidity sensor using graphene oxide as sensing films, Sensors and Actuators, B: Chemical. 191 (2014) 779–783. https://doi.org/10.1016/j.snb.2013.10.076.

[26] KD. Pennell, Specific Surface Area☆, in: Reference Module in Earth Systems and Environmental Sciences, Elsevier, 2016. https://doi.org/10.1016/B978-0-12-409548-9.09583-X.

[27] Q. Liu, P. Liu, Z.-X. Xu, Z.-X. He, Q. Wang, Bio-fuel oil characteristic of rice bran wax pyrolysis, Renewable Energy. 119 (2018) 193–202. https://doi.org/10.1016/j.renene.2017.12.012.

[28] C. Dejoye Tanzi, M. Abert Vian, C. Ginies, M. Elmaataoui, F. Chemat, Terpenes as green solvents for extraction of oil from microalgae, Molecules. 17 (2012) 8196–8205. https://doi.org/10.3390/molecules17078196.

[29] F. Kartal, D. Çimen, N. Bereli, A. Denizli, Molecularly imprinted polymer based quartz crystal microbalance sensor for the clinical detection of insulin, Mater Sci Eng C Mater Biol Appl. 97 (2019) 730–737. https://doi.org/10.1016/j.msec.2018.12.086.

[30] Y. Li, Y. Liu, J. Liu, J. Liu, H. Tang, C. Cao, D. Zhao, Y. Ding, Molecularly imprinted polymer decorated nanoporous gold for highly selective and sensitive electrochemical sensors, Sci Rep. 5 (2015) 7699. https://doi.org/10.1038/srep07699.

[31] H. Tai, Y. Zhen, C. Liu, Z. Ye, G. Xie, X. Du, Y. Jiang, Facile development of high performance QCM humidity sensor based on protonated polyethylenimine-graphene oxide nanocomposite thin film, Sensors and Actuators B: Chemical. 230 (2016) 501–509. https://doi.org/10.1016/j.snb.2016.01.105.

[32] A. Leong, S. Seeneevassen, T. Saha, V. Swamy, N. Ramakrishnan, Low hysteresis relative humidity sensing characteristics of graphene oxide–gold nanocomposite coated langasite crystal microbalance, Surfaces and Interfaces. 23 (2021) 100964. https://doi.org/10.1016/j.surfin.2021.100964.

Chapter 6

Sensitive detection and estimation of 1,8-cineole content in large cardamom using modified castor oil coated QCM sensor

6.1. Introduction

Various research works studied the composition of the cardamom essential oil and reported the maximum abundance of 1,8-cineole VOC. in cardamom. Rout et al. [1] studied the oil extract of large cardamom growing in Sikkim using GCMS and identified 1,8-cineole as the significant compound [81.5-86%]. Sabulal et al. [2] also reported a higher abundance of 1,8-cineole in cardamom essential oil. The major VOCs of different cardamom cultivars in India and worldwide are tabulated in Chapter 1 (Table 1.1). The table indicates the presence of 1,8-cineole in both large and small cardamom varieties. Furthermore, the determination of VOCs from the headspace of both large and small cardamom has been studied in Chapter 2. The GCMS analysis of 21 large cardamom and three small cardamom varieties from India also indicates 1,8-cineole to be the most abundant HSV. **The findings also show that 1,8-cineole has the highest impact on the aroma profile of different cultivars, making it the most significant volatile for detection using QCM sensor.**

Eucalyptol (1,8-cineole) is a monoterpenoid and bicyclic ether present abundantly in nature. It has an incredible mint-like smell and is found in the essential oil of different plants like rosemary (*Rosmarinus officinalis*), sage (*Salvia officinalis*), mint (*Mentha ssp.)* [3]. Owing to its fragrant aroma, 1,8-cineole is used as a flavouring agent in many food products like confectioneries, baked food products, beverages, and meat products [4]. Cai et al. reported that 1,8-cineole has broad uses in cosmetic products, scent goods such as bathing supplements, mouthwashes, and insect repellants [5]. Moreover, the researchers also claimed that 1,8-cineole has various medicinal benefits due to its anti-inflammatory and antioxidant properties. 1,8-cineole is a remedial solution for many respiratory diseases, including asthma, bronchitis, influenza, and COPD. [6–9]. 1,8-cineole shows anticancer properties, and according to various researches, it showed promising anticancer properties for breast [10], colon [11], ovarian [12], skin [13], and oral [14]cancer both *in vitro* and *in vivo*. Furthermore, 1,8-cineole has therapeutic remedies for digestive diseases [15–17], cardiovascular diseases [18,19], and Alzheimer's disease [20,21].

In this chapter, **a quartz crystal sensor was developed using modified castor oil and the sensing characteristics were studied towards 1,8-cineole VOC**. Vegetable oil-coated sensors were successfully applied for sensor coating materials, as discussed in chapters 4 and 5, which showed good sensing behaviour for monoterpenes such as α-pinene and β-pinene. Using 1,8-cineole as a

target VOC, the sensitivity of the sensor was successfully achieved for the entire range of intended concentration. Different sensing parameters like selectivity, repeatability, long-term, short-term stability and effect of humidity were evaluated. The morphology and the chemical composition analysis of the developed sensor were carried out using a scanning electron microscope (SEM), Fourier transform infrared spectroscopy (FTIR), and atomic force microscopy (AFM). The sensing phenomenon was computationally evaluated using Autodock tools. The developed sensor was tested using procured large cardamom samples, and the sensor responses were validated and correlated with its GCMS analyses. Finally, a mathematical model for estimating the 1,8-cineole content from the sensor responses of cardamom samples was developed, and the accuracy of the model was discussed.

6.2. Experimental

6.2.1 Chemicals and materials

All the authentic volatile compounds and experimental materials were purchased as discussed in Chapter 4, Section 4.2.1. Limonene was supplied from Sigma-Aldrich, Germany. Analytical grade chemicals like benzene concentrated sulfuric acid, Fluoroboric acid and alcohols like 1-hexanol and phenol were acquired from E. Merck, India. The various vegetable oils such as olive, rice bran, linseed, and castor were procured from Sigma-Aldrich, Germany.

6.2.2. Measurement setup and sensor measurements

The details of the measurement setup have been discussed in Chapter 3. Furthermore, a similar sensor measurement protocol has been followed, as mentioned in Chapter 4, section 4.2.3.

6.2.3 Synthesis of Phe-CAS-Phe coating material

Initially, ricinoleic acids in the castor oil were derivatised to form hexyl ricinoleate (CAS-Hex) and phenyl ricinoleate (CAS-Phe) using the acid-catalysed transesterification method [22,23]. 1 mL of IP grade castor oil was mixed with 5 mL of respective alcohols (1-hexanol and molten phenol), 0.5 mL of benzene, and 0.8 mL of concentrated sulfuric acid. The prepared reaction mixture was then kept in a water bath at 90-100 °C. The reaction was allowed to continue for 8 hrs under nitrogen. Following this, the solution was taken in a test tube, ~3-4 mL of hot distilled water was added to the esterified mixture, and the nonpolar fraction of the mixtures containing esterified

ricinoleic acids were extracted in n-hexane. The hexane fraction was washed with distilled water (2-3times) to remove any polar residues and dried over anhydrous sodium sulphate. The reaction process is illustrated as step I in Fig. 6.1.

As illustrated in step II (Fig. 6.1.), phenyl esterified ricinoleic acid (CAS-Phe) was modified to form phenolated phenyl ricinoleate (Phe-CAS-Phe) using Friedel-Crafts alkylation of phenol [23]. Recovered phenyl ricinoleate from the first synthesis was mixed with 5 mL of molten phenol under nitrogen at 50-60°C. Fluoroboric acid (HBF_4) was added to the reaction mixture as a catalyst. The reaction was conducted for 6hrs at 90-100 °C in a water bath. A reddish brown-coloured thick viscous mass was developed after the reaction, which was recovered and purified by high vacuum distillation to remove unreacted phenols from the mixture. The viscous semi-liquid mass was then solubilised in 10ml of diethyl ether and used in further study.

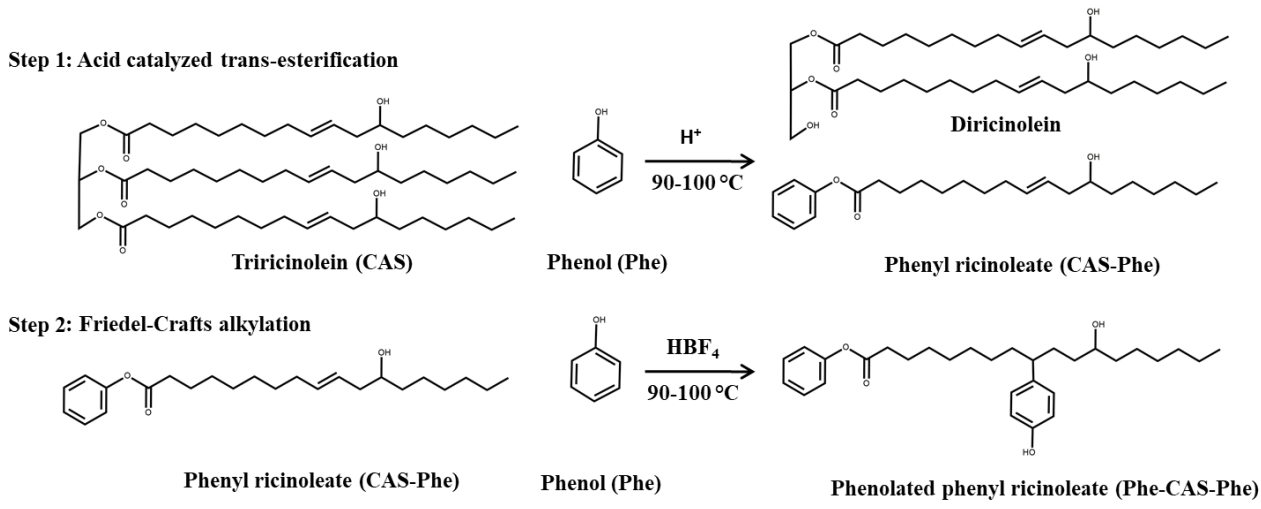

Fig. 6.1. Reaction steps involving synthesis of phenolated phenyl ricinoleate (Phe-CAS-Phe) from castor oil (CAS).

6.2.4. QCM sensor fabrication

QCM sensor (10 MHz fundamental frequency with 8 mm diameter AT-cut quartz electrode and 5 mm diameter silver electrode on both sides) were purchased from Andhra Electronics, India. Four solutions of different vegetable oils, namely rice bran (RB), olive (OLV), linseed (LSEED), and castor (CAS), were prepared for this study with 0.2% (w/v) concentration by dissolving in n-hexane. For the preparation of hexyl ricinoleate (CAS-Hex) and phenyl ricinoleate (CAS-Phe) solution, 20 µL hexane extract of respective derivatives was mixed with 10 mL n-hexane.

Similarly, for the preparation of phenolated phenyl ricinoleate solution, 20 µL diethyl ether extract of mentioned derivate was mixed in 10 mL n-hexane. These dilutions were done to achieve a slow, homogeneous and controlled coating process. The sensor was rinsed with ethanol and deionised water for 15 minutes, followed by drying in the oven at 60 ^{o}C for 30 minutes. The sensors were fabricated using an ultrasonic nebuliser [24]. Moreover, the loading of the sensors was maintained at 7000 Hz in real-time using the developed gas sensing unit. The developed sensors (QCM-OLV, QCM-RB, QCM-LSEED, QCM-CAS, QCM-Hex, QCM-Phe, QCM-Phe-CAS-Phe) were further kept in a vacuum desiccator for 24h for proper stabilisation before the experiment.

6.2.5. Volatile organic compound preparation

The VOCs like 1,8-cineole, α-terpinyl acetate, limonene, α-pinene, β-pinene, α-terpineol, and γ-terpinene were prepared and kept inside 10 L desiccators for the experimental study. All the methodologies are identical, as discussed in Chapter 4, section 4.2.4.

6.2.6. Cardamom sample preparation for the study of QCM-Phe-CAS-Phe sensor

Twenty-one large cardamom samples, marked as LC1 up to LC21, were collected to estimate and quantify the 1,8-cineole content to study the developed sensor. The sample preparation steps were followed, as mentioned in the literature from an earlier report [24,25]. The responses were recorded and correlated with GC-MS results.

6.2.6. Methodology for extraction and determination of 1,8-cineole from cardamom samples

Considering the importance of 1,8-cineole, an attempt has been made to measure the actual 1,8-cineole content in a large cardamom sample using the sensor response. To execute this, a method has been optimised, consisting of three steps.

Sample preparation:

40-50 dried fruits of large cardamom were taken from the same stock, and the seeds were ground into powder in a clean mortar and pestle.

a. **For solvent extraction:** 1-gram powered sample was taken into a clear airtight glass vial containing 5ml chromatography grade dichloromethane (DCM) to extract the total 1,8-cineole present in the sample. The powdered cardamom sample was kept in the DCM for

48 hours in 4 ^{O}C. After 48 hours, yellowish-brown cardamom extract was recovered and centrifuged to obtain a yellowish-brown clear DCM solution. To maintain the volume of the extract to 5 mL, volume makeup was done as per needed.

b. **For headspace (HS) analysis:** Approximately 1 gram of powdered sample was taken into a 25 mL crimp neck clear glass vial and crimped immediately, kept for vapour saturation for 15 minutes to analyse 1,8-cineole present in the headspace of the vial.

c. **For sensor output:** At the same time, 10 grams of powdered sample was taken into 250 mL desiccator and incubated enough times to thoroughly saturate the headspace with the large cardamom volatiles, which were later used to obtain the sample-specific sensor responses.

Step 1: (a) Analysis of 1,8-cineole in the solvent extract:

To assay 1,8-cineole content in 5 mL solvent extract, 0.5µL of DCM extract was injected into GC-MS column and analysed using our pre-optimised program. After the generation of the TIC signal, a total peak area of 1,8-cineole was recorded. The peak area obtained from the chromatogram represents the 1,8-cineole content present in 0.5µL of DCM extract. To obtain the total qualitative 1,8-cineole content in 1gram of cardamom (which is dissolved in 5ml DCM), the peak area was multiplied by 10000 for calculation. The same analytic parameters were maintained for all the experimental samples.

Quantitative estimation of 1,8-cineole content in 1gram of large cardamom was done using gas chromatography followed by tandem mass spectroscopy (Thermo Auto SRM). To execute this, 0.1 µg/mL, 0.25 µg/mL, 0.5 µg/mL, 1 µg/mL, 2 µg/mL, 3 µg/mL, 4 µg/mL, and 5 µg/mL concentrations of 1,8-cineole were prepared in DCM and a calibration curve was prepared in Thermo Auto SRM software. Successively, 0.5 µL of large cardamom extract was injected into GC-MS-MS to obtain absolute 1,8-cineole content (µg/0.5µL) in the injected volume. To acquire the total 1,8-cineole (µg/g) content in 1 gm of sample, the amount of 1,8-cineole, we obtained from MS-MS was recalculated to 10000x (as 0.5 µL extract was injected from 5000 µL extract)

Step 2: (b) Analysis of 1,8-cineole in HS:

To analyse 1,8-cineole content present in the HS, SPME-guided Gas Chromatography-Mass Spectrometry was done following the previous protocol as discussed in Chapter 2, section 2.3.3 and the total peak area of 1,8-cineole in the TIC chromatogram was recorded. A similar analysis was done for all the large cardamom samples considered in this chapter.

Step 3: (c) Generation of sensor output:

Following the incubation of 10 gram large cardamom in 250 mL desiccator for 15 minutes, 50 mL of headspace air, which is saturated with 1,8-cineole from the sample, was injected into the sensor chamber to obtain the frequency shift values generated by the designated chamber. The sampling was repeated five times (in 30 min intervals), and the sensor output was recorded for every sample.

The respective 1,8-cineole content with 1,8-cineole peak areas of each sample is tabulated in Table. 6.1

Table 6.1. 1,8-cineole peak area and absolute content in cardamom samples using SPME-GCMS

Sample	1,8-cineole SPME peak area	Absolute 1,8-cineole content (µg/g)
L1	62428060.7	763.285
L2	82756975.08	1330.954
L3	148014990.7	4095.648
L4	134398608.7	3537.425
L5	114447028.2	2015.262
L6	156699396.8	4347.675
L7	135198906.6	3040.218
L8	124398608.7	2859.396
L9	126721131.9	2999.444
L10	82639710.15	1293.263

L11	75590097.17	1234.816
L12	53068125.13	584.312
L13	163837923.4	5880.772
L14	117375210.3	1658.127
L15	84960325.23	1223.192
L16	112526444.3	2309.529
L17	156314191	4373.059
L18	181097729	8309.629
L19	179285430	7540.390
L20	201927578.3	12069.799
L21	151609861	4874.948

6.3. Results and discussion

6.3.1. Study of the sensing properties of QCM-CAS sensor

In this work, we initially investigated the sensitivity of oil-based sensor layers to detect 1,8-cineole. We have previously observed that due to the large surface area, eighteen carbon-long fatty acids have enough potential to interact with monoterpenes [24,26]. Considering this, we have selected four eighteen carbon-long fatty acids, varying degrees of complexity and chemical nature, in our study. The considered fatty acids and respective oils are olive oil (Oleic acid, MW=282.5), Rice bran oil (Linoleic acid MW=280.4), and linseed oil (Linolenic acid MW=278.4), and castor oil (Ricinoleic acid MW=298.5). Initially, the sensors were exposed to different concentrations (10-1000 ppm) of the saturated headspace of 1,8-cineole. The sensitivity of the different sensors was based on the different oil coatings on the sensor layer and the mass of the incoming volatiles adsorbed on them. The sensitivity plots of the sensors are depicted in Fig. 6.2.

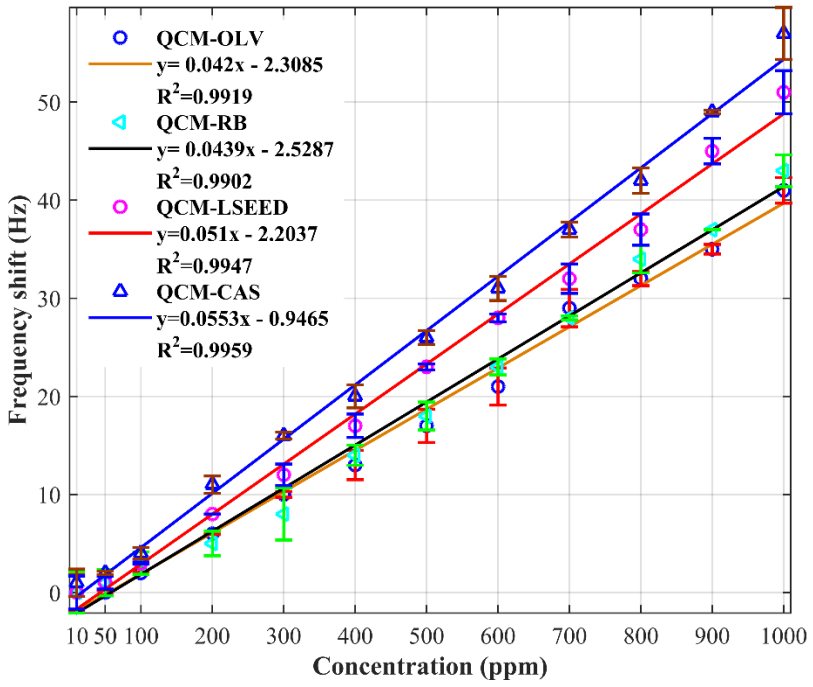

Fig. 6.2. The sensitivity of QCM-OLV, QCM-RB, QCM-LSEED, and QCM-CAS sensor towards 1,8-cineole vapour at 10–1000 ppm concentration operated at (27 ± 1) °C, RH = 67.70% and standard atmospheric pressure.

Detailed properties of the selected fatty acids are given in Table 6.2. Their chain length is the same, so their surface area doesn't vary significantly. However, in terms of polar surface area, ricinoleic acid has the edge over the other fatty acids. Owing to the presence of a hydroxy group at 12th carbon, ricinoleic acid has a significantly higher amount of polar surface area (57.5 Å^2) than the rest (37.3 Å^2). In addition, the hydroxy group's presence also lowers the ricinoleic acid's hydrophobicity (log kow = 6.19). These two factors mentioned above make the ricinoleic acid unique and accountable for sensing less or moderately hydrophobic monoterpenes like 1,8-cineole.

Table 6.2. Detailed properties of fatty acids selected in this study

Properties	**Oleic acid**	**Linoleic acid**	**Linolenic acid**	**Ricinoleic acid**
Molecular weight	282.5	280.5	278.5	298.5
Unsaturation (number/position)	1 (9th C)	2 (9th, 12th C)	3 (9th, 12th, 15th C)	1 (9th C)
Polar molecules	-COOH (1st C)	-COOH (1st C)	-COOH (1st C)	-COOH (1st C), -OH (12th C)

Hydrophobicity (log kow)	7.64	7.05	6.46	6.19
Polar surface area	37.3 $Å^2$ (C-terminal)	37.3 $Å^2$ (C-terminal)	37.3 $Å^2$ (C-terminal)	37.2 $Å^2$ (C-terminal); 20.2 $Å^2$ (12^{th} C position)

1,8-cineole, the principal volatile under the main focus, has a considerable affinity towards oil or fatty acids due to its chemical nature. Besides, some unique features of 1,8-cineole ensure the molecule's enhanced affinity towards ricinoleic acid. This target volatile is a bicyclic monoterpene ether and becomes considerably less hydrophobic due to polar ether group 1,8-cineole. In addition, the polar moiety's presence creates a polar patch on the 1,8-cineole surface (9 $Å^2$).

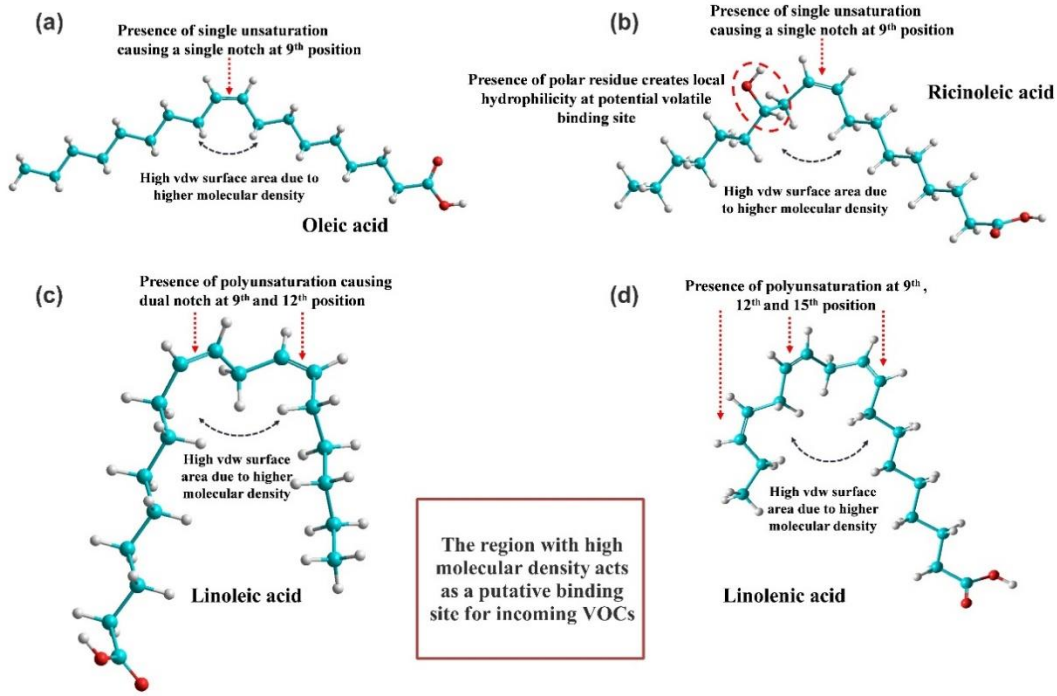

Fig. 6.3. Structural features of (a) olive oil (oleic acid), (b) castor oil (ricinoleic acid), rice bran oil (linoleic acid), and (c) linseed oil (linolenic acid) coated QCM sensor affecting the sensitivity towards 1,8-cineole. (Red- O atom, Blue- C atom, and white-H atom).

These aforesaid chemical properties of the target molecule facilitate the molecule's interaction with the polar surface present in the middle of ricinoleic acid, resulting in higher sensitivity. On the contrary, the other fatty acids do not have any polar patch in the middle of their surface, which indirectly interferes with the interactions between 1,8-cineole and other fatty acids, resulting in lowered sensitivity.

6.3.2. Study of the sensing properties of QCM-Phe-CAS-Phe sensor

As shown in Fig. 6.4, the 1,8-cineole gas sensing properties of castor oil (QCM-CAS) and its modified forms (QCM-CAS-Hex, QCM-CAS-Phe, and QCM-Phe-CAS-Phe) were compared. All sensors were subjected to concentrations ranging from 10 to 1000 parts per million of 1,8-cineole VOC, and the frequency responses were shown. With increased 1,8-cineole concentrations, all sensor responses increased. Compared to CAS, CAS-Hex, and CAS-Phe coated sensors, the Phe-CAS-Phe coated sensor exhibits noticeably enhanced frequency responses at varying 1,8-cineole concentrations. Due to this enhanced sensitivity of 1,8-cineole towards QCM-Phe-CAS-Phe, only this sensor was selected for further studies.

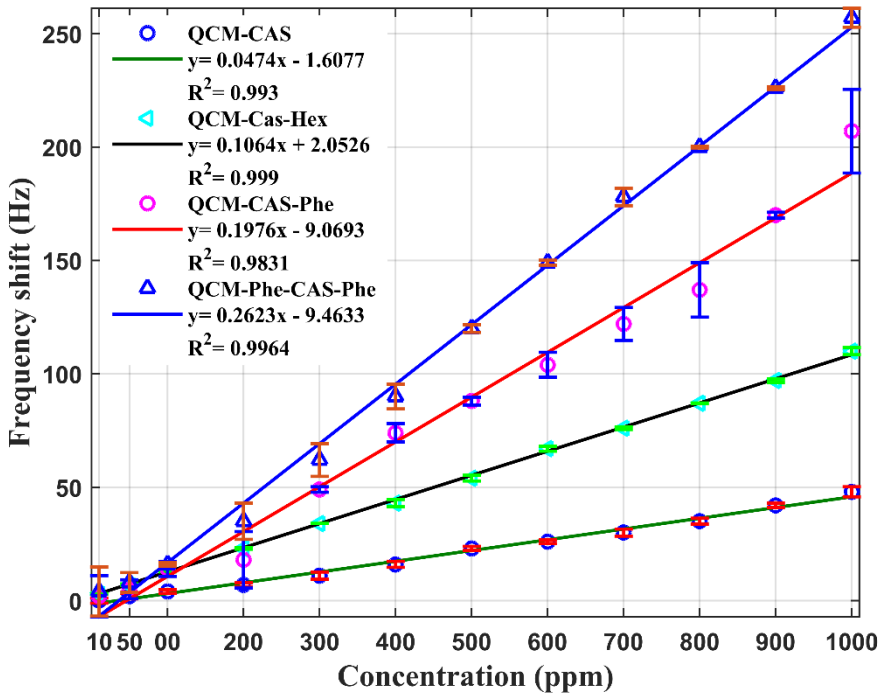

Fig. 6.4. The sensitivity of QCM-CAS, QCM-CAS-Hex, QCM-CAS-Phe, and QCM-Phe-CAS-Phe sensor towards 1,8-cineole vapor at 10–1000 ppm concentration operated at (27 ± 1) °C, RH = 67.70%, and standard atmospheric pressure.

6.3.3. Possible explanation behind the enhanced sensitivity of QCM-Phe-CAS-Phe sensor

Different castor oil modifications were done to attain enhanced sensitivity towards 1,8-cineole, and the modified castor oil products have been screened to select the best suitable modification. Primarily, two transesterifications were done to increase the surface area of sensing material, as it was reported that the interaction between two molecules, especially Van der Waals interaction, is dependent on the molecular surface area. The first two modifications were hexyl ricinoleate (CAS-Hex) and phenyl ricinoleate (CAS-Phe). If the molecular weights and carbon numbers are considered, both the modifications are equivalent. However, if the vdW surface area and hydrophobicity are considered, phenyl ricinoleate comprises superior characteristics like higher vdW surface area and lower hydrophobicity. **Owing to these properties, phenyl ricinoleate secures the best position in terms of sensitivity.** After selecting phenyl ricinoleate, a second step modification was done to add a hydrophilic patch on the surface of the sensing material, increasing the sensitivity of the sensing material. In this step, a phenol molecule was added to the 9^{th} carbon of phenyl ricinoleate (Phe-CAS-Phe) (Phenolated-phenyl ricinoleate). **This addition has increased the quality of sensor material in two ways. Firstly, due to the addition of a second phenol group, the vdW surface area of the molecule increased, and a twisted groove-like structure was developed. Secondly, adding the phenol group on the 9^{th} carbon created a hydrophilic patch in the middle of a possible volatile binding site. The detailed physical properties of the castor oil and its modified form are tabulated in Table 6.3.** The increased vdW surface area of phenolated-phenyl ricinoleate is accountable for the sensing material's augmented sensitivity towards 1,8-cineole. On the other hand, the additional hydrophilic patch made the sensing material selective for 1,8-cineole, which is partially polar. Due to these reasons described above, Phenolated-phenyl ricinoleate showed better sensitivity towards 1,8-cineole, and thus this material was selected for our further study.

Table. 6.3. Different physical properties of castor oil and its modified forms.

Properties	**CAS**	**CAS_Hex**	**CAS_Phe**	**Phe_CAS_Phe**
Molecular weight (Excluding H)	264	336	336	408
Solvent accessible surface ($Å^2$)	890.68	1153.62	1001	1010.18
van der Walls surface ($Å^2$)	442.43	457.08	554.75	652
Hydrophobicity (log P)	**5.09**	**7.12**	**5.61**	**5.62**

Fig. 6.5(a) illustrates the QCM-Phe-CAS-Phe sensor response curve after 1000 ppm 1,8-cineole VOC is injected into the sensor chamber. Before adding the VOC, the sensor frequency remained stable for 10 seconds. After injection, the frequency rapidly decreased to 333 Hz within 15 seconds. Then, the sensor frequency gradually rose until it reached a saturation level of 257 Hz. When the sensor was cleansed with ambient air (as shown by an arrow in the illustration), the sensor frequency increased gradually until it reached the sensor baseline. As a result, the sensor profile demonstrated good reversibility with little drift. The response (t_{res}) and recovery (t_{recov}) times of the QCM-Phe-CAS-Phe sensor were determined to be 6 and 24 s, respectively, when exposed to 1000 ppm 1,8-cineole.

The characteristic responses for the QCM-Phe-CAS-Phe sensor in comparison to the bare QCM sensor for 1,8-cineole at different concentrations (10-1000 ppm) have been displayed in Fig. 6.5(b). It was visible that the bare QCM showed no frequency changes due to the unavailability of the sensing layer. However, in the case of the QCM-Phe-CAS-Phe sensor, the response curves showed identical properties, with increasing frequency shift for increasing input volatile concentrations following Sauerbrey's equation [27]. Moreover, it can be noticed that the time for attaining the saturation state varied for different concentrations of 1,8-cineole. All the sensor responses achieved the initial baseline during the purging process without showing any drift.

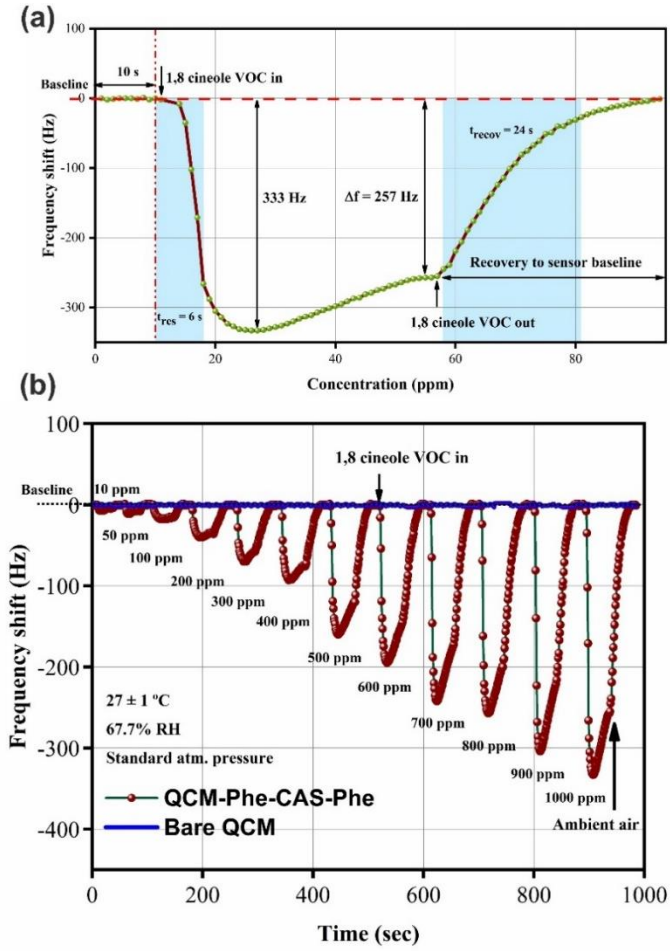

Fig. 6.5. Complete QCM-Phe-CAS-Phe sensor response profile (a) for 1000 ppm of 1,8-cineole (b) at different concentrations of VOC ranging between 10 and 1000 ppm at (27 ± 1) °C, 67.7% RH and standard atmospheric pressure.

The curve fitting function of the frequency shifts at saturation state for a varied concentration of 1,8-cineole is calculated as $\Delta f = 0.262x - 9.463$, where Δf was the frequency response at saturation state (Hz), x was the 1,8-cineole concentration (ppm). The sensitivity of the QCM-Phe-CAS-Phe sensor was calculated as 0.262 Hz/ppm, along with a correlation coefficient, $R^2 = 0.9964$. The standard error estimate (σ_{est}) was evaluated as 6.47 Hz, which estimates the average value of the error generated between the exact sensor output and approximated output derived from the characteristics equation [24,25]. The limit of detection (LOD) and limit of quantification (LOQ) of the sensor was estimated as 6.6 Hz and 21.8 Hz, respectively [24,25].

6.3.4. QCM-Phe-CAS-Phe sensor loading optimisation

The appropriate loading of the fabricated QCM-Phe-CAS-Phe sensor was determined by evaluating the associated frequency changes toward 1,8-cineole. Seven QCM sensors with loadings ranging from 4000 to 10000 Hz were fabricated with the synthesised Phe-CAS-Phe coating material (QCM-Phe-CAS-Phe_4000, QCM-Phe-CAS-Phe_5000, QCM-Phe-CAS-Phe_6000, QCM-Phe-CAS-Phe_7000, QCM-Phe-CAS-Phe_8000, QCM-Phe-CAS-Phe_9000, and QCM-Phe-CAS-Phe_10000). The frequency shift of the seven sensors were measured after exposure to 700 ppm of 1,8-cineole VOC. The frequency loading of the sensors and their responses were displayed in Fig. 6.6. Initially, increased loading had a favourable effect on the sensor responses. However, after a specific frequency (7000 Hz), though the sensor responses increased, the net change in sensor response degraded, thus inclining towards saturation.

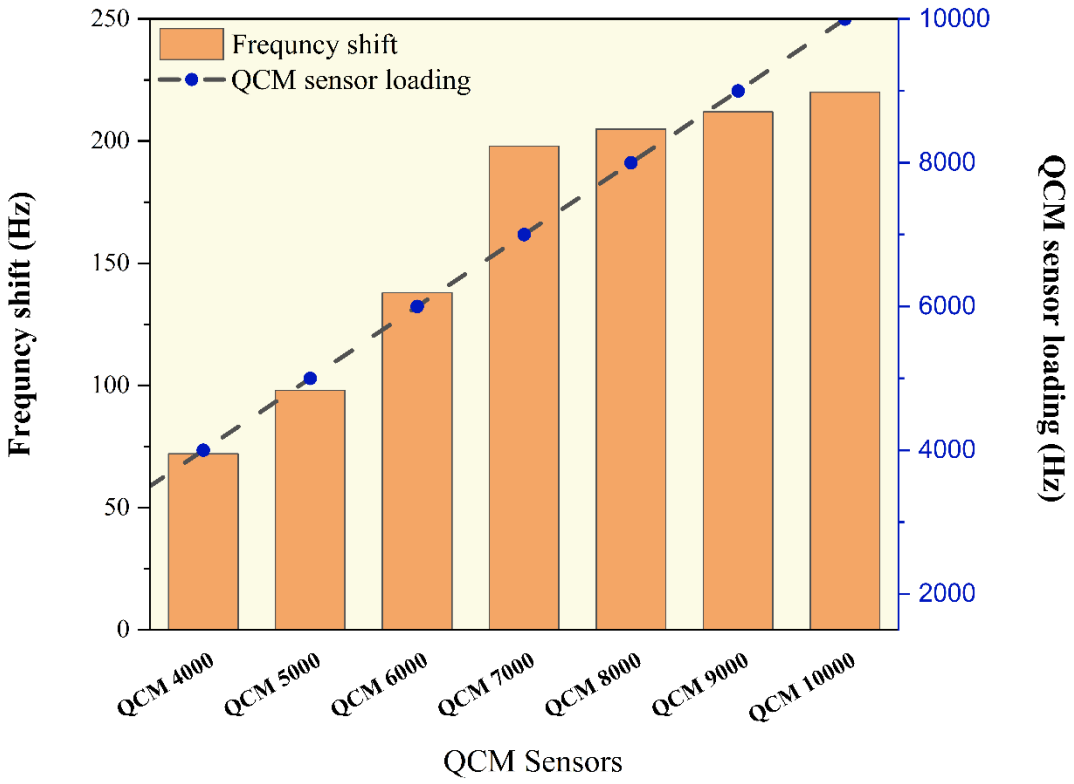

Fig. 6.6. QCM-Phe-CAS-Phe sensor responses towards 700 ppm 1,8-cineole for various sensor loadings (4000 – 10000 Hz).

The short-term stability of QCM-Phe-CAS-Phe sensors above 7000 Hz was further studied to attain the optimum loading state. In order to assess short-term stability, the QCM-Phe-CAS-Phe

sensors with loadings 7000, 8000, and 9000 Hz were mounted in the sensor chamber, and the respective frequency fluctuations were recorded for 200 seconds. Table 6.4 shows the coefficient of variation (CV) that estimates the variations in sensor readings [28].

Table 6.4. Short term stability of QCM-Phe-CAS-Phe sensor at different sensor loading

Sensor loading (Hz)	**7000**	**8000**	**9000**	**10000**
CV (%)	0.000015	0.000060	0.000118	0.000167

It can be seen that the CV of the sensors steadily surged with increasing loading on the sensor surface, making the sensors more unstable and erroneous. Compared to the initial findings, the optimal loading for QCM-Phe-CAS-Phe coating material has been selected at 7000 Hz to guarantee improved sensor responses with less instability.

6.3.5. Study of the binding interaction of QCM-Phe-CAS-Phe sensor with 1,8-cineole using UV-Visible spectroscopy

In the present study, UV-Vis spectroscopy (Shimadzu double beam spectrophotometer, serial no. A116351) was done to investigate whether there is any occurrence of molecular interaction between ligand (1,8-cineole) and sensing material (Phenolated 12-hydroxy stearic acid phenyl ester/ Phenolated phenyl ricinolate). Firstly, we have measured the absorbance of 1,8-cineole and phenolated phenyl ricinolate individually at different concentrations (1-20 µL), which is represented in Figures 6.7(a) and (b), respectively. From the absorbance spectra of 1,8-cineole, it was found that the molecule has an absorbance maxima of 230 nm. The spectrogram of phenolated phenyl ricinolate showed four distinct peaks at 229 nm, 265 nm, 271 nm, and 277 nm, with absorbance maxima at 271 nm.

In the next step, we measured the absorbance of different mixtures of phenolated phenyl ricinolate and 1,8-cineole. In this assay, the concentration of phenolated phenyl ricinolate was kept constant (20 µL), while we gradually increased the concentration of 1,8-cineole (1-20 µL). It was observed that with an increasing concentration of 1,8-cineole in the mixture, the absorbance of phenolated

phenyl ricinolate gradually weakened. This declining absorbance or hypochromatic shift in response to increasing 1,8-cineole concentration, as shown in Fig. 6.7(c), is possibly due to the diminution of free phenolated phenyl ricinolate in the mixture. It was also found that in a lower concentration of 1,8-cineole (1 µL-5 µL), the absorbance of the last three peaks, i.e., 265 nm, 271 nm, and 277 nm, was most affected; however, in higher concentration, the absorbance of all the peaks was equally collapsed. It could be assumed that at a lower concentration, the 1,8-cineole molecules interact primarily with phenol or phenyl residues of phenolated phenyl ricinolate. On the other hand, at a higher 1,8-cineole concentration, the molecule interacts with the whole molecules of phenolated phenyl ricinolate. In addition, it was also found from the experiment that these interactions between two considered molecules are entirely physical, and no chemical reaction is involved in response to the co-incubation of two molecules; no naïve absorbance pattern was generated.

We have also performed a time kinetics assay using UV-Vis spectrophotometry to understand the nature of the interaction between two molecules, as illustrated in Fig. 6.7(d). To fulfil the purpose, we have taken 20 µL of modified castor derivative in a glass cuvette, and its absorbance at 271 nm was recorded for 5 minutes. This specific wavelength was selected based on our previous experience. In our previous step, we found that this 271 nm absorbance peak was affected most in the presence of 1,8-cineole. Following five minutes of data recording, we added 20 µL of 1,8-cineole in the previous mixture, and the absorbance data was recorded for the next ten minutes. It was found that after adding 1,8-cineole, absorbance at 271 nm got rapidly masked. However, after a specific time, absorbance at 271 nm started to recover and eventually reached close to its maximum absorbance value.

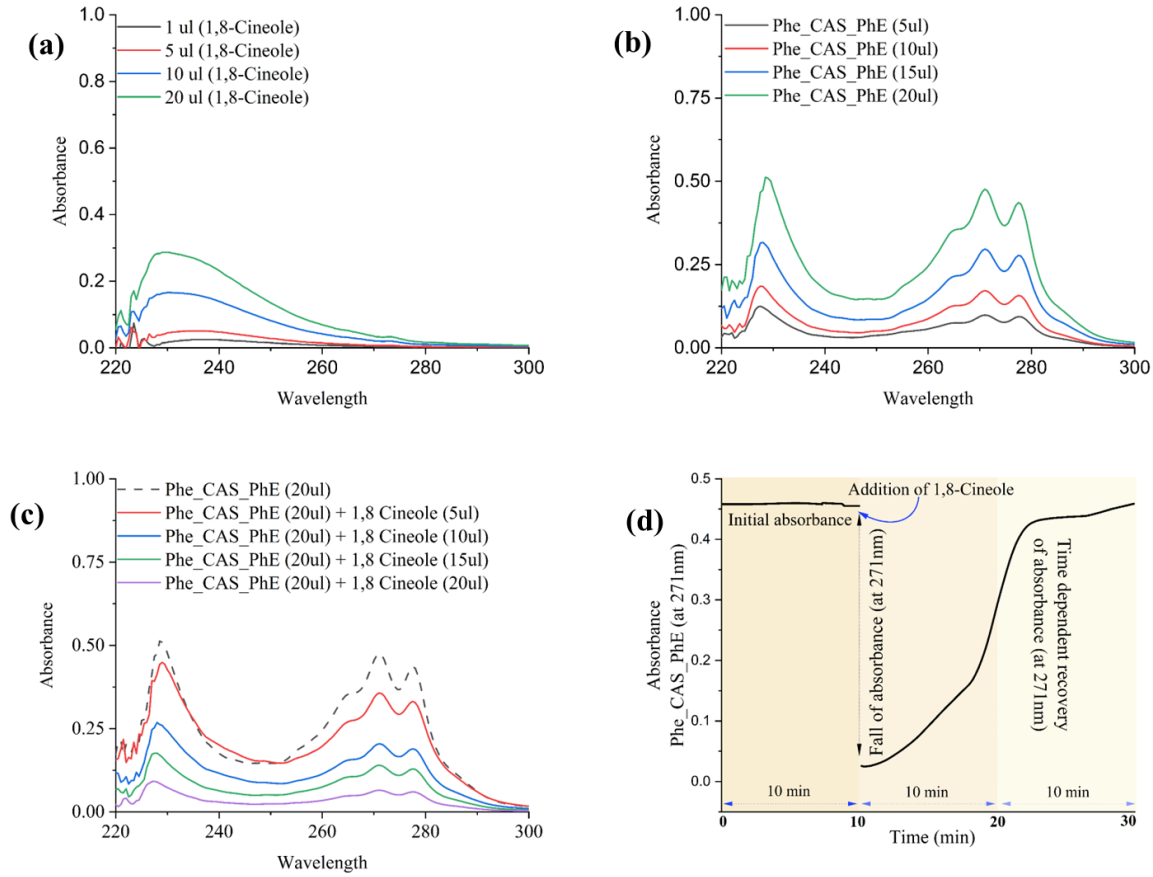

Fig. 6.7. The UV–vis absorption spectra of (a) 1,8-cineole, (b) Phe-CAS-Phe. (c) the interaction between Phe-CAS-Phe and 1,8-cineole, and (d) temporal absorbance shift of Phe-CAS-Phe after the addition of 1,8-cineole.

6.3.6. Study of the binding interaction of QCM-Phe-CAS-Phe sensor with 1,8-cineole using GCMS

The affinity of 1,8-cineole towards phenolated phenyl ricinolate was also determined using GC-MS. In three 22 mL airtight teflon coated screw cap glass vials, 1 mL of n-Hexane, Castor oil (20% in n-Hexane), and Phenolated castor oil phenyl ester (20% in n-Hexane) were mixed thoroughly. In a subsequent step, 5 µL of 1,8-cineole was added to each vial. After 5 minutes of vapour generation, headspace sampling of 1,8-cineole from each vial was done using solid-phase microextraction technology and analysed in GCMS. Similar headspace sampling and subsequent quantification were performed tandemly ten times for all three sampling vials. A constant 5 minutes interval of vapour saturation was maintained between two samplings.

In the absence of castor oil or castor derivative, 1,8-cineole is rapidly released into the headspace in a higher amount and thus rapidly lost from the source. On the other hand, in the presence of castor oil, 1,8-cineole showed a somewhat delayed release pattern, which directly indicates that 1,8-cineole has a sort of affinity towards castor oil, and castor oil acts as a slow releasing agent for 1,8-cineole. However, in the third experimental setup, we obtain a more pleasing outcome as in the presence of modified castor oil, 1,8-cineole is released most reluctantly from the source, which signifies strong affinity of 1,8-cineole towards the castor derivate or phenolated ricinoleic acid phenyl ester.

The two experimental assays involving UV-Vis Spectrophotometer and Gas Chromatography-Mass Spectroscopy suggest that **1,8-cineole have a strong affinity towards the castor derivative, interacting with the derivative reversibly, and both of these features are favourable for the QCM mediated physisorption of gases.**

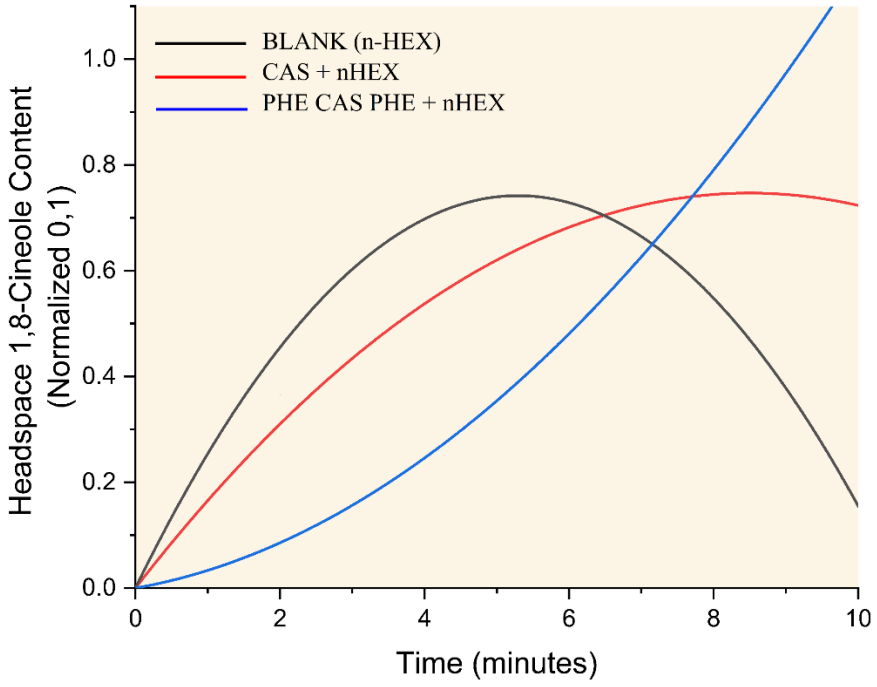

Fig. 6.8. Adsorption affinity of 1,8-cineole towards C.A.S., Phe-CAS-Phe coating materials evaluated by SPME-GCMS 1,8-cineole peak area.

6.3.7. Sensor surface characterisation

The SEM images (SEM: ZEISS, EVO-18, special edition, Germany) of the coated QCM-Phe-CAS-Phe sensor in comparison to the QCM-CAS sensor have been shown in Fig. 6.9. The

difference in morphology of the sensor surface can be visualised in Fig. 6.9 (a) and (c). Using the particle analysis approach (ImageJ software version 1.8.0_172), the average porosity of the QCM-Phe-CAS-Phe sensor was calculated to be 17.509 ± 0.64% which is higher than the QCM-CAS sensor, 3.87% (± 0.617%). Moreover, the nebulisation coating generated a uniform morphological behaviour throughout the sensor surface. Modified castor oil sensor has a rough surface, with the frequent non-uniform indentation that increases the sensor surface area. The increase in roughness and non-uniform indentation enhances the sensor surface area, which enhances the adsorption site of target VOC through different non-covalent bonds [29] which is shown in Fig. 6.9 (b) and (d).

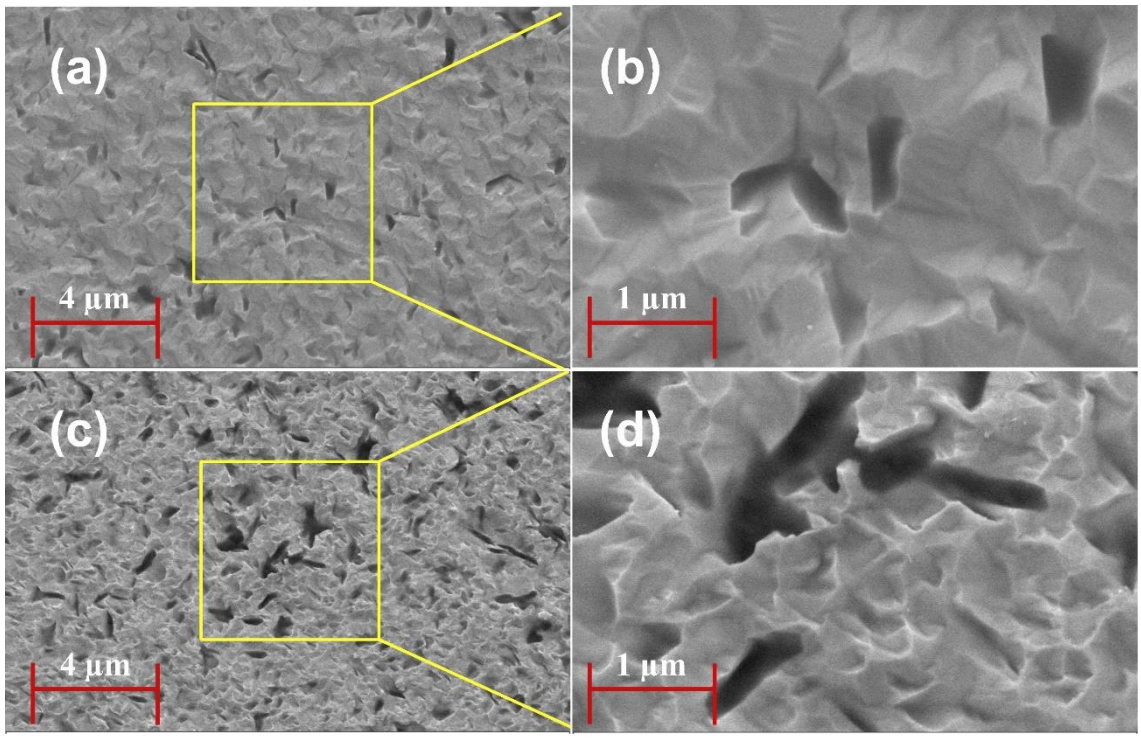

Fig. 6.9. SEM images of (a) QCM-CAS sensor (b) magnified version of the coated film on QCM-CAS sensor at 1 µm ; (c) QCM-Phe-CAS-Phe sensor; (d) magnified version of the coated film on QCM-Phe-CAS-Phe sensor at 1 µm.

The AFM pictures and their 3D visualisation of the sensor surface are shown in Figures 6.10(a) and (b). Fig. 6.10 (c) and 6.10 (d) illustrate the cross-sectional overview of Fig. 6.10 (a). The mean height of surface was determined to be 0.68 µm. The unusual surface of Phe-CAS-Phe coating topography can be visualised as a rugged and uneven rough surface. Additionally, the coated film demonstrates uniform and homogenous oil deposition on the quartz crystal surface. The AFM

analysis was performed on a 100 × 100 μm^2 area of the AFM picture. The roughness was calculated to be 403.4 nm root mean square (RMS), with a surface area of 10127 μm^2. Thus, increasing the surface area definitely aids in binding the target molecule appropriately, as size and symmetry matching are important in the lock-and-key mechanism of the sorption process.

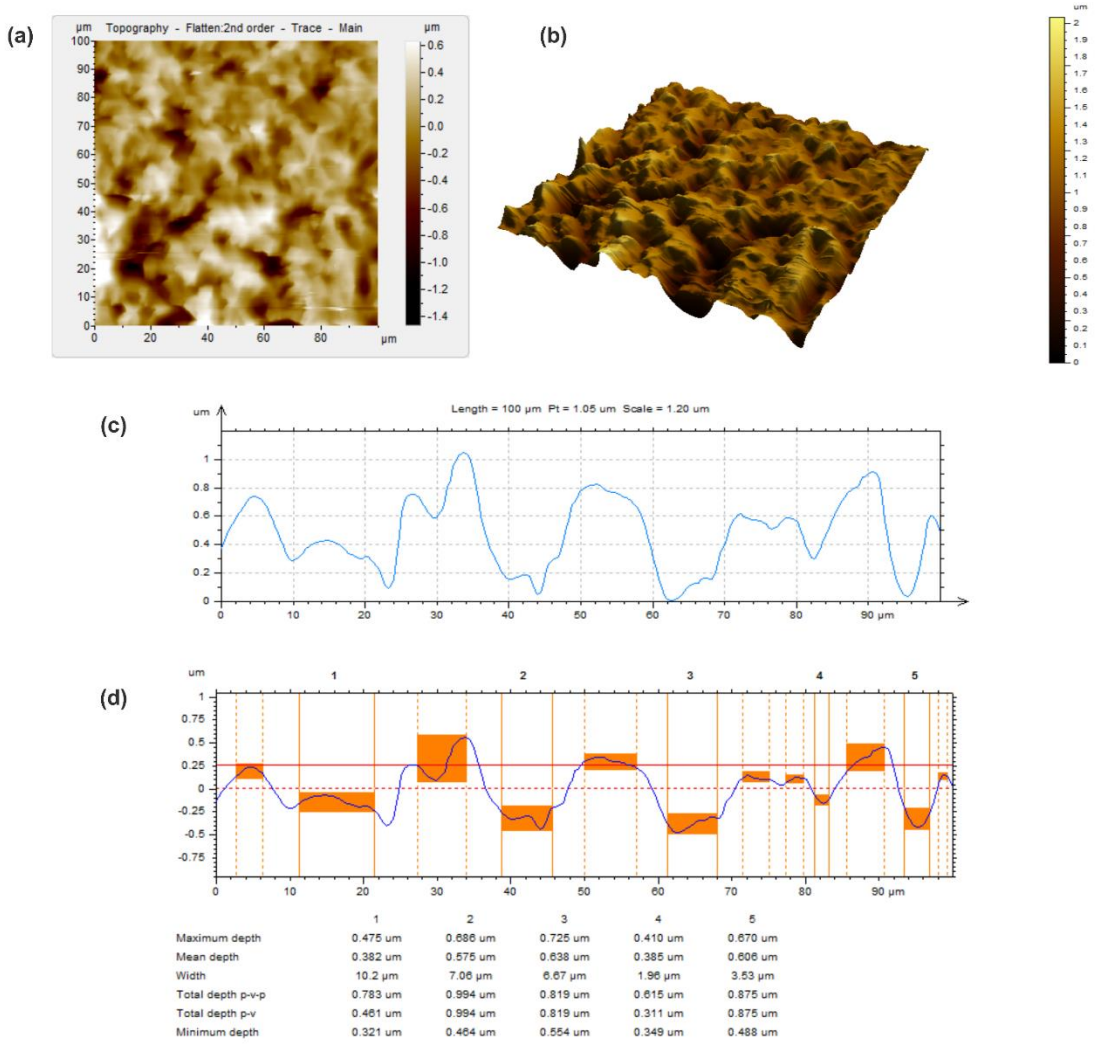

Fig. 6.10. AFM images of QCM-Phe-CAS-Phe sensor surface (a) Topography flattened; (b) 3D view; (c) profile curve; (d) step height measurement.

The FTIR spectrum of castor oil (Shimadzu FTIR spectrometer (IR Prestige), which has an abundance of ricinoleic acid/ 12-hydroxy octadecenoic acid, shows the presence of a prominent peak at 2924 cm^{-1} and 2842 cm^{-1} which are caused by symmetric and asymmetric C-H stretching of alkanes. In addition, the medium peak at 1463 cm^{-1} also hints toward the presence of C-H

bending of alkanes/alkenes. The transmission peak at 3004 cm^{-1}, which is attributed to the stretching of C=C, was also found, reflecting the presence of unsaturation in the coating material, i.e., castor oil. As the major fatty acid of castor oil naturally exists as an ester of glycerol, a prominent peak near 1737 cm^{-1} was also found, which signifies the C=O stretching of esters. Parallelly, a medium peak at 1163 cm-1was also found, which is accredited to C-O stretching. In addition to all these major peaks, a small but broad peak at 3303 cm^{-1} symbolises the free hydroxy group's presence in the coating material. In the modified castor oil or phenolated castor oil, elementary fingerprint peaks of fatty acids, i.e., 2924 cm^{-1}, 2840 cm^{-1}, 1705 cm^{-1} and 1456 cm^{-1}. Interestingly, in the modified castor oil, the peak 3004 cm^{-1} (which signifies unsaturation) was diminished entirely, and the transmittance peak of 3300 cm^{-1} (which implies the presence of hydroxyl group) was intensified. This is probably because of the replacement of mono-unsaturation (9th position) present in the ricinoleic acid with phenol the residue (Fig. 6.11). In addition, two other exclusive peaks at 1582 and 1510 signify the presence of aromatic C=C bond, which is present in the phenol reside.

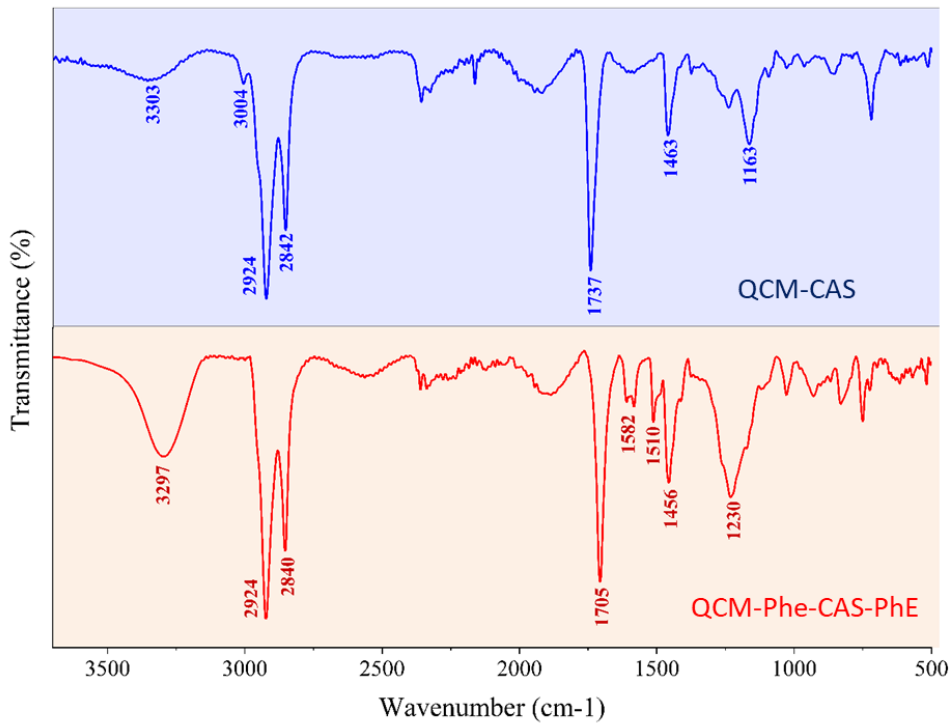

Fig. 6.11. FTIR spectra of castor oil and modified castor oil.

6.3.8. Electrical impedance study of QCM-Phe-CAS-Phe sensor

The conductance and susceptibility spectra of the uncoated QCM and Phe-CAS-Phe coated QCM sensor are shown in Figs. 6.12 (a) and (b), respectively. The conductance spectra of QCM sensors can be used to determine how rigid the film has been deposited on the QCM surface. According to the quality factor (Q-Factor), the rigidity of the QCM is defined as the ratio of the peak frequency to half-bandwidth in the conductance spectrum. Higher Q-factors are preferred for sensors with better stability, lower frequency noise, and less energy loss, as has been shown in the field of micro-/nanoelectromechanical systems (MEMS/NEMS) [30]. In ambient air, the Q–factors of the bare QCM and QCM-Phe-CAS-Phe sensors were measured to be 60488 and 37245, respectively, as per the results. Furthermore, as shown in Table 6.5, the equivalent circuit parameters of the bare crystal and Phe-CAS-Phe coated QCM were derived by fitting the admittance spectrum with Butterworth-Van Dyke (BVD) mode [31].

Table 6.5. Equivalent circuit parameters of Bare QCM and QCM-Phe-CAS-Phe

Sensor	f (Hz)	R (ohm)	L (mH)	C (fF)	C0 (pF)	Q
Bare QCM	9996295	11.17	10.98	23.06	18.13	60488
QCM-Phe-CAS-Phe	9986959	14.64	8.79	28.85	10.7	37245

It demonstrates that the Q-Factor decreased after the coating of the sensing layer. However, the value of the Q-Factor was still considered to be relatively high, indicating that the rigidity of the QCM had not been compromised. In this study, it was demonstrated that the nebulisation coating technique could be used to create rigid films that are resistant to low-frequency noise.

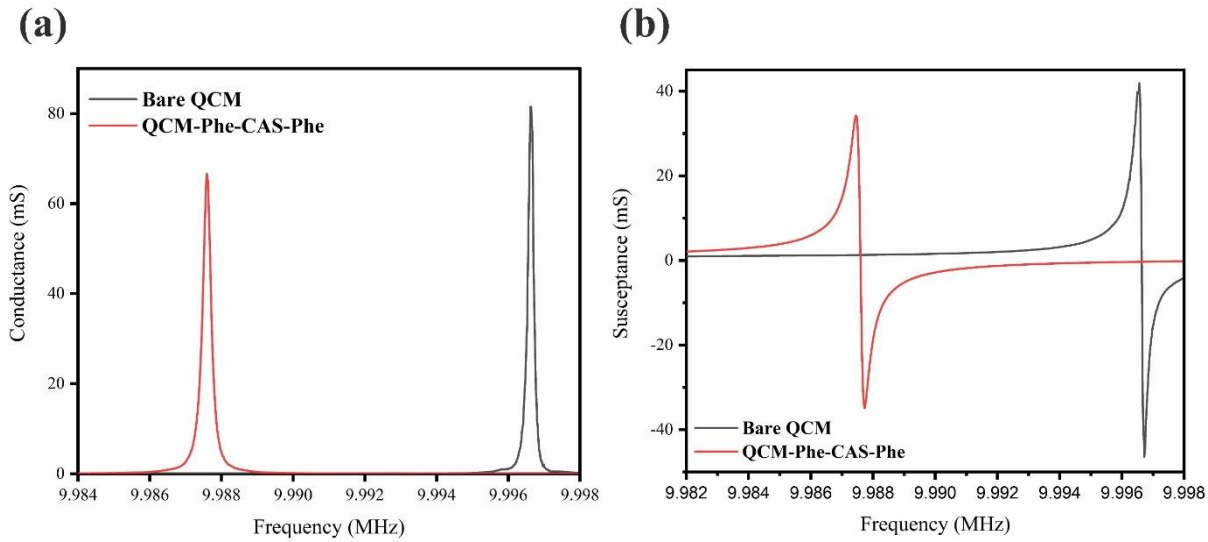

Fig. 6.12. (a) Conductance; (b) susceptance spectra of bare QCM and QCM-Phe-CAS-Phe.

6.3.9. Study of the selectivity properties of QCM-Phe-CAS-Phe sensor

We examined the selectivity of the developed QCM-Phe-CAS-Phe sensor to determine its effectiveness in identifying 1,8-cineole in the presence of other volatiles in actual samples. The developed sensor response was evaluated in the presence of various volatiles at concentrations ranging from 10 to 1000 ppm found in cardamom samples, including α-pinene, β-pinene, α-terpinyl acetate, α-terpineol, limonene, and γ-terpinene. Sensitivity was determined by averaging the sensor response over three sample phases for each VOC concentration.

The sensitivity graphs of the QCM-Phe-CAS-Phe sensor upon exposure to 1,8-cineole and other major volatiles in cardamom are shown in Fig. 6.13(a). The proposed sensor was demonstrated to be more sensitive to 1,8-cineole than to other volatile organic compounds (VOCs). The bar plot in Fig. 6.14 illustrates the susceptibility of competing VOCs to QCM-Phe-CAS-Phe. Fig. 6.13(b) illustrates the responses of the QCM-Phe-CAS-Phe sensor following controlled exposure to 800 ppm of the major VOC.s used in this study. The sensor revealed a high-frequency shift toward 1,8-cineole at both high and low concentrations (100% at 10 ppm; 55.27% at 1000 ppm) compared to the other volatiles tested in our study.

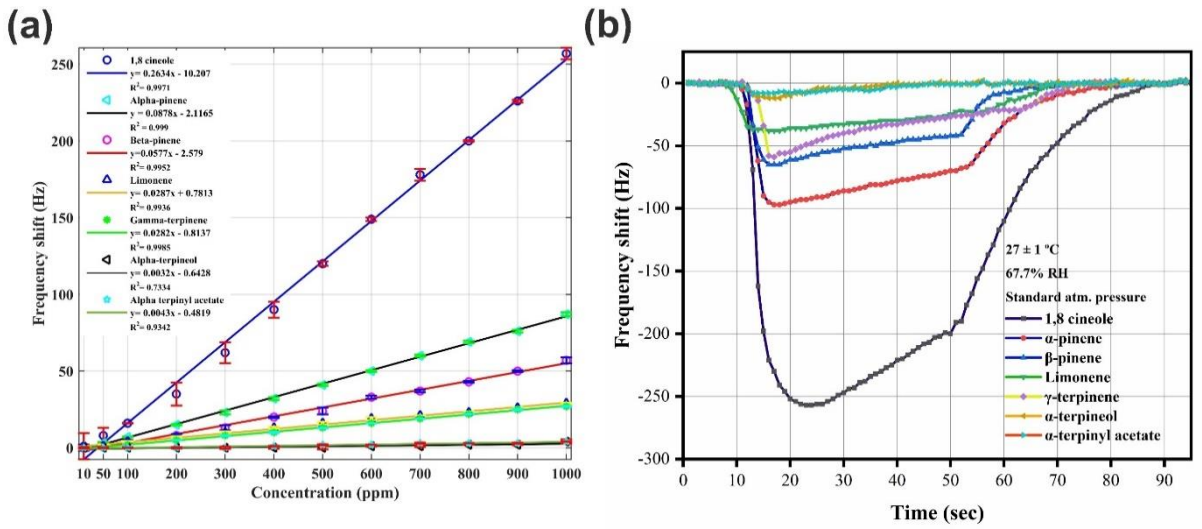

Fig. 6.13 (a. Characteristics QCM-Phe-CAS-Phe sensor responses towards 1,8-cineole and other competing VOCs ranging between 10-1000 ppm; (b) QCM-Phe-CAS-Phe sensor response pattern for 800 ppm of β-pinene, 1,8-cineole, α-terpinyl acetate, α-pinene, limonene, α-terpineol, and γ-terpinene at (27 ± 1) ºC, 67.7% RH and standard atmospheric pressure.

The corresponding selectivity (%) results are calculated as described earlier, and tabulated in Table 6.5

Table 6.5. Selectivity (%) of QCM-Phe-CAS-Phe sensor

Concentration (ppm)	**Selectivity (%)**						
	1,8-cineole	**α-pinene**	**β-pinene**	**Limonene**	**γ-terpinene**	**α-terpinyl acetate**	**α-terpineol**
10	100.00	0.00	0.00	0.00	0.00	0.00	0.00
50	61.54	23.08	7.69	7.69	0.00	0.00	0.00
100	48.48	21.21	12.12	12.12	6.06	0.00	0.00
200	50.00	21.43	11.43	10.00	7.14	0.00	0.00
300	53.45	19.83	11.21	8.62	6.90	0.00	0.00
400	54.22	19.28	12.05	7.83	6.02	0.60	0.00

500	55.56	18.98	11.11	7.41	6.02	0.93	0.00
600	55.19	18.52	12.22	7.04	5.93	0.74	0.37
700	55.80	18.81	11.60	6.58	5.96	0.94	0.31
800	55.25	19.06	11.88	6.35	6.08	0.83	0.55
900	55.39	18.63	12.25	6.37	6.13	0.74	0.49
1000	55.27	18.71	12.26	6.24	5.81	0.86	0.86

All the monoterpenes found in nature have a common property, i.e., they have an affinity towards oils, specifically fatty acids. This is also a significant factor behind the success of our previous two sensors. Due to this nature, all monoterpenes that have considerable hydrophobicity tend to interact with fatty acids. Moreover, as the gas sensing by the sensing material is dependent on adsorption, the monoterpenes with high vapour pressure have an advantage of sensitivity over the monoterpenes with a low vapour pressure at room temperature. Molecular complexity is another essential factor that ensures proper interaction between sensing material and volatile targets. In terms of molecular interaction, volatile with less complexity can bind to multiple sites or grooves, and thus they give a higher hit rate. On the other hand, structurally more complex ligands (in our cases, volatiles) can only bind with specific sites present on the sensing material as they have less freedom to interact with multiple target sites.

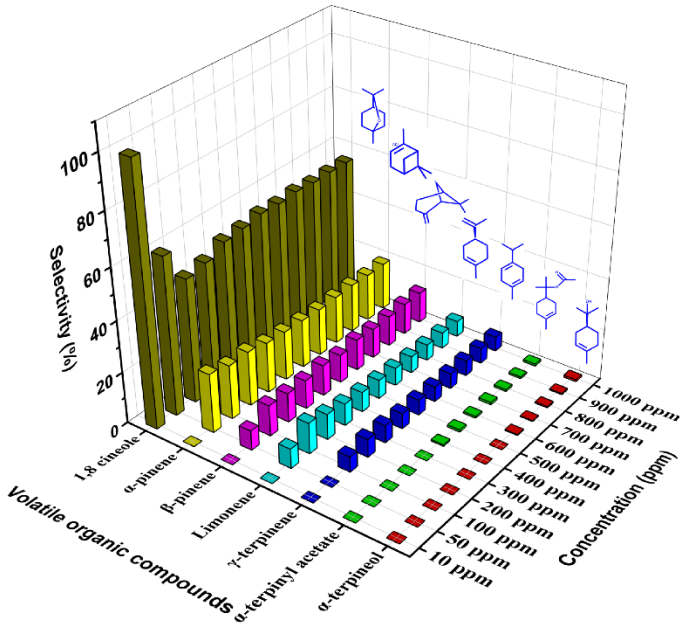

Fig. 6.14. Bar plot diagram of % selectivity of the QCM-Phe-CAS-Phe sensor for β-pinene,1,8-cineole, α-pinene, limonene, α-terpineol, α-terpinyl acetate, and γ-terpinene VOCs at 10-1000 ppm.

The volatiles that is dominant in cardamom HSV are considered in our study for selectivity and sensitivity experiments. All these VOCs are monoterpene in nature with varying degrees of chemical properties. We have mentioned earlier that vapour pressure and hydrophobicity are two major factors behind the sensitivity of target volatile on oil-coated QCM surfaces. Based on this, all the other volatiles excluding 1,8-cineole showed a decreasing adsorption potential on the oil surface as their vapour pressure, and hydrophobicity (Adsorption on oil surface ∝ Vapor pressure x Hydrophobicity) gradually falls (R^2= 0.9825). α-pinene, β-pinene, and limonene have high vapor pressure and hydrophobicity thus, they adsorbed on the hydrophobic coating surface to some extent. On the other hand, terpinyl acetate and terpineol are less hydrophobic and have very low vapor pressure, which is the main cause behind their incompetency to adsorb on oil-coated QCM surfaces. γ-terpinene, though a higher degree of hydrophobicity but due to low vapor pressure, also became ineffectual. The different physical and chemical properties of the volatiles responsible for interaction with monoterpenes are discussed in Table 6.6.

Table 6.6. Physical and chemical properties of dominant monoterpenes in cardamom

Physical and chemical parameters	**α-pinene**	**β-pinene**	**Limonene**	**1,8-cineole**	**γ-Terpinene**	**α-Terpinyl acetate**	**α-Terpineol**
Molecular weight	136.23	136.23	136.23	154.25	136.23	196.28	154.25
Hydrophobicity (log P)	4.83	4.16	4.57	2.74	4.5	3.96	2.67
Vapor pressure (mmHg at 25°C)	4.75	2.93	1.64	1.9	1.07	0.039	0.028
Flash point °C	32.22	35	47.22	50	51.67	99.44	88.33
Odor strength	High	High	Medium	High	Medium	Medium	Medium
Chemical nature	Bicyclic monoterpene	Bicyclic monoterpene	Monocyclic monoterpene	Bicyclic monoterpene ether	Monocyclic monoterpene	Monocyclic monoterpene acetate	Monocyclic monoterpene alcohol
Unsaturation number/type	1, Endocyclic	1, Exocyclic	2, Exo and endocyclic	0	2, Endocyclic	1, Endocyclic	1, Exocyclic
Functional group(s)	None	None	None	Ether (-O-)	None	Carbonyl (C=O)	Hydroxy (-OH)
Polar surface area	0	0	0	9	0	26.3	20.2
Molecular complexity	186	177	163	164	171	251	168

Exclusive of this oil-monoterpene lipophilic interaction, the considered volatiles have least affinity towards the phenolated castor oil. Due to multiple hydrophilic patches on the potential binding surface, volatiles like α-pinene, β-pinene, limonene, and γ-terpinene couldn't interact with the coating surface appropriately, respectively as these volatiles don't have any polar area on their

molecular surface. In addition, due to the presence of a polar patch, the available hydrophobic surface area for these volatile's binding gets reduced, resulting in restricted adsorption. Defiantly, α-terpineol and α-terpinyl acetate, though, have a significant amount of polar area on their surface. They did not adsorb appropriately due to very low vapour pressure. The next factor that made these volatiles ineffectual is their molecular complexity. α-terpinyl acetate, α-pinene, β-pinene, and γ-terpinene have a higher degree of molecular complexity, negatively influencing the molecules' adsorption potential. Due to these factors discussed, these volatiles become incompetent in front of 1,8-cineole in terms of sensitivity.

The target molecule, i.e., 1,8-cineole is not entirely hydrophobic; instead, due to the presence of an ether group, this molecule holds a partial polar surface, which aids the molecule to freely interact with the phenolated castor oil at multiple target sites irrespective of polar-nonpolar interaction. Moreover, 1,8-cineole is one of the least complex molecules in terms of molecular complexity, which helps the molecule adhere to multiple target sites and pass within the indentation, or groove present in the phenolated castor oil, resulting in higher adsorption. Due to these factors, 1,8-cineole get superiority over other volatiles in adsorption and sensitivity.

6.3.10. Study of the sensing mechanism of QCM-Phe-CAS-Phe using an in-silico approach

Molecular docking was conducted with Autodock tools v4.2 to find out the binding energies of each volatile (ligand) complexed with phenol-modified ricinoleic acid (receptor). Firstly, 3D structures of all concerned volatiles (treated here as ligands) were collected in SDF format from NIST online library and subsequently converted to PDB and PDBQT format using Openbabel 3.1.1. In a subsequent step 2D structure of the phenolated ricinoleic acid (regarded as a receptor) was drawn in Hyperchem v8, and in the next stage, it was geometrically optimised using the Polak-Ribiere algorithm, and the output file was saved as mol2 file. In a subsequent step, the mol2 file of the receptor was converted to PDB and PDBQT format using the same method as mentioned in the case of ligand preparation.

In the Autodock suite, a blind molecular docking approach opted for each volatile and phenolated ricinoleic acid. Firstly, in Autodock Tools software, using Autogrid 4.0, a grid box was drawn to cover the whole phenolated ricinoleic acid and trialled volatile. Afterwards, docking was done following Lamarckian GA 4.2 algorithm using Autodock 4.0. From the output conformations of

each volatile, the best ligand state was selected based on the docking score and lowest (Root Mean Square Deviation) RMSD value. The estimated free energy of binding (Kcal/mole) is positively influenced by the final intermolecular energy (vdW, electrostatic bond, hydrogen bond) while negatively influenced by the presence of torsion points in the volatile/ligand molecule(s). The molecular docking analysis revealed that 1,8-cineole has more favourable binding energy (ΔG= -3.46 Kcal/mole) with phenolated ricinoleic acid compared to other candidates monoterpenes (Table 6.7).

Table 6.7. Details of the molecular docking between Phe-CAS-Phe and trialled volatiles in cardamom

	Mean Binding energy (Kcal/mole)	Max Binding energy (Kcal/mole)	Number of vdW contacts	Number of hydrogen bonds
α-pinene	-3.29	-3.3	1	0
β-pinene	-3.28	-3.28	0	0
Limonene	-3.4	-3.41	1	0
1,8-cineole	-3.45	-3.46	5	0
γ-Terpinene	-3.08	-3.11	0	0
α-Terpineol	-3.3	-3.42	3	1
α-Terpinyl acetate	-3.33	-3.42	0	1

For the visualisation of the binding interactions, the best docking state was retrieved from Autodock 4.2 and visualised in PyMOL (vdW radius was set to 1.5 Å) shown in Fig. 6.15. It was found that the best root mean square deviation conformation (RMSD) of 1,8-cineole can make five possible vdW contact with the phenolated ricinoleic acid, with the bond lengths ranging between 2.7Å - 3.2Å. Besides 1,8-cineole, it was found that α-pinene (2.6Å), limonene (2.8Å) and α-Terpineol (2.2Å - 2.6Å) can also make vdW interaction with the receptor. In case of other volatiles, i.e., β-pinene, γ-terpinene and α-terpinyl acetate, no such binding interaction was formed. This computational observation clearly supports our previous finding, and it can be presumed that

higher binding energy of 1,8-cineole and phenolated ricinoleic acid, owing to plenty of vdW interaction, ensures the coating material's higher sorption affinity and capacity towards 1,8-cineole.

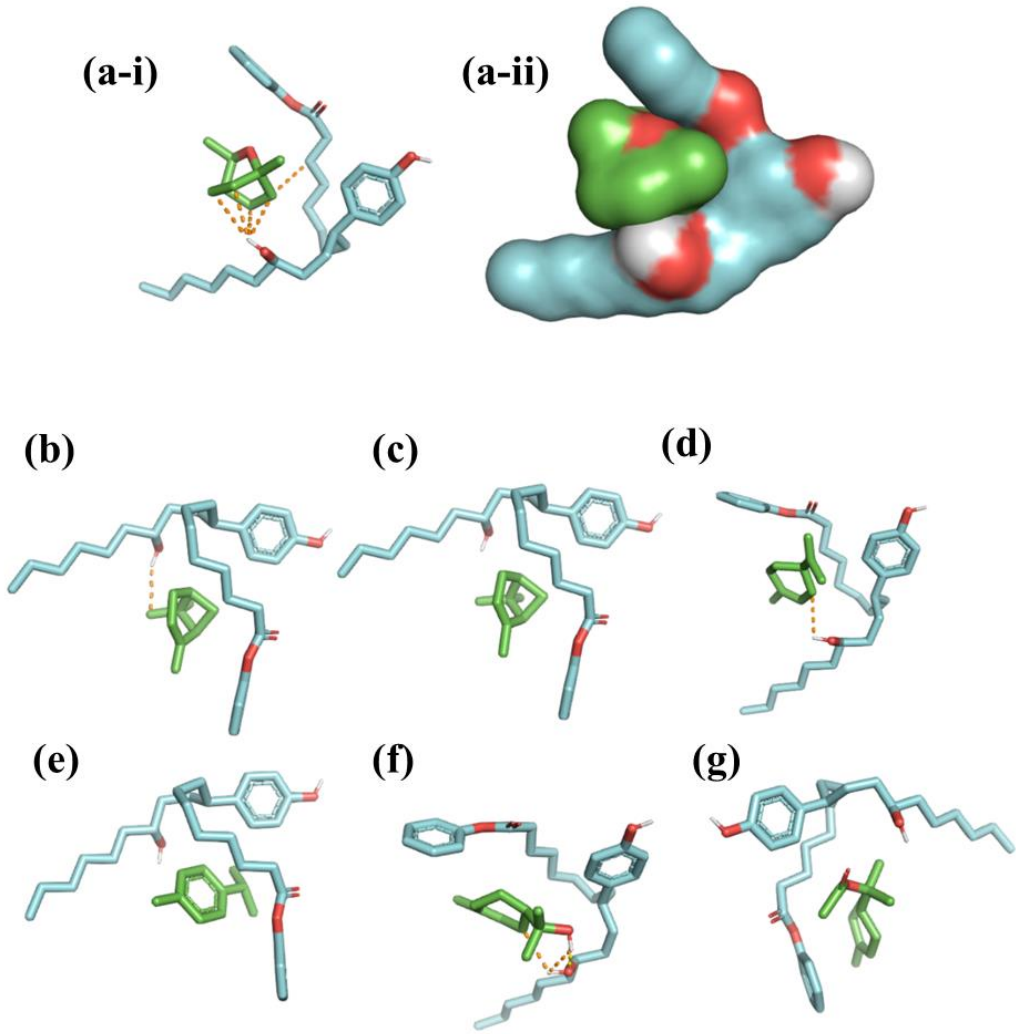

Fig. 6.15. Visualisation of the molecular interactions in the best docking states of (a i-ii) 1,8-cineole (b) α-pinene (c) β-pinene (d) limonene (e) γ-terpinene (f) α-terpineol (g) α-terpinyl acetate with Phe-CAS-Phe.

6.3.11. Equilibrium analysis of QCM-Phe-CAS-Phe sensor

The nature of surface adsorption between 1,8-cineole and the sensor surface across a definite range of concentration have been studied using the adsorption isotherm model. The details of the analysis have been discussed in Chapter 4, section 4.3.7. The isotherm models are depicted in Fig. 6.16.The

interaction between 1,8-cineole and the QCM-Phe-CAS-Phe surface was found to be more correctly described by the Freundlich isotherm than by other isotherms, based on a correlation coefficient of 0.9906 and linearity of y = 0.9893x - 6.8726.

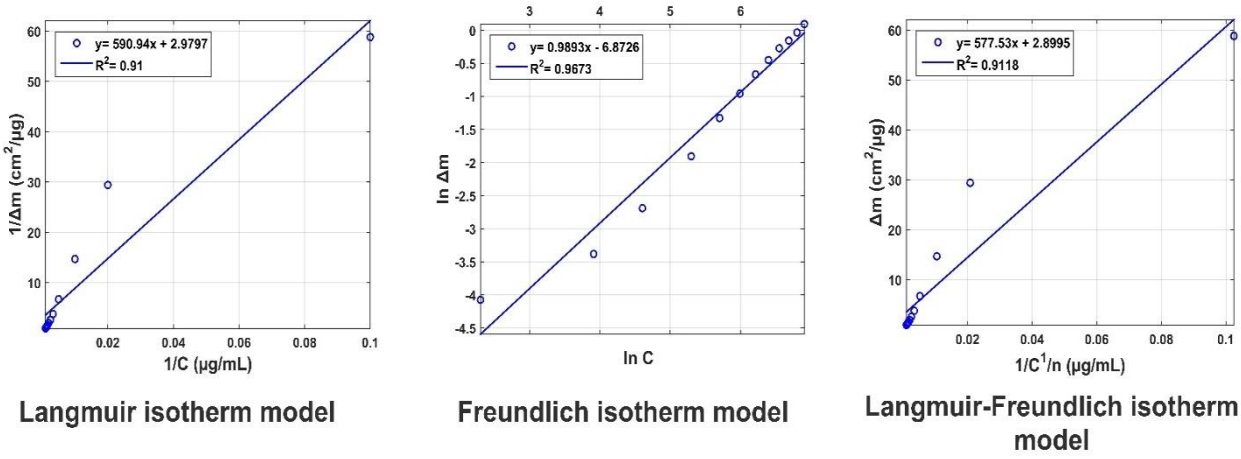

Fig. 6.16. Isotherm models for the equilibrium analysis on the sensor coating surface.

When 1,8-cineole molecules are attached to the coated material on the QCM sensor, it may be assumed that they contain heterogeneous binding sites. Table 6.8 shows the output of the different isotherm models between the interaction of 1,8-cineole and QCM-Phe-CAS-Phe sensor surface.

Table 6.8. Langmuir, Freundlich and Langmuir-Freundlich isotherm constants for QCM-Phe-CAS-Phe sensor.

Langmuir		**Freundlich**		**Langmuir-Freundlich**	
Δm_{max}	0.335	Δm_{max}	0.001	Δm_{max}	0.35
K_A (µg/mL)$^{-1}$	0.005	1/n	0.989	K_A (µg/mL)$^{-1}$	0.005
K_D (µg/mL)	200.91	R^2	0.9673	K_D (µg/mL)	199.13
R^2	0.9099			1/n	0.989
				R^2	0.911

6.3.12. The gas sensing properties of QCM-Phe-CAS-Phe sensor

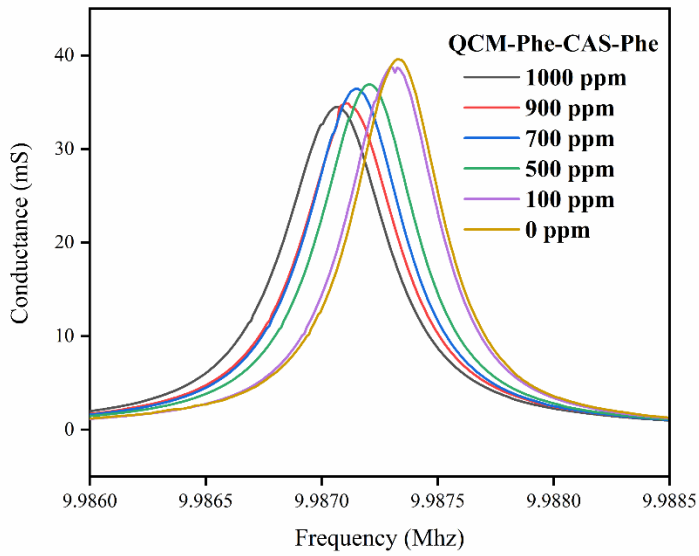

Fig. 6.17. Conductance spectrum of QCM-Phe-CAS-Phe sensor towards different concentration of 1,8-cineole.

The conductance spectra of the QCM-Phe-CAS-Phe sensor were studied for varied concentrations (100-1000 ppm) of 1,8-cineole, as shown in Fig. 6.17. The resonance frequencies followed a decreasing trend with an increasing concentration of 1,8-cineole. The corresponding conductance spectra showed the left shift corresponding to the rising frequency shift due to the sensitivity of the sensor. Moreover, the Q-factor gradually decreases, corresponding to the increasing concentration due to the viscoelastic nature of the prepared sensing film [32].

In a similar experimental condition, the repeatability of the QCM-Phe-CAS-Phe sensor was investigated at varying concentrations (10 – 1000 ppm) of 1,8-cineole. The repeatability percentage (Rp) was computed and given in Table 6.9 based on the relative standard deviation (RSD) for fifteen consecutive samplings.

Table 6.9. Repeatability measurement (n = 15) of QCM-Phe-CAS-Phe sensor for 10-1000 ppm of 1,8-cineole.

Concentration (mg L^{-1})	**Repeatability (n=15)**		
	Frequency shift (Hz)	**R_P (%)**	**CI**
10	4.07 ± 0.96	76.37	± 0.49
50	9.2 ± 1.37	85.07	± 0.69
100	16 ± 1.69	89.44	± 0.86
200	33.8 ± 2.11	93.75	± 1.07
300	64.67 ± 3.27	94.95	± 1.65
400	88.73 ± 1.79	97.98	± 0.91
500	120.73 ± 1.91	98.42	± 0.97
600	151.27 ± 2.15	98.58	± 1.09
700	179.53 ± 1.96	98.91	± 0.99
800	200.27 ± 1.83	99.09	± 0.93
900	226.13 ± 1.73	99.23	± 0.87
1000	257.07 ± 1.94	99.24	± 0.98

Fig. 6.18. depicts the four repeated readings of the as-prepared sensor in the presence of 200, 400, and 900 ppm of 1,8-cineole, followed by appropriate purging with ambient air. The average sensor responses for varied 1,8-cineole concentrations were 33.8 ± 2.11 Hz (200 ppm), 88.73 ± 1.79 Hz (400 ppm), and 226.13 ± 1.72 Hz (900 ppm), respectively. **It was also observed that the repeatability of the sensor enhanced with increasing concentrations of 1,8-cineole, with average repeatability of 94.25%.** Furthermore, the response pattern exhibited a consistent shape with a low change in frequency shift at saturation, indicating the effectiveness of the sensor in producing repeated outputs.

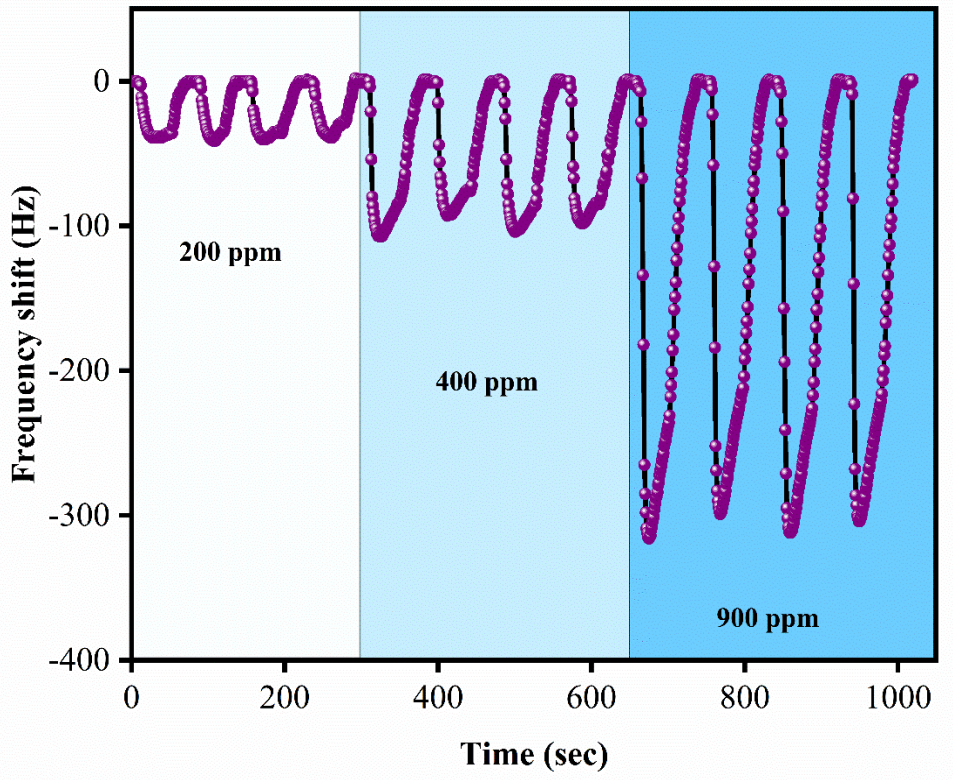

Fig. 6.18. Repeatability profile of QCM-Phe-CAS-Phe sensor towards 200, 400, and 900 ppm of 1,8-cineole at (27 ± 1) ºC, 67.7% RH, and standard atmospheric pressure.

The sensor outputs for varying humidity levels (45-85% RH) were examined by exposing the sensor to the corresponding humid environments. Fig. 6.19(a) depicts the frequency changes of the QCM-Phe-CAS-Phe sensor in response to varied humid conditions. In the region of 45-65 %RH, the sensor revealed a minimal frequency shift (1-5 Hz). This might be attributed to the presence of hydrophobic long-chained fatty acids (primarily ricinoleic acid) on the sensor surface, which have no natural hygroscopic property. However, a considerable shift was detected when exposed to a higher humidity environment, i.e., 8 Hz (75% RH) and 12 Hz (85% RH). Due to the presence of multiple -OH moieties in the coating material, the sensor surface becomes mildly hydrophilic. As a result, the sensor surface tends to attract moisture under higher humidity conditions.

The QCM-Phe-CAS-Phe sensor was next tested in earlier mentioned environments (45-85 %RH) with 500 ppm of 1,8-cineole, as shown in Fig. 6.19(b). The frequency shifts were as follows: 99 Hz (45% RH), 98 Hz (55% RH), 98 Hz (67.5% RH), 95 Hz (75% RH), and 91 Hz (85% RH). It was observed that sensor output remained unchanged at lower RH (45- 67.7 %) values. However,

the molecular interaction between 1,8-cineole and ricinoleic acid was considerably influenced by increasing humidity, resulting in a minor reduction in sensor adsorption towards 1,8-cineole. Reduction in the sensor surface area due to the accumulation of moisture at higher RH possibly interfered with the formation of molecular contacts between 1,8-cineole and the sensor surface. This ensures the sensor can perform efficiently with minimal influence of the ambient humidity.

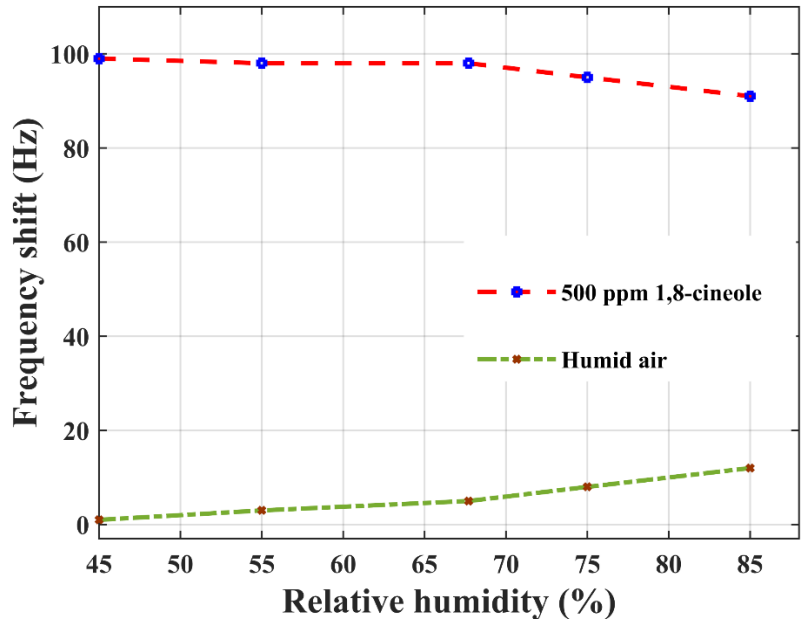

Fig. 6.19. Response profile of QCM-Phe-CAS-Phe sensor (a) towards ambient air, (b) for 500 ppm of 1,8-cineole at the different relative humidity (%), at (27 ± 1) ºC, and standard atmospheric pressure.

The long-term stability of the sensor was evaluated by evaluating its response to a fixed 1000 ppm of 1,8-cineole at a 1-week interval for six weeks following fabrication shown in the bar plot (Fig. 6.20). The sensor responses at saturation following injection of 1,8-cineole were 256.75 ± 0.96 Hz (week 1), 254.25 ± 1.70 Hz (week 2), 238 ± 1.41 Hz (week 3), 211.5 ± 2.08 Hz (week 4), 202.75 ± 2.62 Hz (week 5), and 189.25 ± 2.75 Hz (week 6), as shown in Fig. 6.18. According to the study, the developed sensor output declined by just 1.07% after two weeks, finally reaching 26.36% at the end of the study. **However, after the third week (7.4%), the percentage drop in sensor responses increased. As a result, the sensor may be reused for three weeks without losing its sensitivity.**

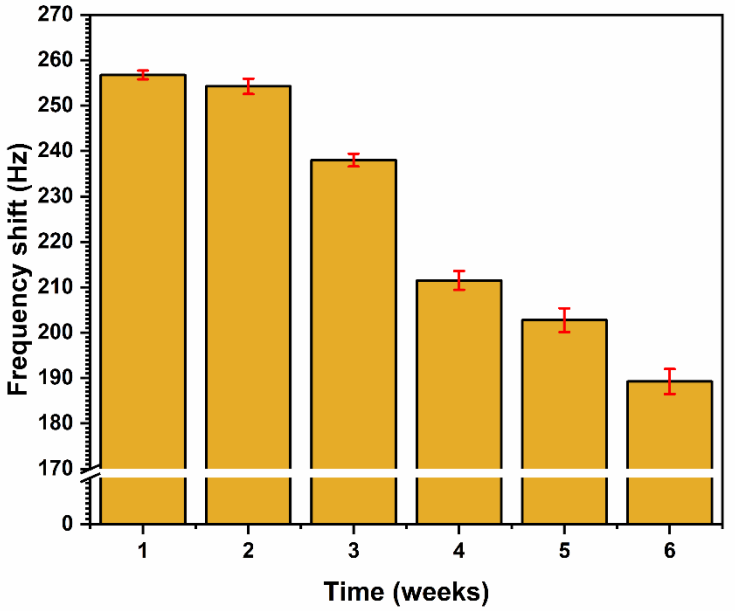

Fig. 6.20. Bar plot representation of long-term stability of the QCM-Phe-CAS-Phe sensor on the application of 1000 ppm of 1,8-cineole.

6.3.13. Sensing properties of QCM-Phe-CAS-Phe sensor with cardamom samples

As described in the earlier section, the QCM-Phe-CAS-Phe sensor was tested with twenty-one large cardamom samples in this study. For each cardamom sample, five sniffs of the sensor were obtained. The average QCM-Phe-CAS-Phe sensor responses of 10 samples are shown in Fig. 6.21(a).

Table 6.10. QCM-Phe-CAS-Phe sensor response and GC-MS 1,8-cineole peak area of cardamom samples.

Sample	**1,8-cineole SPME peak area**	**QCM-Phe-CAS-Phe frequency shift (Hz)**
L1	62428060.7	36
L2	82756975.08	60
L3	148014990.7	116
L4	134398608.7	111
L5	114447028.2	78
L6	156699396.8	126

L7	135198906.6	98
L8	124398608.7	85
L9	126721131.9	92
L10	82639710.15	58
L11	75590097.17	48
L12	53068125.13	28
L13	163837923.4	143
L14	117375210.3	78
L15	84960325.23	55
L16	112526444.3	81
L17	156314191	128
L18	181097729	167
L19	179285430	160
L20	201927578.3	175
L21	151609861	128

The aroma of the samples that were injected causes various frequency profiles. Furthermore, the frequency graphs show rapid sensing characteristics of the incoming aroma at 10 seconds and approach saturation at roughly 40 secs, demonstrating the sensor uniformity and speedy sensing behaviour. The sensor responses for each sample were plotted against their respective 1,8-cineole SPME peak areas, as shown in Table 6.10. The sensor responses and the GCMS peak areas of 1,8-cineole were normalised (0,1), and the curve fit of the scatter plot was $y = 0.1912x - 0.185$ with $R^2 = 0.976$ as given in Fig. 6.21(b).

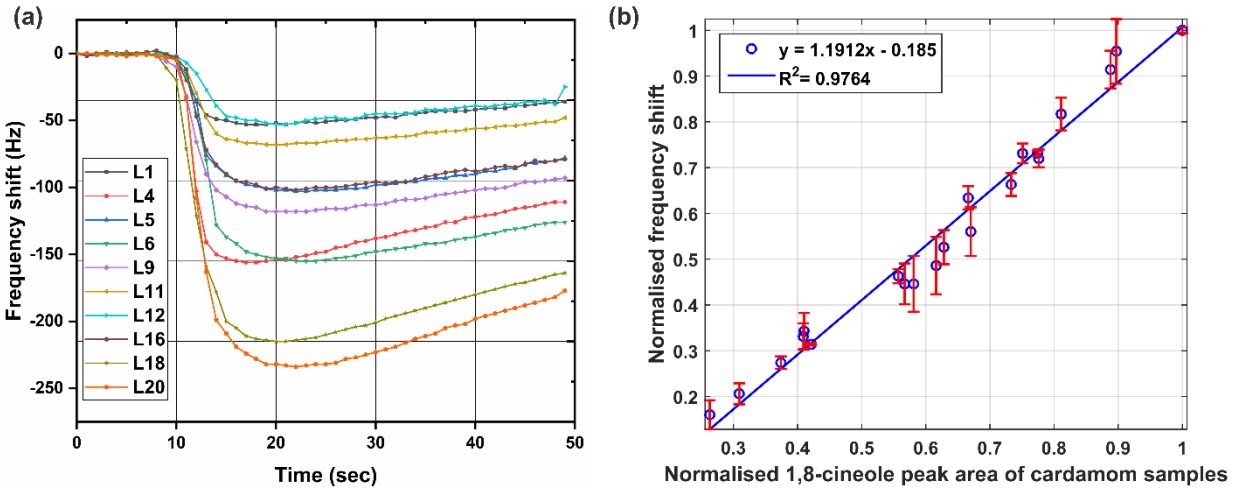

Fig. 6.21. (a) QCM-Phe-CAS-Phe sensor responses; (b) scatter plot of sensor responses and 1,8-cineole peak area of cardamom samples.

The scatter plot's precision revealed the accuracy of the sensor responses towards the variation of 1,8-cineole peak areas in real samples. Finally, the correlation coefficient between GCMS peak areas of the vital VOCs in the headspace of each sample was computed with their respective QCM sensor responses, as tabulated in Table 6.11. The result showed the maximum correlation of 0.98 with 1,8-cineole peak areas among the other participating volatiles. The efficiency of the fabricated sensor was further demonstrated by formulating a mathematical model-based approach to detect 1,8-cineole content in cardamom samples.

Table 6.11. QCM-Phe-CAS-Phe sensor response and GC-MS response of cardamom samples.

Sample	QCM-Phe-CAS-Phe frequency shift (Hz)	α-pinene	β-pinene	Limonene	1,8-cineole	γ-terpinene	α-terpineol
LC1	36	2241670	829951.1	4265912	40667680	579963.6	2578665
LC2	60	18364267	16217905	9105945	82756975	1652728	936379.2
LC3	116	15171067	19863459	650721.2	1.48E+08	619735.4	650721.2
LC4	111	12025617	15514094	10625225	1.34E+08	867734.2	614365
LC5	78	8889224	11612736	14114210	1.14E+08	590496.5	577602.8

LC6	126	10922508	15164129	11194430	1.57E+08	582868.7	549486.1
LC7	98	13867055	15106313	16270731	1.35E+08	1718676	686214.3
LC8	85	12344341	13169897	9693231	1.23E+08	1061573	708649.9
LC9	92	16880838	15649044	10898743	1.27E+08	1663379	748464.8
LC10	58	714228.7	541442.9	6326195	83153238	579039.5	1340608
LC11	48	4344309	5390295	5965579	75590097	570225.6	540902.8
LC12	28	12412451	13476729	13021081	52903887	1558672	1003730
LC13	143	16935473	16984205	39739024	1.63E+08	565113.1	726238.9
LC14	78	13664674	16750352	11530792	1.17E+08	676564.5	1206776
LC15	55	5540324	6660623	6151745	84960325	701087.6	920674.9
LC16	81	19278161	1386489	11765362	1.13E+08	1012501	768432.5
LC17	128	8221895	10137119	13167682	1.56E+08	846465.3	987832.6
LC18	167	16490336	17447068	17372528	1.81E+08	1255380	915818.9
LC19	160	18364267	16217905	9105945	1.69E+08	541465.5	936379.2
LC20	175	23074558	18286511	24035353	2.02E+08	1484603	1128679
LC21	128	12096603	17930174	14370558	1.52E+08	600969	609873.5
Pearson correlation with QCM response		**0.6**	**0.62**	**0.51**	**0.98**	**-0.02**	**-0.31**

6.3.14. Mathematical model for evaluating 1,8-cineole content of cardamom samples

All the aromatic materials, whether of biological or abiotic origin, release specific volatile organic compound(s) at ambient temperature. When kept in a closed system, these volatiles starts to occupy the material's free headspace until they get saturated in the HS. These volatiles present in this region is termed headspace volatiles (HSVs), which directly reflect the material's aroma. As the crude volatile content present in a material and its emission from the material to the HS in a

closed system works in a **"Source to sink dynamics",** it can be said that the quantity of a specific volatile in HS is reliant on the total crude, volatile content present in the actual material.

Parallelly, the QCM sensor output is directly dependent on the amount of volatiles present in the headspace, which is already established in multiple works of literature. Therefore, it can be inferred that the QCM sensor output is indirectly dependent on the actual crude quantity of volatile present in the aromatic material. Thus, it is possible to quantitatively measure a volatile content in an aromatic material using the QCM sensor response of real samples.

Using predictive modelling based on the statistical technique of machine learning, the 1,8-cineole content (µg) is predicted with the aid of measured data from GCMS and sensors. The aroma of the samples (LC1 – LC21) was injected into the sensor chamber to generate respective QCM sensor outputs. Each sample was tested five times, and the data were taken into consideration for further analysis. Subsequently, the peak areas of 1,8-cineole were determined for each sample from GCMS analysis using SPME and solvent extraction methodology as discussed earlier. The average of the sensor readings with associated 1,8-cineole GCMS peak areas is given in Table 6.9.

6.3.14.1. Predictive model to estimate SPME 1,8-cineole peak area from QCM sensor response

The data set of sensor responses and measured SPME 1,8-cineole peak areas for individual samples, were pre-processed using the min-max scaler transformation method using Python after importing the libraries of panda (for data manipulation and analysis) and NumPy (for performing different operations over the multi-dimensional data set). The scaled frequency data increased linearly with the increasing SPME 1,8-cineole peak areas for individual samples. In order to predict the SPME 1,8-cineole peak areas the following mathematical model have been developed using 'sklearn.linear_model' in Python for developing linear regression model as shown in Fig. 6.22. From the linear regression, the accuracy measurement was calculated to be R^2= 0.9728) and MSE= 0.0011 for the available data set.

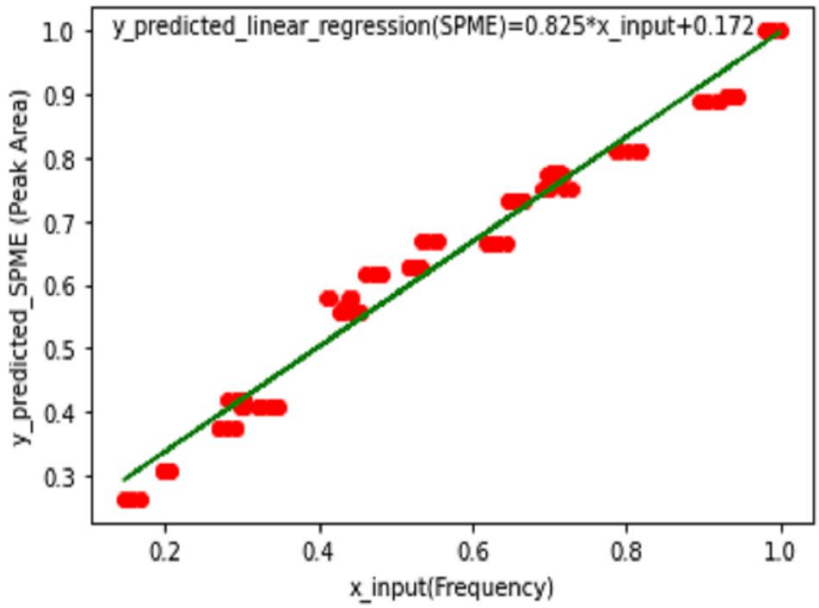

Fig. 6.22. Linear regression model of SPME 1,8-cineole peak areas from sensor frequency responses (n=5).

Using linear regression method, the mathematical model to predict the SPME 1,8-cineole peak areas (y_predicted_linear_regression) using sensor frequency response (x_input) is given below

y_predicted_linear_regression (SPME) = 0.825* x_input (Frequency) + 0.172

The model, as mentioned earlier, has been evaluated to predict the SPME 1,8-cineole content for several randomly chosen test cases. The predicted results with error percentages are shown in Table 6.12.

Table 6.12. Calculation of error between the actual and predicted value of SPME from frequency using the linear regression model for prediction

Sample	Frequency	SPME 1,8-cineole headspace area		
		Actual	**Predicted**	**Percentage Error (%)**
LC1	36	62428060.697	68537854.771	9.787
LC5	77	114447028.247	106921690.618	6.575
LC12	141	163837923.447	166837920.311	1.831
LC19	160	179285430.018	184625551.064	2.978

6.3.14.2. Predictive model to estimate solvent 1,8-cineole peak area from SPME 1,8-cineole peak area

The relationship between the 1,8-cineole SPME headspace area (x_SPME) for its corresponding area of the solvent extract (in specific dilution mentioned in section 6.2.6) (y_solvent) was analysed for the above-mentioned samples by developing a mathematical model. In the pre-processing stage, min-max scaler transformation was applied over the data set. After plotting the scatter plot (Fig. 6.23), the data points showed non-linear characteristics, exponentially increasing in nature.

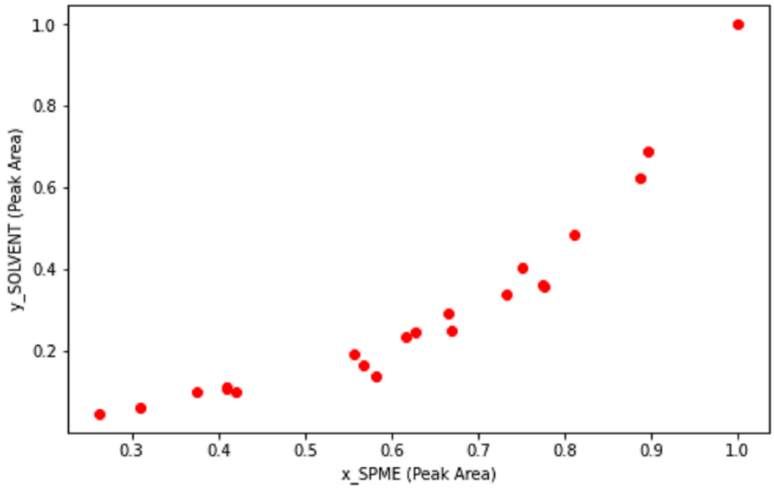

Fig. 6.23. Scatter plot between 1,8-cineole SPME headspace area and its corresponding area of the solvent extract.

Analysing the above result, instead of using linear regression modelling, we have tried to fit a non-linear regression line over the data set. After observing the trend in the above figure, an exponential function, $y = ae^{bx}$ can be a suitable choice of curve fitting before performing non-linear regression modelling. Here, $b \neq 0$, and x is any real number. The base, c, is constant, and the exponent, x, is an independent variable.

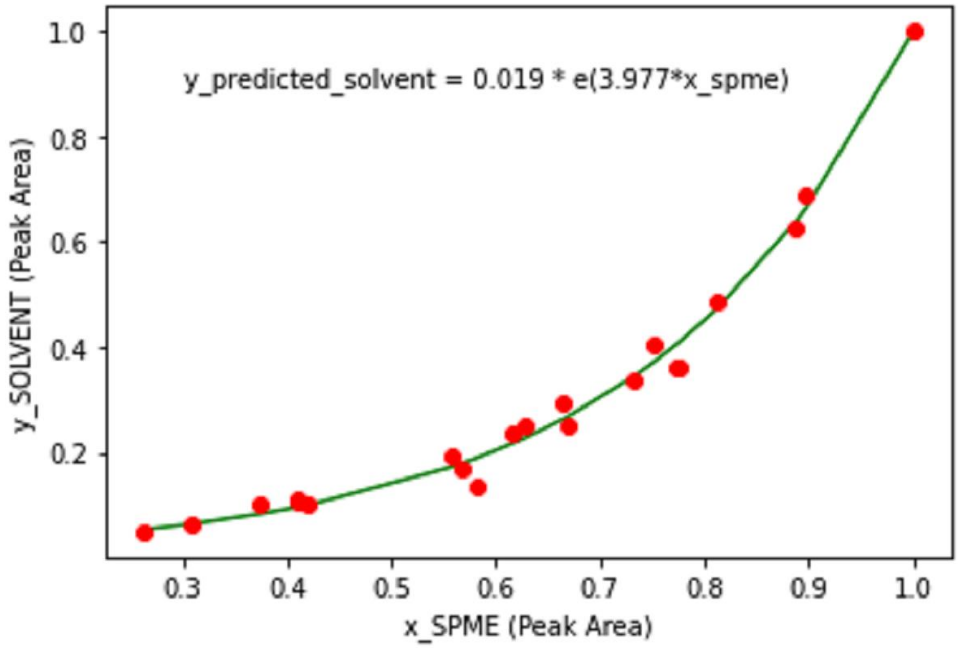

Fig 6.24. Non-linear regression curve fitting between 1,8-cineole content (SPME) and 1,8-cineole content (solvent).

Now using 'curve_fit' from the library' scipy. optimise' in Python , we try to find out the optimum values of the unknown parameters a and b respectively.

. The optimised value for a is 0.019 and b is 3.9777. Hence the estimated fitted curve is,

$$y\_solvent = 0.019 * e3.977*x\_spme$$

As shown in Fig. 6.24, the non-linear regression model shows the value of $R^2 = 0.99$ and MSE= 0, which indicates that the non-linear regression model is working suitably. Implementing the generated model, y_solvent is predicted from x_SPME for the available samples. The error produced are shown in the following Table 6.13.

Table 6.13. Error calculation between actual and predicted solvent 1,8-cineole peak area from 1,8-cineole SMPE peak area.

Sample	1,8-cineole SPME peak area	Solvent 1,8-cineole peak area	Solvent 1,8-cineole peak area (Calculated)	% Error
LC1	62428060.7	4628505.928	5330926.001	15.176
LC2	82756975.08	8069879.814	8451492.684	4.729
LC3	148014990.7	24830245.059	23819549.748	4.070
LC4	134398608.7	21446136.473	21806209.234	1.679
LC5	114447028.2	12218349.966	11561717.155	5.374
LC6	156699396.8	26358107.546	28319278.894	7.440
LC7	135198906.6	18431927.709	16414973.697	10.943
LC8	124398608.7	17335732.210	13011995.080	24.941
LC9	126721131.9	18184743.572	15358970.523	15.539
LC10	82639710.15	7841389.079	7626782.294	2.737
LC11	75590097.17	7487062.395	6929016.634	7.453
LC12	53068125.13	3543521.741	4600972.802	29.842
LC13	163837923.4	35652176.041	38486246.752	7.949
LC14	117375210.3	10053298.565	11320389.066	12.604
LC15	84960325.23	7416597.110	7240740.820	2.371
LC16	112526444.3	14002281.176	11695222.644	16.476
LC17	156314191	26511991.699	28536121.582	7.635
LC18	181097729	50376598.808	59418548.337	17.949
LC19	179285430	45713254.000	54009786.516	18.149
LC20	201927578.3	73171824.000	70408290.440	3.777
LC21	151609861	29554587.000	28140894.652	4.783

6.3.14.3. Development of a standard model to estimate 1,8-cineole content from GCMS peak areas

In this step the GCMS peak area for some known 1,8-cineole content have been standardised to obtain a model **to predict the absolute 1,8-cineole content from unknown peak areas.** 0.25 µg/mL, 0.5 µg/mL, 1 µg/mL, 2 µg/mL, 3 µg/mL, 4 µg/mL, and 5 µg/mL concentrations of 1,8-cineole were prepared in DCM and 0.5µl of DCM extract was injected into the GC-MS. The

process was repeated twice. The obtained peak areas for standard 1,8-cineole content are given in Table 6.14.

Table 6.14. Obtained 1,8-cineole peak area from standard 1,8-cineole content

1,8-cineole content (µg)	**1,8-cineole peak area**	
	Repetition 1	**Repetition 2**
0.5	30569614.01	30219189.52
1	43866548.01	43204468.56
2	62199536.71	60109116.17
3	81329661.88	80064088.51
4	104091769.5	99091769.54
5	123753550.7	120849475.1

The min-max scaler transformation was applied over the data set in the pre-processing stage. Using the linear regressing model, the accuracy measurement was estimated by $R^2 = 0.9963$ and MSE = 0.0002.

Now to predict the actual output (headspace), the following mathematical model is being developed using 'sklearn.linear_model' in Python for developing linear regression model as follows

y_predicted_linear_regression (peak area) = 0.799* x_input (1,8-cineole content) + 0.181

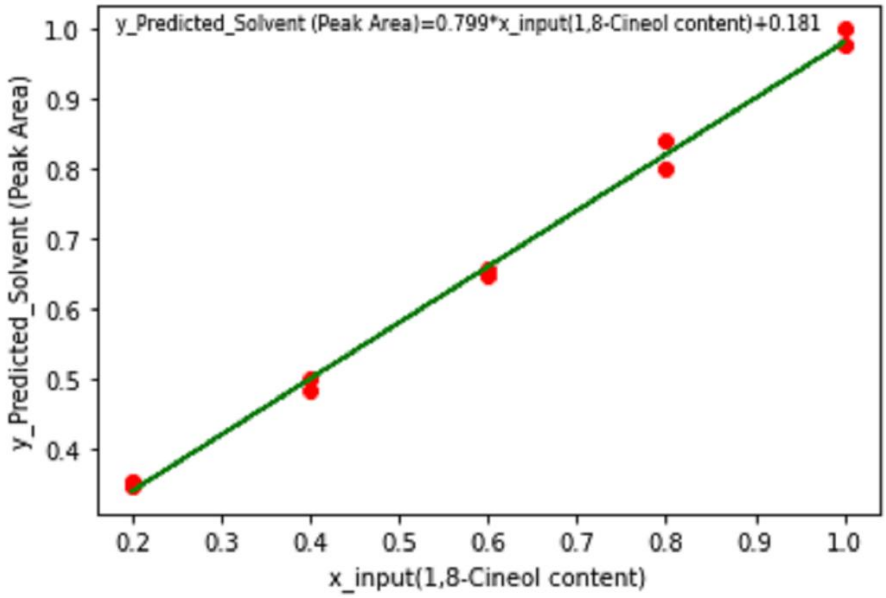

Fig. 6.25. Linear regression model of 1,8-cineole standard content and its peak area in GCMS.

The developed model (Fig. 6.25) was used to estimate the predicted 1,8-cineole content from the expected 1,8-cineole peak area in solvent, as stated in Table 6.14. The detailed predicted output is given in Table 6.15.

Table 6.15. Calculated 1,8-cineole content from 1,8-cineole peak area (solvent) using linear regression

Sample	**Solvent 1,8-cineole peak area**	**1,8-cineole content (Calculated)**
LC1	5330926.001	911.600
LC2	8451492.684	1445.356
LC3	23819549.748	4073.979
LC4	21806209.234	3729.608
LC5	11561717.155	1977.343
LC6	28319278.894	4843.633
LC7	16414973.697	2807.466
LC8	13011995.080	2225.405

LC9	15358970.523	2626.842
LC10	7626782.294	1304.293
LC11	6929016.634	1184.944
LC12	4600972.802	786.745
LC13	38486246.752	6582.638
LC14	11320389.066	1936.065
LC15	7240740.820	1238.263
LC16	11695222.644	2000.178
LC17	28536121.582	4880.723
LC18	59418548.337	10162.995
LC19	54009786.516	9237.855
LC20	70408290.440	12042.731
LC21	28140894.652	4813.121

6.3.14.4 Determination of 1,8-cineole content of cardamom from QCM-Phe-CAS-Phe sensor response

The above-obtained models have been cascaded to predict the 1,8-cineole content from the cardamom samples using the fabricated QCM sensor. Fig. 6.26 describes the complete working module of the above-mentioned models. Initially, the aroma of any cardamom sample injected into the sensor chamber gives a sensor output in the first block, where the predicted SPME 1,8-cineole peak area (y_predicted_SPME) was predicted based on the input sensor frequency response. The predicted SPME 1,8-cineole peak area was subsequently fed into the second block as input. A non-linear regression model has been used to predict the corresponding 1,8-cineole peak area from solvent (y_solvent). As discussed in Section 6.2.6, 0.5 µL of large cardamom extract was injected into GC-MS-MS to obtain absolute 1,8-cineole in 1 gram (or 5ml) of sample. Thus, to get the

predicted 1,8-cineole peak area in 1 gram of sample, the predicted 1,8-cineole peak area from solvent has been multiplied by a factor of 10000. The obtained result was fitted in the linear regression model in the third block to predict the 1,8-cineole content. After multiplying by the scaling factor obtained during linear regression, the final predicted value of 1,8-cineole content per gram of the sample was derived.

The results were compared with the actual 1,8-cineole content obtained by the GC-MS-MS study, and the error percentages are tabulated in Table 6.16.

Table 6.16. Calculation of error between predicted and actual 1,8-cineole content

Sample	Actual 1,8-cineole content (µg/g)	Predicted 1,8-cineole content (µg/g)	Error (%)
LC1	763.2845312	911.5995131	19.3036
LC2	1330.953906	1445.355559	8.479517
LC3	4095.648	4073.978561	0.635259
LC4	3537.424782	3729.607561	5.320304
LC5	2015.261841	1977.342625	1.986351
LC6	4347.675467	4843.632883	11.2885
LC7	3040.218125	2807.465895	7.754349
LC8	2859.395979	2225.404816	22.25529
LC9	2999.444042	2626.842266	12.51585
LC10	1293.26338	1304.293309	0.745191
LC11	1234.815674	1184.944269	4.14124
LC12	584.3117385	786.7449682	34.50092
LC13	5880.771906	6582.637721	11.81545
LC14	1658.127331	1936.064761	16.63748
LC15	1223.192123	1238.263004	1.124002
LC16	2309.528941	2000.178016	13.487
LC17	4373.059317	4880.722652	11.48976
LC18	8309.62856	10162.99464	22.1733
LC19	7540.389844	9237.855198	22.38088
LC20	12069.79867	12042.73056	0.330753
LC21	4874.948455	4813.121224	1.373648
Average			**10.91**

The 1,8-cineole content calculated from the QCM responses of the particular samples showed an average error of 10.91% for all the 21 large cardamom samples considered in this study. The developed model can predict accurately with an error of less than 2% for some samples. However, the study revealed some outputs with higher error percentages. This model can be further improved with more repetitions of standard data to provide more data points for developing the model.

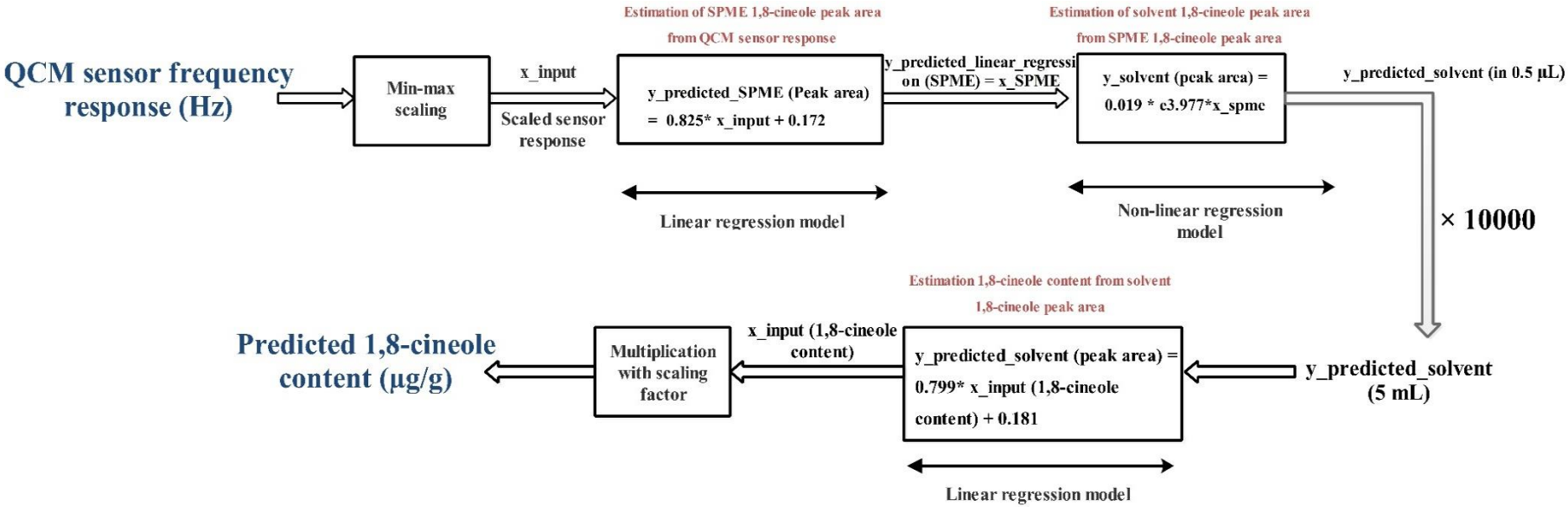

Fig. 6.26. The working module of the developed mathematical model for evaluating 1,8-cineole content of cardamom samples.

6.4. Conclusion

This study discusses the process of fabricating a modified castor oil-coated QCM (phenolated phenyl ricinoleate) sensor to identify 1,8-cineole in cardamom. The designed sensor has a high sensitivity to 1,8-cineole, as indicated by its sensitivity of 0.262 Hz/ppm and its R^2 value of 0.9964. In addition, the sensor has acceptable selectivity for 1,8-cineole despite the presence of other important VOCs present in cardamom. In addition, the created sensor exhibits quick recovery, long-term stability, short-term stability, little humidity impact, and average repeatability of 94.25%. The sensing mechanism was evaluated using UV-Vis spectroscopy, GCMS, and in-silico computational technique using AutoDock tools. The surface morphology of phenolated phenyl ricinoleate showed a rough and uneven surface with increased porosity. The GC-MS technique was used to analyse the interaction between the twenty-one large cardamom samples, and the findings indicated a correlation of 0.98 with the 1,8-cineole peak areas of the chromatogram. Moreover, a mathematical model has been formulated to predict the 1,8-cineole content from the samples using the developed sensor responses. The results showed an accuracy of 89.09% in predicting the 1,8-cineole content from the samples. 1,8-cineole is the most dominant VOC present in the aroma of cardamom and many agro products. Considering its vast medicinal benefits and uses, the developed sensor can provide an easy and accurate sensing solution which can benefit in quality evaluation of cardamom and other food products.

References

[1] P.K. Rout, D. Sahoo, K.S. Jena, Y.R. Rao, Analysis of the Oil of Large Cardamom (Amomum subulatum Roxb.,) Growing in Sikkim, Journal of Essential Oil Research. 15 (2003) 265–266. https://doi.org/10.1080/10412905.2003.9712138.

[2] N. Sabulal, S. Baby, Chemistry of Amomum essential oils, Journal of Essential Oil Research. 33 (2021) 427–441. https://doi.org/10.1080/10412905.2021.1899065.

[3] A.C. Aprotosoaie, V.S. Luca, A. Trifan, A. Miron, Chapter 7 - Antigenotoxic Potential of Some Dietary Non-phenolic Phytochemicals, in: Atta-ur-Rahman (Ed.), Studies in Natural Products Chemistry, Elsevier, 2019: pp. 223–297. https://doi.org/10.1016/B978-0-444-64181-6.00007-3.

[4] Chemical Dictionary of Economic Plants | Wiley, Wiley.Com. (n.d.). https://www.wiley.com/en-us/Chemical+Dictionary+of+Economic+Plants-p-9780471492269 (accessed June 30, 2022).

[5] Z.-M. Cai, J.-Q. Peng, Y. Chen, L. Tao, Y.-Y. Zhang, L.-Y. Fu, Q.-D. Long, X.-C. Shen, 1,8-cineole: a review of source, biological activities, and application, Journal of Asian Natural Products Research. 23 (2021) 938–954. https://doi.org/10.1080/10286020.2020.1839432.

[6] U.R. Juergens, U. Dethlefsen, G. Steinkamp, A. Gillissen, R. Repges, H. Vetter, Anti-inflammatory activity of 1.8-cineol (eucalyptol) in bronchial asthma: a double-blind placebo-controlled trial, Respiratory Medicine. 97 (2003) 250–256. https://doi.org/10.1053/rmed.2003.1432.

[7] Y. Lai, Y. Li, L. Fu, F. Zhao, N. Liu, F. Zhang, P. Xu, Combinations of 1,8-cineol and oseltamivir for the treatment of influenza virus A (H3N2) infection in mice, Journal of Medical Virology. 89 (2017) 1158–1167. https://doi.org/10.1002/jmv.24755.

[8] J. Fischer, U. Dethlefsen, Efficacy of cineole in patients suffering from acute bronchitis: a placebo-controlled double-blind trial, Cough. 9 (2013) 25. https://doi.org/10.1186/1745-9974-9-25.

[9] H. Worth, C. Schacher, U. Dethlefsen, Concomitant therapy with Cineole (Eucalyptole) reduces exacerbations in COPD: A placebo-controlled double-blind trial, Respiratory Research. 10 (2009) 69. https://doi.org/10.1186/1465-9921-10-69.

[10] T. Efferth, F. Herrmann, A. Tahrani, M. Wink, Cytotoxic activity of secondary metabolites derived from Artemisia annua L. towards cancer cells in comparison to its designated active constituent artemisinin, Phytomedicine. 18 (2011) 959–969. https://doi.org/10.1016/j.phymed.2011.06.008.

[11] S. Murata, R. Shiragami, C. Kosugi, T. Tezuka, M. Yamazaki, A. Hirano, Y. Yoshimura, M. Suzuki, K. Shuto, N. Ohkohchi, K. Koda, Antitumor effect of 1, 8-cineole against colon cancer, Oncol Rep. 30 (2013) 2647–2652. https://doi.org/10.3892/or.2013.2763.

[12] W. Wang, N. Li, M. Luo, Y. Zu, T. Efferth, Antibacterial activity and anticancer activity of Rosmarinus officinalis L. essential oil compared to that of its main components, Molecules. 17 (2012) 2704–2713. https://doi.org/10.3390/molecules17032704.

[13] S. Sampath, S. Subramani, S. Janardhanam, P. Subramani, A. Yuvaraj, R. Chellan, Bioactive compound 1,8-cineole selectively induces G2/M arrest in A431 cells through the upregulation of the p53 signaling pathway and molecular docking studies, Phytomedicine. 46 (2018) 57–68. https://doi.org/10.1016/j.phymed.2018.04.007.

[14] J.-D. Cha, Y.-H. Kim, J.-Y. Kim, Essential oil and 1,8-cineole from Artemisia lavandulaefolia induces apoptosis in KB cells via mitochondrial stress and caspase activation, Food Sci Biotechnol. 19 (2010) 185–191. https://doi.org/10.1007/s10068-010-0025-y.

[15] P.R. Lima, T.S. de Melo, K.M.M.B. Carvalho, Í.B. de Oliveira, B.R. Arruda, G.A. de Castro Brito, V.S. Rao, F.A. Santos, 1,8-cineole (eucalyptol) ameliorates cerulein-induced acute pancreatitis via modulation of cytokines, oxidative stress and NF-κB activity in mice, Life Sciences. 92 (2013) 1195–1201. https://doi.org/10.1016/j.lfs.2013.05.009.

[16] S. Murata, K. Ogawa, T. Matsuzaka, M. Chiba, K. Nakayama, K. Iwasaki, T. Kurokawa, N. Sano, T. Tanoi, N. Ohkohchi, 1,8-cineole Ameliorates Steatosis of Pten Liver Specific KO Mice via Akt Inactivation, International Journal of Molecular Sciences. 16 (2015) 12051–12063. https://doi.org/10.3390/ijms160612051.

[17] F.A. Santos, V.S. Rao, 1,8-cineol, a food flavoring agent, prevents ethanol-induced gastric injury in rats, Dig Dis Sci. 46 (2001) 331–337. https://doi.org/10.1023/a:1005604932760.

[18] H.K. Moon, P. Kang, H.S. Lee, S.S. Min, G.H. Seol, Effects of 1,8-cineole on hypertension induced by chronic exposure to nicotine in rats, Journal of Pharmacy and Pharmacology. 66 (2014) 688–693. https://doi.org/10.1111/jphp.12195.

[19] S. Ryu, H. Park, G.H. Seol, I.-Y. Choi, 1,8-cineole ameliorates oxygen-glucose deprivation/reoxygenation-induced ischaemic injury by reducing oxidative stress in rat cortical neuron/glia, Journal of Pharmacy and Pharmacology. 66 (2014) 1818–1826. https://doi.org/10.1111/jphp.12295.

[20] J.M. Rubio-Perez, J.M. Morillas-Ruiz, A Review: Inflammatory Process in Alzheimer's Disease, Role of Cytokines, The Scientific World Journal. 2012 (2012) e756357. https://doi.org/10.1100/2012/756357.

[21] E.-J. Seo, N. Fischer, T. Efferth, Phytochemicals as inhibitors of NF-κB for treatment of Alzheimer's disease, Pharmacological Research. 129 (2018) 262–273. https://doi.org/10.1016/j.phrs.2017.11.030.

[22] V. Thangarasu, R. Anand, Chapter 17 - Comparative evaluation of corrosion behavior of Aegle Marmelos Correa diesel, biodiesel, and their blends on aluminum and mild steel metals, in: A.K. Azad, M. Rasul (Eds.), Advanced Biofuels, Woodhead Publishing, 2019: pp. 443–471. https://doi.org/10.1016/B978-0-08-102791-2.00017-9.

[23] M. Ionescu, Z. Petrović, Phenolation of vegetable oils, J. Serb. Chem. Soc. 76323356253095 (2011) 591–606.

[24] N. Debabhuti, S. Mukherjee, S. Neogi, P. Sharma, U.H. Sk, S. Maiti, M.P. Sarkar, B. Tudu, N. Bhattacharyya, R. Bandyopadhyay, A study of vegetable oil modified QCM sensor to detect β-pinene in Indian cardamom, Talanta. 236 (2022) 122837. https://doi.org/10.1016/j.talanta.2021.122837.

[25] N. Debabhuti, S. Neogi, S. Mukherjee, A. Dhar, P. Sharma, R.L. Vekariya, M.P. Sarkar, B. Tudu, N. Bhattacharyya, R. Bandyopadhyay, Mohd. Muddassir, Development of QCM sensor to detect α-terpinyl acetate in cardamom, Sensors and Actuators A: Physical. 319 (2021) 112521. https://doi.org/10.1016/j.sna.2020.112521.

[26] R. Das, S. Pradhan, S. Biswas, P. Sharma, A. Ghosh, R. Bandyopadhyay, P. Pramanik, Aliphatic amines vapours detection by quartz crystal microbalance sensor, Sensors and Actuators B: Chemical. 198 (2014) 94–101. https://doi.org/10.1016/j.snb.2014.03.020.

[27] G. Sauerbrey, Verwendung von Schwingquarzen zur Wägung dünner Schichten und zur Mikrowägung, Z. Physik. 155 (1959) 206–222. https://doi.org/10.1007/BF01337937.

[28] A. Leong, S. Seeneevassen, T. Saha, V. Swamy, N. Ramakrishnan, Low hysteresis relative humidity sensing characteristics of graphene oxide–gold nanocomposite coated langasite crystal microbalance, Surfaces and Interfaces. 23 (2021) 100964. https://doi.org/10.1016/j.surfin.2021.100964.

[29] K.D. Pennell, Specific Surface Area☆, in: Reference Module in Earth Systems and Environmental Sciences, Elsevier, 2016. https://www.sciencedirect.com/science/article/pii/B978012409548909583X (accessed April 2, 2022).

[30] K. Triyana, A. Rianjanu, D.B. Nugroho, A.H. As'ari, A. Kusumaatmaja, R. Roto, R. Suryana, H.S. Wasisto, A highly sensitive safrole sensor based on polyvinyl acetate (PVAc) nanofiber-coated QCM, Scientific Reports. 9 (2019) 1–12. https://doi.org/10.1038/s41598-019-51851-0.

[31] T. Nan, Y. Hui, M. Rinaldi, N.X. Sun, Self-Biased 215MHz Magnetoelectric NEMS Resonator for Ultra-Sensitive DC Magnetic Field Detection, Sci Rep. 3 (2013) 1985. https://doi.org/10.1038/srep01985.

[32] Z. Kang, D. Zhang, T. Li, X. Liu, X. Song, Polydopamine-modified SnO2 nanofiber composite coated QCM gas sensor for high-performance formaldehyde sensing, Sensors and Actuators, B: Chemical. 345 (2021) 130299–130299. https://doi.org/10.1016/j.snb.2021.130299.

Chapter 7

Development of QCM sensor to detect α-terpinyl acetate in cardamom

Content of the this chapter is based on the following publication:

N. Debabhuti, S. Neogi, S. Mukherjee, A. Dhar, P. Sharma, R.L. Vekariya, M.P. Sarkar, B. Tudu, N. Bhattacharyya, R. Bandyopadhyay, Mohd. Muddassir, Development of QCM sensor to detect α-terpinyl acetate in cardamom, Sensors and Actuators A: Physical. 319 (2021) 112521.

7.1. Introduction

Small cardamom (*Elettaria cardamomum*) is a household spice, famous mainly for its soothing flavour, a pleasant treat to the human olfactory lobe, and it is also known for its practical therapeutic values to improve human digestive power, has wide applications in gum cure, treatment of asthma, cough, and cold, burning, etc. Cardamom powder and its extracted essential oil are commonly used in food processing industries like beverages, flavoured tea, flavoured coffee, and flavoured milk [1,2]. **As discussed in Chapter 2, α-terpinyl acetate is one of the significant distinguishing components between the aroma of small cardamom (*Elettaria cardamomum)* and large cardamom *(Amomum subulatum)*.** Moreover, the PCA analysis and SIMPER test also confirmed that α-terpinyl acetate influences maximum discrimination between small cardamom varieties. All the above studies indicate the importance of α-terpinyl acetate in cardamom and urge a significant need for its detection by fabricating a highly selective and sensitive gas sensor.

α-terpinyl acetate (aTA) is a member of menthane monoterpenoids, a class of monoterpenoids with a structure based on o-, m-, or p-menthane backbone. This monoterpene ester (corresponding acetate ester of α-terpineol) is also considered to be an isoprenoid lipid molecule since it is practically insoluble (in water, 0.14 gm/L) and based on its pKa value; it is deemed to be a poorly basic compound.

In the preceding chapters (chapters 4,5 & 6), oil-based sensors were developed for the detection of the major VOCs of cardamoms. However, aTA has low vapour pressure and very high flash point temperature, which hinders selective absorption of fatty acids for sensor development. Moreover, due to the higher molecular complexity of aTA, a molecularly imprinted polymer (MIP)-based QCM sensor was designed in this chapter to detect α-terpinyl acetate in Indian cardamom selectively. A MIP is synthesised by forming a polymer matrix in the presence of a template. The substrate that is typically sensed by the sensor is referred to as the template. The template is removed after production to generate a cavity. The created cavity aids the polymer matrix in entrapping the target molecule through intermolecular interactions [3]. Thus, the QCM sensor exhibits selective, fast, responsive, and reproducible after the deposition of suitable coating of the MIP [4] and has been successfully implemented for sensor fabrication for gaseous [5,6] and liquid [7,8] mediums effectively. MIP technique has been effectively used to identify aromatic

terpenes like limonene, α-pinene, γ-terpinene, and terpinolene molecule released during different stages of mango fruit maturity [9]. Wang et al. described the fabrication procedure of four QCM sensors using the MIP technique for sensitive detection of terpenes viz. α-pinene, β-phellandrene, 3-carene, and cisthujopsene for the discrimination of wood borers infested *Platycladus orientalis* trunks [10]. Iqbal et al. reported the development of the MIP-modified QCM sensor for detecting six terpenes of interest, i.e., α-pinene, limonene, eucalyptol, β-pinene, terpinene, and estragole in fresh and dried herbs [11]. Dutta et al. developed an e-nose utilising an array of metal oxide semiconductor (MOS) sensors and studied the shelf life based on the spoilage index of black pepper and small cardamom cookies [12]. However, no significant works have been conducted on detecting α-terpinyl acetate using MIP technology and thus attempted to design.

7.2. Experimental section

7.2.1. Chemicals

α-terpinyl acetate (aTA) and Ethylene glycol dimethacrylate (EGDMA) was purchased from TCI, Tokyo, Japan. 1,1′-Azobis(cyclohexanecarbonitrile) (ABCN), Methacrylic Acid (MAA), Chloroform ($CHCl_3$), Ethanol, Methanol, and Acetic acid were purchased from Merck and Co., India. All the authentic volatile compounds and experimental materials were purchased as discussed in Chapter 4, Section 4.2.1.

7.2.2. Apparatus and software

10 MHz AT-cut piezoelectric quartz crystals of 8mm diameter, attached with two gold electrodes of 5 mm diameter on both sides, were purchased from Andhra electronics, Andhra Pradesh, India. Computational design simulation was executed with the help of HyperChem8.0 software, as discussed in Chapter 4, section 4.3.1. The GC-MS analysis was performed using Agilent 7890A (Agilent Technologies Inc., Santa Clara) with an HP-5 MS column (30m×0.25mm×0.25µm) at the Department of Botany, University of Calcutta, India.

7.2.3. Synthesis of molecularly imprinted polymer (MIP) and non-imprinted polymer (NIP)

The molecularly imprinted polymer was synthesised by following the free radical polymerisation method using a non-covalent bulk imprinting approach. This methodology is mounted on making relatively weak non-covalent interactions (i.e., hydrogen bonds, ionic interactions, etc.) between

the template molecule and selected monomers before polymerisation. This approach is mainly implemented for the preparation of MIPs owing to its lucidity and the abundance of a broad range of monomers [13]. 20.6 µL (0.1 millimoles) of the template α-terpinyl acetate was mixed with 25.3 µL (0.3 millimoles) of the functional monomer MAA, and the mixture was dissolved in 1.2 mL $CHCl_3$ (a non-polar, porogenic solvent) in a glass vial. Solvent has inevitable importance in template-monomer binding interaction. Here, chloroform has opted as its low dielectric constant favours the electrostatic interaction and stabilisation of the H-bond. Then 24.5 µL (0.13 millimole) of the crosslinker EGDMA was added to it, followed by the addition of a radical initiator ABCN (0.01 gm). It is important to stress that the presence of a crosslinker not only preserves the binding sites but also directly influences the polymer matrix's physical and chemical properties. EGDMA has been chosen in the present work as it caters to mechanical and thermal durability, appreciable wettability, and accelerated mass transfer. The mixture was purged with nitrogen gas for 3 mins. to prevent any inhibition of the initial radical initiation process imposed by any oxygen content present in the medium. This purging also reduces the percentage of probable side reactions. The vials were made airtight by screw-on tops.

Then the prepolymer solution was made homogeneous by ultrasonication at room temperature for about 10 mins. It was then heated with continuous stirring in a water bath at about 65 $^{\circ}$C. Thus, the polymerisation was initiated, and at the gel point [13] (transition of an amorphous material from the liquid phase to solid phase), when the solution turned opaque by appearance [14], it ceased to obtain the MIP oligomer solution [15]. Likewise, a similar NIP oligomer solution without the template aTA was prepared for our comparative study.

The template moiety must possess functional groups capable of interacting with the monomer(s) to form a stable complex. An equilibrium process highly controls the template-monomer interactions, and henceforth, excess of the monomer is employed to drive the equilibrium to form the template-monomer complex [8,16]. Generally, a suitable template-monomer molar ratio provides better stability to the template monomer complex, ensuring the longed imprint effect or, in the crude sense, a sort of lithographic effect [17]. In the present work, the best result by 1:3 molar ratio has also been confirmed from the binding energy calculation, as shown in the latter part of the manuscript. However, since excess free monomers lead to the formation of nonspecific binding sites, the loading, washing, and elution conditions for MIP must be appropriately

maintained. Since the template (during the imprinting process) or the target (during the binding process) interacts with the polymer by various complementary non-covalent interactions, e.g., hydrogen bonding, hydrophobic interaction, van der Waals interaction, ionic bonding, dipole-dipole or dipole-induced dipole interaction, etc., the choice and the amount of the monomer play the pivotal role behind the effective adsorption by the imprinted polymer. Methacrylic acid (MAA) is chosen as the monomer since it can simultaneously act as a proton donor as well as a proton acceptor (doubled bonded O atom in the carboxylic acid group) and in excess to the no. of moles of the template, aTA to obtain the template-monomer assembly undergoing maximum interactions [15]. The above ratio was obtained after thorough optimisation and was supported by binding energy (ΔE) calculations from *HyperChem8.0* software [9]. The self-assembly is followed by cross-linked copolymerisation with EGDMA imparting the mesoporous nature of the polymer matrix.

7.2.4. Sensor fabrication and extraction

A 10 MHz AT-cut QCM gold crystal was washed properly with ethanol thrice, followed by complete drying of the surface by applying hot air. 1µL of the MIP oligomer solution was drop coated on the surface of the gold electrode. The NIP oligomer solution was also coated similarly. Then the rest of the polymerisation of the oligomer coatings was carried out in a vacuum oven at 60°C for 30 mins. Therefore, at the end of the polymerisation route, the MIP oligomer layer transformed into polymerised methacrylic acid (PMAA) containing the template aTA, producing the aTA-MIP-QCM sensor with the MIP substrate coating.

Similarly, the NIP oligomer one turned into PMAA without the presence of aTA and NIP-QCM was obtained with NIP substrate film. After that, to extract the template aTA, the aTA-MIP-QCM sensors were immersed in a solution containing methanol and acetic acid (9:1, %v/v) for about 30mins. It was followed by immersion in Millipore water obtained for another 30mins. Washing steps continued by drying the sensor surface with hot air until no significant change in frequency was observed. Thus, through a repetitive wash with methanol and an aqueous solution of an acid, the non-covalent interactions can be easily nullified, resulting in imprinted polymers with three-dimensional microcavities that are highly selective as well complementary in shape and chemical functionality for the template. The schematic of the molecularly imprinted polymer synthesis along with sensor fabrication steps is illustrated in Fig. 7.1.

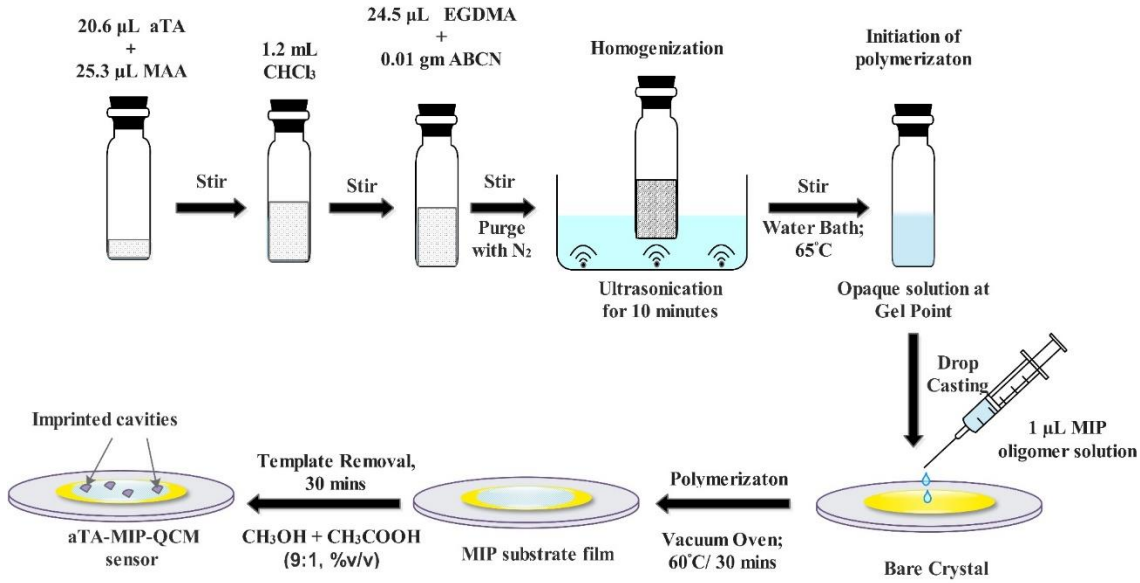

Fig. 7.1. Synthesis and fabrication steps of the aTA-MIP-QCM sensor.

Applying the MIP technique to QCM wasn't easily achievable, as reported by some groups [18–21], because of the poor binding interaction between the QCM surface and MIP, along with the form and size of the MIP particle. To overcome this hindrance, N. Tsuru et al. suggested a fabrication method by self-assembly monomer using Aminoethane thiol (AET) before coating with the MIP prepolymer solution [20]. On the other hand, in the gel point method, the oligomer solution has a higher viscosity which probably leads to increased surface tension, helping it to adhere firmly to the QCM crystal. Also, since the oligomer solution doesn't usually have many accessible carboxylic acid units due to the initiation of the polymerisation, the amine ($-NH_2$) units of AET can't bind with MIP properly, which eventually leads to poor results. Fig. 7.2 shows the interaction of the MIP coating involving the template molecule and the cavity formation following extraction.

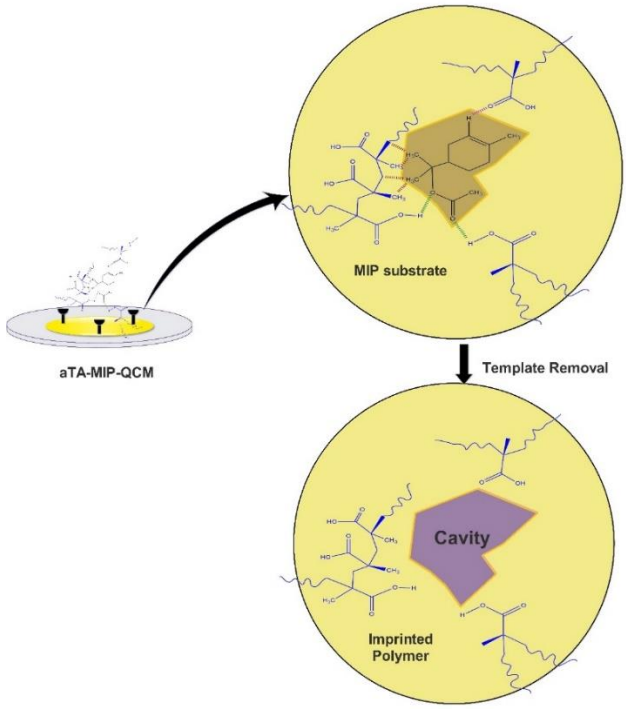

Fig.7.2. Schematic representation of the MIP substrate formed on the aTA-MIP-QCM sensor before and after template removal.

FTIR spectroscopy was chosen as a tool to evaluate the synthesised MIP before and after extraction. For this purpose, the MIP oligomer solution was prepared and coated in the previously described method but using glass slides instead of QCM sensors. After that, the MIP film was removed from the glass slide and was ground homogeneously with KBr (Pottasium Bromide) (MIP substrate:KBr = 1:200, w/w) in a mortar. Finally, the MIP substrate was pressed under a hydraulic pump to form KBr pellet for its FTIR spectral analysis.

7.2.5. Measurement setup and sensor measurements

The portable QCM-based sensing system and measurement setup were developed to monitor the ssensitivity, selectivity, reproducibility, and long-term stability, as discussed in Chapter 3. The detailed information regarding experimental conditions and additional setups was discussed in Chapter 4, section 4.2.3. In addition, an array-based arrangement comprising eight sensors was used to study the reproducibility of the sensors based on the dynamic headspace sampling method [10].

7.2.6. Volatile test analytes preparation

The VOCs like 1,8-cineole, α-terpinyl acetate, α-pinene, β-pinene, α-terpineol, and γ-terpinene were prepared inside 10 L desiccators for the experimental study. All the methodology are identical, as discussed in Chapter 4, section 4.2.4.

7.3. Results and discussion

7.3.1. Study of the optimal ratio of template and monomer

A study was conducted to optimise the template ratio to the monomer to detect aTA VOC with the most effective sensor performance. The test was carried out by fabricating five aTA-MIP-QCM sensors with a various template: monomer ratios (1:1, 1:2, 1:3, 1:4, 1:5) while keeping all sensor fabrication and extraction methods constant. Under similar experimental conditions, the sensors were subjected to 50 ppm of aTA VOC while maintaining the same experimental parameters. Fig. 7.3 demonstrates that when the ratio of template to monomer increases, the sensor output increases until the ratio reaches 1:3, at that point it starts decreasing. The likely cause is the enhanced binding affinity of aTA VOC towards template-specific binding sites produced during template extraction in the aTA-MIP-QCM sensor, which has been examined further using binding energy (ΔE).

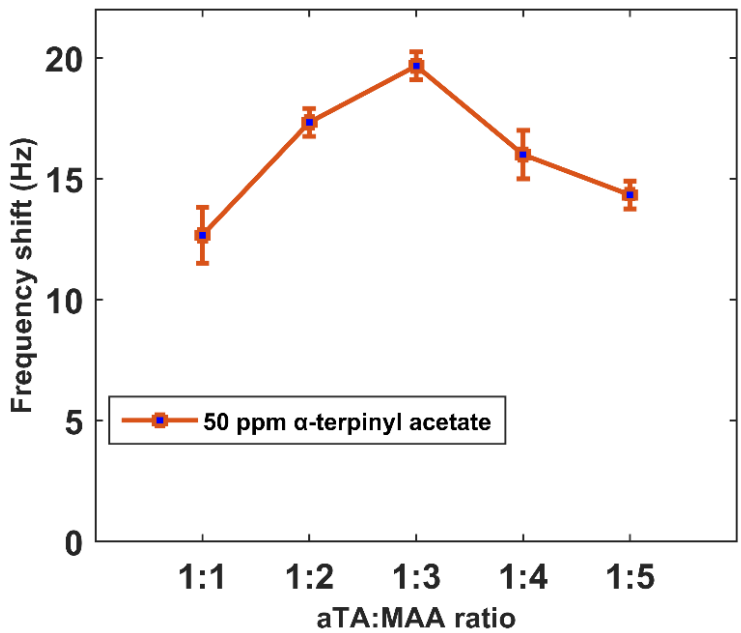

Fig. 7.3. Response profile of aTA-MIP-QCM sensor for different concentrations of the template to monomer ratio (1:1, 1:2, 1:3, 1:4, 1:5) exposed to 50ppm of aTA VOC (27 ± 1) ºC.

7.3.2. Binding energy calculation using HyperChem 8.0

Binding energies (ΔE) required for complexation for different ratios of template and monomer were calculated using equation (7.1), where the individual components of the equation were obtained from *HyperChem 8.0* software [9].

$$\Delta E = E_{Complex} - (E_{Template} + \Sigma E_{Monomer}) \quad (7.1)$$

Where $E_{Complex}$ is the total binding energy (kcal/mol) of α-terpinyl acetate with the MAA molecules in each different ratio, $E_{Template}$ and $E_{Monomer}$ are individual binding energies (kcal/mol) of α-terpinyl acetate and MAA respectively.

Now, binding energy for each MAA unit ($E_{Binding}$) was calculated by modifying equation (7.1) to equation (7.2).

$$E_{Binding} = \frac{\Delta E}{\sum MAA} \quad (7.2)$$

By literature review [22], it can be stated that the high value of the parameter $E_{Binding}$ between the "key" template and the "lock building block" monomer indicates significant binding affinity of the target for the imprinted polymer since proper complementary interactions in a potent template-monomer assembly lead to template-specific receptor sites. Therefore, optimisation of the template: monomer ratio is one of the utmost important factors. $E_{Binding}$ values for the different proportions of aTA and MAA are shown in Table 7.1.

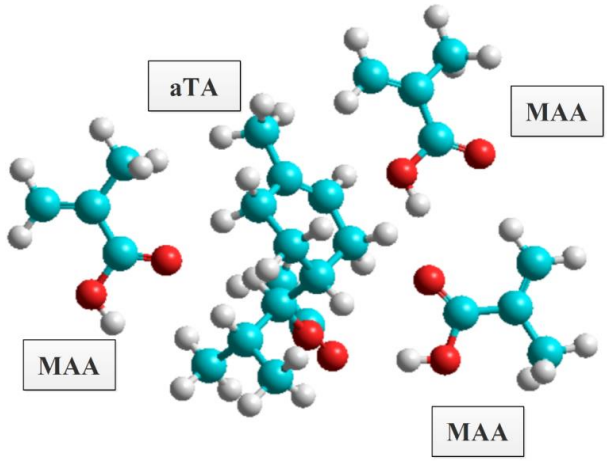

Fig. 7.4. Prepolymer assembly of aTA and MAA molecules.

Hydrogen bonding, van der Waals interaction, and dipole-induced dipole interaction contribute most to developing the pre-polymerisation complex for a single aTA molecule (Fig.7.4), wherein blue colour represents C atom, red colour represents O atom, and white colour represents H atom). Likewise, the range of $E_{Binding}$ values indicates the same [23]. The ideal template-monomer ratio of 1:3 was maintained to provide good sensitivity while retaining a high value of EBinding between the aTA-MIP-QCM sensor and aTA VOC.

Table 7.1. $E_{Binding}$values for different ratios of aTA and MAA

aTA: MAA	**$E_{Complex}$ (kcal/mol)**	**ΔE (kcal/mol)**	**$E_{Binding}$ (kcal/mol)**
1:1	-4797.74	-3.32	-3.32
1:2	-6003.58	-10.97	-5.48
1:3	-7207.66	-16.84	-5.61
1:4	-8406.20	-17.19	-4.29
1:5	-9606.08	-18.88	-3.77
1:6	-10805.17	-19.77	-3.29
1:7	-12004.58	-20.99	-2.99
1:8	-13200.53	-18.74	-2.34

7.3.3. FTIR analysis

Fig.7.5 elucidates the FTIR spectra (Perkin Elmer System 2000 spectrophotometer) of the MIP substrate before (black line) and after extraction (red line). We have tried to ensure the bonds' specification in our synthesised material. The peaks at 1450 and 1640 cm^{-1} in the plot Fig. 7.5(a) were attributed to C=O stretching of the ester group and non-conjugated C=C stretching, respectively [24,25]. The small shoulder around 1500 cm^{-1} arises due to conjugated C=C stretching. This peak appears at a lower frequency as this double bond gets partial single bond character due to a response with the carboxylic acid group.

The peaks at 2861 and 2917 cm^{-1} in Fig. 7.5(a) were assigned to the C-H stretching of the gem dimethyl group present in the α-terpinyl acetate, and the absence of these two peaks in Fig. 7.5(b) confirms the successful removal of the template from the MIP material [24]. Intermolecular H bonding between aTA and PMAA in the MIP film probably results in the peak at 3430 cm^{-1} in Fig. 7.5(a). The absence of this peak in plot Fig. 7.5(b) strengthens the proof of removal of the template aTA. The superimposed peak at 1700 cm^{-1} in plot b certifies the presence of C=O stretching of the conjugated carboxylic acid group. This plot's small peak around 1200 cm^{-1} appears due to C-H rocking vibration. The peaks at 3605 cm^{-1} in both the spectra (plots a & b) confirm the H-bonded O-H stretching of carboxylic acid groups [24,26]. As the H bond formed between two carboxylic acid groups is more substantial than that between one carboxylic acid group and one ester group, so the peak becomes shorter in the case before extraction of the MIP substrate (plot a). The peak at 1704 cm^{-1} in plot b appears due to C=O stretching of the conjugated carboxylic acid group [24]. The C=O bond of the carboxylic acid group becomes weaker here due to the +R effect of the conjugated pie bond. So, this vibration appears at a lower frequency.

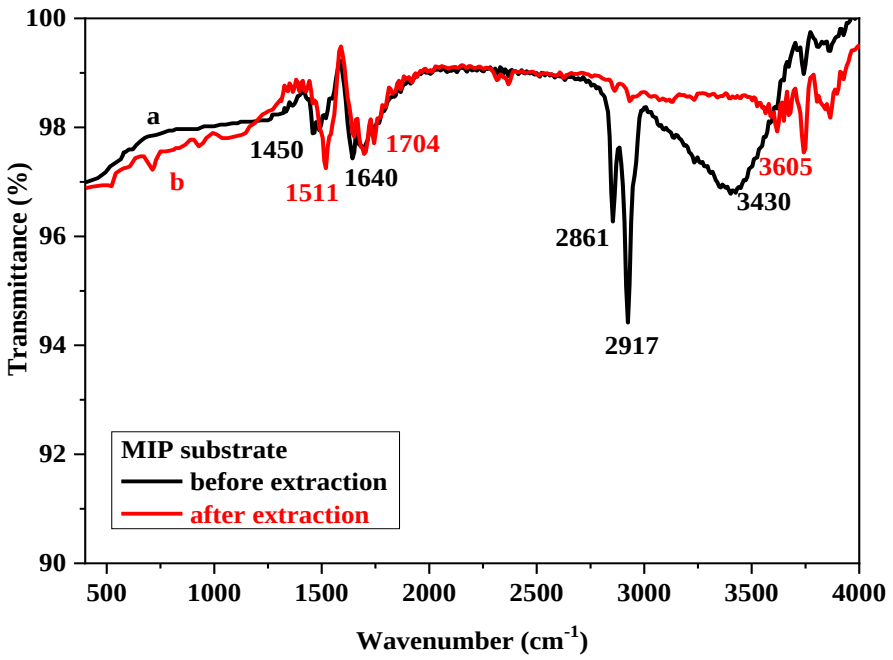

Fig. 7.5. FTIR spectra of the synthesized MIP substrate (a) before (black line) and (b) after (red line) template removal.

7.3.4. SEM analysis

Surface physisorption is a quintessential part of our fabricated QCM gas sensor. So, the idea about the surface morphology and topology of the adsorbent polymethacrylic acid (PMAA) helps us to plunge deeper into the entire process. We have taken the help of SEM micrographs (Carl ZEISS EVO 10) of the aTA-MIP-QCM sensor before Fig. 7.6(a) and after the removal of the template Fig. 7.6(b). There lie distinct differences between the two pictures. This difference confirms the absence of the template, which is the targeted α-terpinyl acetate on the MIP substrate after extraction Fig. 7.6(b). The MIP substrate before extraction Fig. 7.6(a) has nano rod-like morphology, and the generated nanorods possess a rough surface, probably due to the attachment of α-terpinyl acetate on the polymeric surface of PMAA.

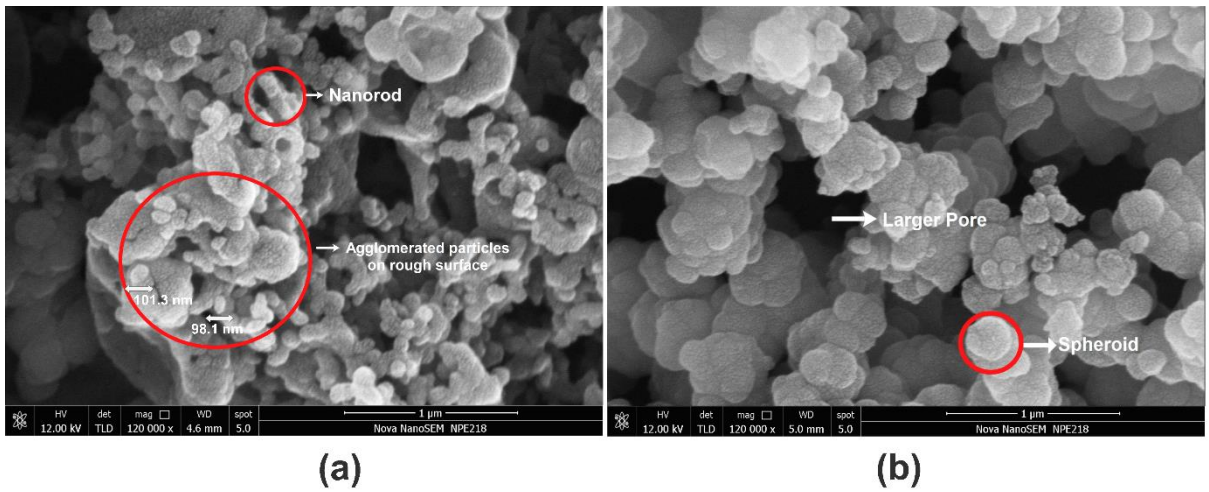

Fig. 7.6. SEM images of aTA-MIP-QCM (a) before and (b) after removal of α-terpinyl acetate template.

The molecules mostly remain in the agglomerated form on this surface [27]. After the template is removed, there is a change in intermolecular torsional strain in the crystals of MIP material, which may result in a modification in the surface morphology of the polymer. It has a spheroidal shape. This surface has a lower degree of particle agglomeration, which leads to the generation of larger pores on the surface. These holes facilitate material surface adsorption by promoting host-guest complexation via a lock and key process. This host-guest interaction is mainly controlled by hydrophobic interaction, dipole-dipole interaction, van der Waals force, and weak hydrogen bonding [28]. The synthesised MIP layer has an agglomerated average particle size of roughly 100 nm. This tiny particle size increases the surface area of the substance, and a larger surface area

favours physisorption on the material surface.

7.3.5. Adsorption-desorption isotherm

The higher the surface area of the adsorbent, the higher the extent of adsorption on the surface. The optimum surface pore size helps entrap the adsorbate molecule properly. So, the adsorption-desorption isotherm of the MIP substrate layer's adsorbent analysis was performed in a Quantachrome Autosorb-1 that has been presented in Fig.7.7 to cater to the idea regarding this film's surface area and pore size. The material's average pore diameter and surface areas are 24.1Å and 480.3 $m^2.g^{-1,}$ respectively. This pore diameter depicts that our synthesised MIP material is mesoporous. It possesses tiny mesoporous polymeric networks stabilised by covalent bonds [29]. The great extent of cross-linking between polar monomer MAA with the crosslinker EGDMA provides two- or three-dimensional architecture to the entire polymeric PMAA surface, which is also supported by its SEM morphology [30]. Rather than micropores or macropores, these mesopores have the best size-matching with the adsorbate α-terpinyl acetate molecules. So, the adsorbate molecules are most adsorbed adequately on the surface pores. The tiny surface mesopores result in a larger surface area of the material. This higher surface area of the material is one of the key reasons behind the effective surface physisorption by the MIP coating film, which is confirmed from our decorated QCM gas sensor data in the latter part of this chapter [31].

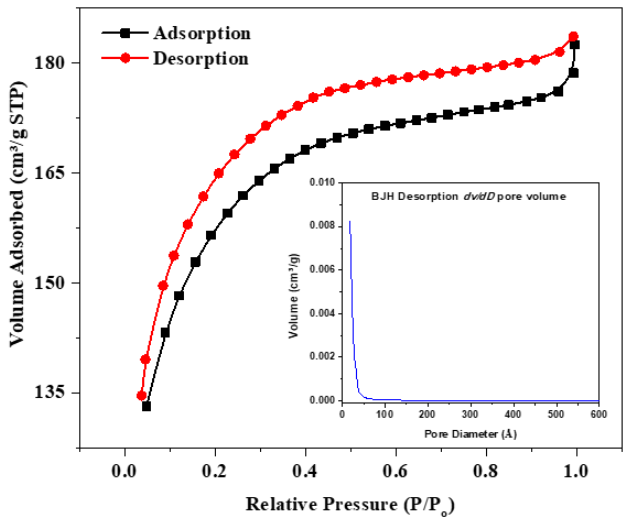

Fig. 7.7. Adsorption and Desorption Isotherm characteristics of the synthesised MIP substrate.

7.3.6. Thermogravimetric analysis

The TGA thermogram (Exstar 2000) of the MIP substrate is depicted in Fig. 7.8. It indicates that the material's thermal stability is relatively high and stable up to 800 ºC. No phase change is observed in this temperature limit. The high molecular weight of the MIP film generates a high intermolecular van der Waals force of attraction within it, and this force probably plays a crucial role in its high thermal stability. A slight decrease in the weight of the material has been observed with a gradual increase in temperature, probably due to the loss of adsorbed water from the surface of the material. The tiny fall of the thermogram at around 305 ºC may have resulted from the thermal decomposition of carboxylic acid group releasing CO_2 [32].

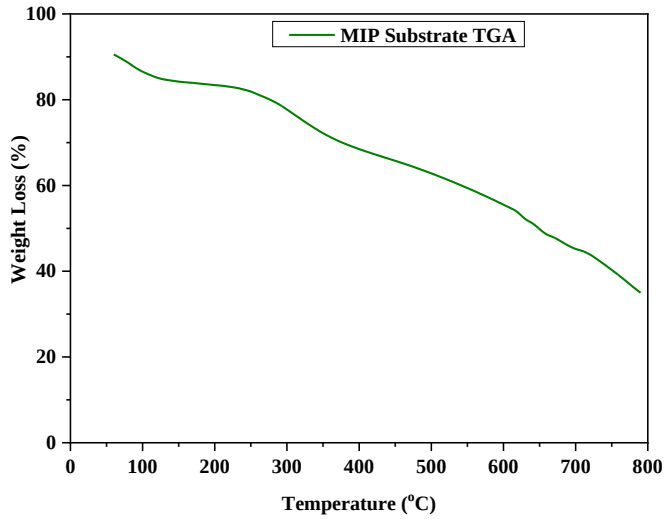

Fig. 7.8. Thermogram of MIP substrate obtained from TGA.

7.3.7. Study of the effect of humidity

Since ambient air was used as the medium for injecting the target VOCs into the sample chamber, it was crucial to determine the effect caused due to humidity in the air on the sensing performance of the as-prepared sensor. The impact of the relative humidity on the response of the aTA-MIP-QCM gas sensor was studied and is shown in Fig. 7.9. The frequency shifts of the fabricated QCM sensor after stabilisation at various relative humidity are represented in Fig. 7.9(a). The frequency shifts were raised from 1 to 3 Hz on escalating the RH from 45 to 85% because a large number of hydrophilic carboxyl groups of PMAA in the mesoporous surface adsorb the polar water molecules, which increases the frequency shift [33,34]. Here the extent of adsorption of H_2O

molecules is relatively low due to the sizeable hydrophobic hydrocarbon moiety in PMAA and low loading of the material. The change in frequency is negligible with the change in relative humidity in ambient air, probably due to almost saturated adsorption of H_2O molecules at higher humidity.

The change in sensing characteristics due to the effect of relative humidity on the application of aTA aroma into the particular MIP sensor is illustrated in Fig. 7.9(b). aTA VOC forms a weak intermolecular H-bond with water molecules. But here, the frequency shift changes also vary slightly with the change in relative humidity due to dominating hydrophobic interaction among the aTA molecules. Because the fabricated aTA-MIP-QCM gas sensor was almost independent of relative humidity, the entire experiments were conducted in ambient humidity of 67.7% during the scheduled investigations.

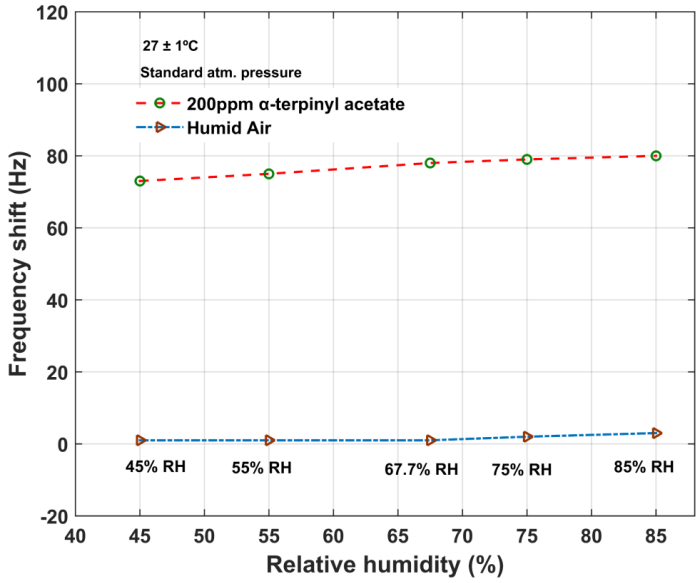

Fig. 7.9. Response profile of aTA-MIP-QCM sensor towards ambient air and 200 ppm of aTA VOC at different relative humidity (45%, 55%, 67.7%, 75%, 85%) at 27 ± 1 ºC and standard atmospheric pressure.

7.3.8 The sensitivity of aTA-MIP-QCM sensor

The sensitivity of the developed aTA-MIP-QCM sensor was studied using the static headspace sampling setup. The fabricated sensor was kept inside the airtight 100 mL Teflon sensor chamber, and the target α-terpinyl acetate VOC was injected by a syringe pump at a rate of 2 mL/sec at a varying concentration from 10 – 1000 ppm. Each sampling of α-terpinyl acetate VOC was continued until the QCM frequency response reached a saturation value and the frequency shift of

the sensor from its initial frequency was calculated, followed by purging of the sample chamber by ambient air. The complete aTA-MIP-QCM sensor response curve towards 1000 ppm of aTA VOC with reference to time was illustrated in Fig.7.10(a). The sensor was ideally kept oscillating at its resonating frequency for 12 sec, and the sensor response showed a stable frequency response. Upon injection of aTA VOC inside the sensor chamber, the resonant frequency of the as-prepared sensor showed a decreasing trend in output. Initially, adsorption of the template towards the specific binding sites promptly decreased the frequency up to 371 Hz in 28 sec, following which the rate of frequency shift was retarded, reaching 384 Hz, attaining the saturation state. During purging the sensor chamber with ambient air, the frequency shift was recovered, getting the initial sensor baseline, which demonstrated rapid reversibility of the fabricated sensor.

The aTA-MIP-QCM sensor frequency responses upon injection of 10-1000 ppm of aTA VOC at 67.7% RH have been illustrated in Fig. 7.10(b). The frequency responses of a blank QCM under similar experimental conditions were explored for a comparative study. The increasing range of concentration of aTA VOC produced almost identical frequency response curves in shape for each applied concentration of input volatile, but with proportional escalating values of frequency shift at the saturation state. All the responses returned to their initial baseline during purging and showed negligible drift during the entire experimentation. The bare crystal, however, showed a imperceptible reaction to aTA VOC.

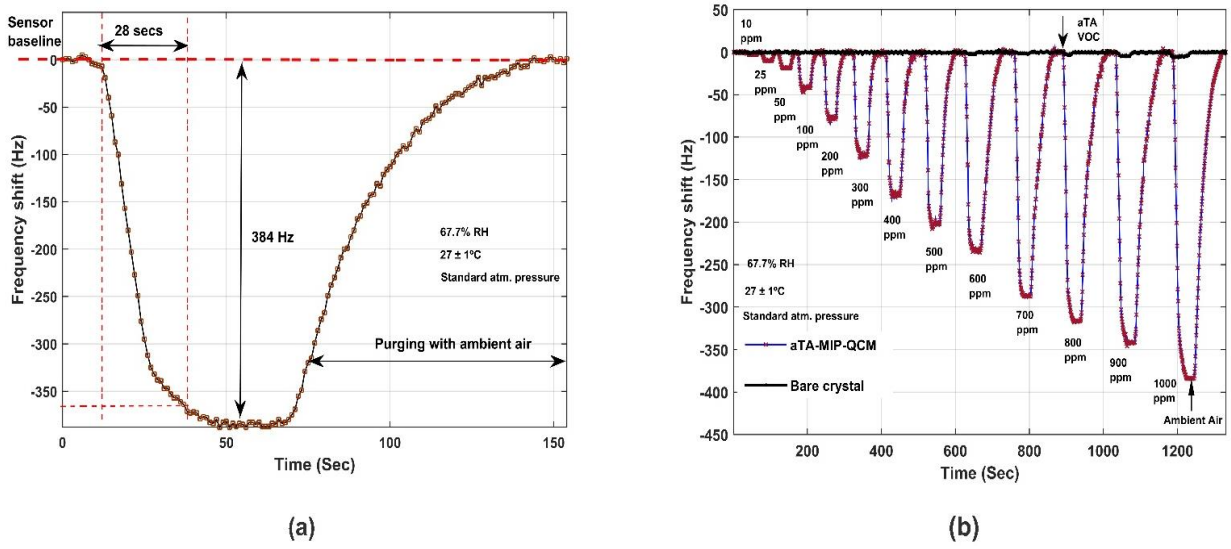

Fig. 7.10. Complete aTA-MIP-QCM sensor response profile (a) for 1000 ppm of aTA, (b) at different ppm values (10 -1000ppm VOC) at (27 ± 1) ºC, 67.7% RH, and standard atmospheric pressure.

The sensitivity characteristics curve of the sensor has been plotted considering frequency shift for each applied ppm of α-terpinyl acetate vapour and other competing VOCs like α-terpineol, α-pinene, β-pinene, and 1,8-cineole. The sensitivity of the fabricated aTA-MIP-QCM sensor showed enhanced sensitivity towards α-terpinyl acetate as compared to other test volatiles were demonstrated by the characteristics calibration curve in Fig. 7.11.The linear equation between the frequency shift of the sensor at the saturation state with the corresponding aTA concentration following Saurbrey's equation stated as

$$y\,(Hz) = 0.3876\left(\frac{Hz}{ppm}\right)x + 3.003 \qquad (7.3)$$

The sensor shows the sensitivity of 0.3876 ± 0.0007 Hz/ppm with a 95% confidence interval, y indicates the frequency shift of aTA-MIP-QCM sensor towards various applied concentrations of aTA in Hz, and x is the concentration of injected aTA VOC in ppm. A good linear correlation is established between the injected concentration of VOC (in ppm) and its corresponding sensor output (in Hz) with a correlation coefficient, R^2 = 0.9979, where R denotes the regression coefficient. The standard error estimate computes the average of the distance that the actual values fall from the regression line.

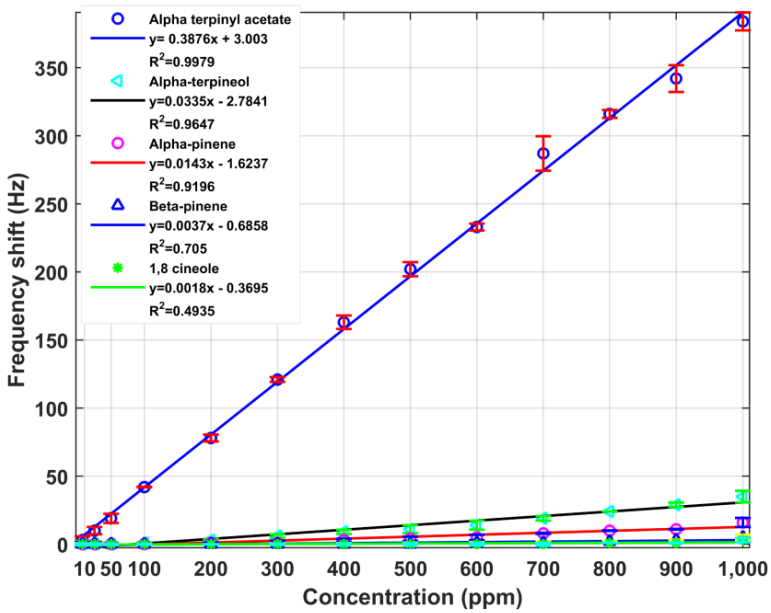

Fig. 7.11. Sensitivity plot of aTA-MIP-QCM sensor for α-terpinyl acetate and other competent VOCs (10 -1000 ppm).

The standard error of the estimate (σ_{est}) has been calculated to be 6.51 Hz strongly shows fewer errors of the actual data points around the linear plot; thus, the data points can be considered well-fitted. The limit of detection (LOD) and limit of quantitation (LOQ) [28] were calculated to be 4.46 ppm and 14.86 ppm. All the calculations were done following the equations mentioned in Chapter 4, section 4.3.2.

The study of the sensitivity of the fabricated aTA-MIP-QCM sensor has been further extended by comparing the response of NIP-QCM and bare gold crystal upon injection of 500 ppm of α-terpinyl acetate vapour. The difference in the sensor output responses is plotted in Fig. 7.12.

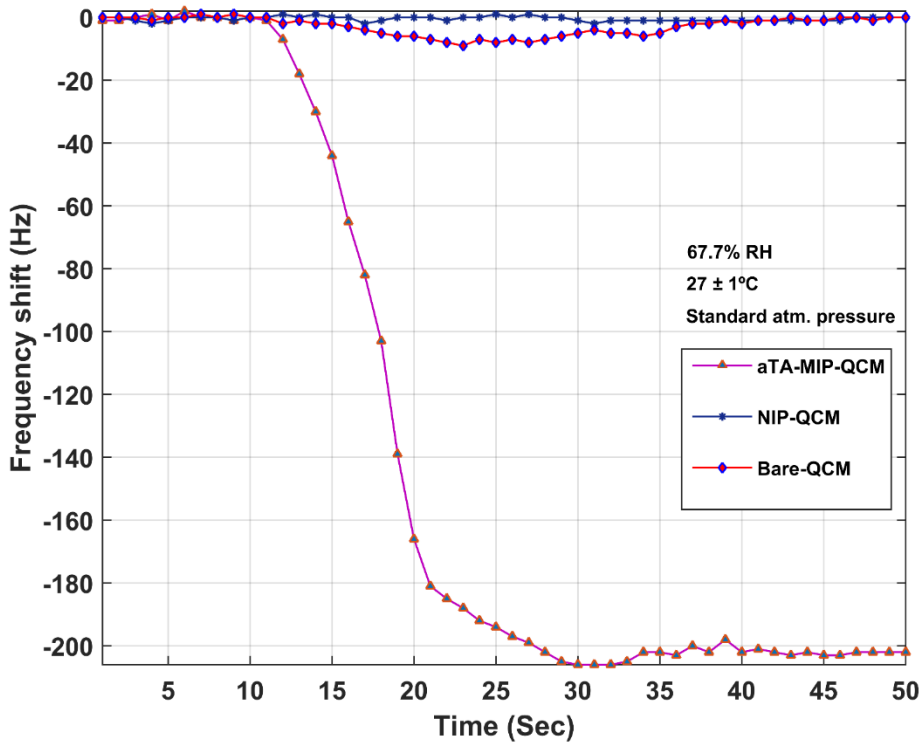

Fig. 7.12. Comparative output response of aTA-MIP-QCM, NIP-QCM, and bare gold crystal towards 500 ppm aTA vapour at (27 ± 1) ºC, 67.7% RH, and standard atmospheric pressure.

The sensor showed a stable response after it reached the saturation stage, indicating good VOC adsorption in the imprinted cavities. The higher frequency shift for the aTA-MIP-QCM sensor than that for the NIP-QCM and bare crystal clearly shows the presence of binding sites in the decorated sensor due to the formation of the cavity. The outcome indicates the removal of the template molecule. It is also evident from the frequency shift of the NIP-QCM sensor that the NIP

substrate formed without the inclusion of the template molecule doesn't play any significant role in the sensitivity of the sensor.

7.3.9. Study of the selectivity of aTA-MIP–QCM sensor

The aTA-MIP-QCM sensors show high selectivity towards the template molecule as the generated specific binding sites on the sensor facilitate very specific adsorption of the target analyte of interest. In this study, the selectivity (S) of the developed aTA-MIP-QCM sensor was tested with other VOCs in the small cardamom, α-terpineol, β-pinene, α-pinene, and 1,8-cineole, which are the most common volatiles present in the aroma profile of small cardamom as reported by several researchers. [35–37]. The aTA-MIP-QCM sensor was sampled with 900 ppm of all the mentioned VOCs along with the target analyte α-terpinyl acetate following the same experimental setup and procedures as stated earlier, and the selectivity is calculated using equation (7.4).

$$S_{VOC} = \frac{R_{VOC}}{\sum_{i=1}^{n} R_i} \times 100\% \qquad (7.4)$$

Where S_{VOC} denotes the selectivity of the sensor towards a particular VOC, R_{VOC} is the sensor response for that VOC, n is the total number of test volatiles, R_i is the sensor response for the individual VOCs.

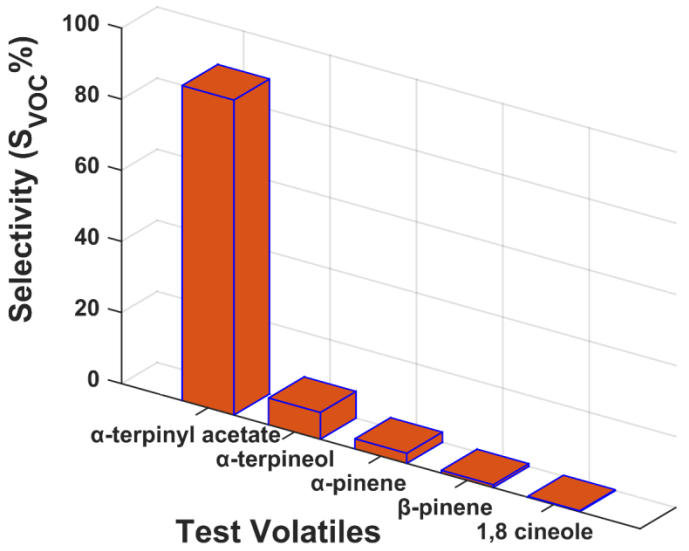

Fig. 7.13. Selectivity (%) bar plot of aTA-MIP-QCM sensor towards α-terpinyl acetate, α-terpineol, β-pinene, α-pinene, and 1,8-cineole at 900 ppm.

The selectivity bar plot shown in Fig. 7.13 indicates that the aTA-MIP-QCM sensor is the most selective towards the target analyte α-terpinyl acetate, binding it with various non-covalent interactions, with a selectivity factor of 88.60% compared to the other competent volatiles like α-terpineol, α-pinene, β-pinene, and 1,8-cineole. α-terpineol has achieved the second position since aTA is the corresponding acetate ester of α-terpineol and has many structural similarities. It is followed by α-pinene also because of having a similar skeleton. Meanwhile, β-pinene and 1,8-cineole (boat structure), not having a bare resemblance of chemical structure with aTA, end up being in the last two spots. According to different researches conducted to detect the volatile components present in cardamom and the solid-phase microextraction followed by gas chromatography-mass spectrometry (SPME-GCMS) evaluation of different cardamom samples in our study, it could be easily deduced that the abundance of α-terpineol and α-pinene was lower than that of α-terpinyl acetate. However, 1,8-cineole occupied the maximum abundance in the SPME-GCMS evaluation of the experimented samples, but it showed very less selectivity towards the as-prepared sensor. Hence, it was understandable that the effect of cross-sensitivity towards α-terpineol and α-pinene had no impact on the accuracy of the as-prepared sensor for detecting aTA in real samples. However, detection of aTA in other samples with variable concentrations of α-terpineol and α-pinene can lead to inaccuracy and may be subject to further studies. Overall, the as-prepared sensor was suitable for identifying the aTA VOC accurately in cardamom or other real samples with a lower abundance of α-terpineol and α-pinene. The frequency responses of aTA-MIP-QCM and NIP-QCM sensors for each competing VOC at 900 ppm are shown as bar plots along with their respective chemical structures in Fig. 7.14. The bar graph portrayed uniform selectivity, without any particular dependency on the sensitivity of the NIP-QCM sensor for the competing VOCs due to the non-availability of the template-specific binding sites, which validated the sensory improvement of the as-prepared MIP sensor.

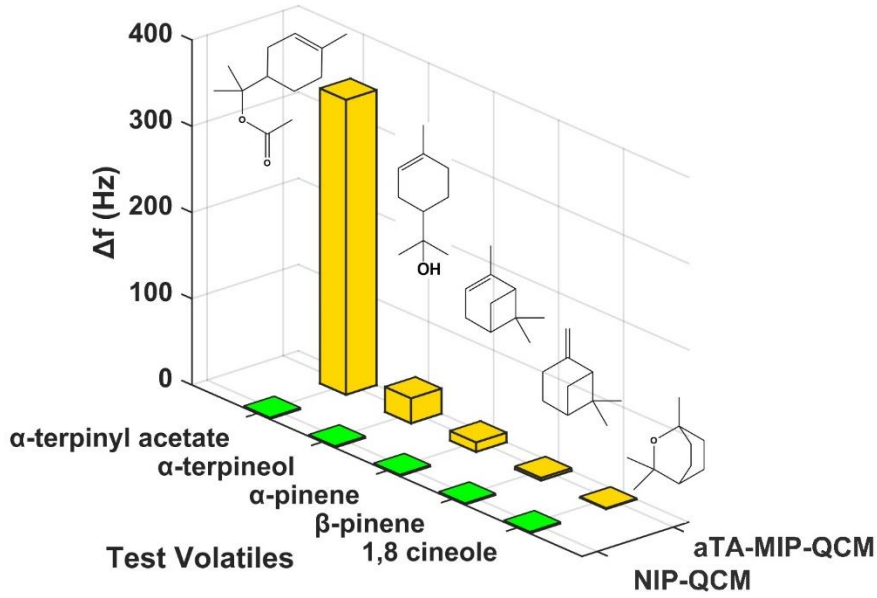

Fig. 7.14. Selectivity pattern of aTA-MIP-QCM and NIP-QCM for different VOCs at 900 ppm.

7.3.10. Study of the long-term stability of aTA-MIP-QCM sensor

The study of the long-term stability of a sensor is useful for its reusability in experimental conditions. The stability of the developed aTA-MIP-QCM sensor was studied by regularly exposing the fabricated sensor to 100 ppm of aTA VOC for an interval of every five days from the day of fabrication. A similar experimental condition was maintained, and the sensor frequency shift for each sampling of aTA VOCs was duly noted. The aTA-MIP-QCM sensor output calculated in (mean ± standard deviation) for four repeated sampling cycles as shown in Fig. 7.15 were 42 ± 0.57 Hz (0 days), 42 ± 1.154 Hz (5 days), 41.25 ± 0.57 Hz (10 days), 39.75 ± 1.52 Hz (15 days), 39.25 ± 0.57 Hz (20 days), 39 ± 1.73 Hz (25 days), 38 ± 0.57 Hz (30 days). The sensor responses showed no significant loss in frequency reading for one month, thus ensuring stable sensing properties of the aTA-MIP-QCM sensor.

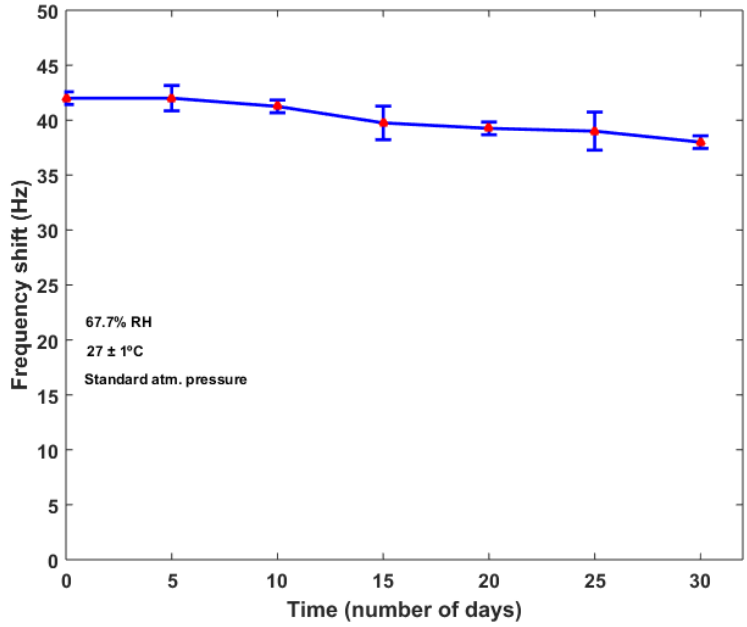

Fig. 7.15. Stability of aTA-MIP-QCM sensor at 100 ppm aTA monitored for 30 days at (27 ± 1) ºC, 67.7% RH, and standard atmospheric pressure

7.3.11. Repeatability and reproducibility

The reproducibility of the developed aTA-MIP-QCM sensor was assessed by fabricating eight aTA-MIP-QCM sensors under similar experimental conditions and chemical procedures. The frequency shift due to the deposition of the polymer after removal of the template was kept identical. All the sensors were injected with 10 -1000 ppm of α-terpinyl acetate vapour inside the sensor chamber and the corresponding frequency shift was considered for estimating the percentage reproducibility (R_D) as given by the equation (7.5).

$$R_{P,D} = (1 - RSD) \times 100\% \qquad (7.5)$$

Repeatability is a crucial sensor characteristic and was examined for the developed aTA-MIP-QCM sensor by continuously exposing the sensor to 300 ppm of aTA VOC and purging with ambient air for four repeated cycles. Fig. 7.16 depicts the sensor response for four repeated cycles, and the time of injection of VOC into the sample chamber and purging of the test volatiles were adequately marked. The response curves were alike, with almost similar frequency shifts to the incoming VOC and time of recovery to the baseline during purging. The sensor value for the as-prepared sensor examined for repeatability was 122.75 ± 1.70 Hz. The percentage repeatability

(R_P), was obtained by sampling α-terpinyl acetate VOC repeatedly four times with 10 – 1000 ppm of each concentration. The average frequency shift was taken for the calculation by using equation (7.5). The result also shows an increasing trend in repeatability with increasing concentration of the analyte. The average repeatability value is 94.72%, confirming the ability of our sensor for repeated detection of α-terpinyl acetate vapour at higher concentrations.

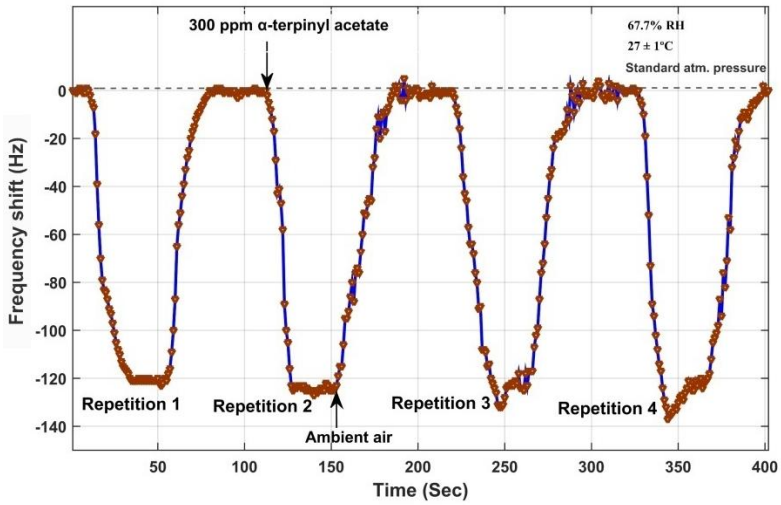

Fig. 7.16. aTA-MIP-QCM sensor responses for four repeatable exposure towards 300 ppm of aTA at (27 ± 1) ºC, 67.7% RH, and standard atmospheric pressure.

The corresponding sensitivity of the eight reproduced aTA-MIP-QCM sensors were compared and shown in Fig. 7.17. The sensors showed sensitivity ranging from 0.3844 to 0.3888 Hz/ppm with an average sensitivity of 0.387 ± 0.0013 Hz/ppm. The average reproducibility (R_D) of the sensor deviation value is estimated to be 93.76%, ensuring the easy removal and substitution of a sensor fabricated in different batches. This result indicates that the sensor output can be achieved with negligible variation insensitivity. It could be concluded that the polymer synthesis mechanism and coating arrangement followed in this experiment were able to fabricate identical aTA-MIP-QCM sensors.

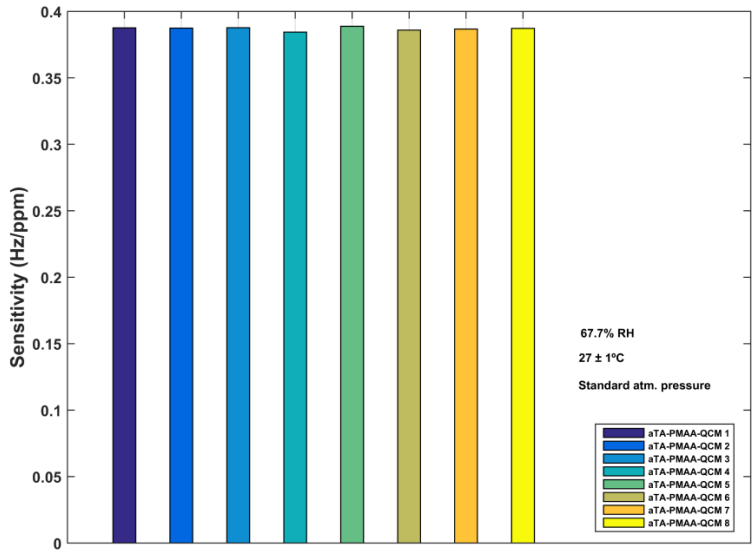

Fig. 7.17. Bar plot of the sensitivity (Hz/ppm) of eight reproducible aTA-MIP-QCM sensors at (27 ± 1) ºC, 67.7% RH, and standard atmospheric pressure.

Table 7.2 presents the R_P and R_D values and a 95% confidence interval for each concentration. The confidence interval values conclude that the repeatability and reproducibility of the sensor are exact with less deviation from the mean of the sensor data at every varying concentration.

Table 7.2. Repeatability and Reproducibility values of aTA-MIP-QCM sensor with 95% confidence interval

Concentration (ppm)	**Repeatability**		**Reproducibility**	
	R_P (%)	**95% CI**	**R_D (%)**	**95% CI**
10	71.31	±1.26	67.81	±0.97
50	93.70	±1.26	90.57	±1.32
100	94.47	±2.44	94.72	±1.57
200	96.92	±2.44	96.54	±1.88
400	98.53	±2.44	98.25	±2.02
600	99.27	±1.63	99.21	±1.28
800	99.45	±1.69	99.58	±0.90
1000	99.52	±1.78	99.33	±1.76

7.3.12. Extraction of volatile flavour compound (VFC) of cardamom samples using SPME and GC-MS technique

Four varieties (1 large and three small) of cardamom samples, labelled as SC-1, SC-2, SC-3, and LC-1, were collected to study the response of the developed aTA-MIP-QCM sensor. The sample preparation steps were followed, as mentioned in Chapter 2, section 2.3.2. 1 gm seed of each sample was crushed correctly and the sample was transferred to a 50 mL sample vial, properly sealed for headspace generation.

Optimisation of the absorption of VFCs was done by connecting a 1 cm 50/30 µm divinylbenzene / carboxen / polydimethylsiloxane [(DVB/CAR/PDMS); (Supelco, USA) stableflexTM, 24 Ga] SPME fiber with manual assembly holder (Supelco, USA) over the sample vials. In each case, the equilibration to absorb the vapour phase was maintained at room temperature for 10 mins. GC-MS analysis was executed using Agilent 7890A (Agilent Technologies Inc., Santa Clara) coupled to a quadruple triple-axis mass detector (Agilent MS-5975C) with wall coated open tubular column (WCOT), HP-5 MS (30 m×0.25 mm×0.25 µm), a 10 m Duraguard capillary column. The samples were desorbed at the injection port with a front inlet temperature of 250 ºC. Helium was used as the carrier gas at a flow rate of 1 mL/min. The column temperature was initially kept on hold for 1 minute at 45 ºC and ramped to 150 ºC at a rate of 2 ºC/min. It was kept on hold for 0 minutes and then again ramped to 220ºC at a rate of 8ºC/min. And finally kept on hold for 2 minutes. The temperatures of MS quadrupole and MS sources were kept fixed at 150ºC and 230ºC, respectively with 70 eV electron energy ($2.21e^{-0.5}$ Torr) and an auxiliary heater at 280ºC (Total Runtime 64.25 minutes).

7.3.13. Study of the aTA-MIP-QCM sensor with cardamom samples

Table 7.3 explains the percentage peak areas of the major VOC present in the samples as estimated by the GC-MS analysis. It is evident from the Table 7.3 that 1,8-cineole and α-terpinyl acetate occupy the majority area percentage of the chromatogram of small cardamom. The absence of α-terpinyl acetate can also be noticed in the case of large cardamom as described by many researchers [16,38].

Table 7.3. Correlation of aTA-MIP-QCM sensor response with GC-MS results

The % peak area of samples					
VOC	**SC-1**	**SC-2**	**SC-3**	**LC-1**	**Correlation with QCM response**
α-pinene	4.803	8.91	5.761	10.73	-0.915
β-pinene	1.287	6.02	0.666	2.985	-0.672
1,8-cineole	75.11	75	69.92	81.02	-0.919
γ-terpinene	1.379	1.22	1.354	1.83	-0.584
terpinen-4-ol	0.103	0	0.258	0.313	-0.035
α-terpinyl acetate	17.32	8.82	22.04	0	0.992
α-terpeniol	0	0	0	3.13	-0.756

α-pinene, β-pinene, γ-terpinene, and terpinen-4-ol occupy minor areas in the chromatogram but can be consistently noticed in the aroma profile of each of the samples. 5 gm of crushed seeds from each cardamom sample was kept in a 250 mL desiccator for approximately 50 mins. to generate enough headspace. 50 mL of the headspace generated from the samples were injected within the sensor chamber, and Fig. 7.18. shows the frequency shift induced by the aTA-MIP-QCM sensor for each of the aromas obtained from the sample. The amount of α-terpinyl acetate headspace VOC generation from the samples can be related to the various testing parameters like the weight of the sample, injection volume, headspace generation time, and volume of the generation of the SPME-GCMS analysis. The sensor obtained its equilibrium within 52 sec from the absorbance of the volatiles, which is evident from the frequency curve of highly sensitive behaviour. The sensor frequency shift obtained for samples SC-1, SC-2, SC-3, and LC-1 were shown in Fig. 7.18(a). The correlation factor of the frequency responses of the sensor with the obtained GC-MS estimates of α-terpinyl acetate obtained from each sample was calculated to be 0.9925, which is much higher than the correlation obtained with other VFCs obtained from the chromatogram.

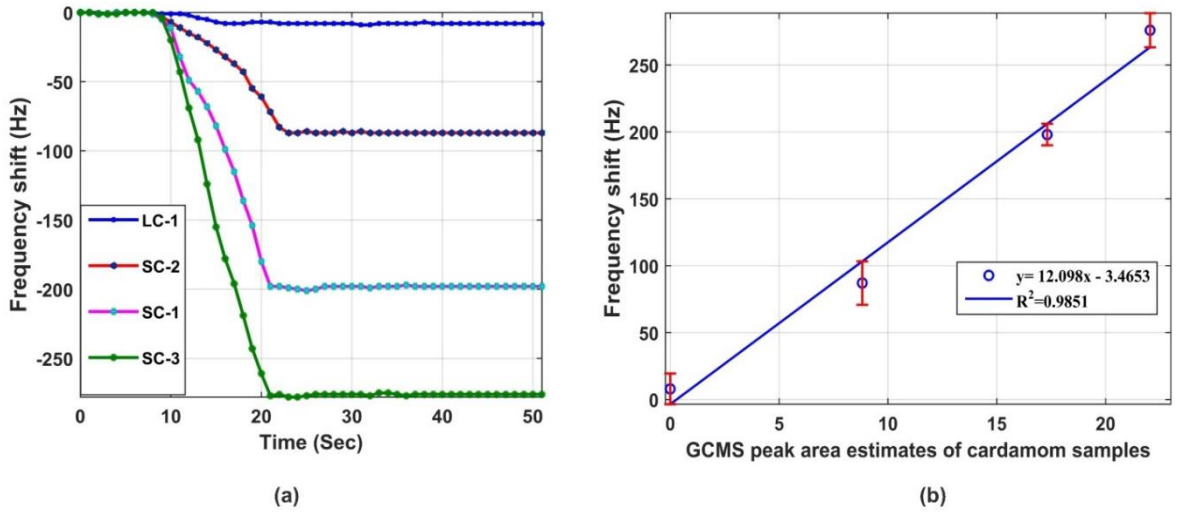

Fig. 7.18 (a). aTA-MIP-QCM sensor frequency shift at different cardamom samples at (27 ± 1) ºC, 67.7% RH, and standard atmospheric pressure, (b) Scatter plot for GC-MS estimates of the cardamom samples SC-1, SC-2, SC-3, and LC-1 respectively and its corresponding and aTA-MIP-QCM sensor response.

The bar plot of all the correlation coefficients of VOCs obtained from GC-MS of the samples, and their aTA-MIP-QCM sensor responses are shown in Fig. 7.19, which shows the accuracy and selectivity toward the detection of α-terpinyl acetate aroma.

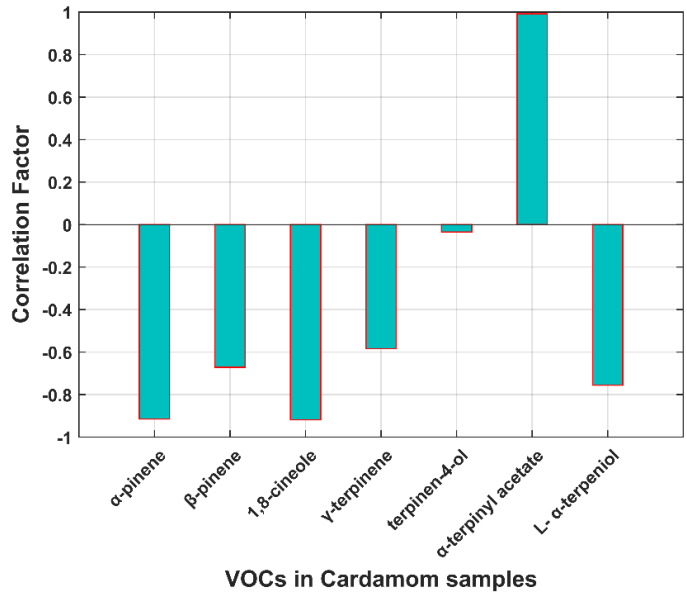

Fig. 7.19. Bar plot of all the correlation coefficients for cardamom VFCs obtained from GC-MS estimation with aTA-MIP-QCM sensor responses.

The scatter plot of the sensor frequency with GC-MS estimates was found to be linear with R^2 = 0.985, as shown in Fig. 7.18(b). Hence, it is pretty evident that the results procured from the aTA-MIP-QCM sensor are closely similar to those obtained from the GC-MS technique for four different cardamom samples.

7.3.14. Comparison of high-end techniques with the aTA-MIP -QCM sensor parameters

The performance of the as-prepared MIP sensor for detecting aTA had been compared with various known analytical instrumentation techniques using different sensitive column materials reported in the literature tabulated in Table 7.4. The mentioned techniques could detect aTA conforming to various sensor parameters with linear sensing ranges. The analytical instruments, however, are costly, time-consuming, and require expert individuals to operate. The experimental detection time for aTA VOC using aTA-MIP-QCM sensor ranged between 7 - 39 sec for the different sniffing cycles of 10-1000 ppm of aTA, which provided a quick sensing solution compared to other analytical techniques. The fabricated aTA-MIP-QCM sensor could be a low-cost and efficient alternative for detecting aTA with low sensing time.

Table 7.4. Comparison of aTA sensing parameters of the fabricated sensor with reported high-end techniques

Detection method	**Sensitivity**	**Linear range**	**LOD**	**LOQ**	**Sensing Time**	**Ref.**
DES-3 (deep eutectic solvent)-based HS-SME (Headspace-solvent microextraction)	-	2.129 (ng mL^{-1})	2.129 (ng mL^{-1})	7.099 (ng mL^{-1})	21.00 min	[39]
Fused silica capillary column coupled with a 5973-network mass detector equipped with HP5-MS	-	0.001(mg L^{-1})	0.05-50 (mg L^{-1})	-	29.54 min	[40]
Octadecylsilane (ODS) columns coated with Wakosil II C18 in isocratic mode	-	70.0-700.0 (µg mL^{-1})	2.76 (µg mL^{-1})	9.72 (µg mL^{-1})	88.56 min	[41]
Headspace single-drop microextraction (HS-SDME) mode DB-1701 capillary column with a flame ionisation detector (FID)	-	-	1.939 (ng mL^{-1})	6.957 (ng mL^{-1})	19.00 min	[42]
aTA-MIP-QCM sensor	0.3876 Hz/ppm	10-1000 ppm	4.46 ppm	14.86 ppm	7-39 sec	This work

7.4. Conclusion

This study has reported the customisation of a MIP-based QCM gas sensor for precisely detecting α-terpinyl acetate in cardamom. The sensor is highly responsive towards aTA and exhibits sufficient rejection of the competing volatiles of small cardamoms like1,8-cineole, α-pinene, and β-pinene. Several factors like mesoporous structure and the higher surface area of the adsorbent imprinted polymer ignite the sensitivity of the QCM gas sensor. The sensitivity of our fabricated sensor is 0.3876 Hz/ppm. The average repeatability and reproducibility of the sensor are obtained as 94.72% and 93.76%, respectively. The as-prepared sensor exhibited good reversibility and long-term stability towards aTA VOC for 30 days. The aTA-MIP-QCM sensor has shown a minor change in the frequency shift due to the change in relative humidity. The study also determines that the sensor is capable of detecting aTA aroma at various changes in a humid environment. The performance of the sensor has been tested with four different cardamom samples, and it has been found that the QCM frequency shift has a correlation of 0.9925 with gas chromatographic estimations of aTA. Thus, the aTA present in small cardamom can effectively and precisely be identified using imprinted polymer coating material. **Our developed QCM gas sensor can be a smart and sagacious alternative for devising methodologies to make qualitative differentiation among various types of small cardamom and subsequent grading based on the presence of aTA in the small cardamom samples.**

References

[1] PN Ravindran, K.J. Madhusoodanan, eds., Cardamom: The Genus Elettaria, CRC Press, London, 2002. https://doi.org/10.1201/9780203216637.

[2] Y. Hamamura, Food selection by silkworm larvae, Nature. 183 (1959) 1746–1747. https://doi.org/10.1038/1831746a0.

[3] A.-I. Gopalan, S. Komathi, N. Muthuchamy, K.-P. Lee, M.J. Whitcombe, L. Dhana, G. Sai-Anand, Functionalised conjugated polymers for sensing and molecular imprinting applications, (2019). https://nova.newcastle.edu.au/vital/access/manager/Repository/uon:37222;jsessionid=26C9938F2FF10005391B4E8C351B0E5E?exact=sm_creator%3A%22Whitcombe%2C+Michael+J.%22&sort=sort_ss_title%2F (accessed April 2, 2022).

[4] S. Suriyanarayanan, P.J. Cywinski, A.J. Moro, G.J. Mohr, W. Kutner, Chemosensors based on molecularly imprinted polymers, Top Curr Chem. 325 (2012) 165–265. https://doi.org/10.1007/128_2010_92.

[5] S.K. Jha, C. Liu, K. Hayashi, Molecular imprinted polyacrylic acids based QCM sensor array for recognition of organic acids in body odor, Sensors & Actuators: B. Chemical. Complete (2014) 74–87. https://doi.org/10.1016/j.snb.2014.07.098.

[6] C. Liu, L. Shang, H.-T. Yoshioka, B. Chen, K. Hayashi, Preparation of molecularly imprinted polymer nanobeads for selective sensing of carboxylic acid vapors, Anal Chim Acta. 1010 (2018) 1–10. https://doi.org/10.1016/j.aca.2018.01.004.

[7] G. Fang, H. Wang, Y. Yang, G. Liu, S. Wang, Development and application of a quartz crystal microbalance sensor based on molecularly imprinted sol-gel polymer for rapid detection of patulin in foods, Sensors and Actuators B: Chemical. C (2016) 239–246. https://doi.org/10.1016/j.snb.2016.06.099.

[8] J. Dai, Y. Zhang, M. Pan, L. Kong, S. Wang, Development and application of quartz crystal microbalance sensor based on novel molecularly imprinted sol-gel polymer for rapid detection of histamine in foods, J Agric Food Chem. 62 (2014) 5269–5274. https://doi.org/10.1021/jf501092u.

[9] H.F. Hawari, N.M. Samsudin, A.Y. Md Shakaff, Supri.A. Ghani, M.N. Ahmad, Y. Wahab, U. Hashim, Development of Interdigitated Electrode Molecular Imprinted Polymer Sensor for Monitoring Alpha Pinene Emissions from Mango Fruit, Procedia Engineering. 53 (2013) 197–202. https://doi.org/10.1016/j.proeng.2013.02.026.

[10] Z. Wang, W. Chen, S. Gu, J. Wang, Y. Wang, Discrimination of wood borers infested Platycladus orientalis trunks using quartz crystal microbalance gas sensor array, Sensors and Actuators B: Chemical. 309 (2020) 127767. https://doi.org/10.1016/j.snb.2020.127767.

[11] N. Iqbal, G. Mustafa, A. Rehman, A. Biedermann, B. Najafi, P.A. Lieberzeit, F.L. Dickert, QCM-Arrays for Sensing Terpenes in Fresh and Dried Herbs via Bio-Mimetic MIP Layers †, Sensors (Basel). 10 (2010) 6361–6376. https://doi.org/10.3390/s100706361.

[12] S. Dutta, P. Bhattacharjee, N. Bhattacharyya, Assessment of Shelf Lives of Black Pepper and Small Cardamom Cookies by Metal Oxide-Based Electronic Nose Using Spoilage Index, Food Bioprocess Technol. 10 (2017) 2023–2033. https://doi.org/10.1007/s11947-017-1962-8.

[13] W. Sroysee, S. Chunta, M. Amatatongchai, P.A. Lieberzeit, Molecularly imprinted polymers to detect profenofos and carbofuran selectively with QCM sensors, Physics in Medicine. 7 (2019) 100016. https://doi.org/10.1016/j.phmed.2019.100016.

[14] M. Herman F., Encyclopedia of Polymer Science and Technology, Concise, John Wiley & Sons, 2013.

[15] J. Phan, S. Koli, W. Minor, R.B. Dunlap, S.H. Berger, L. Lebioda, Human thymidylate synthase is in the closed conformation when complexed with dUMP and raltitrexed, an antifolate drug, Biochemistry. 40 (2001) 1897–1902. https://doi.org/10.1021/bi002413i.

[16] H.-L. Lu, C.-J. Lu, W.-C. Tian, H.-J. Sheen, A vapor response mechanism study of surface-modified single-walled carbon nanotubes coated chemiresistors and quartz crystal microbalance sensor arrays, Talanta. 131 (2015) 467–474. https://doi.org/10.1016/j.talanta.2014.08.027.

[17] D. Zhang, Y. Sun, Y. Zhang, Fabrication and characterisation of layer-by-layer nano self-assembled ZnO nanorods/carbon nanotube film sensor for ethanol gas sensing application at room temperature, J Mater Sci: Mater Electron. 26 (2015) 7445–7451. https://doi.org/10.1007/s10854-015-3378-4.

[18] E. Yilmaz, K. Mosbach, K. Haupt, Influence of functional and cross-linking monomers and the amount of template on the performance of molecularly imprinted polymers in binding assays, Anal. Commun. 36 (1999) 167–170. https://doi.org/10.1039/A901339C.

[19] C.J. Percival, S. Stanley, T.M. Galle, A. Braithwaite, M.I. Newton, G. McHale, W. Hayes, Molecular-imprinted, polymer-coated quartz crystal microbalances for the detection of terpenes, Anal Chem. 73 (2001) 4225–4228. https://doi.org/10.1021/ac0155198.

[20] M. Kikuchi, N. Tsuru, S. Shiratori, Recognition of terpenes using molecular imprinted polymer coated quartz crystal microbalance in air phase, Science and Technology of Advanced Materials. 7 (2006) 156–161. https://doi.org/10.1016/j.stam.2005.12.004.

[21] A. Kugimiya, T. Takeuchi, Molecularly Imprinted Polymer-Coated Quartz Crystal Microbalance for Detection of Biological Hormone, Electroanalysis. 11 (1999) 1158–1160. https://doi.org/10.1002/(SICI)1521-4109(199911)11:15<1158::AID-ELAN1158>3.0.CO;2-P.

[22] M. Yan, O. Ramström, Molecularly imprinted materials: science and technology, Marcel Dekker, New York, 2005.

[23] H.F. Lodish, Molecular Cell Biology, 4th ed., W.H. Freeman, New York, U.S.A, 2000. https://www.academia.edu/10355171/Molecular_Cell_Biology_5th_ed_Lodish_et_al (accessed April 2, 2022).

[24] K. Nakamoto, Infrared and Raman Spectra of Inorganic and Coordination Compounds, Part A: Theory and Applications in Inorganic Chemistry, 6th Edition | Wiley, 6th ed., John Wiley & Sons, Inc., 2009. https://www.wiley.com/en-in/Infrared+and+Raman+Spectra+of+Inorganic+and+Coordination+Compounds%2C+Part+A%3A+Theory+and+Applications+in+Inorganic+Chemistry%2C+6th+Edition-p-9780471743392 (accessed April 2, 2022).

[25] J. Lunagariya, N.S. Kumar, M. Asif, A. Dhar, R.L. Vekariya, Dependency of Anion and Chain Length of Imidazolium Based Ionic Liquid on Micellization of the Block Copolymer F127 in Aqueous Solution: An Experimental Deep Insight, Polymers. 9 (2017) 285. https://doi.org/10.3390/polym9070285.

[26] S. Bakhtiar, SA Bhawani, SR Shafqat, Synthesis and characterisation of molecular imprinting polymer for the removal of 2-phenylphenol from spiked blood serum and river water, Chemical and Biological Technologies in Agriculture. 6 (2019) 15. https://doi.org/10.1186/s40538-019-0152-5.

[27] P.X. Medina Rangel, S. Laclef, J. Xu, M. Panagiotopoulou, J. Kovensky, B. Tse Sum Bui, K. Haupt, Solid-phase synthesis of molecularly imprinted polymer nanolabels: Affinity tools for cellular bioimaging of glycans, Sci Rep. 9 (2019) 3923. https://doi.org/10.1038/s41598-019-40348-5.

[28] Y. Li, Y. Liu, J. Liu, J. Liu, H. Tang, C. Cao, D. Zhao, Y. Ding, Molecularly imprinted polymer decorated nanoporous gold for highly selective and sensitive electrochemical sensors, Sci Rep. 5 (2015) 7699. https://doi.org/10.1038/srep07699.

[29] A. Poma, A. Guerreiro, M.J. Whitcombe, E.V. Piletska, A.P.F. Turner, S.A. Piletsky, Solid-Phase Synthesis of Molecularly Imprinted Polymer Nanoparticles with a Reusable Template – "Plastic Antibodies," Adv Funct Mater. 23 (2013) 2821–2827. https://doi.org/10.1002/adfm.201202397.

[30] A.-M. Poller, E. Spieker, P.A. Lieberzeit, C. Preininger, Surface Imprints: Advantageous Application of Ready2use Materials for Bacterial Quartz-Crystal Microbalance Sensors, ACS Appl Mater Interfaces. 9 (2017) 1129–1135. https://doi.org/10.1021/acsami.6b13888.

[31] E. Preis, C. Widling, U. Scherf, S. Patil, G. Brunklaus, J. Schmidt, A. Thomas, Aromatic, microporous polymer networks with high surface area generated in Friedel–Crafts-type polycondensations, Polym. Chem. 2 (2011) 2186–2189. https://doi.org/10.1039/C1PY00251A.

[32] J. Xu, S. Ambrosini, E. Tamahkar, C. Rossi, K. Haupt, B. Tse Sum Bui, Toward a Universal Method for Preparing Molecularly Imprinted Polymer Nanoparticles with Antibody-like Affinity for Proteins, Biomacromolecules. 17 (2016) 345–353. https://doi.org/10.1021/acs.biomac.5b01454.

[33] B. Ding, M. Yamazaki, S. Shiratori, Electrospun fibrous polyacrylic acid membrane-based gas sensors, Sensors and Actuators B: Chemical. 106 (2005) 477–483. https://doi.org/10.1016/j.snb.2004.09.010.

[34] B. Mumyakmaz, A. Özmen, M.A. Ebeoğlu, C. Taşaltın, İ. Gürol, A study on the development of a compensation method for humidity effect in QCM sensor responses, Sensors and Actuators B: Chemical. 147 (2010) 277–282. https://doi.org/10.1016/j.snb.2010.03.019.

[35] S.P. Bhatia, C.S. Letizia, A.M. Api, Fragrance material review on alpha-terpineol, Food Chem Toxicol. 46 Suppl 11 (2008) S280-285. https://doi.org/10.1016/j.fct.2008.06.027.

[36] P. Sharma, A. Ghosh, B. Tudu, L.P. Bhuyan, P. Tamuly, N. Bhattacharyya, R. Bandyopadhyay, A. Chatterjee, Detection of linalool in black tea using a quartz crystal microbalance sensor, Sensors and Actuators B: Chemical. 190 (2014) 318–325. https://doi.org/10.1016/j.snb.2013.08.088.

[37] G. Sauerbrey, Verwendung von Schwingquarzen zur Wägung dünner Schichten und zur Mikrowägung, Z. Physik. 155 (1959) 206–222. https://doi.org/10.1007/BF01337937.

[38] M. Yang, J. He, Graphene oxide as quartz crystal microbalance sensing layers for detection of formaldehyde, Sensors and Actuators B: Chemical. 228 (2016) 486–490. https://doi.org/10.1016/j.snb.2016.01.046.

[39] B. Tang, W. Bi, H. Zhang, K.H. Row, Deep Eutectic Solvent-Based HS-SME Coupled with GC for the Analysis of Bioactive Terpenoids in Chamaecyparis obtusa Leaves, Chromatographia. 77 (2014) 373–377. https://doi.org/10.1007/s10337-013-2607-3.

[40] H. Sereshti, A. Rohanifar, S. Bakhtiari, S. Samadi, Bifunctional ultrasound assisted extraction and determination of Elettaria cardamomum Maton essential oil, Journal of Chromatography A. 1238 (2012) 46–53. https://doi.org/10.1016/j.chroma.2012.03.061.

[41] A. Porel, Y. Sanyal, A. Kundu, Simultaneous HPLC Determination of 22 Components of Essential Oils; Method Robustness with Experimental Design, Indian J Pharm Sci. 76 (2014) 19–30.

[42] B. Tang, M. Tian, KH Row, Determination of Terpenoids in Chamaecyparis obtusa Leaves by Headspace Single-Drop Microextraction with Gas Chromatography Detection, Analytical Letters. 47 (2014) 48–57. https://doi.org/10.1080/00032719.2013.832278.

Chapter 8

Conclusion and future scope

8.1. Concluding remarks

Cardamom is an aromatic spice having broad economic and medicinal benefits. It is considered the third costliest spice after saffron and vanilla. India is one of the leading producers and exporters of large and small cardamom worldwide. The spice thus has considerable influence on the Indian economy. Due to the high demand in the export market, the quality of cardamom must be ensured to be as good as possible and proper analysis and gradation of spices can alleviate better export opportunities, consumer appeal, and financial benefit to the producers. However, despite its benefits, the quality of the spice is not taken care of and suffers heavily due to improper post-harvest and gradation techniques. Gradations of cardamom are currently established based on the size of the pod, which does not necessarily reflect its aroma quality. Considering the importance of cardamom in the global market, it becomes necessary to bridge these shortcomings in a possible scientific manner.

Since cardamom is highly aromatic, the difference in the concentration of VOCs in the aroma can be an organoleptic criterion for determining its quality and price. A quantitative and qualitative approach for studying gas components, such as gas chromatography, has been utilised to characterise various aromatic compounds. Although this procedure is exceptionally selective, precise, and consistent, it is also expensive and tedious. Thus, there is a pressing need for sensory evaluation of VOCs using an electronic device that can simulate the human sense of smell and offer low-cost and rapid outputs.

Generally, an odour sensor contains a chemo-sensitive layer mounted onto the surface of a suitable physical transducer. Recently, QCM sensors are now attracting the attention of researchers and scientists because of their convenience of fabrication, efficiency and minimal cost compared to other transducers. There are several applications for QCM sensors, including food product's quality assurance, health care, environmental monitoring, etc.

This thesis focussed on the shortcomings mentioned above, and necessary research was conducted towards its solutions. Four important headspace volatiles responsible for the unique aroma of cardamom was recognised using SPME-guided GCMS, namely 1,8-cineole, α-terpinyl acetate, α-pinene, and β-pinene. Following this, four QCM sensors with suitable coating materials were

identified and fabricated for sensitive adsorption of the VOCs. Moreover, a low-cost microcontroller-operated QCM-based gas sensing device was developed to estimate volatiles using the fabricated sensors rapidly. The works described in this thesis address the research questions discussed in Chapter 1, section 1.7, that were based on the perennial problems in Indian market of cardamom.

The research work in this thesis initially focused on investigating the important volatiles present in the headspace of cardamom. *Chapter 2* discusses the different steps and sample preparation procedures for VOC detection from 21 large cardamoms and three small cardamom varieties. 1,8-cineole was found to be the most abundant HSV in large cardamom. It was also determined that 1,8-cineole has the most variability due to different post-harvesting methods. Moreover, small cardamom showed a different aroma profile due to the presence of α-terpinyl acetate alongside 1,8-cineole. The aroma profile showed variation among the cardamom varieties due to the presence of α-pinene and β-pinene to some extent in both large and small cardamom. The outcome of the chapter highlights the possibility of identifying various cultivars of cardamom based on their aroma, which addresses research question 1. Moreover, the results sorted out the critical VOC profile by GCMS responsible for cardamom's distinct aroma, which answered our research *question 2*.

Chapter 3 demonstrated the development of a portable gas sensing device to rapidly identify important cardamom VOCs using respective QCM sensors. The system was designed to be portable for the ease of field applications. The developed device housed a microcomputer, microprocessor, sensor sensing unit, and associated electrical circuits that showed real-time data acquisition capability of the sensor output. The setup was used extensively for the sensor fabrication, calibration, and experimental procedures for detecting the important VOCs in cardamom, presented in the following chapters. Chapter 3 thus provided the solution for research *question 3.*

Chapters 4, 5, 6, and 7 demonstrate the sensor fabrication steps and the study of sensing parameters for detecting four important VOCs responsible for forming unique aroma in cardamom. Two sensors were developed using natural vegetable oils like olive (OLV-QCM) and rice bran (RB-QCM) to detect the bicyclic monoterpenes β-pinene and α-pinene, respectively. In the case of bicyclic monoterpene ether, i.e., 1,8-cineole, castor oil was modified with phenol to enhance its

hydrophilicity and van der Waal's surface area, which facilitates its adsorption. In the case of α-terpinyl acetate, a MIP sensor was developed for highly sensitive adsorption. Due to its molecular complexity and lower vapour pressure, it was not suitable to selectively adsorb α-terpinyl acetate using oil-based coating procedures. The detailed sensor parameters for detecting α-pinene, β-pinene, 1,8-cineole, and α-terpinyl acetate are presented in Table 8.1.

Table 8.1. Details of the developed sensors

Sensing parameters	**Fabricated sensors**			
	OLV coated QCM sensor	**RB coated QCM sensor**	**Phe-CAS-Phe coated sensor**	**aTA-MIP-QCM coated sensor**
Target VOC	α-pinene	β-pinene	1,8-cineole	α-terpinyl acetate
Coating material	Olive oil	Rice bran oil	Phenolated phenyl ricinoleate	Molecularly imprinted polymer
Fabrication procedure	Nebulisation coating	Nebulisation coating	Nebulisation coating	Drop coating of oligomer solution
Sensitivity (Hz/ppm)	0.3105	0.367	0.262	0.387
Repeatability	95.14	95.91	94.25	94.72
LOD (ppm)	5.57	4.71	6.6	4.46
LOQ (ppm)	18.59	15.73	21.8	14.86
Long term stability (weeks)	14	8	3	4

It was revealed from the results, the sensor specifications are adequate in terms of sensitivity, selectivity, and other sensing factors for all cases. Electronic noses might benefit significantly from using these sensors to discriminate between cardamom samples and identify different quality

attributes based on the aroma. Moreover, the sensor responses and GCMS estimations have an excellent correlation which answers our research *question 4.*

In order to incorporate the developed sensor for real-time applications, a mathematical model was established, as discussed in chapter 6. The model aimed to find a relationship between the eluted 1,8-cineole VOC content with the amount of 1,8-cineole content in the natural sample. The sensor responses of the developed QCM-Phe-CAS-Phe sensor were used to predict the absolute 1,8-cineole content obtained through GC-MS-MS. Using predictive modelling-based techniques, the developed model can predict with an accuracy of 89.09%. This chapter thus answers research *question 5.*

The results and methodologies in this research work provided a positive approach towards detecting important VOCs in Indian cardamom. The findings of this thesis have the following key features:

i. The developed sensors for detecting monoterpenes VOCs in cardamom showed modest sensitive behaviours. Using different multivariate analysis, these sensors can be used as an array for determining qualitative parameters of cardamom and other spices.
ii. The methodologies in this thesis discussed the efficiency of vegetable oil as a coating material for α-pinene and β-pinene. These sensors can provide low-cost, natural and reusable solutions with least health hazards that can be widely implemented for sensing purposes with minimum fabrication complexities.
iii. The portable sensing system can be used in various agricultural and industrial applications that can provide real-time sensing features for a wide range of VOCs.

8.2. Future scope of research

The research work discussed in this thesis sought to investigate the usefulness of QCM-based gas sensors to detect important VOCs in Indian cardamom. The results obtained proved beneficial for aroma detection in Indian cardamom and opened up many opportunities for further research in many unexplored domains. Some of the critical research scopes are discussed below:

i. This thesis discusses the detection of the four most important volatiles in cardamom: α-pinene, β-pinene, α-terpinyl acetate, and 1,8-cineole using QCM sensors are discussed in this thesis. Developing QCM sensors for detecting other VOCs in the

headspace of cardamom like limonene, α-terpineol, γ-terpinene can be further done to achieve a more precise sensor array for correctly evaluating the quality of cardamom in an e-nose.

ii. Further research needed to be carried out regarding the sensitivity of different vegetable oils for the detection of lipophilic volatiles in different plant and food products. Vegetable oils are found to produce stable sensors with good sensitivity and reusability.

iii. The mathematical model to predict absolute 1,8-cineole content from the sensor output can be further developed using more datasets to improve the prediction accuracy. Moreover, similar modelling approaches can also be taken for other important volatiles in the aroma of cardamom. With a proper mathematical approach, it can be possible to predict the GCMS profile of a cardamom sample using an array of selected sensors, which can be a benchmark for the gradation system of cardamom.

iv. The developed system can be further enriched by integrating a predictive modelling algorithm with the internet of things (IoT) for easy access and interpretation of the data by the user.

v. The QCM sensor-based monitoring of volatilome of cardamom is essential for commercial purpose to examine the aroma quality during storage, because absorption of atmospheric moisture induces fungal infection and thereby altering the volatilome profile and aroma quality. Therefore, a structured database to identify the shelf-life of the cardamon seeds during preservation using the developed QCM sensors might be explored in the next phase of work.

vi. Above all, Cardamom cultivated in more different eco-geographical locations of India would be used for the above experiments to generate an extensive database so that it can be an essential databank for the commercialization of cardamom and to revamp the export market in future.

8.3. Conclusion

This thesis attempted to develop QCM gas sensors to detect the essential volatile organic compounds responsible for the distinct aroma of Indian cardamom. The global trade of cardamom suffers significantly due to the lack of quality control by modern technology and with the aid of high-throughput analysis during the spice post-harvest. Moreover, despite its abundant medicinal and culinary benefits, no proper gradation procedure is still not in vogue. Finding an appropriate

solution to this drawback was the primary motivation for this research. Due to its aromatic nature, QCM sensors coated with sensitive coating materials were developed to detect the vital volatiles in the aroma of cardamom. The development of the specific sensors for VOCs can be an initial advancement to replace the ongoing gradation system prevalent in the cardamom industry with a more scientific approach. Monitoring the quality of the spices can be achieved by determining their aroma profile which can lead to a broader field of artificial olfaction. The recommended methodologies may be applied effectively to evaluate the volatiles that is present in several other spices, fruits, and vegetables apart from cardamom. The development of a portable gas-sensing device along with the developed sensors can provide a low-cost, hassle-free solution for aroma detection in real-time. These findings and methodologies can be an essential reference to carry forward the research work for the quality assessment of cardamom based on aroma.

Nilava Debabhuti

25.07.2022